

New Insights into Circumstellar Disk Evolution in the Era of ALMA

Thesis by
Scott Alexander Barenfeld

In Partial Fulfillment of the Requirements for the
Degree of
Doctor of Philosophy in Astrophysics

The logo for the California Institute of Technology (Caltech), featuring the word "Caltech" in a bold, orange, sans-serif font.

CALIFORNIA INSTITUTE OF TECHNOLOGY
Pasadena, California

2019
Defended October 5, 2018

© 2019

Scott Alexander Barenfeld
ORCID: 0000-0001-5222-6851

All rights reserved

ACKNOWLEDGEMENTS

The list of people who have helped guide me to where I am today is too long to fit into a single section of my thesis. While there are so many people I would like to thank, I must start with my two advisors, John Carpenter and Anneila Sargent. Working with each of them has been an absolute privilege. John's high standards and attention to detail have constantly pushed me to be the best scientist that I can be. While his vision was instrumental in developing the project that would become my thesis, he always encouraged me to think independently about my research and find answers on my own. Though I did not begin working closely with Anneila until the second half of my time at Caltech, her influence has proven invaluable as well. Through the process of repeatedly returning paper drafts to me looking, as she put it, "like the Dead Sea Scrolls," she has made me a far better writer. I am extremely thankful for the encouragement she has given me in recent months to push ahead and finish my thesis more quickly than I thought was possible. I am also grateful to my thesis committee members, Dimitri Mawet, Chuck Steidel, and Phil Hopkins, and in particular to my committee chair, Lynne Hillenbrand, who served as my research advisor during my first two years at Caltech.

Of course, it takes more than just advisors to get someone through a Ph.D. I would therefore like to also thank Andrea Isella, Luca Ricci, and Tiffany Meshkat, all of whom I worked closely with during my time here, and of course, all of the administrators and staff in Cahill, who keep our department running smoothly. Looking beyond Caltech, I would not be where I am today if not for my undergraduate research advisors at the University of Rochester and Arecibo Observatory, Eric Mamajek, Eric Bubar, Chris Salter, and Tapasi Ghosh. And of course, Janet Fogg, who has been a parent-away-from-home to every student who has come through Rochester's Physics and Astronomy department. My time at Rochester was hugely transformative, thanks in large part to the lifelong friends I made there, including Marc Nuzzo, Gabrielle Mariano, and Rachel Blomberg. In addition, I will never forget the time I spent screaming my lungs out as part of the "actually pretty decent" University of Rochester Pep Band.

I want to thank all of my fellow graduate students with whom I have shared Cahill for making our department such an enjoyable place to be. In particular, I would like to thank Marin Anderson, who had the unfortunately luck of having a desk next to mine in our first year as I was learning how to juggle. It was fortunate for

me, however, as in addition to evidently having very quick reflexes, she has been a great friend ever since. Also, thank you to Swarnima Manohar, the only person I've ever met who enjoys Marvel movies as much as I do, and to Lee Rosenthal, a close second. Thank you to Gina Duggan for working so hard to make the department, and Caltech as a whole, a better place, and to Mark Duggan for all of the awesome game nights. Thank you to Ryan Monroe for all the fun times in the department and on the slopes of Mammoth. Broken thumb or not, I still beat you down the hill! Thank you to Jake Jencson, who has more love for the state of Ohio than I've ever seen in another human being, to Denise Schmitz, for some amazing sessions of Dungeons and Dragons, and to Rachel Theios, for all the adorable pictures of Bailey and all the times spent chatting in each others' offices when one of us needed a break. And last, but not least, thank you to Donal O'Sullivan, my officemate and best man, for giving a reason to look forward to coming into work every day.

As every graduate student knows, working towards a Ph.D. has its ups and downs. As such, I would like to thank Lee Coleman and the rest of the Caltech Counseling Center for getting me and so many others through our toughest moments. At times like those, it was always so helpful to have things to focus on outside of Caltech, which is why I am so grateful to Seed Consulting Group for the opportunity to volunteer with them in my spare time. Working with Seed was the most rewarding thing I have done during my time as a graduate student, and I would like to thank all of the consultants I teamed with for making Seed possible. Seed would not exist without the vision and passion of Ajay Bawa, so I am incredibly grateful to him for starting something that has been truly special to be a part of.

Of course, none of this would have happened without my parents. Whether through watching documentaries on the Discovery Channel, visiting the Bronx Zoo, or going on incredible adventures to see nature in person, my parents instilled in me a fascination with the natural world from a young age. As I've grown, they have always been incredibly supportive of whatever I decided to pursue, and were always there for me to turn to whenever I struggled. I am so grateful for the close relationship we still share. Beyond my parents, my extended family has played a huge part in my life, especially my grandparents. I still remember, while visiting my Grandfather in Florida during high school, watching back-to-back documentaries on String Theory and Stephen Hawking's latest ideas about black holes. I didn't understand a single word in either one, but I knew right then that physics and astronomy were what I wanted to pursue.

Finally, I could not be more grateful to my incredible wife, Faye. You have been the most supportive person anyone has ever had in their lives during our nearly ten years together. I could go on and on about just the last few weeks, as you've single-handedly gotten us ready to move to New York so that I could concentrate on my thesis. I cannot thank you enough for always being there for me no matter how difficult things have gotten. I cannot believe that when I started at Caltech, we had only just finished our first year of living together in campus housing, and now we are married and getting ready to make our second move across the country together. And after all this time, there is still no one I would rather spend 5 straight days stuck in a car with!

ABSTRACT

In recent decades, it has become clear that solar systems such as our own form within the circumstellar disks of gas and dust that surround young stars. Thus, to understand how these solar systems come to be, it is necessary to study the conditions within these disks. Until recently, such studies have required a focus on intrinsically brighter and younger disks that are easier to observe. However, a full picture of planet formation requires the characterization of older disks to determine how these systems change over time. The unprecedented capabilities of the Atacama Large Millimeter/submillimeter Array (ALMA) now present the opportunity to study populations of these disks in detail for the first time. In this thesis, I present a study of over 100 such disks in the 5-11 Myr old Upper Scorpius OB Association (Upper Sco) using ALMA, as well as Keck Observatory, with the aim of comparing the properties of these systems to younger disks in order to shed new light on disk evolution.

Following background discussion on disks and their evolution, ALMA measurements of the continuum and CO line fluxes of these disks at 0.88 mm are reported in Chapter 3. The continuum fluxes are used to show that the majority of these systems contain less than $1 M_{\oplus}$ of dust. It is then shown that dust masses around these stars are on average a factor of ~ 4.5 lower than their younger counterparts in the Taurus star-forming region, placing important constraints on the mass evolution of these systems. Finally, constraints on depletion of gas in these disks are discussed using the CO measurements.

The spatial distributions of the gas and dust within these Upper Sco disks are modeled in Chapter 4. The radial extents of gas and dust are measured and compared, with several systems showing evidence of the gas being more extended. The sizes of the dust disks are compared to younger systems, showing that these disks shrink by a factor of approximately three as they age. These results suggest that dust evolves from the outside-in within disks, perhaps through radial drift. Despite this evolution, dust disks in Upper Sco fall on the same correlation between size and millimeter luminosity as their younger counterparts. This implies a link between the radial structures of disks of different ages, perhaps indicating that these systems are composed of optically-thick dust substructure.

Of course, an understanding of planetary system formation would be incomplete

without accounting for the presence of stellar companions, which are common around young stars and are expected to shorten disk lifetimes by truncating their sizes. As such, Chapter 5 presents a search for stellar companions in the Upper Sco disk sample analyzed in Chapters 3 and 4. Using adaptive optics imaging and aperture masking observations with the NIRC2 instrument on the Keck II telescope, stellar companions are identified in 27 of 112 systems. It is then shown that the companion fraction of systems with disks is lower than those without, confirming the harmful effects of stellar companions on disks seen in younger systems. However, the fraction of disk systems in Upper Sco with a close companion is shown to match that of younger disks in Taurus. This indicates that these effects occur within the first \sim Myr of disk evolution, after which stellar companions have little to no effect. Additionally, while the millimeter luminosities of disks with stellar companions are observed to be lower than those around single stars in Taurus, there exists no such difference in Upper Sco. This provides further support for outside-in dust evolution, as the shrinking of disks around single stars would cause them by the 5-11 Myr age of Upper Sco to match the sizes and brightnesses of truncated disks in binary systems.

Taken together, the results presented in this thesis show the masses and radial extents of the dust-component of circumstellar disks decrease with age. This thesis concludes by summarizing these results and discussing their link within a scenario of outside-in dust evolution involving radial drift and dust substructure. To close, potential avenues are presented to continue the study of disk evolution with ALMA.

PUBLISHED CONTENT AND CONTRIBUTIONS

Barenfeld, S. A., et al. 2019. “The Effect of Binarity of Circumstellar Disk Evolution”. *ApJ* In Press.

S.A.B helped to write the observing proposal, led the observations, reduced and analyzed the data, organized collaborators, and wrote the manuscript.

Barenfeld, S. A., et al. 2017. “Measurement of Circumstellar Disk Sizes in the Upper Scorpius OB Association with ALMA”. *ApJ* 851, 85 (): 85, doi:10.3847/1538-4357/aa989d. arXiv: 1711.04045 [astro-ph.SR].

S.A.B analyzed the data, organized collaborators, and wrote the manuscript.

Barenfeld, S. A., et al. 2016. “ALMA Observations of Circumstellar Disks in the Upper Scorpius OB Association”. *ApJ* 827, 142 (): 142, doi:10.3847/0004-637X/827/2/142. arXiv: 1605.05772 [astro-ph.EP].

S.A.B analyzed the data, organized collaborators, and wrote the manuscript.

TABLE OF CONTENTS

Acknowledgements	iii
Abstract	vi
Published Content and Contributions	viii
Table of Contents	ix
List of Illustrations	xi
List of Tables	xx
Chapter I: Introduction	1
1.1 The Formation of Stars, Disks, and Planets	2
1.2 Properties of Circumstellar Disks	5
1.3 Thesis Summary	10
Chapter II: Circumstellar Disk Evolution	13
2.1 Dust Evolution	13
2.2 Mass Loss through Accretion	15
2.3 Photoevaporation	18
2.4 A Combined Picture of Disk Evolution	20
2.5 Transitional and Debris Disks	23
Chapter III: ALMA Observations of Circumstellar Disks in the Upper Scorpius OB Association	26
Abstract	27
3.1 Introduction	28
3.2 Stellar Sample	30
3.3 ALMA Observations	34
3.4 ALMA Results	35
3.5 Disk Properties in Upper Sco	63
3.6 Comparison Between Upper Sco and Taurus	68
3.7 Discussion	74
3.8 Summary	78
Acknowledgements	80
Chapter IV: Measurement of Circumstellar Disk Sizes in the Upper Scorpius OB Association with ALMA	81
Abstract	82
4.1 Introduction	83
4.2 Sample and Observations	84
4.3 Continuum Modeling	85
4.4 CO Modeling	102
4.5 Discussion	110
4.6 Summary	119
Acknowledgements	121
Chapter V: The Effect of Binarity on Circumstellar Disk Evolution	122

Abstract	123
5.1 Introduction	124
5.2 Sample and Observations	126
5.3 Candidate Companion Identification	132
5.4 Disks and Multiplicity in Upper Sco	145
5.5 Discussion	159
5.6 Summary	167
Acknowledgments	169
Chapter VI: Conclusions and Future Directions	171
Bibliography	176

LIST OF ILLUSTRATIONS

<i>Number</i>	<i>Page</i>
1.1 <i>Hubble Space Telescope</i> Wide Field Camera image of Orion 114-426. The edge-on disk can be clearly seen silhouetted against the background of the Orion Nebula. Images such as these offered definitive proof of the existence of circumstellar disks. Figure adapted from McCaughrean and O'dell (1996).	2
1.2 An overview of the formation and evolution of a star-disk system. The right column shows an illustration of each phase and left column shows the resulting SED. From top to bottom: initially, a dense core forms within a molecular cloud. The core then collapses into a protostar, with conservation of angular momentum forming a disk and bipolar outflow (Class 0 YSO). As the surrounding envelope begins to clear, the central star becomes visible. The remnants of the cloud continue to accrete onto the central star (Class I YSO). The envelope is then fully dissipated, leaving an unobscured star and disk (Class II YSO). After a few Myr, the disk is lost, leaving the central star and, potentially, planets and debris (Class III YSO). Figure adapted from Dauphas and Chaussidon (2011).	4
1.3 Two-dimensional map of regions probed by different wavelengths in a disk, based on the best-fit model to the SED of the young star GO Tau. Each colored area shows the part of the disk responsible for 80% of the continuum emission at the given wavelength. The trapezoid in the lower right encloses 80% of the disk mass in the model, showing that mass is most closely traced by millimeter continuum emission. Figure adapted from Andrews (2015).	6
1.4 Composite 1.3 mm and 0.87 mm ALMA image of the disk around HL Tau. With a spatial resolution corresponding to ~ 4 au, the image shows a pattern of bright and dark rings. Recent ALMA observations of several other disks reveal a similar pattern. Figure adapted from ALMA Partnership et al. (2015).	10

2.1	Fraction of disks detected through infrared excess as a function of age. Although disks are extremely common at 1-2 Myr ages, their frequency declines to less than 20% by an age of 5-10 Myr. This decrease occurs over slightly longer timescales for disks identified at 22 – 24 μm , possibly indicating a radial-dependent evolution. Figure from Gorti et al. (2016).	14
2.2	Fraction of young stars showing signs of accretion (red points) and infrared excess between 3.6 μm and 8 μm (blue squares) for stellar associations of different ages. The exponential fits to both sequences show that the gas and dust in the inner regions of disks disappear on similar timescales. Figure from Fedele et al. (2010).	17
2.3	Illustration of the standard picture of disk evolution. Initially, accretion dominates over mass loss due to photoevaporative and MHD-driven winds and governs the evolution of the gas within the disk. Millimeter and centimeter grains, meanwhile, drift inwards due to gas drag (top). Once the photoevaporation becomes comparable to accretion, a gap forms at $\sim 1 - 10$ au, cutting off the inner disk from replenishment by the outer disk (middle). The inner disk then rapidly accretes, directly exposing the outer disk to photoevaporation (bottom). Once this occurs, the outer disk is evaporated on a timescale of $\sim 10^5$ years. Figure adapted from Ercolano and Pascucci (2017).	22
2.4	Images of the debris disk around Fomalhaut in optical scattered light (panel a Kalas et al. 2013) and 70 μm (panel b Acke et al. 2012) and 1.3 mm (panel c MacGregor et al. 2017) thermal emission, showing the narrow ring structure commonly exhibited by debris disks. Figure adapted from Hughes, Duchene, and Matthews (2018).	24
3.1	Distribution of disk types, as defined by Luhman and Mamajek (2012), in the Upper Sco sample grouped by spectral type.	31
3.2	Continuum flux density at 0.88 mm as a function of spectral type for all targets in our sample. Black symbols show the primordial disks, while gray symbols represent the debris/evolved transitional disks. Arrows represent 3σ upper limits.	41
3.3	Images of the 0.88 mm continuum for the 58 primordial and debris/evolved transitional disks detected ($> 3\sigma$) in the Upper Sco sample. Each image is centered on the fitted position of the source and is $3'' \times 3''$ in size.	42

3.4	Left: real part of the visibilities as a function of projected baseline length for the 75 primordial disks in the Upper Sco sample. The phase center has been shifted to the centroid of the continuum for each source, or to the expected stellar position in the case of non-detections. The host star and its spectral type are given above each plot. Center: images of the 0.88 mm continuum and integrated CO $J = 3 - 2$ line, centered on the expected stellar position. Contour levels are given at the top of each image, with the point-source sensitivity at the bottom. Right: spectra of the CO $J = 3 - 2$ line. The yellow shaded region indicates, for 5σ detections, the velocity range given in Table 3.4 over which the line is integrated to measure the flux and generate the integrated intensity map. The aperture radii used to make the spectra are also given in Table 3.4.	43
3.4	Continued.	44
3.4	Continued.	45
3.4	Continued.	46
3.4	Continued.	47
3.4	Continued.	48
3.4	Continued.	49
3.4	Continued.	50
3.4	Continued.	51
3.4	Continued.	52
3.4	Continued.	53
3.4	Continued.	54
3.4	Continued.	55
3.5	Same as Figure 3.4, but for the 31 debris/evolved transitional disks in the Upper Sco sample.	56
3.5	Continued.	57
3.5	Continued.	58
3.5	Continued.	59
3.5	Continued.	60
3.5	Continued.	60
3.6	Moment 1 maps showing the mean LSRK velocity of the $^{12}\text{CO } J = 3 - 2$ line for all sources detected ($> 5\sigma$) in CO. Each image is centered on the expected stellar position. A color bar indicating the velocity range of each map in km s^{-1} is shown at the top of each map.	63

3.7	Disk dust mass as a function of stellar mass for the Taurus (orange) and Upper Sco (black) primordial disk samples. Upper limits (3σ) are plotted as arrows. Typical error bars are shown in the upper left.	68
3.8	Stacked continuum image of the debris/evolved transitional disks which are not detected. Four sources were excluded due to the possibility of being identified as disks due to contamination from background sources (see the text). The flux density inside a $0''.4$ radius aperture at the center of the image is 0.03 ± 0.05 mJy.	69
3.9	Ratio of disk dust mass to stellar mass as a function of stellar mass for the Taurus (orange) and Upper Sco (black) primordial disk samples. Upper limits (3σ) are plotted as arrows. Typical error bars are shown in the upper right. The probability that the dust mass over stellar mass values in each sample are drawn from the same distribution is $p = 1.4 \times 10^{-7} - 4.8 \times 10^{-7}$	72
3.10	Cumulative distribution of the ratio of disk dust mass to stellar mass in Taurus and Upper Sco for the primordial disks. The shaded regions show the 68.3% confidence intervals of the distributions. Using the Kaplan–Meier estimate of the mean of $\log(M_{\text{dust}}/M_*)$ in Taurus and Upper Sco, we find that $\Delta\langle\log(M_{\text{dust}}/M_*)\rangle = 0.64 \pm 0.09$, with (M_{dust}/M_*) a factor of ~ 4.5 lower in Upper Sco than in Taurus.	73
3.11	$^{12}\text{CO } J = 3 - 2$ flux versus 0.88 mm continuum flux density for the primordial disks in our Upper Sco sample. Upper limits in the CO and continuum flux are shown with arrows. The gray circles are upper limits for both the CO and continuum. Black points show CO and continuum detections.	76
4.1	ALMA 0.88 mm observed, model, and residual images corresponding to the best-fit dust model parameters for each source. The real part of the deprojected visibilities for the observations (solid points) and best-fit model (solid curve) are also shown as a function of baseline length.	91
4.1	Continued.	92
4.1	Continued	93
4.1	Continued	94
4.1	Continued	95
4.1	Continued	96
4.1	Continued	97

4.1	Continued	98
4.1	Continued	99
4.1	Continued	100
4.1	Continued	101
4.2	Observed, model, and residual images corresponding to the best-fit CO model parameters for each source. The real part of the deprojected visibilities for the observations (solid points) and best-fit model (solid curve) are also shown as a function of baseline length.	103
4.2	Continued.	104
4.2	Continued	105
4.2	Continued	106
4.2	Continued	107
4.3	Observational and model fluxes for CO $J = 3-2$ emission for sources detected in the continuum, for models with (left panel) and without (right panel) photodissociation. Model fluxes were calculated based on the expected CO emission given the disk dust properties, as discussed in Section 4.4. CO detections are shown as black points, while upper limits are shown with blue arrows. The four well-constrained sources with larger CO outer radii than dust outer radii are shown as stars. Horizontal error bars represent the 68.3% confidence range for the model fluxes. The dashed line represents agreement between the model and observed fluxes.	111
4.4	Posterior distributions of dust outer radius for the 25 disks with continuum signal-to-noise of at least 15. The distributions are sharply peaked around the best-fit values (dashed lines), indicating that these disks are well-constrained to be compact. The blue shaded regions show the 68.3% confidence range for the outer radii.	112
4.5	Continuum (black circles) and CO (open circles) deprojected visibilities for the sources with well-constrained dust and CO outer radii. The black and blue curves show the best-fit models for the dust and CO, respectively. Four sources, 2MASS J16001844-2230114, 2MASS J16075796-2040087, 2MASS J16123916-1859284, and 2MASS J16142029-1906481, exhibited detectable CO emission extending beyond their dust emission.	114

- 4.6 best-fit CO and dust outer radii for sources where both are well constrained. Four sources, 2MASS J16001844-2230114, 2MASS J16075796-2040087, 2MASS J16123916-1859284, and 2MASS J16142029-1906481, have CO outer radii larger than their dust outer radii. 115
- 4.7 Dust effective radius versus continuum flux density at 0.88 mm for circumstellar disks in Taurus and Ophiuchus (gray points, Tripathi et al. 2017) and Upper Sco (black points, this work). Flux densities have been scaled to a distance of 140 pc. The dashed line shows the disk size-luminosity relation from Tripathi et al. (2017), which has been extrapolated to the flux densities of the Upper Sco disks. The Upper Sco sources shown are those with a continuum signal-to-noise of at least 15. 118
- 5.1 Projected separations and K magnitudes of the 79 detected sources around Upper Sco stars with disks. We consider sources within $2''$ and brighter than $K = 15$ to be candidate companions. This region is shown with dashed lines. A number of sources outside these limits may also be physically bound, but we expect significant background contamination among these sources. Red circles show sources that met our bound criteria and for which Gaia data was available, while blue stars show sources with Gaia data that did not meet our criteria. Sources with Gaia data are also shown in Figure 5.2. The yellow circles show sources for which no Gaia data was available. The grayscale background indicates the fraction of primary stars in the sample where the observations are sensitive to each K magnitude and separation. 143
- 5.2 Color-magnitude diagram of Upper Sco primaries in our sample (gray points) and additional sources that meet (red circles) and fail to meet (blue stars) our criteria of separation $< 2''$ and $K < 15$ to be considered candidate companions. Sources that meet our criteria lie along the same color-magnitude sequence as the Upper Sco primaries, as expected. Sources outside of these criteria are typically bluer and fainter than this sequence, consistent with background stars. 144

5.3	Parallaxes (left) and proper motions (right) of all sources in the Gaia DR2 Catalog within $1'$ of the targets in our Upper Sco disk sample. Most sources have parallaxes and proper motions close to zero, as expected for background objects. The black points show the primaries and candidate wide companions. The candidate wide companions have parallaxes and proper motions similar to their primaries and clearly distinct from the background sources.	145
5.4	NIRC2 K' images of the Upper Sco disk systems with new companions discovered by imaging in this survey. The angular extent of each image is indicated for each panel.	148
5.5	ALMA 880 μm continuum images of the Upper Sco systems with disks and companions in this sample. This excludes 2MASS J16033471-1829303, which was not observed with ALMA. The relative positions of the primary (blue “X”) and companion(s) (red “+”) are overlaid. SEDs of the seven sources where the millimeter-wavelength emission cannot be conclusively assigned to the primary or secondary are shown in Figure 5.6.	149
5.5	Continued.	150
5.6	Infrared SEDs of the systems in Figure 5.5 for which the millimeter-wavelength emission cannot be conclusively assigned to the primary or secondary. Stellar photospheric emission is estimated assuming blackbody emission with the stellar parameters calculated in Barenfeld et al. (2016). With the exception of 2MASS J16043916-1942459, all systems show excess at wavelengths $\leq 8\mu\text{m}$, indicating that warm dust is present around the primary and/or companion(s) in these systems.	151
5.6	Continued.	152
5.7	Spectral type distributions of Upper Sco primary stars with (red) and without (cyan) disks. This disk sample includes 62 systems with spectral types later than M3, compared to only two such systems without disks. Restricting to spectral types M3 and earlier, the samples are consistent with being drawn from the same parent distribution.	155

- 5.8 Apparent magnitude detection limits as a function of separation for Upper Sco disk-hosts with no candidate companions and spectral types of M3 or earlier. The dashed curves show the contrast limits for the three sources with poor tip-tilt in this spectral type range. The blue points show the companions found by Kraus et al. (2008) among a sample of Upper Sco stars without disks. The majority of observations in the current disk sample were sensitive enough to have detected all of these companions if they were present around the disk-hosting stars. Under the assumption that the stars with disks have the same population of companions as those without disks, we would have only expected to miss approximately two to three of these companions due to lower sensitivities. 157
- 5.9 Total 880 μm continuum flux density and project companion separations of Upper Sco systems with primordial disks. Flux densities have been scaled to a common distance of 145 pc. Single stars are shown in the hatched region to the right of the figure. Taurus systems from Akeson et al. (2019) are shown in blue. Unlike in Taurus, where disks are significantly fainter in systems with companions, the brightness distributions of disks in systems with and without companions are indistinguishable in Upper Sco. 162
- 5.10 Cumulative distributions of 880 μm continuum flux density for the Taurus (left) and Upper Sco (right) systems shown in Figure 5.9, calculated using the Kaplan-Meier product-limit estimator. Flux densities have been scaled to a common distance of 145 pc. In the case of Upper Sco, the distribution is only shown to the flux density of the faintest detection. Below this, the assumptions of the Kaplan-Meier product-limit estimator are violated, as all sources are upper limits. In Taurus, single stars are significantly brighter than systems with companions within a projected separation of 300 au. In Upper Sco, however, the brightnesses are similar. 163

- 5.11 CO $J = 3 - 2$ integrated line fluxes versus projected companion separations of Upper Sco systems with disks. Fluxes have been scaled to a common distance of 145 pc. Single stars are shown in the hatched region to the right of the figure. Although the distributions of fluxes for the single stars and systems with companions within 300 au are statistically indistinguishable, 11 out of 37 single-star systems with fluxes below 0.5 Jy km s^{-1} are detected, compared to none of the 14 such systems with companions separated by less than 300 au. 164
- 5.12 Cumulative distributions of the CO $J = 3 - 2$ integrated line fluxes of Upper Sco systems with disks, calculated using the Kaplan-Meier product-limit estimator. Fluxes have been scaled to a common distance of 145 pc. The distribution is only shown to the flux of the faintest detection. Below this, the assumptions of the Kaplan-Meier product-limit estimator are violated, as all sources are upper limits. The log-rank and Peto & Peto Generalized Wilcoxon two-sample tests cannot distinguish between the flux distributions of single stars and systems with a companion within a projected separation of 300 au. 165
- 6.1 Cumulative dust mass distributions of different stellar regions and associations. There is a clear evolutionary trend, with the 1-3 Myr Taurus (Andrews et al. 2013), Lupus (Ansdell et al. 2016), and Chamaeleon I (Pascucci et al. 2016) regions exhibiting similar dust masses to one another, while the 3-5 Myr old σ Orionis (Pascucci et al. 2016) and 5-11 Myr old Upper Sco (Barenfeld et al. 2016, this thesis) regions show successively lower dust masses. Dust masses in the ~ 1 Myr old Orion Nebula Cluster appear lower than those of similarly-aged disks in Taurus, Lupus, and Chamaeleon I, although these masses may be underestimated (Eisner et al. 2018). Figure from Eisner et al. (2018). 173

LIST OF TABLES

<i>Number</i>	<i>Page</i>
3.1 Stellar Properties	32
3.1 Stellar Properties	33
3.1 Stellar Properties	34
3.2 Observations	35
3.3 Secondary Source Properties	37
3.4 Continuum and CO $J = 3 - 2$ Flux Measurements	38
3.4 Continuum and CO $J = 3 - 2$ Flux Measurements	39
3.4 Continuum and CO $J = 3 - 2$ Flux Measurements	40
3.5 Derived Dust Masses	64
3.5 Derived Dust Masses	65
3.5 Derived Dust Masses	66
4.1 Continuum Fitting Results	89
4.1 Continuum Fitting Results	90
4.2 Secondary Source Properties	90
4.3 CO Fitting Results	108
5.1 Upper Sco Disk Sample	127
5.1 Upper Sco Disk Sample	128
5.1 Upper Sco Disk Sample	129
5.2 Results from Previous Surveys	130
5.3 Newly Detected Sources	136
5.3 Newly Detected Sources	137
5.4 Contrast Limits for Systems without Detected Companions	137
5.4 Contrast Limits for Systems without Detected Companions	138
5.4 Contrast Limits for Systems without Detected Companions	139
5.4 Contrast Limits for Systems without Detected Companions	140
5.4 Contrast Limits for Systems without Detected Companions	141
5.4 Contrast Limits for Systems without Detected Companions	142
5.5 Candidate Wide Companions from Gaia	146
5.5 Candidate Wide Companions from Gaia	147
5.6 Upper Sco Systems without Disks	153
5.6 Upper Sco Systems without Disks	154

Chapter 1

INTRODUCTION

Among the oldest pursuits in science is the quest to understand where we came from and how the Earth came to be. We now know that the Earth, along with the other planets in our solar system, formed in a disk of gas and dust around the young Sun. The idea of the solar system forming from a disk dates back to the 18th century and the works of Kant (1755) and Laplace (1796) as an explanation for the coplanar orbits of the planets. Two centuries later, the concept of circumstellar disks entered into modern astronomy in the 1960s as a natural consequence of angular momentum conservation during star formation (e.g., Hoyle 1960; Cameron 1962). In the following two decades, observational evidence of disks mounted, including the detection of excess continuum and line emission from young stars as well as polarization measurements consistent with disk-like structures (see review by Shu, Adams, and Lizano 1987, and references therein). A key step forward in the understanding of these objects came with the *IRAS* satellite, which was used to measure the infrared spectral energy distributions (SEDs) of a large number of young stars and show that these observations could be explained by thermal emission from an irradiated disk (Adams and Shu 1986; Adams, Lada, and Shu 1987, 1988; Kenyon and Hartmann 1987). Final proof of the existence of circumstellar disks came with direct images of these systems using the first millimeter interferometers, as well as the *Hubble Space Telescope* (O'dell, Wen, and Hu 1993; O'dell and Wen 1994; McCaughrean and O'dell 1996, see Figure 1.1).

In the years since, we have amassed a considerable amount of knowledge on circumstellar disks. Infrared surveys of hundreds of young stars with the *Spitzer Space Telescope* and *Widefield Infrared Survey Explorer (WISE)* (e.g., Gutermuth et al. 2004; Hartmann et al. 2005; Megeath et al. 2005; Carpenter et al. 2006; Lada et al. 2006; Sicilia-Aguilar et al. 2006; Balog et al. 2007; Barrado y Navascués et al. 2007; Cieza et al. 2007; Dahm and Hillenbrand 2007; Hernández et al. 2007a, 2007b; Flaherty and Muzerolle 2008; Gutermuth et al. 2008; Hernández et al. 2008; Luhman and Mamajek 2012) have revealed the near ubiquitous presence of disks around $\sim 1 - 2$ Myr old stars and the subsequent decline in disk frequencies by an age of $\sim 5 - 10$ Myr (Hernández et al. 2008; Ribas et al. 2014). Meanwhile, a new generation of millimeter interferometers such as the Submillimeter Array, the



Figure 1.1: *Hubble Space Telescope* Wide Field Camera image of Orion 114-426. The edge-on disk can be clearly seen silhouetted against the background of the Orion Nebula. Images such as these offered definitive proof of the existence of circumstellar disks. Figure adapted from McCaughrean and O'dell (1996).

Combined Array for Research in Millimeter-wave Astronomy, and the Plateau de Bure interferometer were used to obtain resolved images of individual disks, revealing the total masses and spatial distributions of gas and dust in these systems (e.g., Kitamura et al. 2002; Andrews and Williams 2007; Andrews et al. 2009; Isella, Carpenter, and Sargent 2009, 2010; Guilloteau et al. 2011; Andrews et al. 2013). The concurrent discovery of thousands of planets beyond our solar system with surveys such as *Kepler* (e.g., Borucki et al. 2010; Wright et al. 2011; Batalha and Kepler Team 2012; Burke et al. 2014) has prompted renewed interest in understanding the origin of these diverse planetary systems. We have now entered a new era in the study of disks and planet formation with the development of the Atacama Large Millimeter/submillimeter Array (ALMA). This new telescope, offering an order of magnitude improvement in sensitivity and resolution over previous millimeter interferometers, has opened a new window into the study of how solar systems are born and promises to continue delivering groundbreaking results for years to come.

1.1 The Formation of Stars, Disks, and Planets

The process of solar system formation is summarized in Figure 1.2, following the nomenclature introduced by Lada and Wilking (1984). The story begins with giant molecular clouds (GMCs) (see reviews by Shu, Adams, and Lizano 1987; Dobbs et al. 2014). Within these regions of molecular hydrogen, overdense filaments

fragment and collapse under their own gravity into hydrostatically supported cores (André et al. 2014, and references therein). Once enough gas accretes onto a core, it collapses further, forming a protostar at the center. At this stage, the protostar remains heavily obscured, lacking observable emission short of $\sim 25 \mu\text{m}$, and is often referred to as a Class 0 young stellar object (YSO, André, Ward-Thompson, and Barsony 1993). As the surrounding envelope continues its collapse, conservation of angular momentum leads to the formation of a rotationally supported disk (e.g., Shu, Adams, and Lizano 1987; Li et al. 2014). Within ~ 0.5 Myr, the newly formed star-disk system enters the Class I phase as the central star becomes visible (Evans et al. 2009). The remnants of the surrounding envelope continue to accrete onto the star until the supply of gas is exhausted by an age of ~ 1 Myr, leaving the young star and disk as an unobscured Class II YSO. In these early stages, the system is often referred to as a protoplanetary or primordial disk. Over the next several million years, the disk itself will dissipate, leaving behind a Class III YSO composed of the central star orbited by any debris and planets that may have formed within the disk.

The presence of a stellar companion complicates the above picture. Given that binarity is common among YSOs (Ratzka, Köhler, and Leinert 2005; Kraus et al. 2008; Lafrenière et al. 2008; Kraus et al. 2011; Chen et al. 2013; Cheetham et al. 2015), such companions have an important role to play in shaping the evolution of disks. Gravitational interactions between a disk and stellar companion are expected to tidally truncate the disk, hastening its subsequent evolution and dissipation (Papaloizou and Pringle 1977; Artymowicz and Lubow 1994; Pichardo, Sparke, and Aguilar 2005). Indeed, observations show that disks are less common in systems with a close stellar companion (Bouwman et al. 2006; Cieza et al. 2009; Kraus et al. 2012; Cheetham et al. 2015; Daemgen et al. 2016; Long et al. 2018), while also being fainter at millimeter wavelengths (Jensen, Mathieu, and Fuller 1994, 1996; Harris et al. 2012). Despite these effects, results from *Kepler* show that planet formation still occurs in binary systems (e.g., Dupuy et al. 2016), although less frequently than around single stars (Wang et al. 2014a, 2014b, 2015a, 2015b; Kraus et al. 2016).

Once a circumstellar disk forms, it provides the raw material necessary for planet formation through a mechanism known as core accretion (see review by Johansen et al. 2014). This process begins with the growth of sub-micron-sized dust grains into millimeter- and centimeter- sized pebbles through collisional “sticking.” These pebbles then grow further through the transfer of mass from smaller particles to

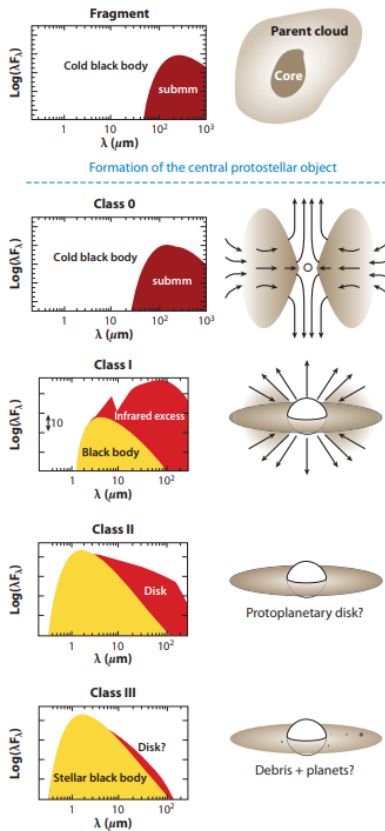


Figure 1.2: An overview of the formation and evolution of a star-disk system. The right column shows an illustration of each phase and left column shows the resulting SED. From top to bottom: initially, a dense core forms within a molecular cloud. The core then collapses into a protostar, with conservation of angular momentum forming a disk and bipolar outflow (Class 0 YSO). As the surrounding envelope begins to clear, the central star becomes visible. The remnants of the cloud continue to accrete onto the central star (Class I YSO). The envelope is then fully dissipated, leaving an unobscured star and disk (Class II YSO). After a few Myr, the disk is lost, leaving the central star and, potentially, planets and debris (Class III YSO). Figure adapted from Dauphas and Chaussidon (2011).

larger particles during destructive collisions, growing into kilometer-sized planetesimals on a timescale of ~ 1 Myr (Windmark et al. 2012; Garaud et al. 2013). A recent modification to this theory is the “streaming instability” in which interactions between gas and centimeter to meter sized solid particles in the disk cause overdense regions of solids to form (Youdin and Goodman 2005). These overdensities can become gravitationally unstable and collapse directly into 100-1000 km-sized planetesimals (Johansen et al. 2007; Johansen, Klahr, and Henning 2011; Kato, Fujimoto, and Ida 2012). Once planetesimals form through either mechanism, they

rapidly accrete smaller bodies through gravitational focusing and grow to planetary sizes, large enough to begin accreting gas. If any such planetary embryos reach a critical solid core mass of $10 M_{\oplus}$, runaway accretion of gas occurs and a gas giant planet is formed. Cores that do not reach this size in time may become Neptune-mass gaseous planets or smaller terrestrial planets. In this way, the lifetime of gas within a disk sets a limit on the timescale for giant planet formation. In addition, the timescale to grow dust grains into giant planet cores and terrestrial planets is determined by the density of solids within the disk. Thus, the distribution of mass within a disk, and how this varies over time, controls the disk's ability to form planets.

1.2 Properties of Circumstellar Disks

Dust Properties

Thermal emission from dust is used to study circumstellar disks across the electromagnetic spectrum (see review by Andrews 2015). Radiation from the central star is absorbed by dust grains at the disk surface and is re-emitted either deeper into the disk, setting the internal temperature structure, or out into space where it can eventually be observed on Earth. Emission at different wavelengths originates in distinct regions of the disk due to optical depth effects and radial temperature variations (see Figure 1.3). For example, while near-infrared emission can be used to probe the surface of the inner disk, millimeter observations are required to study the midplane of the outer disk where most of the mass resides.

Because dust continuum emission is optically thin at millimeter wavelengths, the measured millimeter flux density is proportional to the total emitting area of the dust grains. Given an assumed dust opacity, this can be used to calculate the total dust mass as:

$$M_d = \frac{S_\nu d^2}{\kappa_\nu B_\nu(T_d)}, \quad (1.1)$$

where S_ν is the continuum flux density, d is the distance of the disk from Earth, κ_ν is the opacity, and $B_\nu(T_d)$ is the Planck function for the dust temperature, T_d . The dust temperature is determined by the vertical height and flaring angle of the disk (see Section 1.2), while the opacity depends on the grain composition and size distribution. Current models of dust composition, based on expected chemical processes in disks and the ISM as well as measured compositions of meteorites, asteroids, and comets (e.g., Lodders 2003), suggest that disk dust grains are primarily composed of silicates, metallic compounds, water ice, and carbonaceous material

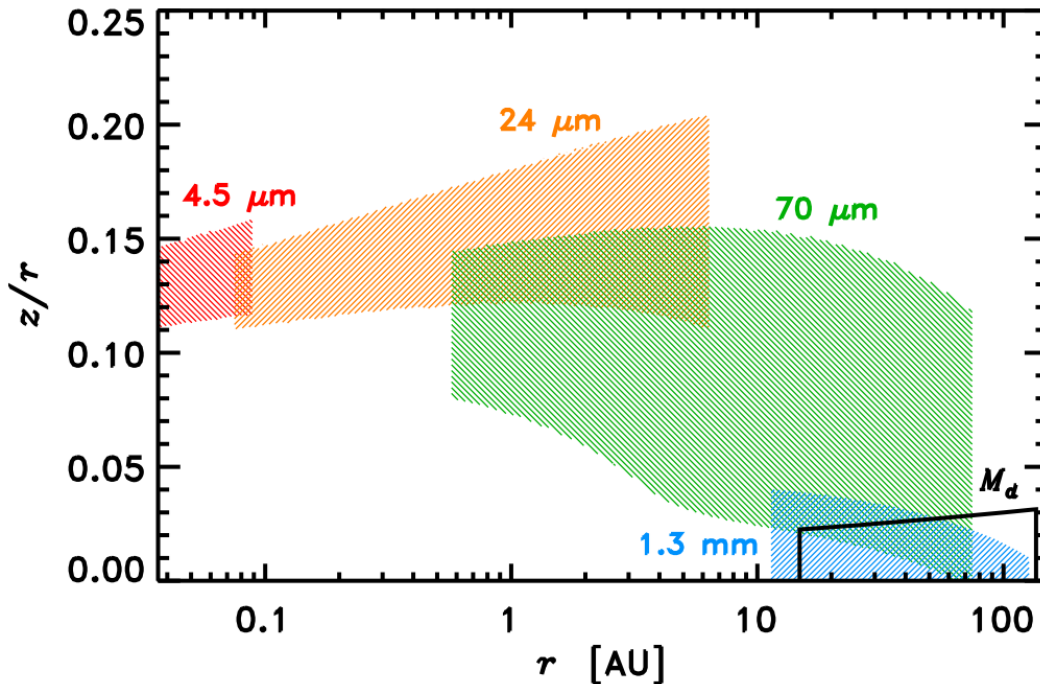


Figure 1.3: Two-dimensional map of regions probed by different wavelengths in a disk, based on the best-fit model to the SED of the young star GO Tau. Each colored area shows the part of the disk responsible for 80% of the continuum emission at the given wavelength. The trapezoid in the lower right encloses 80% of the disk mass in the model, showing that mass is most closely traced by millimeter continuum emission. Figure adapted from Andrews (2015).

(e.g., Pollack et al. 1994). Emission features in the mid-infrared spectra of disks confirm the presence of these components in disks (see review by Watson 2009, and references therein).

Dust grains emit most efficiently at a wavelength similar to their size (e.g., Testi et al. 2014). Thus, infrared observations are sensitive to a different set of grains than millimeter observations. This dependence of emitting wavelength on grain size can be used to constrain the size distribution of grains within a disk. For a full population of grains, optically thin millimeter and centimeter wavelength emission can be parameterized as a function of frequency as $S_\nu \propto \nu^{2+\beta}$, where β encapsulates the grain emission properties, including the size distribution. For sub-micron-sized grains in the ISM, $\beta \sim 2$ (Hildebrand 1983; Goldsmith, Bergin, and Lis 1997; Finkbeiner, Davis, and Schlegel 1999; Li and Draine 2001). In a disk, the presence of larger grains causes β to decrease, flattening the slope of the millimeter/centimeter SED. Observations of numerous disks have revealed values

of β less than one, indicating the presence of centimeter-sized grains (Beckwith and Sargent 1991; Mannings and Emerson 1994; Andrews and Williams 2005; Wilner et al. 2005; Lommen et al. 2007, 2009; Ricci et al. 2010b, 2010a; Ubach et al. 2012; Pérez et al. 2012).

Gas Properties

While dust is the most commonly observed component of primordial circumstellar disks, gas dominates the total mass of these objects. Though the vast majority of this gas is in the form of molecular hydrogen, this molecule is difficult to detect in disks due to its lack of a dipole moment (e.g., Carmona et al. 2008). As such, the most common method to estimate the gas mass of disks is to measure the dust mass and assume a gas-to-dust mass ratio, typically 100 based on this ratio in the interstellar medium (ISM Bohlin, Savage, and Drake 1978).

Direct observations of gas most commonly use CO as a tracer of the total gas mass. With its abundance relative to other gas species and rotational transitions easily observable at millimeter wavelengths, CO has seen wide usage in studies of disk chemistry, kinematics, and mass (e.g., Dutrey, Guilloteau, and Simon 2003; Chapillon et al. 2008; Isella et al. 2010; Williams and Best 2014). As the emission lines of ^{12}CO are optically thick in primordial disks, these lines can only be used to study the disk surface. Thus, to probe deeper within the disk and estimate a total mass, lines of ^{13}CO and C^{18}O , with lower optical depth, are often used (e.g., Williams and Best 2014; Miotello, Bruderer, and van Dishoeck 2014; Ansdell et al. 2016). This technique has been used by numerous studies to measure gas masses of disks, surprisingly revealing gas-to-dust ratios well below ISM values (Dutrey, Guilloteau, and Simon 2003; Chapillon et al. 2008, 2010; Williams and Best 2014; Hardy et al. 2015; Ansdell et al. 2016, 2017; Miotello 2018).

However, gas masses estimated from CO measurements are subject to a number of uncertainties associated with the assumed abundance of CO relative to H_2 . There are several processes which can reduce the CO abundance by orders of magnitude from the typically assumed ISM value of 7×10^{-5} molecules of CO per molecule of H_2 (Beckwith and Sargent 1993; Dutrey et al. 1996, and references therein). CO at the disk surface will be photodissociated by stellar and interstellar UV radiation (e.g., Aikawa and Nomura 2006; Gorti and Hollenbach 2008; Visser, van Dishoeck, and Black 2009), while in the outer regions of disks, CO will form ice on the surface of dust grains at temperatures below 20 K, a process known as freeze-out (Collings

et al. 2003; Bisschop et al. 2006). In fact, chemical processing of CO into molecules with higher freeze-out temperatures, as well as disk turbulence that transports CO to regions below 20 K, can trap within ices CO that would otherwise have remained in gas form (Aikawa et al. 1999; Bergin et al. 2014; Reboussin et al. 2015; Schwarz et al. 2016). These effects are a likely cause of the low CO-derived gas-to-dust ratios described above. As further evidence for CO depletion, Bergin et al. (2013) used observations of hydrogen deuteride in the disk around TW Hya to measure a total gas mass up to a factor of 100 higher than implied by CO measurements.

Disk Structure

The most important feature of circumstellar disks in terms of their ability to form planets is the distribution of mass. In particular, the surface density, Σ , defined as the vertically integrated mass density, determines the amount of planet-forming material available as a function of radius (Kokubo and Ida 2002; Raymond, Quinn, and Lunine 2005; Miguel, Guilera, and Brunini 2011). Millimeter and submillimeter interferometric observations, capable of spatially resolving the optically thin dust continuum emission, are the primary tools used to constrain the disk surface density. Under the assumption that the gas surface density is traced by the dust emission, parametric models of the surface density can be compared to such observations (e.g., Kitamura et al. 2002; Andrews and Williams 2007; Andrews et al. 2009; Isella, Carpenter, and Sargent 2009, 2010; Guilloteau et al. 2011; Tazzari et al. 2017).

The simplest model to assume is surface density following a radial power law, $\Sigma \propto R^{-p}$, truncated at an outer radius. The minimum mass solar nebula (MMSN), an estimated surface density profile of the protoplanetary disk from which the Solar System formed, is parameterized as a truncated power law based on the minimum mass required to form Jupiter, Saturn, Uranus, and Neptune (Weidenschilling 1977; Hayashi 1981). A more sophisticated model for disk surface density can be derived by assuming the surface density evolves over time through viscous accretion (see Section 2.2). Under the assumption that viscosity follows a radial power law, $\nu \propto R^\gamma$, the viscous diffusion equation (e.g., Lynden-Bell and Pringle 1974) can be solved to give the radial dependence of Σ :

$$\Sigma \propto \left(\frac{R}{R_c}\right)^{-\gamma} \exp\left[-\left(\frac{R}{R_c}\right)^{2-\gamma}\right]. \quad (1.2)$$

Rather than a truncated power law, Σ behaves like a power law with an exponentially-declining tail with characteristic radius R_c . Numerous studies have used this param-

eterization to fit for the disk surface density, finding values of γ typically between 0 and 1.5 and characteristic radii ranging from a few astronomical units to beyond 100 au (e.g., Isella, Carpenter, and Sargent 2009, 2010; Guilloteau et al. 2011; Piétu et al. 2014).

Observationally, emission from disks is governed by not only the disk surface density profile, but also the temperature profile. Disk temperature is governed by the absorption of stellar radiation at the disk surface and its re-emission into the interior of the disk (Adams and Shu 1986; Adams, Lada, and Shu 1987; Calvet et al. 1991, 1992; Malbet and Bertout 1991). The vertical height and flaring angle, how rapidly the height increases with radius, determine the fraction of stellar irradiation that is absorbed and in turn control the disk temperature (Kenyon and Hartmann 1987; Calvet et al. 1991; Chiang and Goldreich 1997). Disks are pressure-supported in the vertical direction, and thus the vertical structure is determined by hydrostatic equilibrium (see review by Andrews 2015). Assuming a shallow vertical temperature gradient, the solution for the density as a function of height, z , is given by:

$$\rho = \frac{\Sigma}{H\sqrt{2\pi}} \exp\left[-\frac{1}{2}\left(\frac{z}{H}\right)^2\right], \quad (1.3)$$

where H is the scale height. The degree of flaring is typically parameterized as $H(R)/R$, where H/R increasing with R indicates that the disk surface curves upward and intercepts more stellar irradiation. Modeling of SEDs and scattered light images of disks give values of H/R between ~ 0.05 and ~ 0.25 , with a radial variation of $R^{0.1-0.3}$ (Andrews 2015, and references therein).

In recent years, the spatial resolution of ALMA has shown that this standard picture of radially smooth, azimuthally symmetric disks is not always correct. Numerous disks have been observed to have azimuthal asymmetries in continuum emission (see review by van der Marel 2017). These features are likely due to so-called “dust traps”, gas pressure maxima that lead to overdensities of solid particles (see Section 2.1). Even in the radial direction, high-resolution observations with ALMA have revealed bright and dark rings of continuum emission on scales as small as ~ 1 au (ALMA Partnership et al. 2015; Andrews et al. 2016; Isella et al. 2016; Canovas et al. 2016; Hendlar et al. 2017a; Loomis et al. 2017; van der Plas et al. 2017; Fedele et al. 2017; 2018; Dipierro et al. 2018; Sheehan and Eisner 2018, see Figure 1.4), while the disk around the star Elias 2-27 shows a spiral-arm structure (Pérez et al. 2016). Scattered light images show similar structures (de Boer et al. 2016; Ginski et al. 2016; Pohl et al. 2017; van Boekel et al. 2017). While

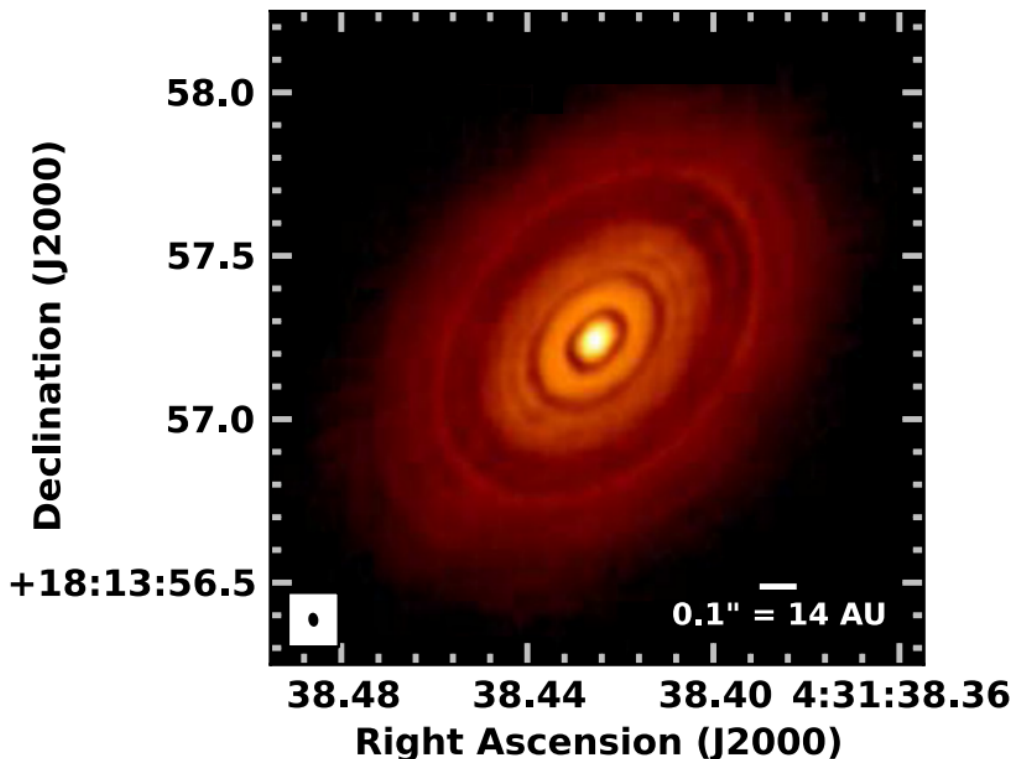


Figure 1.4: Composite 1.3 mm and 0.87 mm ALMA image of the disk around HL Tau. With a spatial resolution corresponding to ~ 4 au, the image shows a pattern of bright and dark rings. Recent ALMA observations of several other disks reveal a similar pattern. Figure adapted from ALMA Partnership et al. (2015).

the physical mechanisms responsible for these structures remain an open question (possible explanations include a change in dust properties at the sublimation fronts of icy grains, dust traps generated by turbulence, and planet-disk interactions, see discussion in Andrews et al. 2016), it is clear that disk structure is more complicated than the typically assumed parameterizations imply.

1.3 Thesis Summary

While there has been considerable progress over the last several decades in understanding the properties of circumstellar disks, most advancements have come through observations of young, 1-3 Myr old disks. To understand the evolution of these systems, and in particular how their ability to form planets changes over time, it is necessary to study and compare disks of different ages. Among possible samples of more evolved disks, the Upper Scorpius OB association (hereafter Upper Sco) provides an ideal target. The 5-11 Myr age of Upper Sco places its disks in the later

phases of their evolution, while its distance of 145 parsecs is a factor of three closer than the next nearest similarly-aged population, allowing for superior sensitivity and resolution. However, the relative scarcity and intrinsic faintness of disks in Upper Sco have made large-scale studies difficult (e.g., Mathews et al. 2012). With the advent of ALMA, it is now possible to conduct large surveys of regions such as Upper Sco, opening a new door into the study of disks at the end of their evolution.

In this thesis, I present new insights into circumstellar disk evolution achieved through a study of over 100 circumstellar disks in Upper Sco. I use ALMA observations of these disks to study their properties with an order of magnitude improvement in sensitivity over previous such surveys of Upper Sco. To obtain a more complete picture of these systems, I survey them for stellar companions using the NIRC2 AO imager on the Keck II telescope. These new observations allow for the first large-scale comparisons of the millimeter and multiplicity properties of disks in Upper Sco with those of younger disks, providing new constraints on how disks evolve. The contents of this thesis are as follows.

- In Chapter 2, the current understanding of circumstellar disk evolution is discussed from both a theoretical and observational perspective. This includes the growth of dust grains and their interactions with the gas in the disk. The evolution of the gas governed by viscous accretion and photoevaporation are presented next. The effects of the above processes are then combined into a single picture of disk evolution. Finally, late phases of disk evolution, transitional and debris disks, are described.
- Chapter 3 presents ALMA measurements of the $^{12}\text{CO } J = 3 - 2$ line and 0.88 mm continuum fluxes of the disks in the Upper Sco sample. A version of this chapter is published in Barenfeld et al. (2016). Continuum fluxes are used to estimate the dust mass within these disks and possible explanations of the faint CO associated fluxes are considered. A comparison of disk dust masses in Upper Sco with their younger counterparts in the Taurus region shows that dust masses in Upper Sco are lower by a factor of ~ 4.5 .
- In Chapter 4, the spatial structure of the gas and dust in the Upper Sco disks is modeled. A version of this chapter is published in Barenfeld et al. (2017). Using a radiative transfer code to simulate emission from these disks, power-law models of the dust surface density and $^{12}\text{CO } J = 3 - 2$ surface brightness are fit to the ALMA observations. The measured sizes of dust disks in Upper

Upper Sco are a factor of approximately three times smaller in size than their younger counterparts. These small disk sizes provide a possible explanation of the lack of CO detections described in Chapter 3, although some disks show evidence of CO extending beyond the dust. Despite the smaller sizes of disks in Upper Sco, the dust surface densities of the inner disks are similar to those measured in younger systems. This suggests that the reduction in visible dust mass measured in Chapter 3 is due to dust lost from the outer disk, either through its complete removal from the system or by becoming hidden in optically thick regions of the disk. As further support for the latter scenario, disks in Upper Sco lie along the same relation between millimeter continuum luminosity and dust disk size as younger disks.

- In Chapter 5, the effects of stellar companions on disk evolution are examined. A version of this chapter has been submitted for publication in the *Astrophysical Journal* (Barenfeld et al., submitted). Adaptive optics imaging and nonredundant aperture masking are used to search for stellar companions to the stars in the Upper Sco disk sample, with 30 such companions found in 27 systems, including 20 newly discovered companions. While the companion fraction is lower for stars with disks than for those without in Upper Sco, the fraction of disk systems with a companion within 40 au is consistent with that in Taurus. This implies that while stellar companions can cause an initial reduction in disk frequency, they have no further effect after ages of 1-2 Myr. In addition, single and binary systems with disks have statistically indistinguishable millimeter luminosities in Upper Sco, in contrast to Taurus where disk luminosities are significantly lower in binary systems. This discrepancy can be explained if single-star disks shrink in size with age, as found in Chapter 4, and become fainter as a result. The loss of material from the outer disk would allow single star disks to “catch-up” to disks that were initially truncated by a stellar companion. This provides further evidence for the outside-in evolution of dust disks presented in Chapter 4.
- Chapter 6 summarizes the main conclusions of this thesis and discusses possible future directions in the study of disk evolution.

Chapter 2

CIRCUMSTELLAR DISK EVOLUTION

2.1 Dust Evolution

The most commonly used tracer of circumstellar disk evolution is infrared dust emission (e.g., Hernández et al. 2008; Ribas et al. 2014; Ribas, Bouy, and Merín 2015). Large surveys using *Spitzer* and *WISE* have revealed the presence of disks around hundreds of young stars of different ages through near- and mid-infrared excesses (e.g., Gutermuth et al. 2004; Hartmann et al. 2005; Megeath et al. 2005; Carpenter et al. 2006; Lada et al. 2006; Sicilia-Aguilar et al. 2006; Balog et al. 2007; Barrado y Navascués et al. 2007; Cieza et al. 2007; Dahm and Hillenbrand 2007; Hernández et al. 2007a, 2007b; Flaherty and Muzerolle 2008; Gutermuth et al. 2008; Hernández et al. 2008; Luhman and Mamajek 2012). While such excesses are nearly ubiquitous around ~ 1 Myr old stars, the fraction of systems with such excesses decreases to less than 20% by an age of 5-10 Myr (see Figure 2.1 Hernández et al. 2008; Ribas et al. 2014). This exponential decline in the fraction of disks detected at 3.4-12 μm occurs with an e-folding timescale of 2-3 Myr. At 22-24 μm , however, the disk fraction declines on a longer timescale of 4-6 Myr (Ribas et al. 2014, see Figure 2.1). This may be evidence of different evolutionary timescales as a function of disk radius, but may also be due to an increasing fraction of debris disks in older samples (Currie et al. 2008, see Section 2.5).

Infrared observations have also shown that the timescales for disk evolution depend on stellar mass. *Spitzer* surveys of individual stellar regions and associations provided evidence of more rapid disk evolution around higher mass stars (e.g., Carpenter et al. 2006; Dahm and Hillenbrand 2007; Kennedy and Kenyon 2009; Roccatagliata et al. 2011; Fang et al. 2012; Bayo et al. 2012; Yasui et al. 2014). Ribas, Bouy, and Merín (2015) confirmed these initial results, finding a more rapid infrared disk-dissipation timescale for stars $\geq 2 M_{\odot}$ than for lower mass stars. This likely reflects the higher accretion rates and stronger radiation fields of high-mass stars (Calvet et al. 2005; Garcia Lopez et al. 2006; Hillenbrand 2008), which lead to more rapid disk dispersal (e.g., Alexander et al. 2014, see Section 2.4).

The evolution of dust grains within disks are expected to be governed by a number of processes. Smaller dust grains that are coupled to the gas will be subject to

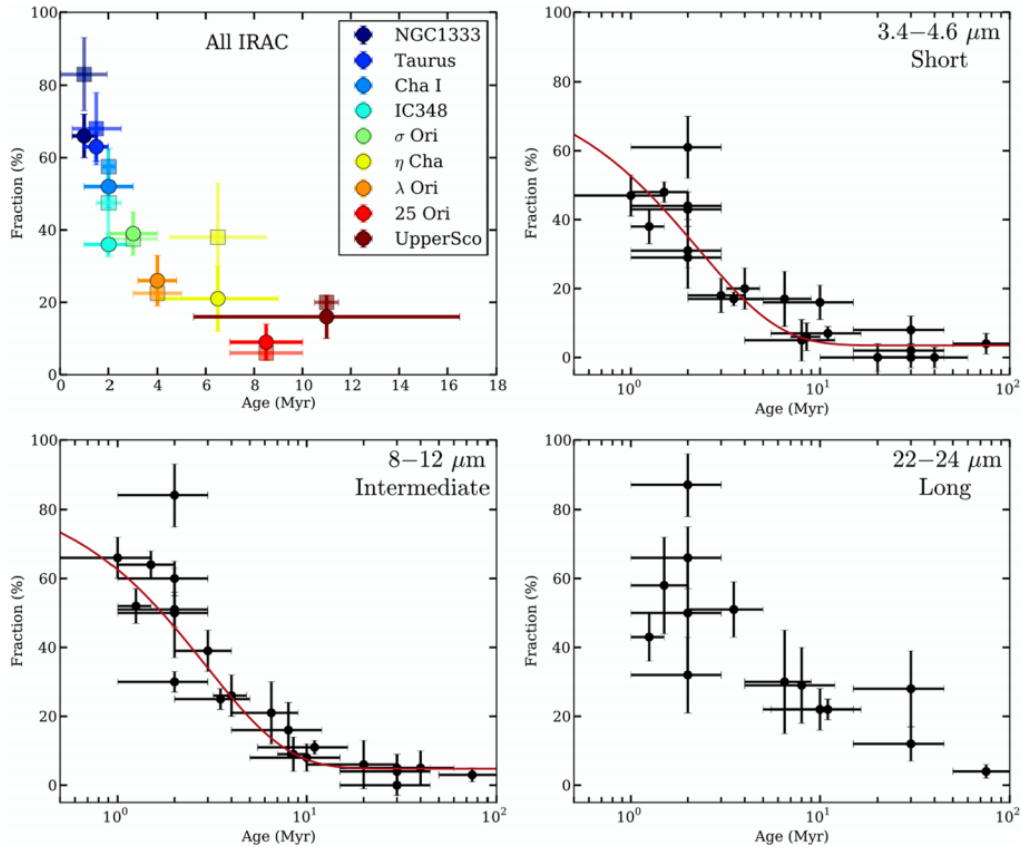


Figure 2.1: Fraction of disks detected through infrared excess as a function of age. Although disks are extremely common at 1–2 Myr ages, their frequency declines to less than 20% by an age of 5–10 Myr. This decrease occurs over slightly longer timescales for disks identified at 22–24 μm , possibly indicating a radial-dependent evolution. Figure from Gorti et al. (2016).

the effects of viscous accretion (e.g., Hartmann et al. 1998, see Section 2.2) and photoevaporation (e.g., Gorti, Hollenbach, and Dullemond 2015, Section 2.3). In addition, grain growth and radial drift will alter both the size and radial distributions of dust grains (see review by Testi et al. 2014). As discussed in Section 1.1, planet formation theory requires that dust grains grow from sub-micron sizes, through millimeter and centimeter sizes, and all the way into planetesimals. Observationally, measurements of the spectral slope of disk continuum emission at millimeter and centimeter wavelengths have revealed the presence of centimeter-sized grains in disks (see Section 1.2). In addition, Pérez et al. (2012) detected evidence of grain sizes decreasing with disk radius in the disk around AS 209, with grains reaching millimeter and centimeter sizes at radii within 70 au, with smaller grain sizes beyond (see also, Tazzari et al. 2016; Tripathi et al. 2018). This sorting by size has been

interpreted as evidence for the inward migration of centimeter and millimeter sized grains, a process known as radial drift.

Radial drift of dust grains is caused by the different rotational velocities of the gas and dust in disks (Whipple 1972; Weidenschilling 1977). The gas disk is partially supported by pressure in the radial direction, causing it to rotate at sub-Keplerian speeds. The dust, meanwhile, is not pressure-supported and undergoes normal Keplerian rotation, causing it to feel a headwind from the gas. This drag leads to an inward radial velocity of the dust grains that depends on the Keplerian orbital frequency, the drag physics, and, most importantly, the size of the dust grains. The drift velocity is maximized for millimeter, centimeter, and meter sized grains (Whipple 1972; Weidenschilling 1977). Under typical disk conditions, such grains will drift inwards on a timescale of 100-1000 orbits, much shorter than the observed lifetime of these grains in disks (Brauer et al. 2007; Brauer, Dullemond, and Henning 2008).

Solutions to this discrepancy involve mechanisms to both slow the drift of dust grains and concentrate them at high densities to increase their growth rate. At local pressure maxima within the disk, parcels of gas will feel equal radial pressure in both directions, negating the headwind effect described above and causing concentrations of dust grains to form (Whipple 1972; Haghighipour and Boss 2003). These pressure maxima can be caused by a number of effects, including turbulence (Johansen, Youdin, and Klahr 2009; Simon, Beckwith, and Armitage 2012), vortices (Barge and Sommeria 1995), evaporation fronts (Kretke and Lin 2007; Brauer, Dullemond, and Henning 2008), and gap-opening by a giant planet (Lyra et al. 2009). Observational evidence for these so-called “dust traps” was first obtained by van der Marel et al. (2013), who detected a large azimuthal asymmetry in the millimeter-sized grains in the transition disk around Oph IRS 48. Complimentary observations of CO and micron-sized dust grains revealed no such asymmetries, implying the trapping of the millimeter grains. Similar asymmetries have since been observed in other disks (see review by van der Marel 2017).

2.2 Mass Loss through Accretion

One of the clearest pieces of evidence for disk evolution is the observation of the accretion of gas onto the central star. Observational signatures of this process include measurement of ultraviolet and optical excess emission above the stellar photosphere caused by the accretion luminosity of the infalling material, which

can be directly converted into a mass accretion rate (e.g., Hartigan et al. 1991; Hartigan, Edwards, and Ghandour 1995; Valenti, Basri, and Johns 1993; Calvet and Gullbring 1998; Gullbring et al. 1998; Muzerolle et al. 2003; Herczeg and Hillenbrand 2008). In addition, numerous ultraviolet, optical, and infrared emission lines found to correlate with the total accretion luminosity can be used to identify accretion and measure the mass accretion rate (e.g., Herczeg et al. 2002; Natta et al. 2004; Mohanty, Jayawardhana, and Basri 2005; Herczeg and Hillenbrand 2008; Gatti et al. 2008; Fang et al. 2009; Yang et al. 2012). The most commonly used such tracer is the width of the H α emission (e.g., White and Basri 2003) line, which has been used to show that both the fraction of systems exhibiting signs of accretion and measured accretion rates follow an approximately exponential decay on a similar timescale to that of infrared-detected dust (Pascucci and Tachibana 2010; Fedele et al. 2010; Sicilia-Aguilar, Henning, and Hartmann 2010, see Figure 2.2). By an age of ~ 10 Myr, accretion rates and the accretion fraction approach zero, indicating the removal of gas from the inner disk by this age. Infrared and millimeter observations of gas within the disk itself show evidence for loss of the gas at wider separations on a similar timescale (Zuckerman, Forveille, and Kastner 1995; Pascucci et al. 2006; Dent et al. 2013).

While there is convincing evidence for accretion from disks onto their host stars, the physical mechanisms behind this process remain an active area of research. The key factor governing accretion in protoplanetary disks is angular momentum. To accrete from a Keplerian orbit at the outer edge of a disk to an orbit at the surface of the central star, disk material must lose $\sim 99\%$ of its angular momentum to material moving outwards or through outflows and disk winds (see review by Turner, Lee, and Sano 2014). The exchange of angular momentum within disks is governed by the viscosity, ν , typically parameterized as

$$\nu = \alpha c_s H, \quad (2.1)$$

where c_s is the local disk sound speed, H is the disk scale height, and $\alpha \ll 1$ encapsulates the underlying physics causing the viscosity (Shakura and Sunyaev 1973; Pringle 1981). Hartmann et al. (1998) measured the mass accretion rates of a sample of disk-hosting stars in the Taurus and Chamaeleon I star-forming regions, finding rates of $\sim 10^{-9} - 10^{-7} M_\odot \text{ yr}^{-1}$, decreasing with age as $\dot{M} \propto t^{-\eta}$, with $\eta \sim 1.5$. The mass accretion rates of the observed disks were best explained by viscous accretion with $\alpha \sim 10^{-2}$, suggesting viscosity generated by the magneto-rotational instability (e.g., Balbus and Hawley 1991).

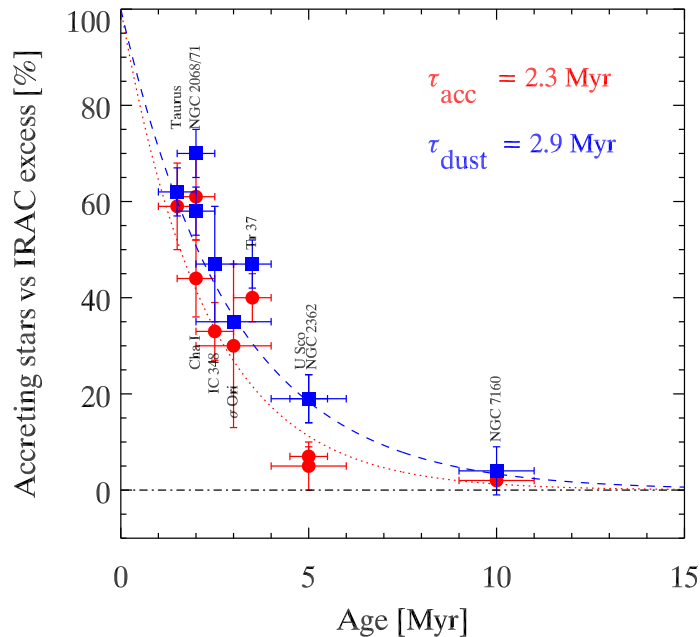


Figure 2.2: Fraction of young stars showing signs of accretion (red points) and infrared excess between $3.6 \mu\text{m}$ and $8 \mu\text{m}$ (blue squares) for stellar associations of different ages. The exponential fits to both sequences show that the gas and dust in the inner regions of disks disappear on similar timescales. Figure from Fedele et al. (2010).

The magneto-rotational instability (MRI) operates when magnetic field lines connect gas parcels at adjacent radii in a disk. Due to Keplerian rotation, the parcels will drift apart azimuthally. The connection of the field line then slows the inner parcel and accelerates the outer parcel, transferring angular momentum in the process. This causes the gas parcels to radially separate further, leading to an instability (Balbus and Hawley 1991). This process is an efficient mechanism for transferring angular momentum in a magnetized disk. However, in recent years the effectiveness of the MRI in circumstellar disks has been called into question. In realistic disks, large regions near the midplane, known as deadzones, will be shielded from ionizing radiation and cosmic rays, preventing magnetic fields from coupling to the gas (e.g., Bai and Stone 2013). While the upper layers of the disk may still be sufficiently ionized to allow the MRI to operate (Gammie 1996), simulations show that non-ideal MHD effects such as ambipolar diffusion weaken the MRI (Bai and Stone 2013; Bai 2014; Gressel et al. 2015; Simon et al. 2015). Observationally, limits placed on turbulence within disks based on direct measurements of turbulent velocities

(Flaherty et al. 2015) and on the presence of fragile dust substructure (Zhu and Baruteau 2016; Bae, Zhu, and Hartmann 2017; Dong et al. 2017) suggest low levels of MRI-induced turbulence.

A more recently proposed mechanism to drive accretion in disks is magnetohydrodynamic winds (e.g., Wardle and Koenigl 1993; Suzuki and Inutsuka 2009; Bai and Stone 2013; Bai et al. 2016). In a magnetized, rotating disk, poloidal field lines can centrifugally accelerate gas, forming a wind from the disk surface. Torques on the disk surface from this wind then remove angular momentum from the disk (Blandford and Payne 1982). Unlike MRI-driven accretion, which redistributes angular momentum outwards and causes disks to spread over time, MHD winds remove angular momentum from the systems and prevent this expansion (Bai et al. 2016). Rafikov (2017) use resolved ALMA observations of disks in Lupus to directly measure α , finding none of the correlations between α and global disk or stellar parameters predicted for MRI-driven accretion. This suggests that a non-viscous mechanism such as MHD winds is responsible for angular momentum transport in these disks.

While the underlying mechanisms remain an open question, it is clear that viscous accretion plays a key role in disk evolution. However, the observed sharp decline in accretion rates with age (e.g., Fedele et al. 2010) imply that accretion cannot continue indefinitely (Gorti et al. 2016). An additional mechanism is required to explain the final stages of disk evolution and dissipation.

2.3 Photoevaporation

As viscous accretion transports the gas in disks, some of this gas is lost from the disk through photoevaporation (see review by Alexander et al. 2014). Photoevaporation occurs when high-energy stellar ultraviolet and X-ray radiation heats the gas in the upper layers of the disk to $10^3 - 10^4$ K. At these temperatures, the thermal energy of the gas exceeds the gravitational binding energy to the central star, causing a pressure-driven wind to escape from the surface of the disk (e.g., Bally and Scoville 1982; Shu, Johnstone, and Hollenbach 1993; Hollenbach et al. 1994; Gorti, Hollenbach, and Dullemond 2015). Early in the lifetime of the disk, the rate of viscous accretion exceeds that of photoevaporation and this lost gas can be replaced. Once accretion rates decrease, however, photoevaporation becomes the dominant process that disperses the disk. Models of photoevaporation typically simplify the underlying physics based on the wavelength regime assumed as the dominant source

of heating: far-ultraviolet (FUV, 6-13.6 eV), extreme-ultraviolet (EUV, 13.6-100 eV), and X-ray (0.1-10 keV).

Photoevaporation by FUV radiation is the most complicated regime to model (see review by Clarke 2011). At these wavelengths, absorption by dust grains and polycyclic aromatic hydrocarbons (PAHs) is the dominant source of opacity in disks. The gas, down to a column density of $10^{21} - 10^{23} \text{ cm}^{-2}$, is collisionally heated by photoelectrons from these absorbers to temperatures of $10^2 - 10^3 \text{ K}$ (Adams et al. 2004). Simulations of FUV photoevaporation typically show disk mass loss rates of $\sim 10^{-8} M_{\odot} \text{ yr}^{-1}$ (Gorti, Dullemond, and Hollenbach 2009), comparable to accretion rates (Section 2.2). Mass loss peaks at $\sim 5 - 10 \text{ au}$, but is also significant at larger radii with the potential to truncate disks beyond 100 au (Gorti and Hollenbach 2004, 2008; Gorti, Dullemond, and Hollenbach 2009). Although these results remain highly uncertain due to strong dependence on the assumed dust properties, PAH abundance, and stellar FUV spectrum, the importance of FUV photoevaporation in disk evolution is clear.

By contrast, EUV photoevaporation involves simpler physics than FUV and is thus better understood. Beyond 13.6 eV, EUV radiation ionizes hydrogen atoms in disks with a large cross section that decreases as ν^{-3} (Osterbrock and Ferland 2006). Therefore, the ionization rate, and subsequent heating by photoelectrons, is dominated by EUV photons close to 13.6 eV and the details of the rest of the stellar spectrum are negligible. The problem can thus be treated analogously to an HII region, with an ionized disk atmosphere at a temperature of $\sim 10^4 \text{ K}$ (e.g., Clarke 2011). Because this layer is approximately isothermal, the thermal energy can be easily balanced with gravitational binding energy. The total mass loss rate due to EUV photoevaporation is $\sim 10^{-10} M_{\odot} \text{ yr}^{-1}$, peaking at $\sim 1 \text{ au}$ (Font et al. 2004) and sharply falling off at smaller radii as the gravitational binding energy can no longer be overcome.

Young stars are strong sources of X-rays, with luminosities $L_X \sim 10^{30} \text{ erg s}^{-1}$ and X-ray spectra peaking at $\sim 1 \text{ keV}$ (Feigelson et al. 2007). In the X-ray regime of photoevaporation, heating primarily comes from photoelectrons ejected from the K-shells of metals such as O, C, and Fe by this ionizing radiation (Ercolano et al. 2008). This creates a tenuous, $\sim 10^6 \text{ K}$ disk corona above a partially ionized layer extending down to a column density of $10^{21} - 10^{22} \text{ cm}^{-2}$ with temperatures of $10^3 - 10^4 \text{ K}$ (Ercolano et al. 2008; Ercolano, Clarke, and Drake 2009; Gorti, Dullemond, and Hollenbach 2009). The varying temperatures mean that, unlike

in the case of EUV photoevaporation, there is not a single critical radius beyond which photoevaporation can occur. Thus, there is a broad peak in the mass loss as a function of radius, extending to both small and large radii (Owen, Clarke, and Ercolano 2012). The total mass loss rate is $\sim 6 \times 10^{-9} M_{\odot} \text{ yr}^{-1}$, with a peak at 2 – 3 au (Owen, Ercolano, and Clarke 2011; Owen, Clarke, and Ercolano 2012).

Observational evidence of photoevaporation comes in the form of forbidden emission lines originating in the low-density photoevaporative wind (Alexander et al. 2014, and references therein). Numerous optical and infrared forbidden lines, including [NII] (6583 Å), [SII] (6716/6731 Å), [NeII] (12.81 μm), [NeIII] (15.55 μm), and [ArII] (6.99 μm), as well as several H and He recombination lines, are predicted with line widths of $\sim 10 - 30 \text{ km s}^{-1}$ and blue-shifts of $5 - 10 \text{ km s}^{-1}$ (Font et al. 2004; Alexander 2008; Hollenbach and Gorti 2009; Ercolano and Owen 2010). The ratios of the [NeII], [NeIII], and [ArII] lines, in particular, are highly sensitive to the ionizing spectrum and can be used to distinguish between the different regimes of photoevaporation (Hollenbach and Gorti 2009). Observations have confirmed the presence of these lines in disks. The Infrared Spectrograph on *Spitzer* has detected [NeII] 12.81 μm emission from a number of star-disk systems (Pascucci et al. 2007; Lahuis et al. 2007; Güdel et al. 2010; Baldovin-Saavedra et al. 2011). While this emission is dominated by shocked circumstellar gas in systems with jets, it has also been detected in sources lacking jets, pointing to a photoevaporative origin (Güdel et al. 2010; Baldovin-Saavedra et al. 2011). Follow-up observations from the ground have found that approximately half of *Spitzer* [NeII] sources exhibit linewidths and blue-shifts consistent with theoretical predictions of photoevaporative winds (Herczeg 2007; Pascucci and Sterzik 2009; van Boekel et al. 2009; Najita et al. 2009; Sacco et al. 2012; Baldovin-Saavedra et al. 2012). Finally, measurement of [NeII], [NeIII], and [ArII] line ratios in a sample of transitional disks (see Section 2.5) have revealed [NeII]/[NeIII] ratios of ~ 10 , consistent with X-ray-dominated photoevaporation (Glassgold, Najita, and Igea 2007; Hollenbach and Gorti 2009). However, [NeII]/[NeIII] ratios of order one or lower are more common in Class I and II sources, suggesting EUV photoevaporation.

2.4 A Combined Picture of Disk Evolution

As the preceding sections have demonstrated, the two main processes thought to govern disk evolution are viscous accretion and photoevaporation. A full picture of how this evolution proceeds therefore requires modeling of both processes simultaneously. This was first done by Clarke, Gendrin, and Sotomayor (2001), who

simulated the evolution of a disk under the influence of viscous accretion and EUV photoevaporation only. Initially, photoevaporation is negligible compared to accretion and any mass that is lost through photoevaporation is quickly replenished by viscous spreading. As accretion causes the disk surface density to decline, however, the mass accretion rate slows and becomes comparable to the rate of photoevaporation. Once this occurs, photoevaporation opens a gap in the disk at a radius of $\sim 1 - 10$ au which can no longer be filled in by viscous spreading. This effectively cuts-off the inner disk from being replenished by the accretion of outer disk material. The inner disk thus accretes onto the central star on a viscous timescale of only $\sim 10^5$ years, a small fraction of the several Myr total disk lifetime. Once the inner disk is lost, the inner rim of the outer disk becomes directly illuminated by the central star, dramatically increasing the photoevaporation rate and causing the rest of the disk to dissipate on a timescale of order 10^5 years (Alexander, Clarke, and Pringle 2006a, 2006b). This entire process, shown schematically in Figure 2.3, operates over a timescale of several Myr (Alexander, Clarke, and Pringle 2006b), in approximate agreement with observational constraints on disk lifetimes (e.g., Hernández et al. 2008; Ribas et al. 2014; Fedele et al. 2010).

Refinements to the above picture include incorporating X-ray and FUV photoevaporation into disk evolution models (e.g., Gorti, Dullemond, and Hollenbach 2009; Owen et al. 2010; Owen, Clarke, and Ercolano 2012). While these models result in qualitatively similar evolution to the scenario described above, the larger mass-loss rates associated with X-ray and FUV photoevaporation become comparable to accretion rates at an earlier stage, shortening overall disk lifetimes. As accretion and photoevaporation are shaping the disk, the dust is undergoing growth and transport as well, as described in Section 2.1. Though the dust only makes up a small fraction of the total disk mass, its role as the primary source of opacity in FUV photoevaporation makes it important to consider in disk evolution models. Gorti, Hollenbach, and Dullemond (2015) successfully incorporated dust effects and X-ray/FUV photoevaporation into disk evolutionary models. As in the standard picture, once photoevaporation becomes comparable to accretion, a gap rapidly forms and the inner disk is drained of material on a short timescale. These simulations also show that while micron and submicron dust grains remain coupled to the gas, millimeter-sized grains experience significant radial drift, concentrating within 20 au by the time of gap formation in the gas.

One further assumption inherent in simulations of disk evolution is the α prescription

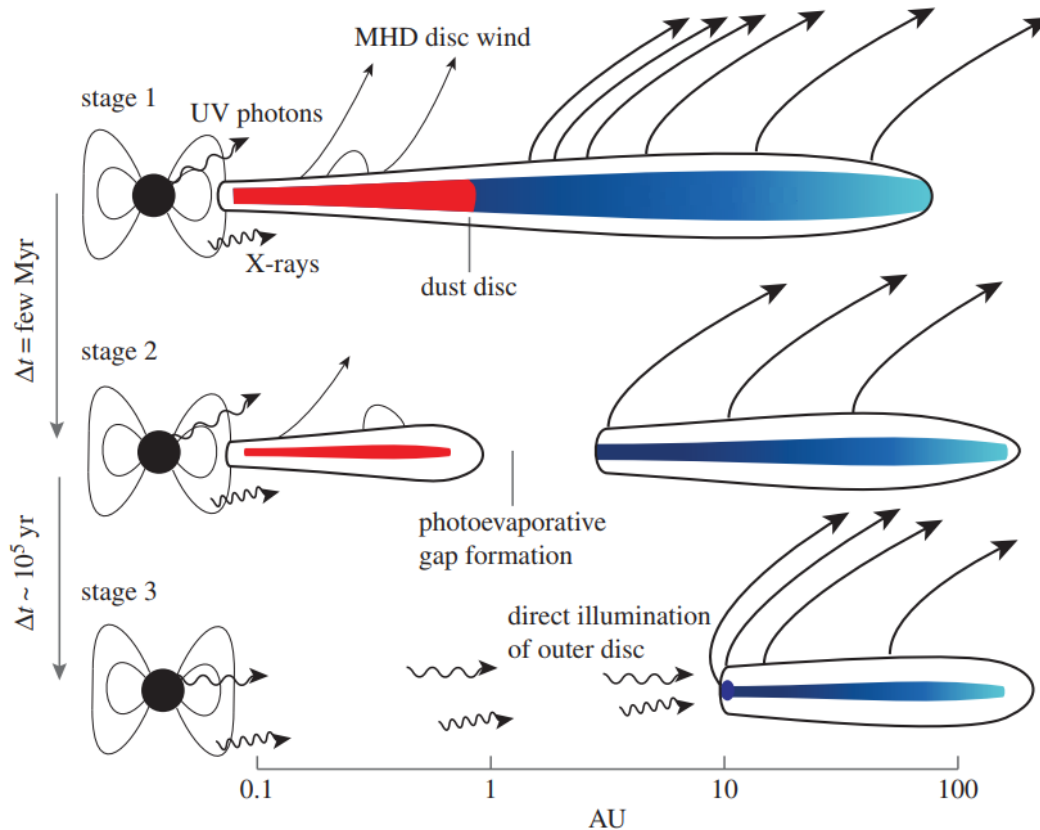


Figure 2.3: Illustration of the standard picture of disk evolution. Initially, accretion dominates over mass loss due to photoevaporative and MHD-driven winds and governs the evolution of the gas within the disk. Millimeter and centimeter grains, meanwhile, drift inwards due to gas drag (top). Once the photoevaporation becomes comparable to accretion, a gap forms at $\sim 1 - 10$ au, cutting off the inner disk from replenishment by the outer disk (middle). The inner disk then rapidly accretes, directly exposing the outer disk to photoevaporation (bottom). Once this occurs, the outer disk is evaporated on a timescale of $\sim 10^5$ years. Figure adapted from Ercolano and Pascucci (2017).

used to treat viscosity (see Section 2.2). If viscosity is lower than is typically assumed, accretion will take longer to sufficiently decrease disk surface densities for photoevaporation to become important, delaying gap formation and extending disk lifetimes (e.g., Gorti, Hollenbach, and Dullemond 2015). Once a gap does form, longer accretion timescales will also extend the lifetime of the inner disk (Morishima 2012; Bae et al. 2013).

2.5 Transitional and Debris Disks

A key piece of evidence for the above picture of disk evolution is the existence of disks with inner cavities depleted of dust, known as transitional disks (see review by Alexander et al. 2014). The presence of such cavities in these disks has historically been inferred by a deficit of near-infrared and/or mid-infrared flux in the SEDs of these systems (e.g., Strom et al. 1989). Subsequent resolved millimeter images of these systems have unambiguously revealed large central cavities (e.g., Hughes et al. 2007, 2009; Brown et al. 2008, 2009; Andrews et al. 2009, 2011; Isella et al. 2010; Zhang et al. 2014). Many transitional disks match the expected properties of systems created by inside-out photoevaporation, including cavity sizes of $\sim 1 - 10$ au, little or no signs of accretion, and low outer disk masses (e.g., Cieza et al. 2007; Wahhaj et al. 2010; Cieza et al. 2013). Indeed, such transitional disks represent $\sim 10\%$ of the pre-main-sequence population of nearby star-forming regions (Cieza et al. 2007), matching the expectation of photoevaporating disks spending $\sim 10\%$ of their lifetimes in this phase.

However, observations have revealed a subset of transitional disks that are brighter (and thus more massive) in the outer disk than full disks, show signs of ongoing accretion, and have inner cavities 20-80 au in size (e.g., Andrews et al. 2011; Owen, Ercolano, and Clarke 2011; Morishima 2012; Pinilla et al. 2018). These systems are difficult to explain with models of photoevaporation, which are predicted to open inner cavities only when the disk has lost a significant fraction of its mass through accretion (see Section 2.4). The most likely alternative explanation of these systems is the dynamical opening of the inner cavity by a giant planet (e.g., Artymowicz and Lubow 1994; Lubow and D'Angelo 2006). However, the observed scarcity of giant planets in exoplanet surveys (e.g., Winn and Fabrycky 2015) and the close match between giant planet formation and disk dispersal timescales (e.g., D'Angelo, Durisen, and Lissauer 2010) make it difficult to explain the full population of transitional disks with this mechanism. It is now thought that there exist two distinct populations of transitional disks- millimeter-bright systems with large inner cavities likely created by planet-disk interactions and fainter systems with smaller cavities that are a consequence of photoevaporative disk dissipation (e.g., Owen, Clarke, and Ercolano 2012).

Long after the dissipation of primordial circumstellar disks, a number of systems maintain dust disks, in some cases over Gyr timescales (see reviews by Matthews et al. 2014; Hughes, Duchene, and Matthews 2018). Known as debris disks, these

systems are identified by infrared excess in a similar manner to primordial disks. Unlike primordial systems, however, these disks often lack excess emission at certain wavelengths and the excess they do show is weaker, indicating that the dust is radially confined to narrow rings and is heavily depleted relative to primordial disks (Wyatt et al. 2015, Figure 2.4). The dust in debris disks is continuously being removed by stellar radiation pressure, stellar winds, and Poynting-Robertson drag on timescales much shorter than the age of these systems (van Lieshout et al. 2014). Therefore, the debris disks must be constantly replenished by a collisional cascade of larger bodies creating new dust, rather than being direct remnants of primordial systems.

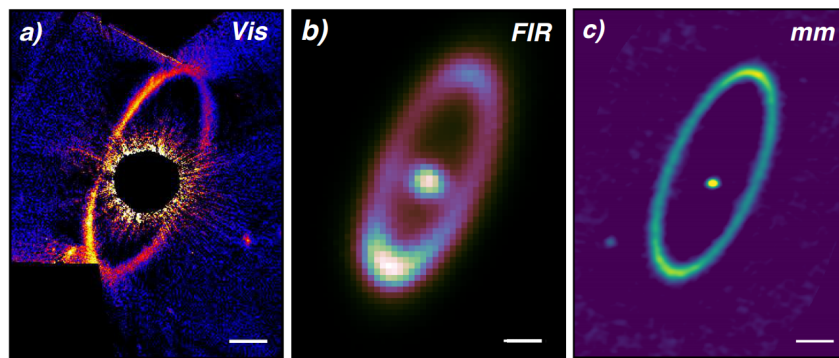


Figure 2.4: Images of the debris disk around Fomalhaut in optical scattered light (panel a Kalas et al. 2013) and $70 \mu\text{m}$ (panel b Acke et al. 2012) and 1.3 mm (panel c MacGregor et al. 2017) thermal emission, showing the narrow ring structure commonly exhibited by debris disks. Figure adapted from Hughes, Duchene, and Matthews (2018).

Our own solar system is an example of a debris disk containing two main regions of dust. In the inner solar system, dust from the disintegration of Jupiter-family comets is responsible for the zodiacal light (Nesvorný et al. 2011), while beyond the orbit of Neptune, collisions of comets in the Edgeworth-Kuiper belt (e.g., Jewitt 2008) form a second annulus of dust. Both of these components of the solar system's debris disk are too faint to detect around other stars; current sensitivities only allow for the detection of systems 10-100 times brighter in the infrared than the Kuiper Belt and 1000 times brighter than the zodiacal dust belt (Hughes, Duchene, and Matthews 2018). Infrared surveys have found that $\sim 20\%$ of solar-type stars host debris disks down to this sensitivity (Sibthorpe et al. 2018), while only a few percent of M stars host such disks (Matthews et al. 2014). Among the detected systems, multiple component disks, analogous to the Solar System, are common, suggesting the presence of planets to maintain gaps in these disks (Kennedy and Wyatt 2014).

While debris disks have been observed around stars with a wide range of ages, they are most common in systems with ages of tens of Myr or younger (Montesinos et al. 2016). In fact, debris disks have been identified in stellar associations as young as 2-3 Myr (Espaillat et al. 2017). At these young ages, it can be difficult to distinguish debris disks from faint, evolved primordial disks. Historically, one key distinction has been the absence of gas in debris disks. However, in recent years the sensitivity of ALMA and the Herschel Space Observatory has allowed for the detection of atomic and molecular gas in debris disks, even in 100 Myr to Gyr old systems, using both absorption of starlight as it passes through the disk and direct emission of the disk itself (see compilation by Hughes, Duchene, and Matthews 2018). Because the emission from the gas in these disks is so faint, most have only been observed in a single emission line, making it difficult to determine the excitation temperature and optical depth of the the gas. In addition, the abundance of emitting gases such as CO relative to H₂ is unknown, although measurements of debris disk scale heights suggest mean molecular weights higher than those found in the ISM (Hughes et al. 2017). Despite these uncertainties, estimates of the total gas mass of debris disks are typically of the order of a lunar mass or less (Hughes, Duchene, and Matthews 2018, and references therein). As is the case for dust, this gas should be short-lived. Such small amounts of gas would be photodissociated by the central star in less than 10⁴ years without replenishment (e.g., Kóspál et al. 2013). The source of this gas is thus likely to be volatiles released from solid bodies through collisions and vaporization of icy dust grains, comets, and planetary embryos (Zuckerman and Song 2012; Dent et al. 2014; Kral et al. 2016; Matrà et al. 2017). Simulations of a collisional cascade of comets with solar-system composition show that this mechanism can explain the observed CO line fluxes in most debris disks (Kral et al. 2017). However, some young debris disks have 1-2 orders of magnitude more gas than can be reasonably produced by comets and are therefore likely to be remnant primordial disks (e.g., Kóspál et al. 2013). The origin of the gas in these young debris disks and their link to primordial disks remain open questions.

*Chapter 3*ALMA OBSERVATIONS OF CIRCUMSTELLAR DISKS IN THE
UPPER SCORPIUS OB ASSOCIATION

ABSTRACT

We present ALMA observations of 106 G-, K-, and M-type stars in the Upper Scorpius OB Association hosting circumstellar disks. With these data, we measure the 0.88 mm continuum and $^{12}\text{CO } J = 3 - 2$ line fluxes of disks around low-mass ($0.14 - 1.66 M_{\odot}$) stars at an age of 5-11 Myr. Of the 75 primordial disks in the sample, 53 are detected in the dust continuum and 26 in CO. Of the 31 disks classified as debris/evolved transitional disks, 5 are detected in the continuum and none in CO. The lack of CO emission in approximately half of the disks with detected continuum emission can be explained if CO is optically thick but has a compact emitting area ($\lesssim 40$ au), or if the CO is heavily depleted by a factor of at least ~ 1000 relative to interstellar medium abundances and is optically thin. The continuum measurements are used to estimate the dust mass of the disks. We find a correlation between disk dust mass and stellar host mass consistent with a power-law relation of $M_{\text{dust}} \propto M_{*}^{1.67 \pm 0.37}$. Disk dust masses in Upper Sco are compared to those measured in the younger Taurus star-forming region to constrain the evolution of disk dust mass. We find that the difference in the mean of $\log(M_{\text{dust}}/M_{*})$ between Taurus and Upper Sco is 0.64 ± 0.09 , such that M_{dust}/M_{*} is lower in Upper Sco by a factor of ~ 4.5 .

3.1 Introduction

The lifetime of protoplanetary disks is closely linked to planet formation. In the core accretion theory of planet formation, the formation of gas giant planets is a race to accumulate a solid core large enough to rapidly accrete gas before the gas and dust in the disk disappear. A key step in this process is the growth of solid material from micron-sized dust grains to kilometer-sized planetesimals, which can then collisionally grow into the cores of gas giants (Mordasini et al. 2010). The ability to form these planetesimals depends strongly on conditions within the disk, and in particular on the disk mass in solids. The time available for planetesimals to form is therefore set by the decline in disk dust mass as the disk evolves.

The past decade has seen tremendous growth in our understanding of circumstellar disks. Infrared observations with the *Spitzer Space Telescope* (Werner et al. 2004) and the *Wide-field Infrared Survey Explorer* (*WISE*, Wright et al. 2010) have cataloged hundreds of disks in nearby star-forming regions, revealing spectral energy distributions indicative of optically thick, irradiated dust disks surrounding an exposed stellar photosphere (e.g., Gutermuth et al. 2004; Hartmann et al. 2005; Megeath et al. 2005; Carpenter et al. 2006; Lada et al. 2006; Sicilia-Aguilar et al. 2006; Balog et al. 2007; Barrado y Navascués et al. 2007; Cieza et al. 2007; Dahm and Hillenbrand 2007; Hernández et al. 2007a, 2007b; Flaherty and Muzerolle 2008; Gutermuth et al. 2008; Hernández et al. 2008; Luhman and Mamajek 2012). Collectively, these surveys have shown that disks surround $\sim 80\%$ of K- and M-type stars at an age of ~ 1 Myr, but by an age of ~ 5 Myr, only $\sim 20\%$ of stars retain a disk as traced by infrared dust emission.

Submillimeter observations complement this picture by revealing disk dust masses. While infrared data probe only the warm dust within 1 au of the star, most of the solid mass in disks will be in the outer regions. To study this colder dust, submillimeter observations are required. At these wavelengths, dust emission in disks is generally optically thin, providing a measure of the total surface area of millimeter-sized grains in the disk (e.g., Ricci et al. 2010c). Combined with assumptions about the disk temperature and dust opacity, this can be used to derive the total mass of solids in the disk (e.g., Beckwith et al. 1990; Andre and Montmerle 1994; Motte, Andre, and Neri 1998; Andrews and Williams 2005, 2007). By further obtaining spatially resolved images of the disk with interferometers, the surface density of the disk can be inferred (e.g., Kitamura et al. 2002; Andrews and Williams 2007; Andrews et al. 2009; Isella, Carpenter, and Sargent 2009, 2010; Guilloteau et al. 2011). Andrews

et al. (2013) combined new observations and literature values to create a catalog of disk fluxes at 1.3 mm for 179 stars earlier than M8.5 in the 1-2 Myr old Taurus star-forming region. The authors found a statistically significant, approximately linear correlation between disk mass and stellar mass, with the disk mass typically between 0.2% and 0.6% of the stellar host mass.

To study the *evolution* of disks, it is necessary to compare disk properties in Taurus to disk properties in regions of different ages. However, observational constraints on older disks remain relatively sparse at submillimeter wavelengths. Surveys of IC 348 (age \sim 2-3 Myr, Carpenter 2002; Lee, Williams, and Cieza 2011), Lupus (age \sim 3 Myr, Nuernberger, Chini, and Zinnecker 1997), σ Orionis (age \sim 3 Myr, Williams et al. 2013), λ Orionis (age \sim 5 Myr, Ansdell, Williams, and Cieza 2015), and the Upper Scorpius OB association (age \sim 5-11 Myr, Mathews et al. 2012) suggest that these older regions lack disks as bright as the most luminous objects in younger regions. However, the small number of detected objects in these surveys make it difficult to draw firm conclusions about the nature of disks at older ages or how disk properties change in time (see discussion in Andrews et al. 2013). Of the older systems studied thus far, the Upper Scorpius OB association (hereafter Upper Sco) in particular represents an ideal sample for studying disk evolution. The 5-11 Myr age of Upper Sco (Preibisch et al. 2002; Pecaute, Mamajek, and Bubar 2012) places its disks at the critical stage when infrared observations indicate that disk dissipation is nearly complete. Carpenter, Ricci, and Isella (2014) presented results of an ALMA 0.88 mm continuum survey of 20 disk-bearing stars in Upper Sco, achieving an order of magnitude improvement in sensitivity over previous surveys. By comparing their results with the Andrews et al. (2013) Taurus catalog, they found that, on average, disk dust masses in Upper Sco are lower than in Taurus. However, due to the small size of the Upper Sco sample, the difference was not statistically significant.

We present additional ALMA observations of disks in Upper Sco, expanding the Carpenter, Ricci, and Isella (2014) sample to 106 stars. This study represents the largest survey of its kind for 5-11 Myr old stars. With these data, we measure continuum and CO line emission to establish the demographics of disk luminosities at an age of 5-11 Myr, when disks are in the final stages of dissipation. We then compare the distribution of disk dust masses in Upper Sco to that in Taurus in order to quantify the evolution of dust mass in disks between an age of 1-2 Myr and 5-11 Myr. In a future paper, we will analyze the CO measurements in detail to study the

gas in disks at the end of their evolution.

3.2 Stellar Sample

Our ALMA sample consists of 106 stars in Upper Sco between spectral types of M5 and G2 (inclusive) that are thought to be surrounded by a disk based on the presence of excess infrared emission observed by *Spitzer* or *WISE* (Carpenter et al. 2006; Luhman and Mamajek 2012). Twenty of these stars were observed in ALMA Cycle 0 using the disk sample obtained by Carpenter et al. (2006) who used *Spitzer* observations. The remaining stars were observed in Cycle 2 based on the compilation of 235 stars with disks in Upper Sco identified by Luhman and Mamajek (2012).¹ The combined ALMA Cycle 0 and Cycle 2 observations observe all 100 disk-host candidates in Luhman and Mamajek (2012) with spectral types between M4.75 and G2, as well as six M5 stars. The ALMA sample is not complete at M5.

Of our sources, 75 are classified by Luhman and Mamajek (2012) as “full” (optically thick in the infrared with an SED that shows no evidence of disk clearing, 53 sources), “transitional” (with an SED showing evidence for gaps and holes, 5 sources), or “evolved” (becoming optically thin in the infrared, but no evidence of clearing, 17 sources) disks. We consider these systems to be “primordial” disks. The remaining 31 sources have infrared SEDs indicative of an optically thin disk with a large inner hole. These are classified by Luhman and Mamajek (2012) as “debris/evolved transitional” disks and represent either young debris disks composed of second-generation dust originating from the collisional destruction of planetesimals, or the final phase of primordial disk evolution. Figure 3.1 shows the distribution of disk types in our sample.

Stellar luminosities (L_*), effective temperatures (T_*), and masses (M_*) were determined as described in Carpenter, Ricci, and Isella (2014). Briefly, luminosity was estimated using J-band photometry from the Two Micron All Sky Survey (2MASS, Cutri et al. 2003; Skrutskie et al. 2006) and bolometric corrections for 5-30 Myr stars from Pecaut and Mamajek (2013). Visual extinction (A_V) was calculated using DENIS $I - J$ colors (DENIS Consortium 2005), intrinsic colors from Pecaut and

¹One star in this compilation, 2MASS J16113134-1838259 (AS 205), has been previously considered a member of the ρ Ophiuchus region by numerous authors (e.g., Prato, Greene, and Simon 2003; Eisner et al. 2005; Andrews et al. 2009). More recently, Reboussin et al. (2015) considered AS 205 to be a member of Upper Sco, and this star was included in the Luhman and Mamajek (2012) Upper Sco disk catalog. Given the fact that AS 205 is well separated from the main ρ Ophiuchus clouds (see Figure 1 of Reboussin et al. 2015), we consider this star to be a member of Upper Sco and include it in our sample.

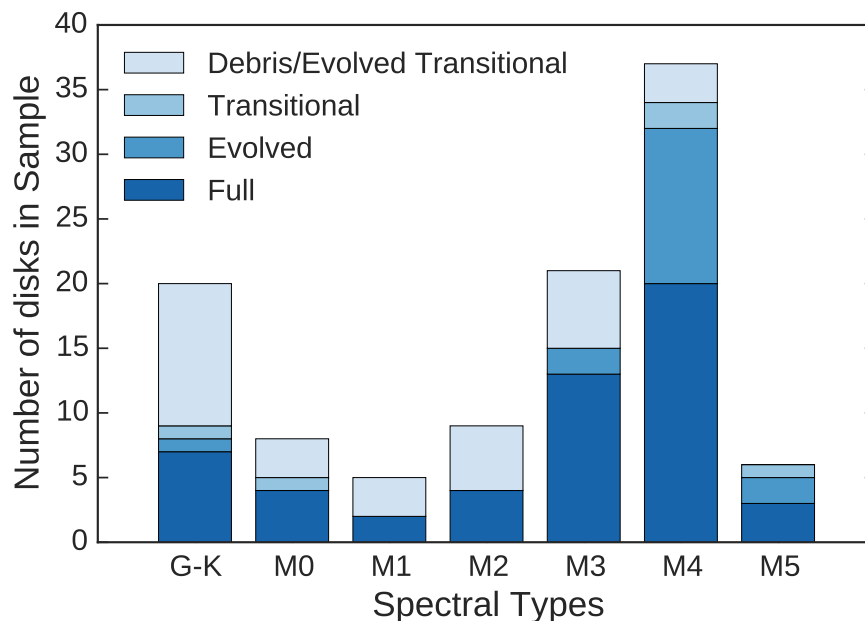


Figure 3.1: Distribution of disk types, as defined by Luhman and Mamajek (2012), in the Upper Sco sample grouped by spectral type.

Mamajek (2013), and the Cardelli, Clayton, and Mathis (1989) extinction law. Effective temperatures were estimated from spectral type as in Andrews et al. (2013) using the temperature scales of Schmidt-Kaler (1982), Straižys (1992), and Luhman (1999). Spectral types were taken from Luhman and Mamajek (2012), with an assumed uncertainty of ± 1 subclass. Stellar masses were then determined from T_* and L_* using the Siess, Dufour, and Forestini (2000) pre-main-sequence evolutionary tracks with a metallicity of $Z = 0.02$ and no convective overshoot. Uncertainties in stellar mass reflect uncertainties in luminosity (incorporating photometric, bolometric correction, and extinction uncertainties, as well as a ± 20 pc uncertainty in the distance to Upper Sco of 145 pc) and temperature (reflecting uncertainty in spectral type). The derived stellar properties are given in Table 3.1.

Table 3.1: Stellar Properties

Source	SpT	Disk Type	A_v	$\log(T_*/K)$	$\log(L_*/L_\odot)$	$\log(M_*/M_\odot)$
2MASS J15354856-2958551	M4	Full	0.7±0.5	3.51±0.02	-0.60±0.15	-0.58(-0.09, +0.09)
2MASS J15514032-2146103	M4	Evolved	0.38±0.36	3.51±0.02	-1.31±0.14	-0.70(-0.12, +0.13)
2MASS J15521088-2125372	M4	Full	3.32±0.48	3.51±0.02	-1.81±0.14	-0.75(-0.13, +0.13)
2MASS J15530132-2114135	M4	Full	1.27±0.40	3.51±0.02	-1.2±0.14	-0.68(-0.12, +0.13)
2MASS J15534211-2049282	M3.5	Full	1.71±0.38	3.52±0.02	-0.84±0.14	-0.57(-0.09, +0.10)
2MASS J15551704-2322165	M2.5	Debris/Ev. Trans.	0.7±0.5	3.54±0.02	-0.54±0.15	-0.46(-0.08, +0.08)
2MASS J15554883-2512240	G3	Debris/Ev. Trans.	0.7±0.5	3.77±0.00	0.37±0.15	0.07(-0.05, +0.04)
2MASS J15562477-2225552	M4	Full	0.71±0.37	3.51±0.02	-1.18±0.14	-0.68(-0.12, +0.13)
2MASS J15570641-2206060	M4	Full	0.7±0.5	3.51±0.02	-1.44±0.15	-0.72(-0.13, +0.14)
2MASS J15572986-2258438	M4	Evolved	0.7±0.5	3.51±0.02	-1.33±0.15	-0.70(-0.12, +0.13)
2MASS J15581270-2328364	G6	Debris/Ev. Trans.	0.7±0.5	3.76±0.00	0.40±0.15	0.10(-0.06, +0.05)
2MASS J15582981-2310077	M3	Full	1.10±0.41	3.53±0.02	-1.31±0.14	-0.59(-0.11, +0.12)
2MASS J15583692-2257153	G7	Full	0.7±0.5	3.75±0.00	0.47±0.15	0.14(-0.05, +0.05)
2MASS J15584772-1757595	K4	Debris/Ev. Trans.	0.7±0.5	3.65±0.01	-0.01±0.15	0.08(-0.04, +0.05)
2MASS J16001330-2418106	M0	Debris/Ev. Trans.	0.7±0.5	3.59±0.01	-0.56±0.15	-0.24(-0.05, +0.05)
2MASS J16001730-2236504	M4	Full	0.7±0.5	3.51±0.02	-0.82±0.15	-0.61(-0.10, +0.11)
2MASS J16001844-2230114	M4.5	Full	0.7±0.5	3.50±0.02	-1.13±0.15	-0.73(-0.12, +0.14)
2MASS J16014086-2258103	M4	Full	0.83±0.35	3.51±0.02	-0.90±0.14	-0.63(-0.11, +0.11)
2MASS J16014157-2111380	M4	Full	0.7±0.5	3.51±0.02	-1.56±0.15	-0.73(-0.13, +0.14)
2MASS J16020039-2221237	M1	Debris/Ev. Trans.	0.7±0.5	3.57±0.02	-0.32±0.15	-0.33(-0.09, +0.08)
2MASS J16020287-2236139	M0	Debris/Ev. Trans.	0.75±0.33	3.59±0.01	-1.41±0.14	-0.30(-0.05, +0.05)
2MASS J16020757-2257467	M2.5	Full	0.41±0.33	3.54±0.02	-0.82±0.14	-0.47(-0.09, +0.08)
2MASS J16024152-2138245	M4.75	Full	0.43±0.37	3.50±0.02	-1.44±0.14	-0.81(-0.15, +0.10)
2MASS J16025123-2401574	K4	Debris/Ev. Trans.	0.7±0.5	3.65±0.01	-0.20±0.15	0.04(-0.04, +0.05)
2MASS J16030161-2207523	M4.75	Full	0.66±0.44	3.50±0.02	-1.59±0.14	-0.82(-0.15, +0.09)
2MASS J16031329-2112569	M4.75	Full	0.45±0.42	3.50±0.02	-1.38±0.14	-0.80(-0.15, +0.11)
2MASS J16032225-2413111	M3.5	Full	0.59±0.32	3.52±0.02	-0.97±0.14	-0.58(-0.10, +0.11)
2MASS J16035767-2031055	K5	Full	0.7±0.5	3.64±0.01	-0.17±0.15	0.02(-0.05, +0.05)
2MASS J16035793-1942108	M2	Full	0.7±0.5	3.55±0.02	-0.96±0.15	-0.44(-0.10, +0.08)
2MASS J16041740-1942287	M3.5	Full	0.36±0.37	3.52±0.02	-1.07±0.14	-0.60(-0.10, +0.12)
2MASS J16042165-2130284	K2	Transitional	0.7±0.5	3.69±0.02	-0.24±0.15	0.00(-0.06, +0.05)
2MASS J16043916-1942459	M3.25	Debris/Ev. Trans.	0.37±0.36	3.53±0.02	-1.17±0.14	-0.59(-0.11, +0.12)
2MASS J16050231-1941554	M4.5	Debris/Ev. Trans.	-0.07±0.40	3.5±0.02	-1.57±0.14	-0.79(-0.15, +0.12)
2MASS J16052459-1954419	M3.5	Debris/Ev. Trans.	0.36±0.38	3.52±0.02	-1.08±0.14	-0.6(-0.11, +0.11)
2MASS J16052556-2035397	M5	Evolved	0.38±0.42	3.49±0.02	-1.37±0.14	-0.83(-0.15, +0.09)
2MASS J16052661-1957050	M4.5	Evolved	0.70±0.40	3.5±0.02	-1.13±0.14	-0.73(-0.12, +0.14)
2MASS J16053215-1933159	M5	Evolved	0.20±0.43	3.49±0.02	-1.59±0.14	-0.85(-0.14, +0.08)
2MASS J16054540-2023088	M2	Full	1.61±0.30	3.55±0.02	-0.90±0.14	-0.44(-0.10, +0.08)
2MASS J16055863-1949029	M4	Evolved	0.39±0.35	3.51±0.02	-1.20±0.14	-0.68(-0.12, +0.13)
2MASS J16060061-1957114	M5	Evolved	0.22±0.38	3.49±0.02	-1.20±0.14	-0.80(-0.14, +0.11)
2MASS J16061330-2212537	M4	Debris/Ev. Trans.	0.7±0.5	3.51±0.02	-0.67±0.15	-0.59(-0.09, +0.10)
2MASS J16062196-1928445	M0	Transitional	1.16±0.26	3.59±0.01	-0.25±0.14	-0.25(-0.05, +0.04)
2MASS J16062277-2011243	M5	Transitional	-0.20±0.38	3.49±0.02	-1.41±0.14	-0.83(-0.15, +0.09)
2MASS J16063539-2516510	M4.5	Evolved	-0.08±0.37	3.50±0.02	-1.60±0.14	-0.80(-0.15, +0.12)
2MASS J16064102-2455489	M4.5	Evolved	0.7±0.5	3.50±0.02	-1.70±0.15	-0.80(-0.15, +0.11)
2MASS J16064115-2517044	M3.25	Evolved	0.56±0.31	3.53±0.02	-1.22±0.14	-0.60(-0.11, +0.12)
2MASS J16064385-1908056	K6	Evolved	0.75±0.26	3.62±0.01	-0.39±0.14	-0.05(-0.04, +0.05)
2MASS J16070014-2033092	M2.75	Full	0.04±0.30	3.54±0.02	-0.95±0.14	-0.51(-0.09, +0.10)
2MASS J16070211-2019387	M5	Full	0.66±0.44	3.49±0.02	-1.52±0.14	-0.84(-0.15, +0.08)
2MASS J16070873-1927341	M4	Debris/Ev. Trans.	1.15±0.37	3.51±0.02	-1.28±0.14	-0.70(-0.12, +0.13)
2MASS J16071971-2020555	M3	Debris/Ev. Trans.	1.43±0.36	3.53±0.02	-1.05±0.14	-0.55(-0.10, +0.11)
2MASS J16072625-2432079	M3.5	Full	0.00±0.37	3.52±0.02	-0.92±0.14	-0.58(-0.10, +0.11)

Table 3.1: Stellar Properties

Source	SpT	Disk Type	A_v	$\log(T_*/K)$	$\log(L_*/L_\odot)$	$\log(M_*/M_\odot)$
2MASS J16072747-2059442	M4.75	Evolved	0.7±0.5	3.50±0.02	-0.99±0.15	-0.73(-0.12, +0.13)
2MASS J16073939-1917472	M2	Debris/Ev. Trans.	0.76±0.35	3.55±0.02	-0.76±0.14	-0.43(-0.09, +0.08)
2MASS J16075796-2040087	M1	Full	0.7±0.5	3.57±0.02	-0.82±0.15	-0.35(-0.10, +0.10)
2MASS J16080555-2218070	M3.25	Debris/Ev. Trans.	0.21±0.34	3.53±0.02	-0.82±0.14	-0.54(-0.09, +0.10)
2MASS J16081566-2222199	M3.25	Full	0.17±0.33	3.53±0.02	-0.85±0.14	-0.55(-0.09, +0.10)
2MASS J16082324-1930009	K9	Full	0.7±0.5	3.59±0.01	-0.59±0.15	-0.18(-0.04, +0.05)
2MASS J16082751-1949047	M5	Evolved	0.72±0.40	3.49±0.02	-1.16±0.14	-0.79(-0.14, +0.11)
2MASS J16083455-2211559	M4.5	Evolved	1.07±0.39	3.50±0.02	-1.46±0.14	-0.78(-0.14, +0.12)
2MASS J16084894-2400045	M3.75	Full	0.57±0.35	3.52±0.02	-1.25±0.14	-0.66(-0.12, +0.12)
2MASS J16090002-1908368	M5	Full	0.31±0.40	3.49±0.02	-1.33±0.14	-0.82(-0.15, +0.09)
2MASS J16090075-1908526	K9	Full	0.7±0.5	3.59±0.01	-0.45±0.15	-0.19(-0.05, +0.05)
2MASS J16093558-1828232	M3	Full	2.00±0.29	3.53±0.02	-1.06±0.14	-0.55(-0.09, +0.11)
2MASS J16094098-2217594	M0	Debris/Ev. Trans.	0.7±0.5	3.59±0.01	-0.17±0.15	-0.25(-0.04, +0.04)
2MASS J16095361-1754474	M3	Full	1.71±0.37	3.53±0.02	-1.34±0.14	-0.59(-0.11, +0.12)
2MASS J16095441-1906551	M1	Debris/Ev. Trans.	0.7±0.5	3.57±0.02	-0.65±0.15	-0.34(-0.10, +0.09)
2MASS J16095933-1800090	M4	Full	0.58±0.37	3.51±0.02	-1.00±0.14	-0.64(-0.11, +0.12)
2MASS J16101473-1919095	M2	Debris/Ev. Trans.	0.87±0.34	3.55±0.02	-0.84±0.14	-0.43(-0.09, +0.08)
2MASS J16101888-2502325	M4.5	Transitional	0.7±0.5	3.50±0.02	-1.35±0.15	-0.77(-0.13, +0.13)
2MASS J16102174-1904067	M1	Debris/Ev. Trans.	0.7±0.5	3.57±0.02	-0.67±0.15	-0.34(-0.10, +0.09)
2MASS J16102819-1910444	M4	Full	0.7±0.5	3.51±0.02	-1.62±0.15	-0.74(-0.13, +0.14)
2MASS J16102857-1904469	M3	Evolved	0.7±0.5	3.53±0.02	-0.35±0.15	-0.49(-0.08, +0.07)
2MASS J16103956-1916524	M2	Debris/Ev. Trans.	0.7±0.5	3.55±0.02	-0.94±0.15	-0.44(-0.10, +0.08)
2MASS J16104202-2101319	K5	Debris/Ev. Trans.	0.7±0.5	3.64±0.01	-0.14±0.15	0.02(-0.05, +0.06)
2MASS J16104636-1840598	M4.5	Full	0.7±0.5	3.50±0.02	-1.57±0.15	-0.79(-0.15, +0.12)
2MASS J16111330-2019029	M3	Full	1.68±0.35	3.53±0.02	-0.76±0.14	-0.52(-0.08, +0.09)
2MASS J16111534-1757214	M1	Full	0.7±0.5	3.57±0.02	-0.48±0.15	-0.33(-0.10, +0.08)
2MASS J16112057-1820549	K5	Debris/Ev. Trans.	0.7±0.5	3.64±0.01	-0.13±0.15	0.03(-0.05, +0.06)
2MASS J16113134-1838259	K5	Full	0.7±0.5	3.64±0.01	0.45±0.15	0.05(-0.09, +0.10)
2MASS J16115091-2012098	M3.5	Full	0.65±0.39	3.52±0.02	-1.04±0.14	-0.60(-0.11, +0.11)
2MASS J16122737-2009596	M4.5	Full	1.24±0.45	3.50±0.02	-1.44±0.14	-0.78(-0.14, +0.13)
2MASS J16123916-1859284	M0.5	Full	0.7±0.5	3.58±0.01	-0.50±0.15	-0.29(-0.07, +0.07)
2MASS J16124893-1800525	M3	Debris/Ev. Trans.	0.81±0.38	3.53±0.02	-0.96±0.14	-0.54(-0.09, +0.10)
2MASS J16125533-2319456	G2	Debris/Ev. Trans.	0.7±0.5	3.77±0.00	0.78±0.15	0.21(-0.07, +0.09)
2MASS J16130996-1904269	M4	Full	1.13±0.38	3.51±0.02	-1.11±0.14	-0.67(-0.12, +0.12)
2MASS J16133650-2503473	M3.5	Full	0.7±0.5	3.52±0.02	-1.00±0.15	-0.59(-0.10, +0.11)
2MASS J16135434-2320342	M4.5	Full	-0.55±0.37	3.50±0.02	-1.07±0.14	-0.72(-0.12, +0.13)
2MASS J16141107-2305362	K2	Full	0.7±0.5	3.69±0.02	0.43±0.15	0.23(-0.05, +0.05)
2MASS J16142029-1906481	M0	Full	2.0±0.5	3.59±0.01	-0.33±0.15	-0.25(-0.05, +0.04)
2MASS J16142893-1857224	M2.5	Debris/Ev. Trans.	0.7±0.5	3.54±0.02	-0.61±0.15	-0.46(-0.08, +0.08)
2MASS J16143367-1900133	M3	Full	0.7±0.5	3.53±0.02	-0.47±0.15	-0.50(-0.08, +0.07)
2MASS J16145918-2750230	G8	Debris/Ev. Trans.	0.7±0.5	3.74±0.01	0.07±0.15	0.03(-0.04, +0.02)
2MASS J16145928-2459308	M4.25	Full	4.29±0.24	3.51±0.02	-0.92±0.14	-0.66(-0.11, +0.12)
2MASS J16151239-2420091	M4	Transitional	1.39±0.36	3.51±0.02	-1.62±0.14	-0.74(-0.13, +0.13)
2MASS J16153456-2242421	M0	Full	0.7±0.5	3.59±0.01	-0.13±0.15	-0.25(-0.04, +0.04)
2MASS J16154416-1921171	K5	Full	0.7±0.5	3.64±0.01	-0.31±0.15	-0.01(-0.04, +0.05)
2MASS J16163345-2521505	M0.5	Full	1.13±0.29	3.58±0.01	-0.83±0.14	-0.29(-0.08, +0.08)
2MASS J16181618-2619080	M4.5	Evolved	1.64±0.36	3.5±0.02	-1.26±0.14	-0.75(-0.13, +0.13)
2MASS J16181904-2028479	M4.75	Evolved	1.86±0.39	3.5±0.02	-1.32±0.14	-0.79(-0.14, +0.12)
2MASS J16215466-2043091	K7	Debris/Ev. Trans.	0.7±0.5	3.61±0.01	-0.35±0.15	-0.10(-0.04, +0.04)
2MASS J16220961-1953005	M3.75	Debris/Ev. Trans.	0.7±0.5	3.52±0.02	-0.50±0.15	-0.56(-0.08, +0.08)
2MASS J16230783-2300596	K3.5	Debris/Ev. Trans.	0.7±0.5	3.66±0.01	0.09±0.15	0.12(-0.04, +0.05)
2MASS J16235385-2946401	G2.5	Debris/Ev. Trans.	0.7±0.5	3.77±0.00	0.66±0.15	0.16(-0.11, +0.10)

Table 3.1: Stellar Properties

Source	SpT	Disk Type	A_v	$\log(T_*/K)$	$\log(L_*/L_\odot)$	$\log(M_*/M_\odot)$
2MASS J16270942-2148457	M4.5	Full	1.8 ± 0.38	3.50 ± 0.02	-1.55 ± 0.14	$-0.79(-0.15, +0.12)$
2MASS J16303390-2428062	M4	Full	0.7 ± 0.5	3.51 ± 0.02	-1.11 ± 0.15	$-0.66(-0.12, +0.12)$

3.3 ALMA Observations

ALMA observations were obtained in Cycle 0 and Cycle 2 using the 12 m array. Twenty sources were observed in Cycle 0 between 2012 August and 2012 December. Eighty-seven sources were observed in 2014 June and 2014 July. 2MASS J16064385-1908056 was observed in Cycle 0 and had a marginal (2.5σ) continuum disk detection. Since the Cycle 0 observations did not achieve the requested sensitivity, the source was re-observed in Cycle 2. The Cycle 2 data have a factor of 2.8 better signal- to-noise for this source than the Cycle 0 data; therefore, the Cycle 2 data are used throughout the paper for this source.

All observations used band 7 with the correlator configured to record dual polarization. Spectral windows for Cycle 2 were centered at 334.2, 336.1, 346.2, and 348.1 GHz for a mean frequency of 341.1 GHz (0.88 mm). The bandwidth of each window is 1.875 GHz. The 345.8 GHz window has channel widths of 0.488 MHz (0.429 km s^{-1}) to observe the $^{12}\text{CO } J = 3 - 2$ line. The spectral resolution is twice the channel width. Table 3.2 summarizes the observations, showing the number of antennas, baseline range, precipitable water vapor (pwv), and calibrators for each day. Cycle 0 observations used between 17 and 28 antennas with maximum baselines of ~ 400 m, for an angular resolution of $\sim 0''.55$. Cycle 2 observations used between 34 and 36 antennas with baselines extending out to 650 m, corresponding to an angular resolution of $0''.34$. The full-width-at-half-maximum (FWHM) primary beam size of the observations is $18''.5$. The typical on-source integration times were 5.5 minutes for Cycle 0 observations and 2.5 minutes for Cycle 2 observations.

The data were calibrated using the Common Astronomy Software Applications (CASA) package (McMullin et al. 2007). The reduction scripts were kindly provided by the ALMA project. Data reduction steps include atmospheric calibration using the 183 GHz water vapor radiometers, bandpass calibration, flux calibration, and gain calibration. The calibrators for each observation date are listed in Table 3.2. We assume a 1σ calibration uncertainty of 10%.

We rescaled the uncertainties of the visibility measurements to reflect the empirical scatter in the data so that the appropriate values of the uncertainties are used in model fitting (see Section 3.4). For each source, the visibilities were placed on a grid in uv space for each spectral window and polarization. At every grid cell, a scale factor was calculated to match the σ values of the visibilities within that cell to their empirical scatter. The median scaling factor of the cells with at least 10 visibilities was then applied to all σ values for that polarization and spectral window.

Table 3.2: Observations

UT Date	Number Antennas	Baseline Range (m)	pwv (mm)	Calibrators		
				Flux	Passband	Gain
2012 Aug 24	25	17-375	0.77	Neptune	J1924-0939	J1625-2527
2012 Aug 28	28	12-386	0.68	Titan	J1924-0939	J1625-2527
2012 Dec 16	17	16-402	1.16	Titan	J1924-0939	J1625-2527
2014 Jun 15	34	16-650	0.78	Titan, J1733-130	J1517-2422	J1517-2422
2014 Jun 16	36	16-650	0.56	Titan	J1517-2422	J1517-2422
2014 Jun 30	36	16-650	0.52	Titan	J1517-2422	J1517-2422
2014 Jul 07	36	19-650	0.60	Titan	J1517-2422	J1517-2422

3.4 ALMA Results

In this section, we use the ALMA observations described above to measure the 0.88 mm continuum and $^{12}\text{CO } J = 3 - 2$ line fluxes of the 106 Upper Sco targets in our sample.

Continuum Fluxes

To measure the submillimeter continuum flux density, the four spectral windows were combined after excluding a -15 to $+30 \text{ km s}^{-1}$ region about the $^{12}\text{CO } J = 3 - 2$ rest frequency in the frame of the local standard of rest (LSR). This safely excludes CO emission at the expected $0-10 \text{ km s}^{-1}$ LSR radial velocities (de Zeeuw et al. 1999; Chen et al. 2011; Dahm, Slesnick, and White 2012) of our Upper Sco targets. Flux densities were determined by first fitting a point-source to the visibility data using the *uvmodelfit* routine in CASA. The point-source model contains three free parameters: the integrated flux density and the right ascension and declination offsets from the phase center. If the flux density of a source is less than three times its statistical uncertainty, the source is considered a non-detection and we re-fit a point-source to the visibilities with the offset position fixed at the expected stellar position.

Expected positions were estimated using stellar positions from 2MASS (Cutri et al. 2003; Skrutskie et al. 2006) and proper motions from the PPMXL catalog (Roeser, Demleitner, and Schilbach 2010). For stars lacking PPMXL measurements, the median proper motion of the remainder of the sample (-11.3 km s^{-1} , -24.9 km s^{-1}) was used. 2MASS J16041740-1942287 has a PPMXL proper motion discrepant from the median proper motion of Upper Sco. However, this star may be blended with two neighboring stars, calling into question the PPMXL data, which may compromise the measured proper motion. We therefore also adopt the sample median proper motion for this star.

If the source was detected, an elliptical Gaussian model was also fit with *uvmodelfit*. This model includes an additional three parameters: the FWHM, aspect ratio, and position angle of the major axis. To determine which model best describes the data, we used the Bayesian Information Criterion (BIC) test. This test evaluates the relative probabilities of models describing a data set, while penalizing models for having additional free parameters. For each source, if the probability of a point-source model relative to an elliptical Gaussian model is < 0.0027 (3σ confidence), we adopt the latter model for the source. Otherwise, we adopt the point-source model. Nine sources were fit with elliptical Gaussians, with deconvolved FWHM disk sizes ranging from $0''.140$ to $0''.492$, corresponding to $\sim 20\text{--}70$ au at the 145 pc distance of Upper Sco. Two additional sources, 2MASS J15583692-2257153 and 2MASS J16042165-2130284, were well-resolved and showed centrally depleted cavities that were not well described by either a point-source or elliptical Gaussian at the resolution of our data. We measured the flux of 2MASS J15583692-2257153 using aperture photometry with a $0''.6$ radius circular aperture. For 2MASS J16042165-2130284, we adopt a flux of 218.76 ± 0.81 mJy measured by Zhang et al. (2014) using a $1''.5$ radius circular aperture. At the distance of Upper Sco, these apertures correspond to radii of 87 and 218 au, respectively.

Unlike in the image domain, it is not possible to specify a boundary within which to fit the brightness profile of a source when fitting visibilities directly. Thus, if there is a second bright source in the field, this could potentially bias the fit of a single source. To account for possible contamination to the measured flux from sources elsewhere in the field, we searched each field in the image domain for any pixels (not including those associated with the target star) brighter than five times the RMS noise of the image. Ten such sources were detected toward 9 of the 106 fields (see Table 3.3). For these sources, multiple-component models of a point

source or elliptical Gaussian (determined as described above) were fit to each source using the *uvmultifit* Python library (Martí-Vidal et al. 2014). Point-source models were used to fit all secondary sources. Fluxes and positions determined in this way for the secondary detections are listed in Table 3.3. A search of the NASA/IPAC Extragalactic Database reveals that no known background galaxies are present at the positions of the secondary sources.

Table 3.3: Secondary Source Properties

Field	Secondary Source Position (J2000)		S_{tot} (mJy)	$\Delta\alpha$ (arcsec)	$\Delta\delta$ (arcsec)
	Right Ascension	Declination			
2MASS J15584772-1757595	15 ^h 58 ^m 47 ^s .49	-17°57'59".11	1.33 ± 0.15	-3.19 ± 0.14	0.81 ± 0.17
2MASS J16020287-2236139	16 ^h 02 ^m 03 ^s .15	-22°36'11".75	2.19 ± 0.15	4.02 ± 0.13	2.67 ± 0.14
2MASS J16025123-2401574	16 ^h 02 ^m 51 ^s .50	-24°01'54".04	1.35 ± 0.15	3.87 ± 0.13	3.78 ± 0.17
2MASS J16032225-2413111	16 ^h 03 ^m 21 ^s .75	-24°13'11".71	1.54 ± 0.15	-6.62 ± 0.13	-0.15 ± 0.14
2MASS J16032225-2413111	16 ^h 03 ^m 22 ^s .30	-24°13'11".46	0.86 ± 0.15	0.84 ± 0.13	0.10 ± 0.14
2MASS J16071971-2020555	16 ^h 07 ^m 19 ^s .42	-20°20'57".99	0.84 ± 0.16	-4.12 ± 0.13	-2.13 ± 0.14
2MASS J16113134-1838259 ^a	16 ^h 11 ^m 31 ^s .30	-18°38'27".26	76.95 ± 0.31	-0.42 ± 0.12	-0.88 ± 0.13
2MASS J16123916-1859284	16 ^h 12 ^m 39 ^s .21	-18°59'28".98	1.09 ± 0.16	0.63 ± 0.14	-0.21 ± 0.15
2MASS J16125533-2319456	16 ^h 12 ^m 54 ^s .97	-23°19'36".97	0.94 ± 0.13	-4.87 ± 0.12	9.02 ± 0.12
2MASS J16135434-2320342 ^a	16 ^h 13 ^m 54 ^s .36	-23°20'34".76	5.82 ± 0.13	0.41 ± 0.13	-0.13 ± 0.14

^a Secondary source also detected in CO at the same velocity as the primary source.

The secondary sources in the fields of 2MASS J16113134-1838259 and 2MASS J16135434-2320342 are also detected in CO at the expected radial velocity of Upper Sco. 2MASS J16113134-1838259 is a known hierarchical triple system, in which the southern source is itself a spectroscopic binary. The southern binary is separated by 1".31 from the northern single star (Eisner et al. 2005). 2MASS J16135434-2320342 has not been previously classified as a multiple system. The fitted continuum positions of the two components reveal a separation of $0''.61 \pm 0''.19$ (88 ± 28 au). Luhman and Mamajek (2012) classify both systems as single stars since their multiplicity is unresolved by 2MASS and the United Kingdom Infrared Telescope (UKIRT) Infrared Deep Sky Survey (UKIDSS, Lawrence et al. 2007). We therefore only consider the brighter continuum component of these sources throughout the remainder of this paper, so as not to bias our sample by including additional stars found only because of their 880 μm continuum emission.

The measured continuum flux for each source is listed in Table 3.4 and plotted against spectral type in Figure 3.2. We detect 53 of 75 primordial and 5 of 31 debris/evolved transitional sources at $> 3\sigma$. Images of all (primordial and debris/evolved transitional) continuum detections are shown in Figure 3.3. The real part of the visibilities as a function of baseline length for all primordial and debris/evolved transitional

sources are shown in the left columns of Figures 3.4 and 3.5. Most of the sources show flat visibility profiles indicating that these sources are compact relative to the beam size of $\sim 0''.35$ (50 au). This agrees with our visibility fitting, for which only 11 sources were conclusively spatially resolved. The compact nature of the majority of the dust disks in our sample matches previous findings in younger star-forming regions that faint disks tend to be radially compact. Andrews et al. (2010a) observed a correlation between disk mass (and flux density) and disk radius for sources in the Ophiuchus star-forming region, while Piétu et al. (2014) found dust disk sizes of tens of astronomical units or less among faint disks in Taurus. Note that the faintest sources in Upper Sco detected with ALMA are an order of magnitude less luminous than the faintest disks detected by these authors.

The second column of Figure 3.4 shows continuum images of the 75 primordial disks in the sample. Images of the 31 debris/evolved transitional disks are shown in the second column of Figure 3.5; the five detected debris/evolved transitional disks are 2MASS J16043916-1942459, 2MASS J16073939-1917472, 2MASS J16094098-2217594, 2MASS J16095441-1906551, and 2MASS J16215466-2043091. All detected sources are consistent with the expected stellar position, with the exception of 2MASS J15534211-2049282, 2MASS J16113134-1838259, and 2MASS J16153456-2242421. These three sources are offset from the expected stellar position by slightly more than three times the uncertainty in the offset (see Table 3.4). However, $^{12}\text{CO } J = 3 - 2$ emission is detected in all three sources at a velocity consistent with Upper Sco. We therefore assume these continuum sources are associated with the target Upper Sco stars.

Table 3.4: Continuum and CO $J = 3 - 2$ Flux Measurements

Source	0.88 mm Continuum				CO $J = 3 - 2$		
	S_ν (mJy)	$\Delta\alpha^a$ (arcsec)	$\Delta\delta^a$ (arcsec)	FWHM ^b (arcsec)	Flux (mJy km s ⁻¹)	Velocity Range (km s ⁻¹)	Aperture Radius (arcsec)
2MASS J15354856-2958551	1.92 ± 0.15	-0.40 ± 0.14	-0.04 ± 0.15	...	55 ± 34	-1.5 – 10.5	0.3
2MASS J15514032-2146103	0.76 ± 0.16	0.01 ± 0.14	0.06 ± 0.16	...	87 ± 38	-1.5 – 10.5	0.3
2MASS J15521088-2125372	-0.10 ± 0.15	285 ± 45	-2.5 – 7.5	0.3
2MASS J15530132-2114135	5.78 ± 0.14	-0.15 ± 0.13	0.02 ± 0.14	...	160 ± 28	-1.5 – 10.5	0.3
2MASS J15534211-2049282	2.93 ± 0.29	-0.52 ± 0.14	-0.03 ± 0.15	0.478 ± 0.068	511 ± 59	0.0 – 17.0	0.4
2MASS J15551704-2322165	0.11 ± 0.15	5 ± 37	-1.5 – 10.5	0.3
2MASS J15554883-2512240	-0.14 ± 0.15	-14 ± 44	-1.5 – 10.5	0.3
2MASS J15562477-2225552	0.28 ± 0.18	133 ± 19	-1.5 – 10.5	0.3
2MASS J15570641-2206060	0.32 ± 0.20	-9 ± 23	-1.5 – 10.5	0.3
2MASS J15572986-2258438	-0.04 ± 0.20	56 ± 36	-1.5 – 10.5	0.3
2MASS J15581270-2328364	0.00 ± 0.15	30 ± 37	-1.5 – 10.5	0.3
2MASS J15582981-2310077	5.86 ± 0.18	0.10 ± 0.11	-0.01 ± 0.11	...	56 ± 23	-1.5 – 10.5	0.3
2MASS J15583692-2257153 ^c	174.92 ± 0.27	-0.12 ± 0.11	0.06 ± 0.12	...	4607 ± 75	-1.0 – 14.0	1.0

Table 3.4: Continuum and CO $J = 3 - 2$ Flux Measurements

Source	0.88 mm Continuum				CO $J = 3 - 2$		
	S_ν (mJy)	$\Delta\alpha^a$ (arcsec)	$\Delta\delta^a$ (arcsec)	FWHM ^b (arcsec)	Flux (mJy km s ⁻¹)	Velocity Range (km s ⁻¹)	Aperture Radius (arcsec)
2MASS J15584772-1757595	-0.20 ± 0.15	-75 ± 30	-1.5 - 10.5	0.3
2MASS J16001330-2418106	0.05 ± 0.15	-32 ± 40	-1.5 - 10.5	0.3
2MASS J16001730-2236504	0.10 ± 0.15	-35 ± 33	-1.5 - 10.5	0.3
2MASS J16001844-2230114	3.89 ± 0.15	-0.14 ± 0.13	0.08 ± 0.13	...	1835 ± 69	3.5 - 24.0	0.6
2MASS J16014086-2258103	3.45 ± 0.14	-0.03 ± 0.14	-0.24 ± 0.15	...	507 ± 39	-5.0 - 8.5	0.4
2MASS J16014157-2111380	0.66 ± 0.14	-0.01 ± 0.14	0.01 ± 0.14	...	9 ± 35	-1.5 - 10.5	0.3
2MASS J16020039-2221237	-0.08 ± 0.14	60 ± 27	-1.5 - 10.5	0.3
2MASS J16020287-2236139	0.04 ± 0.15	-30 ± 32	-1.5 - 10.5	0.3
2MASS J16020757-2257467	5.26 ± 0.27	0.12 ± 0.14	-0.06 ± 0.15	0.257 ± 0.029	632 ± 63	-2.0 - 10.0	0.6
2MASS J16024152-2138245	10.25 ± 0.19	-0.03 ± 0.13	-0.06 ± 0.14	0.142 ± 0.011	40 ± 26	-1.5 - 10.5	0.3
2MASS J16025123-2401574	0.07 ± 0.15	-24 ± 30	-1.5 - 10.5	0.3
2MASS J16030161-2207523	2.81 ± 0.12	-0.03 ± 0.14	-0.08 ± 0.15	...	55 ± 25	-1.5 - 10.5	0.3
2MASS J16031329-2112569	0.06 ± 0.12	-12 ± 25	-1.5 - 10.5	0.3
2MASS J16032225-2413111	2.42 ± 0.15	0.03 ± 0.13	0.04 ± 0.14	...	40 ± 17	-1.5 - 10.5	0.3
2MASS J16035767-2031055	4.30 ± 0.39	0.01 ± 0.08	0.06 ± 0.08	...	180 ± 26	-1.5 - 10.5	0.3
2MASS J16035793-1942108	1.17 ± 0.14	0.02 ± 0.13	-0.05 ± 0.14	...	1490 ± 158	-1.0 - 15.5	0.9
2MASS J16041740-1942287	0.89 ± 0.14	0.09 ± 0.14	0.03 ± 0.15	...	67 ± 44	-1.5 - 10.5	0.3
2MASS J16042165-2130284 ^c	218.76 ± 0.81	0.01 ± 0.11	-0.03 ± 0.11	...	20268 ± 67	2.5 - 6.0	2.1
2MASS J16043916-1942459	0.49 ± 0.15	-0.03 ± 0.15	0.08 ± 0.15	...	-31 ± 37	-1.5 - 10.5	0.3
2MASS J16050231-1941554	-0.16 ± 0.15	-14 ± 41	-1.5 - 10.5	0.3
2MASS J16052459-1954419	0.22 ± 0.15	-43 ± 34	-1.5 - 10.5	0.3
2MASS J16052556-2035397	1.53 ± 0.20	-0.09 ± 0.19	0.52 ± 0.19	...	8 ± 31	-1.5 - 10.5	0.3
2MASS J16052661-1957050	0.07 ± 0.15	111 ± 37	-1.5 - 10.5	0.3
2MASS J16053215-1933159	0.25 ± 0.20	2 ± 25	-1.5 - 10.5	0.3
2MASS J16054540-2023088	7.64 ± 0.15	0.09 ± 0.13	-0.02 ± 0.13	...	101 ± 39	-1.5 - 10.5	0.3
2MASS J16055863-1949029	-0.08 ± 0.15	-59 ± 37	-1.5 - 10.5	0.3
2MASS J16060061-1957114	0.00 ± 0.13	3 ± 31	-1.5 - 10.5	0.3
2MASS J16061330-2212537	-0.20 ± 0.12	-13 ± 31	-1.5 - 10.5	0.3
2MASS J16062196-1928445	4.08 ± 0.52	0.02 ± 0.22	0.50 ± 0.22	...	23 ± 50	-1.5 - 10.5	0.3
2MASS J16062277-2011243	0.59 ± 0.14	0.09 ± 0.19	0.05 ± 0.19	...	151 ± 27	2.0 - 11.5	0.4
2MASS J16063539-2516510	1.69 ± 0.15	0.04 ± 0.13	0.00 ± 0.14	...	48 ± 31	-1.5 - 10.5	0.3
2MASS J16064102-2455489	3.05 ± 0.14	-0.15 ± 0.13	-0.06 ± 0.14	...	14 ± 31	-1.5 - 10.5	0.3
2MASS J16064115-2517044	0.20 ± 0.15	-46 ± 23	-1.5 - 10.5	0.3
2MASS J16064385-1908056	0.84 ± 0.15	-0.04 ± 0.15	-0.15 ± 0.15	...	60 ± 29	-1.5 - 10.5	0.3
2MASS J16070014-2033092	0.22 ± 0.15	16 ± 44	-1.5 - 10.5	0.3
2MASS J16070211-2019387	-0.09 ± 0.20	45 ± 24	-1.5 - 10.5	0.3
2MASS J16070873-1927341	-0.09 ± 0.15	53 ± 45	-1.5 - 10.5	0.3
2MASS J16071971-2020555	0.16 ± 0.16	18 ± 36	-1.5 - 10.5	0.3
2MASS J16072625-2432079	13.12 ± 0.24	-0.03 ± 0.14	0.12 ± 0.15	0.140 ± 0.013	171 ± 49	-1.5 - 10.5	0.3
2MASS J16072747-2059442	2.13 ± 0.12	-0.21 ± 0.13	0.13 ± 0.13	...	34 ± 48	-1.5 - 10.5	0.3
2MASS J16073939-1917472	0.58 ± 0.16	-0.32 ± 0.15	-0.35 ± 0.15	...	-18 ± 42	-1.5 - 10.5	0.3
2MASS J16075796-2040087	23.49 ± 0.12	-0.07 ± 0.13	0.16 ± 0.14	...	3258 ± 73	-17.0 - 17.0	0.6
2MASS J16080555-2218070	0.02 ± 0.12	17 ± 33	-1.5 - 10.5	0.3
2MASS J16081566-2222199	0.97 ± 0.12	0.09 ± 0.14	-0.01 ± 0.15	...	191 ± 31	-1.5 - 10.5	0.3
2MASS J16082324-1930009	43.19 ± 0.81	0.21 ± 0.20	0.29 ± 0.21	0.400 ± 0.015	246 ± 42	-1.5 - 10.5	0.3
2MASS J16082751-1949047	0.76 ± 0.13	0.01 ± 0.15	-0.03 ± 0.15	...	21 ± 35	-1.5 - 10.5	0.3
2MASS J16083455-2211559	0.01 ± 0.12	23 ± 28	-1.5 - 10.5	0.3
2MASS J16084894-2400045	-0.06 ± 0.15	-8 ± 23	-1.5 - 10.5	0.3
2MASS J16090002-1908368	1.73 ± 0.13	0.04 ± 0.12	0.09 ± 0.12	...	35 ± 16	-1.5 - 10.5	0.3
2MASS J16090075-1908526	47.28 ± 0.91	0.42 ± 0.20	-0.27 ± 0.21	0.315 ± 0.018	815 ± 64	-0.5 - 15.5	0.5

Table 3.4: Continuum and CO $J = 3 - 2$ Flux Measurements

Source	0.88 mm Continuum				CO $J = 3 - 2$		
	S_ν (mJy)	$\Delta\alpha^a$ (arcsec)	$\Delta\delta^a$ (arcsec)	FWHM ^b (arcsec)	Flux (mJy km s ⁻¹)	Velocity Range (km s ⁻¹)	Aperture Radius (arcsec)
2MASS J16093558-1828232	0.69 ± 0.15	0.08 ± 0.14	0.14 ± 0.14	...	55 ± 38	-1.5 - 10.5	0.3
2MASS J16094098-2217594	0.44 ± 0.12	0.16 ± 0.14	-0.10 ± 0.15	...	-15 ± 37	-1.5 - 10.5	0.3
2MASS J16095361-1754474	0.87 ± 0.16	-0.12 ± 0.13	-0.02 ± 0.17	...	60 ± 44	-1.5 - 10.5	0.3
2MASS J16095441-1906551	0.50 ± 0.16	-0.48 ± 0.16	0.43 ± 0.16	...	56 ± 34	-1.5 - 10.5	0.3
2MASS J16095933-1800090	0.67 ± 0.18	-0.19 ± 0.26	-0.13 ± 0.26	...	460 ± 91	-0.5 - 10.5	0.9
2MASS J16101473-1919095	0.01 ± 0.16	-4 ± 18	-1.5 - 10.5	0.3
2MASS J16101888-2502325	0.30 ± 0.14	63 ± 30	-1.5 - 10.5	0.3
2MASS J16102174-1904067	-0.05 ± 0.16	-7 ± 32	-1.5 - 10.5	0.3
2MASS J16102819-1910444	0.05 ± 0.16	-18 ± 30	-1.5 - 10.5	0.3
2MASS J16102857-1904469	0.66 ± 0.16	-0.22 ± 0.15	-0.30 ± 0.15	...	-86 ± 30	-1.5 - 10.5	0.3
2MASS J16103956-1916524	0.07 ± 0.16	63 ± 26	-1.5 - 10.5	0.3
2MASS J16104202-2101319	0.17 ± 0.12	20 ± 19	-1.5 - 10.5	0.3
2MASS J16104636-1840598	1.78 ± 0.16	0.10 ± 0.14	0.03 ± 0.14	...	216 ± 40	-1.5 - 10.5	0.3
2MASS J16111330-2019029	4.88 ± 0.16	0.03 ± 0.14	-0.08 ± 0.14	...	59 ± 29	-1.5 - 10.5	0.3
2MASS J16111534-1757214	0.18 ± 0.16	97 ± 39	-1.5 - 10.5	0.3
2MASS J16112057-1820549	-0.06 ± 0.16	-2 ± 33	-1.5 - 10.5	0.3
2MASS J16113134-1838259	903.56 ± 0.85	0.38 ± 0.12	0.17 ± 0.13	0.401 ± 0.001	22748 ± 91	-1.0 - 11.5	0.8
2MASS J16115091-2012098	0.66 ± 0.16	0.15 ± 0.14	-0.01 ± 0.14	...	235 ± 45	-1.5 - 10.5	0.3
2MASS J16122737-2009596	0.53 ± 0.16	-0.09 ± 0.16	-0.15 ± 0.17	...	55 ± 38	-1.5 - 10.5	0.3
2MASS J16123916-1859284	6.01 ± 0.29	-0.12 ± 0.14	-0.06 ± 0.14	...	1554 ± 125	-1.5 - 8.5	1.3
2MASS J16124893-1800525	0.11 ± 0.16	24 ± 31	-1.5 - 10.5	0.3
2MASS J16125533-2319456	0.08 ± 0.13	31 ± 25	-1.5 - 10.5	0.3
2MASS J16130996-1904269	-0.05 ± 0.16	60 ± 31	-1.5 - 10.5	0.3
2MASS J16133650-2503473	0.88 ± 0.19	0.17 ± 0.14	0.02 ± 0.14	...	21 ± 41	-1.5 - 10.5	0.3
2MASS J16135434-2320342	7.53 ± 0.13	-0.17 ± 0.13	0.06 ± 0.14	...	110 ± 29	-1.5 - 10.5	0.3
2MASS J16141107-2305362	4.77 ± 0.14	0.09 ± 0.04	-0.07 ± 0.04	...	-14 ± 18	-1.5 - 10.5	0.3
2MASS J16142029-1906481	40.69 ± 0.22	-0.12 ± 0.20	0.11 ± 0.20	0.169 ± 0.005	4681 ± 118	-17.0 - 15.0	1.0
2MASS J16142893-1857224	0.10 ± 0.16	14 ± 29	-1.5 - 10.5	0.3
2MASS J16143367-1900133	1.24 ± 0.16	-0.16 ± 0.14	-0.22 ± 0.14	...	339 ± 49	-3.0 - 8.5	0.3
2MASS J16145918-2750230	0.03 ± 0.19	-53 ± 33	-1.5 - 10.5	0.3
2MASS J16145928-2459308	-0.03 ± 0.12	110 ± 29	-1.5 - 10.5	0.3
2MASS J16151239-2420091	0.22 ± 0.12	-8 ± 25	-1.5 - 10.5	0.3
2MASS J16153456-2242421	11.75 ± 0.12	0.26 ± 0.14	-0.55 ± 0.15	...	139 ± 36	-1.5 - 10.5	0.3
2MASS J16154416-1921171	23.57 ± 0.16	0.14 ± 0.14	-0.17 ± 0.14	...	14147 ± 138	-3.0 - 11.5	1.5
2MASS J16163345-2521505	2.88 ± 0.30	0.00 ± 0.13	0.01 ± 0.14	0.492 ± 0.067	164 ± 30	-1.5 - 10.5	0.3
2MASS J16181618-2619080	-0.07 ± 0.12	82 ± 29	-1.5 - 10.5	0.3
2MASS J16181904-2028479	4.62 ± 0.12	0.11 ± 0.13	0.19 ± 0.13	...	177 ± 31	-1.5 - 10.5	0.3
2MASS J16215466-2043091	0.49 ± 0.12	0.10 ± 0.14	0.25 ± 0.22	...	-56 ± 31	-1.5 - 10.5	0.3
2MASS J16220961-1953005	0.07 ± 0.16	15 ± 45	-1.5 - 10.5	0.3
2MASS J16230783-2300596	-0.35 ± 0.12	75 ± 32	-1.5 - 10.5	0.3
2MASS J16235385-2946401	0.11 ± 0.12	-24 ± 28	-1.5 - 10.5	0.3
2MASS J16270942-2148457	2.87 ± 0.12	-0.02 ± 0.14	0.08 ± 0.16	...	109 ± 32	-1.5 - 10.5	0.3
2MASS J16303390-2428062	0.60 ± 0.12	0.07 ± 0.13	-0.02 ± 0.14	...	6 ± 31	-1.5 - 10.5	0.3

^a Offsets of the continuum source from the expected stellar position. Ellipses indicate a non-detection, for which the fit position is held fixed at the expected stellar position.

^b Full width at half maximum for sources fitted with an elliptical Gaussian. Ellipses indicate point-sources and sources measured with aperture photometry.

^c Continuum flux density measured using aperture photometry.

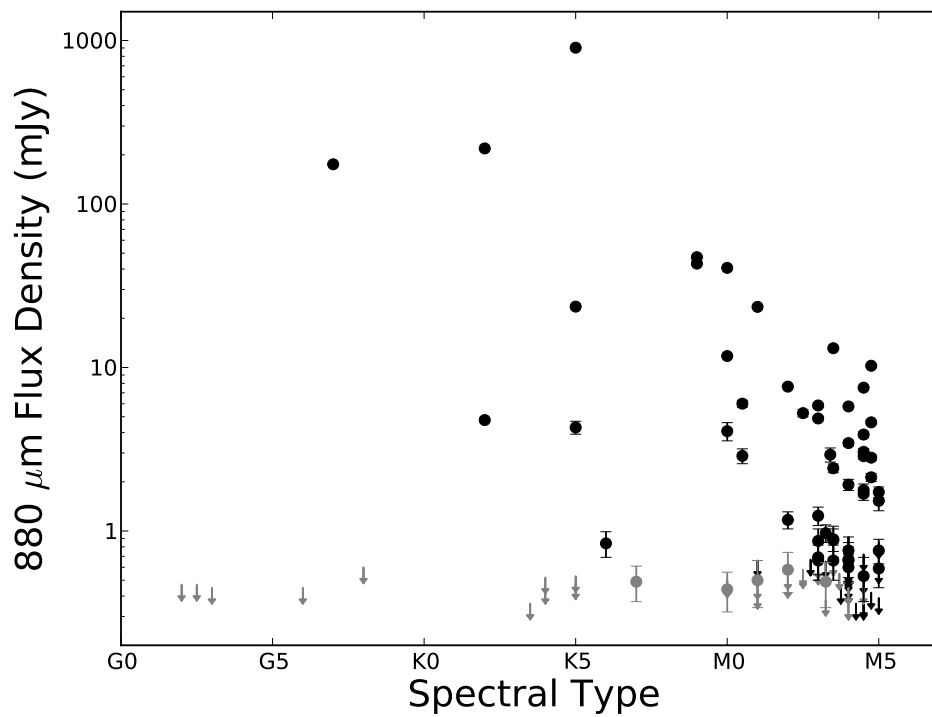


Figure 3.2: Continuum flux density at 0.88 mm as a function of spectral type for all targets in our sample. Black symbols show the primordial disks, while gray symbols represent the debris/evolved transitional disks. Arrows represent 3σ upper limits.

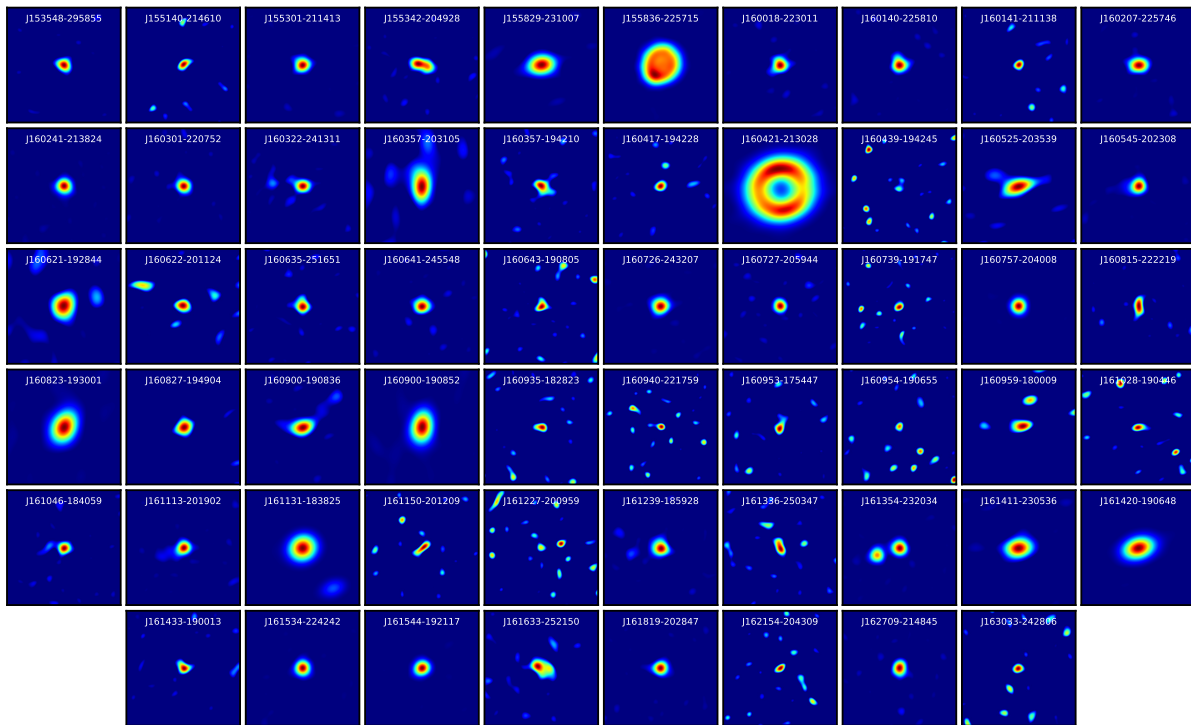


Figure 3.3: Images of the 0.88 mm continuum for the 58 primordial and debris/evolved transitional disks detected ($> 3\sigma$) in the Upper Sco sample. Each image is centered on the fitted position of the source and is $3'' \times 3''$ in size.

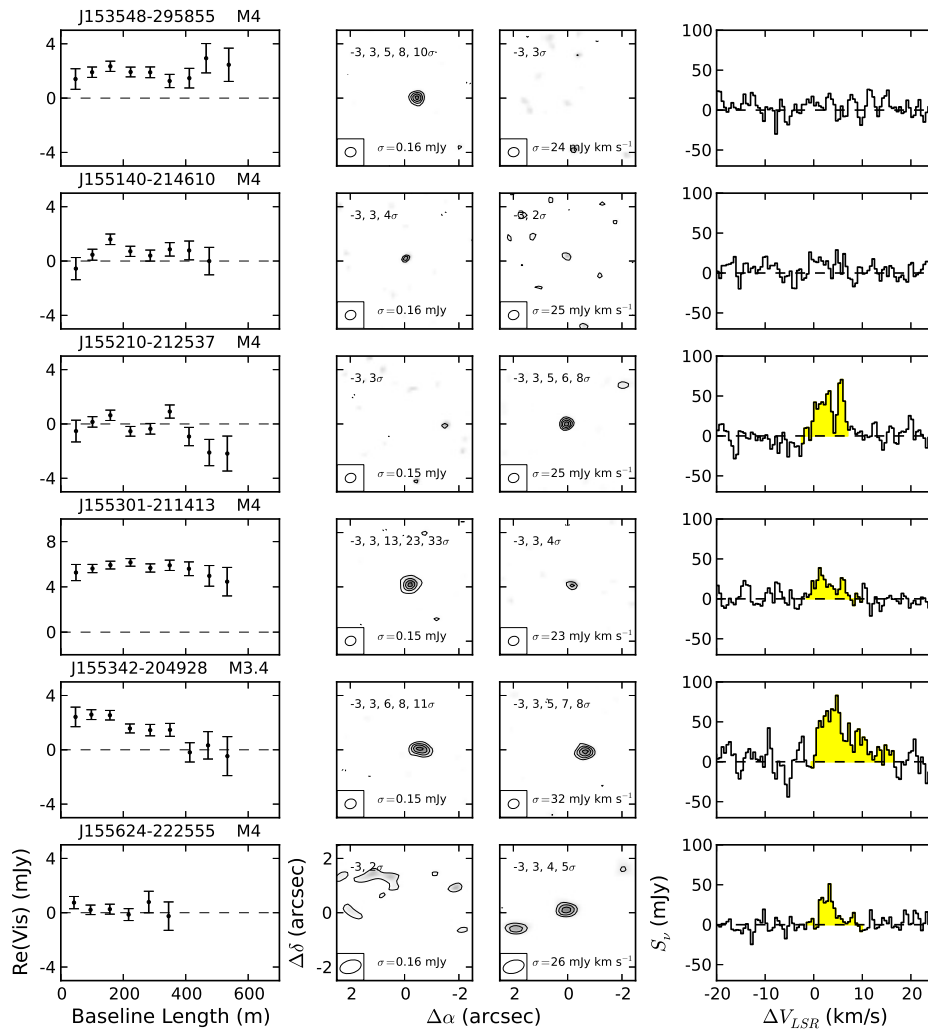


Figure 3.4: Left: real part of the visibilities as a function of projected baseline length for the 75 primordial disks in the Upper Sco sample. The phase center has been shifted to the centroid of the continuum for each source, or to the expected stellar position in the case of non-detections. The host star and its spectral type are given above each plot. Center: images of the 0.88 mm continuum and integrated CO $J = 3 - 2$ line, centered on the expected stellar position. Contour levels are given at the top of each image, with the point-source sensitivity at the bottom. Right: spectra of the CO $J = 3 - 2$ line. The yellow shaded region indicates, for 5σ detections, the velocity range given in Table 3.4 over which the line is integrated to measure the flux and generate the integrated intensity map. The aperture radii used to make the spectra are also given in Table 3.4.

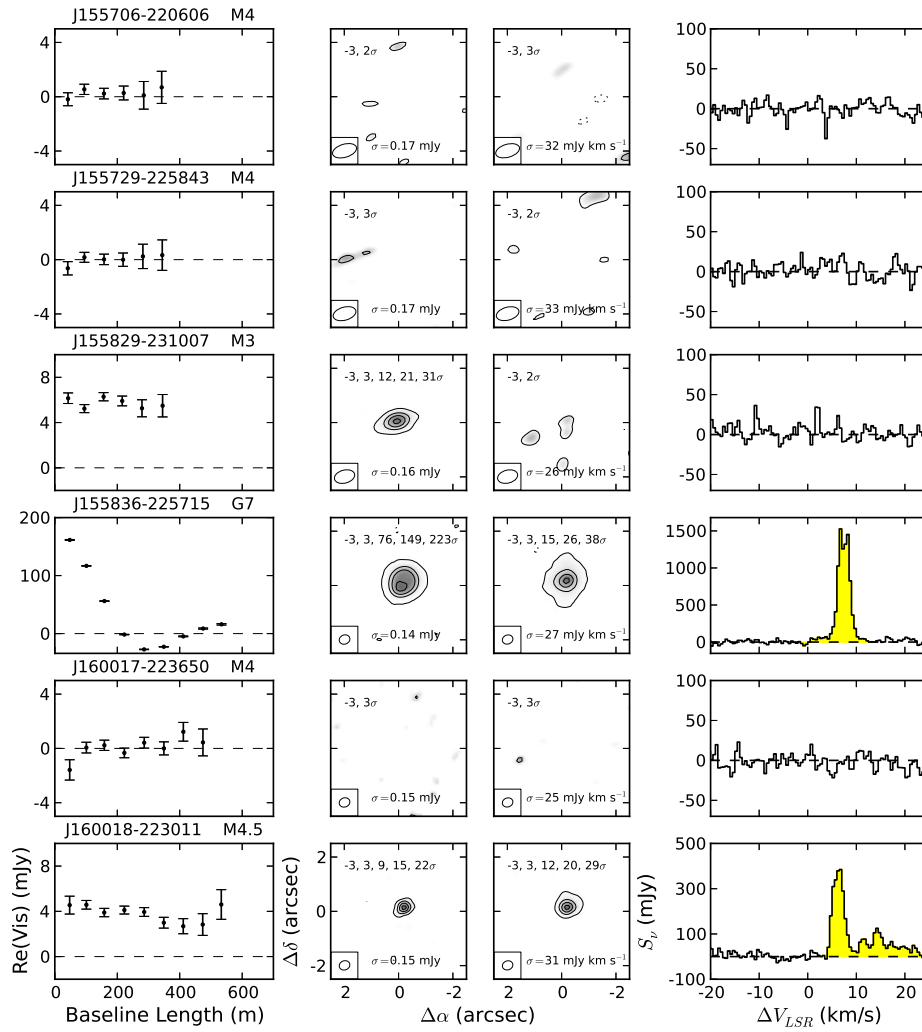


Figure 3.4: Continued.

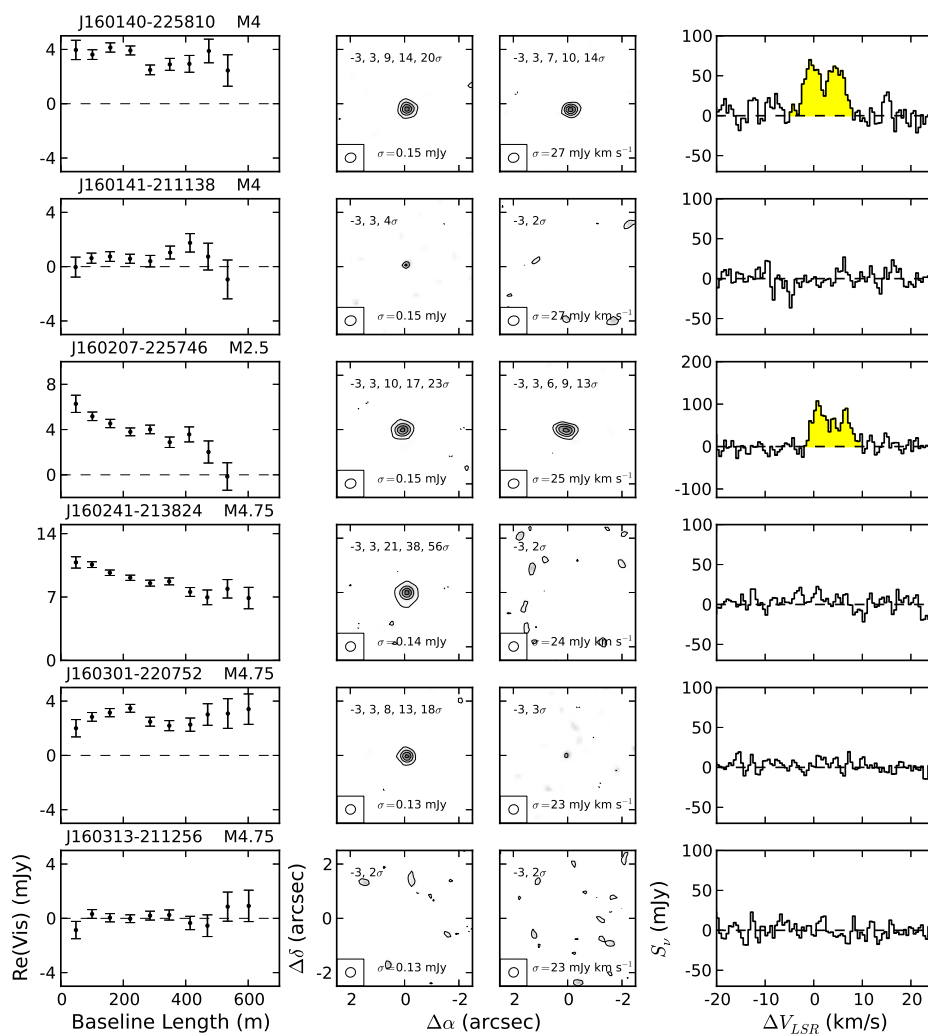


Figure 3.4: Continued.

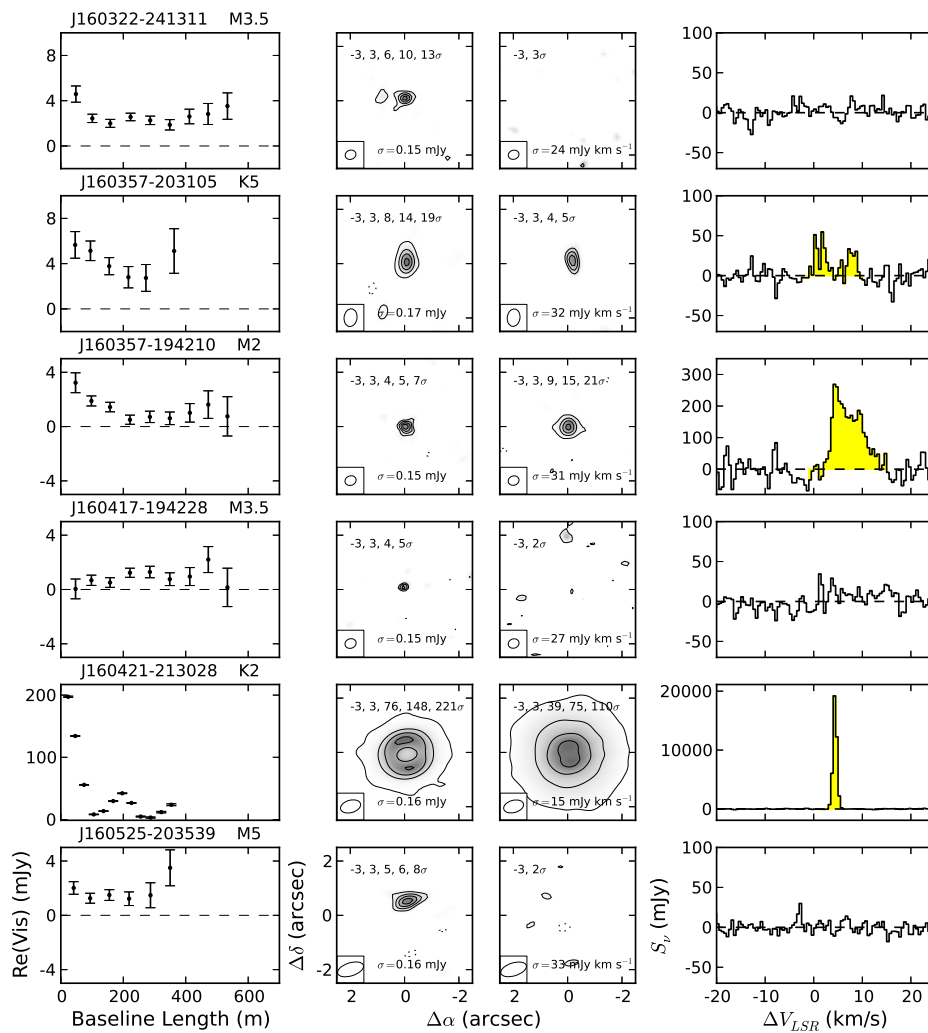


Figure 3.4: Continued.

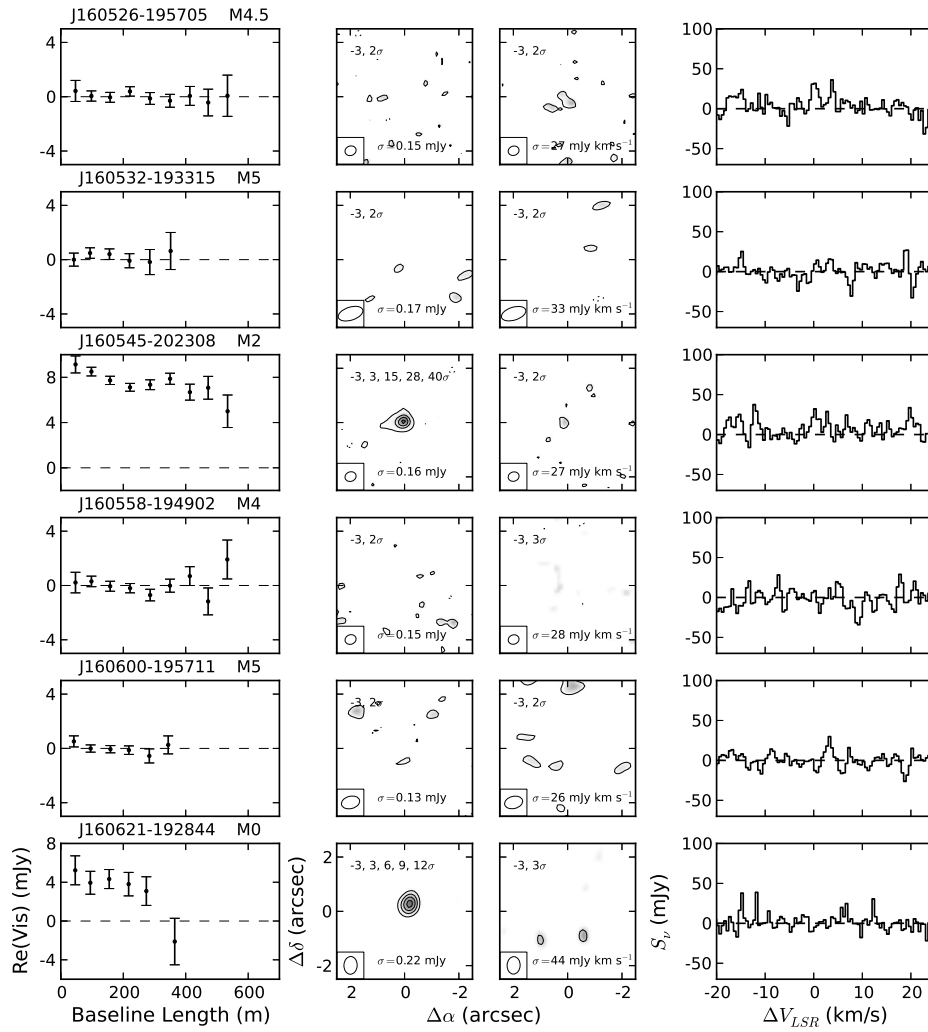


Figure 3.4: Continued.

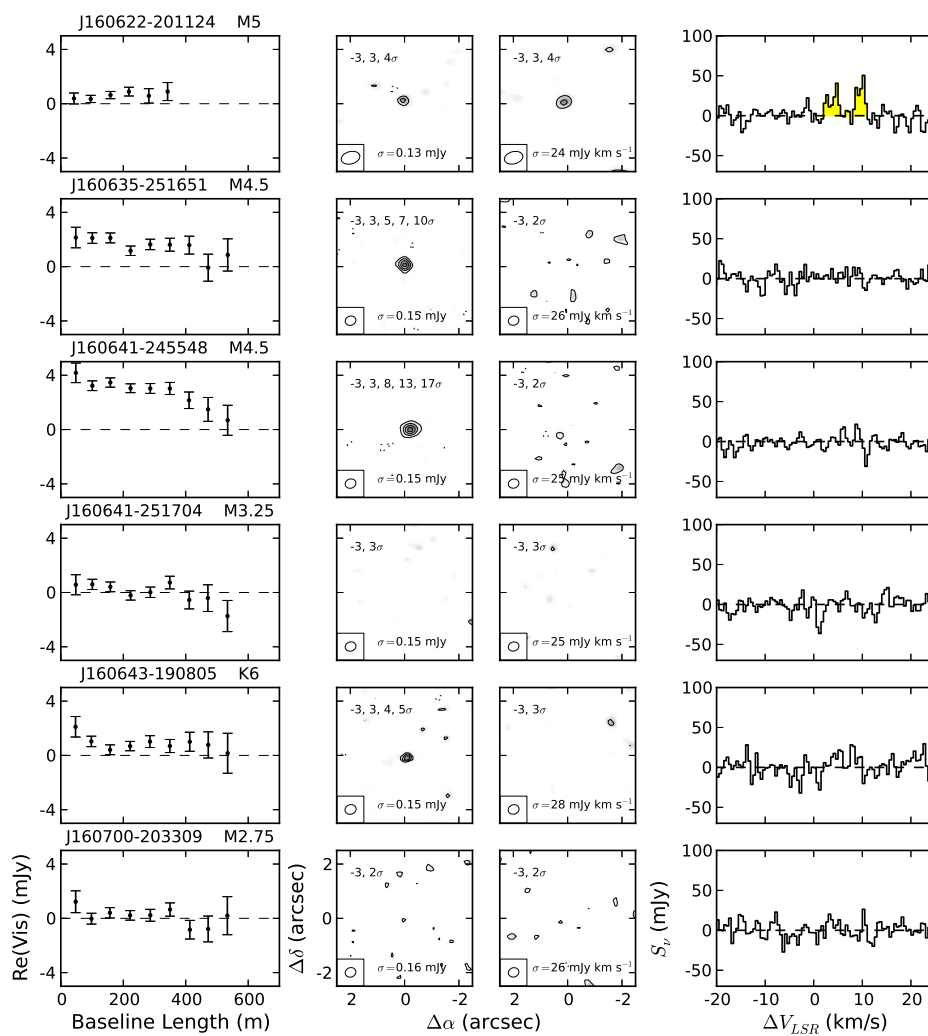


Figure 3.4: Continued.

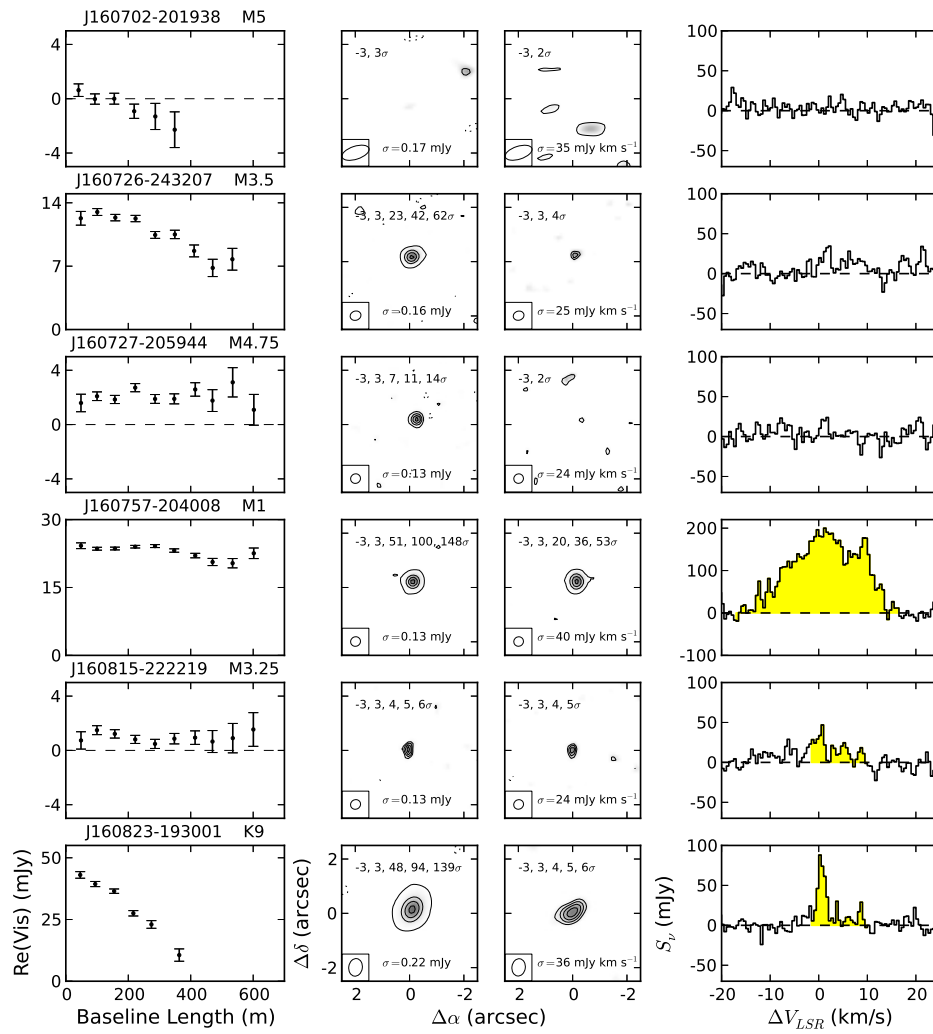


Figure 3.4: Continued.

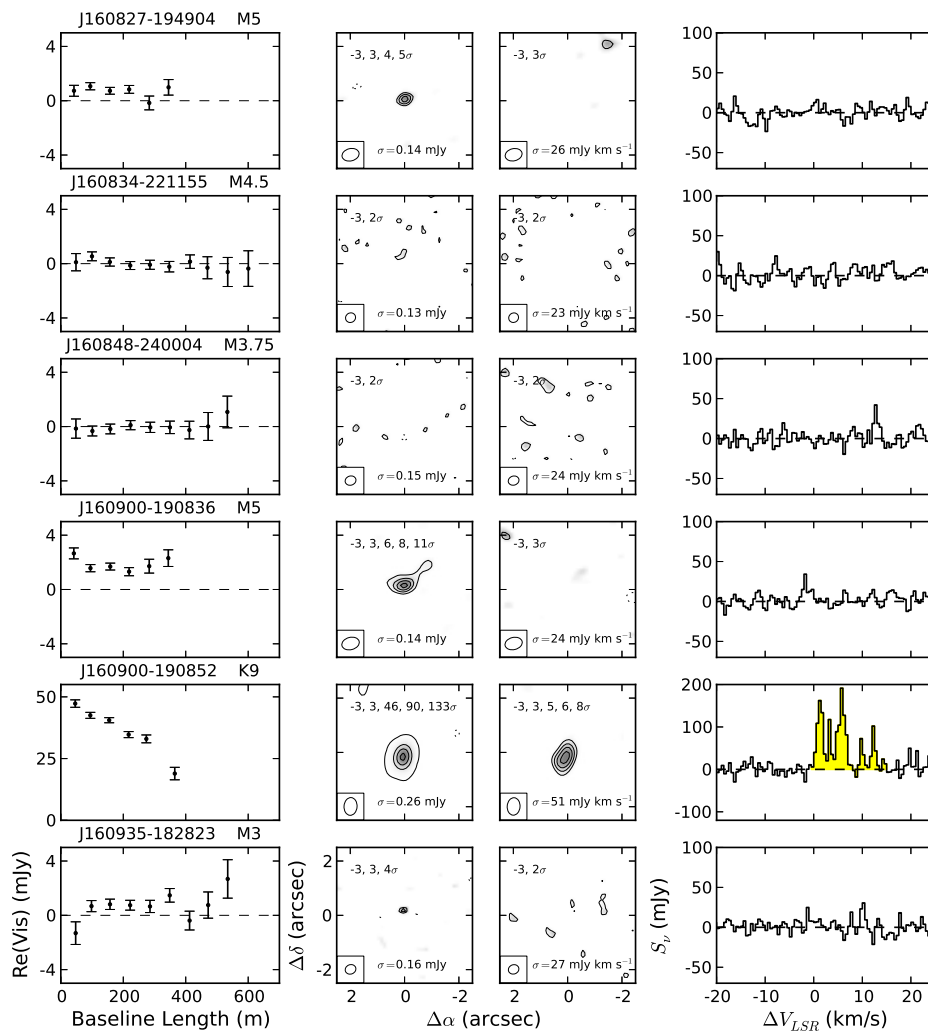


Figure 3.4: Continued.

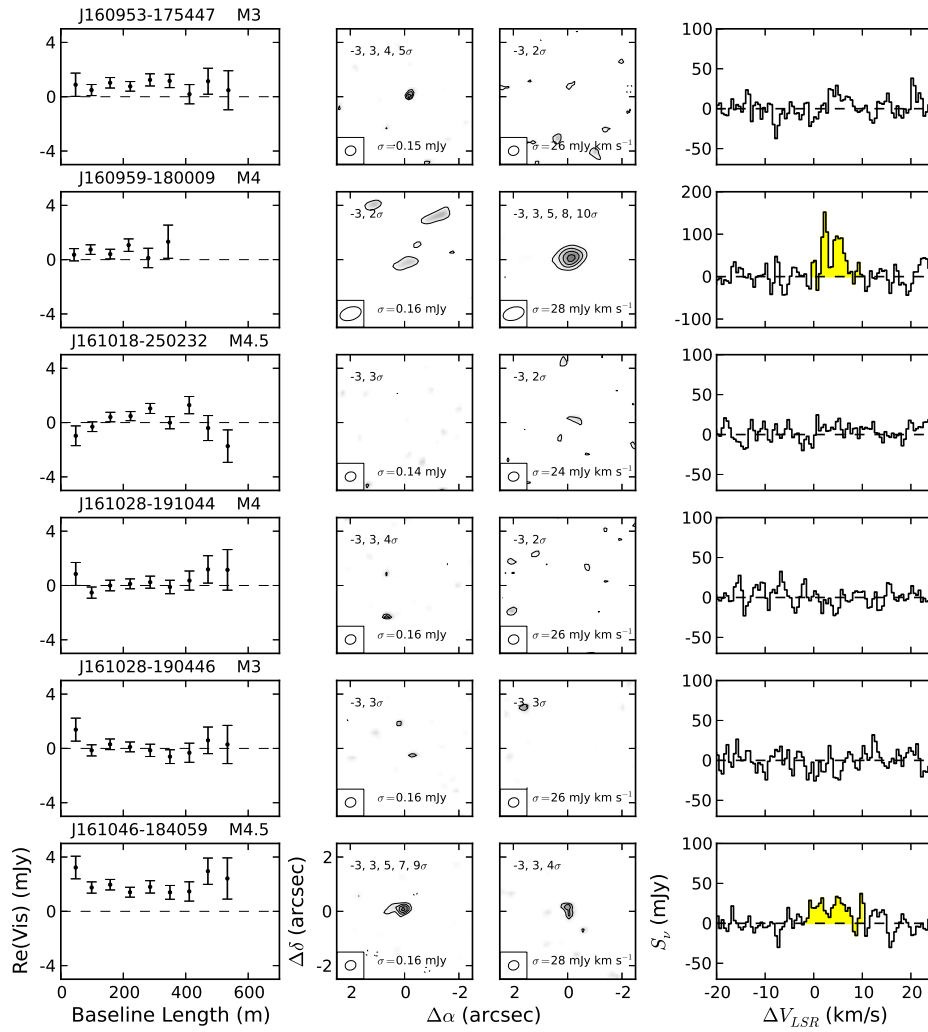


Figure 3.4: Continued.

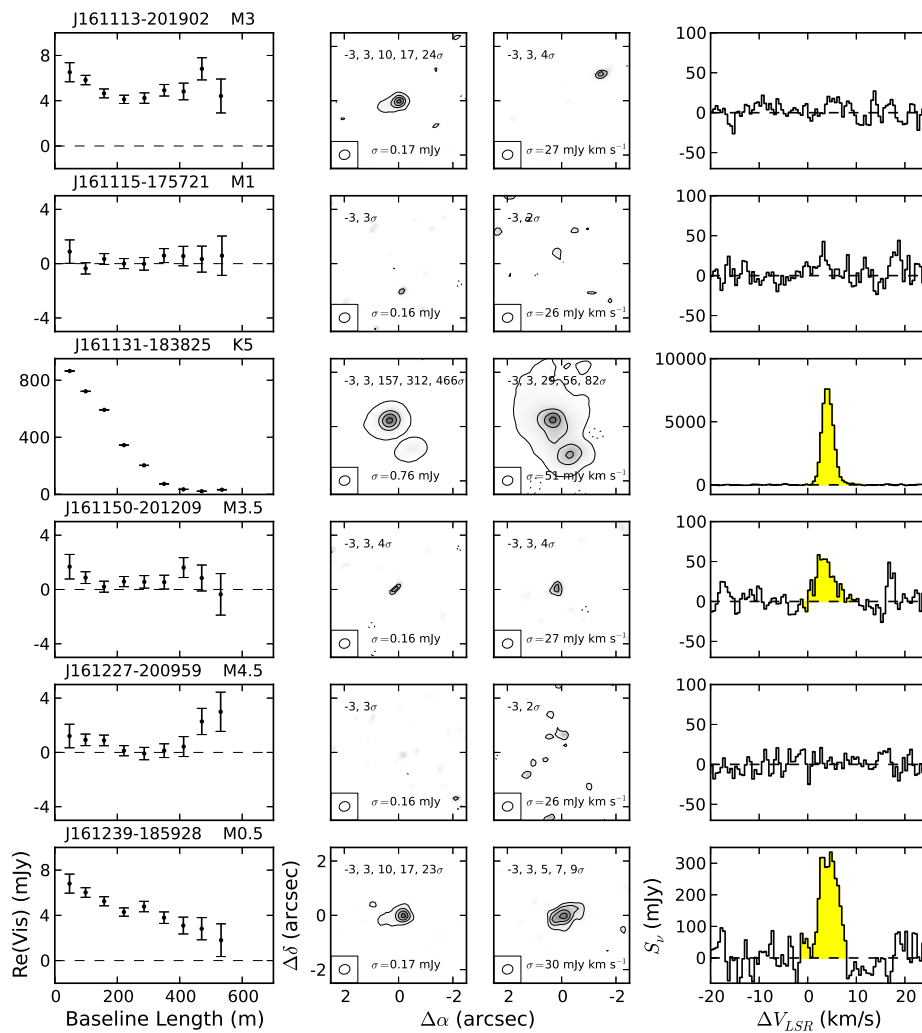


Figure 3.4: Continued.

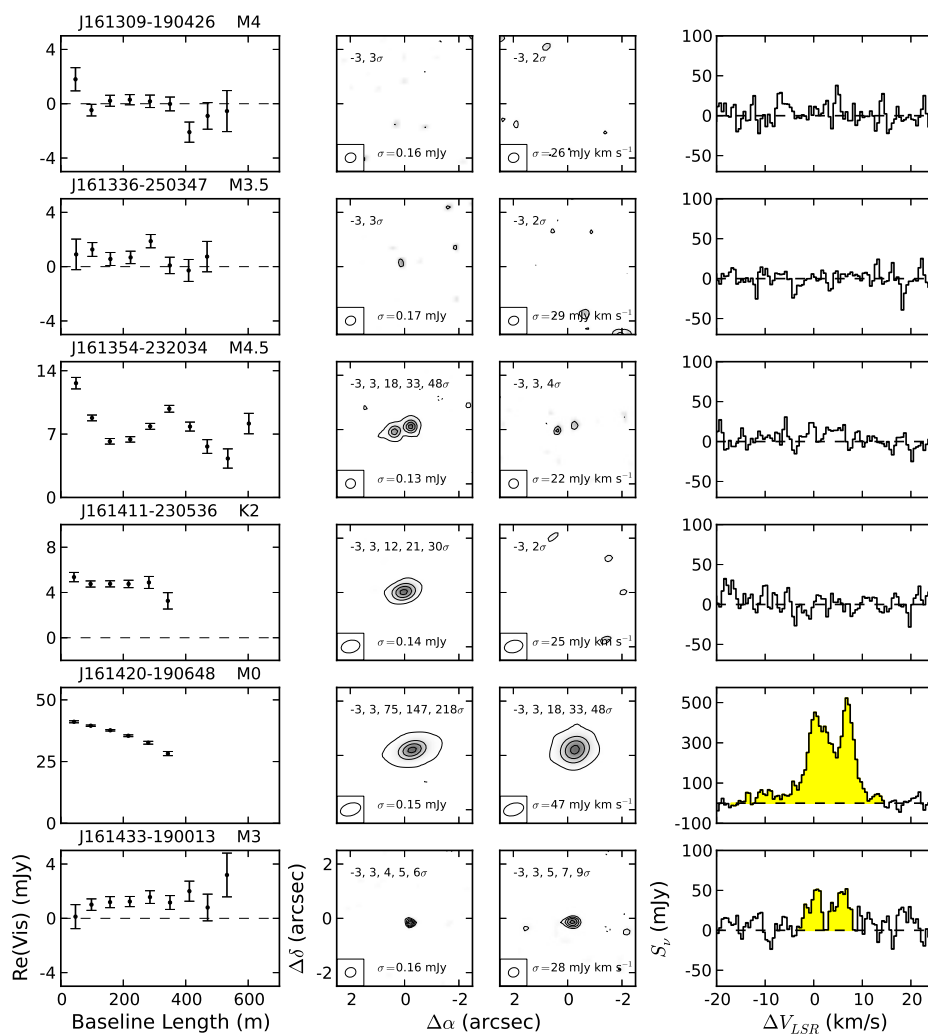


Figure 3.4: Continued.

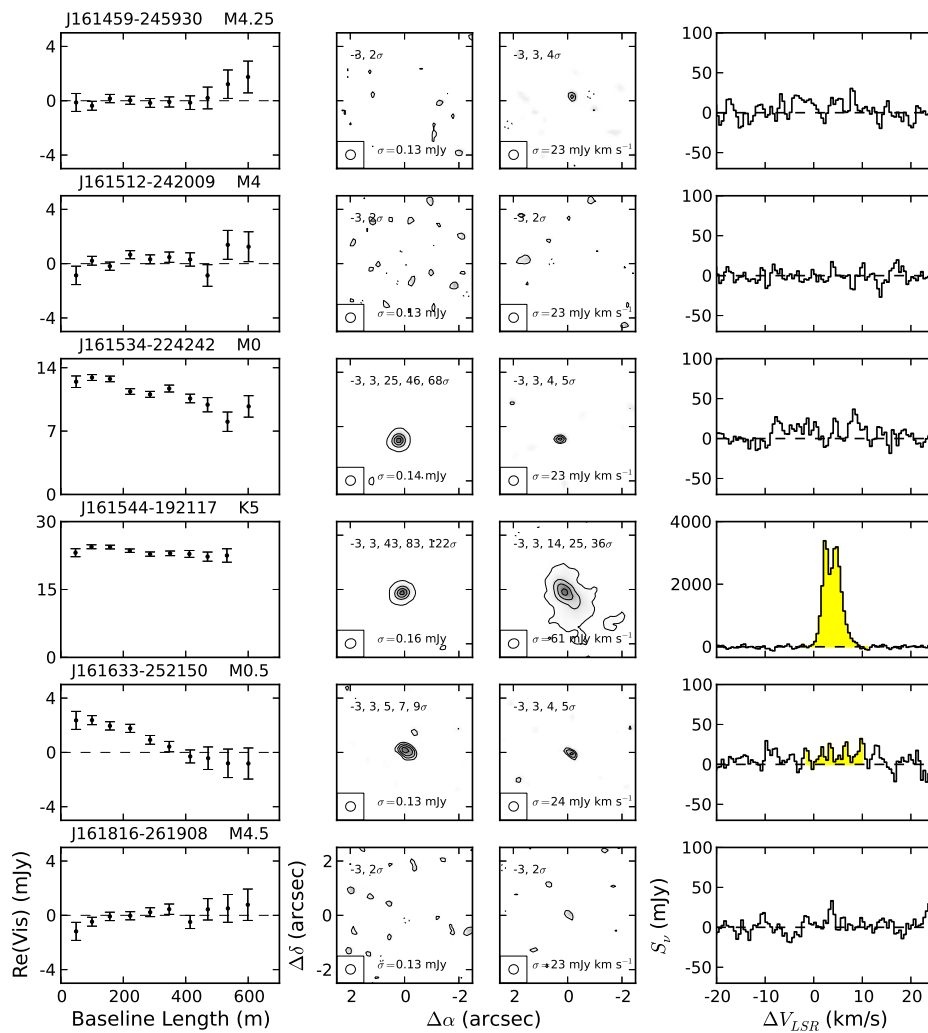


Figure 3.4: Continued.

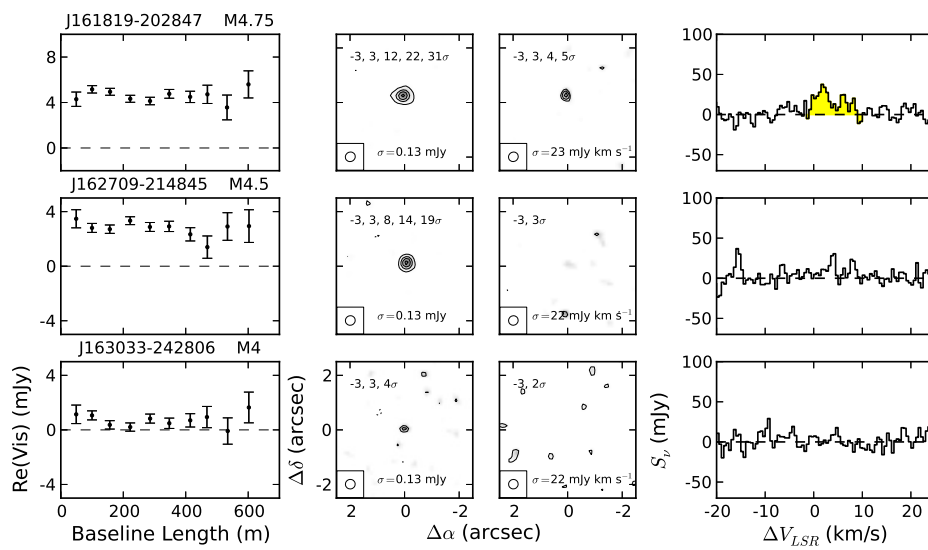


Figure 3.4: Continued.

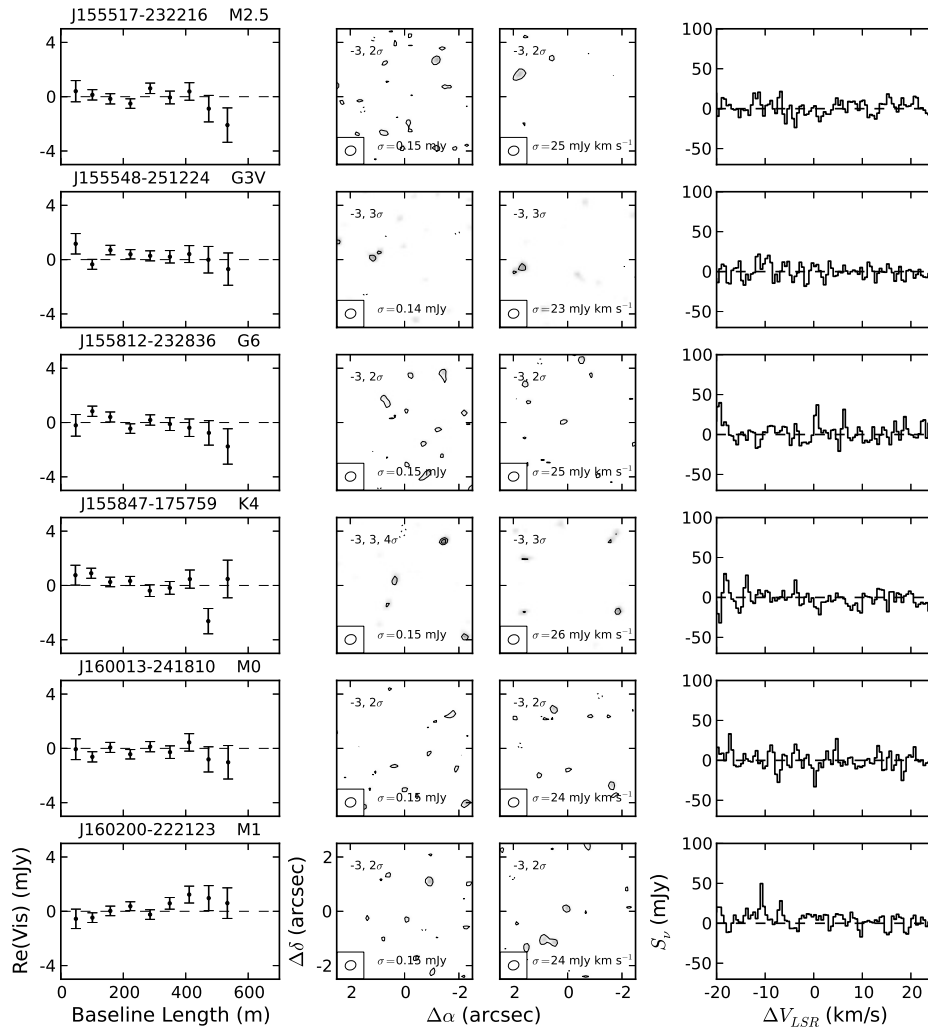


Figure 3.5: Same as Figure 3.4, but for the 31 debris/evolved transitional disks in the Upper Sco sample.

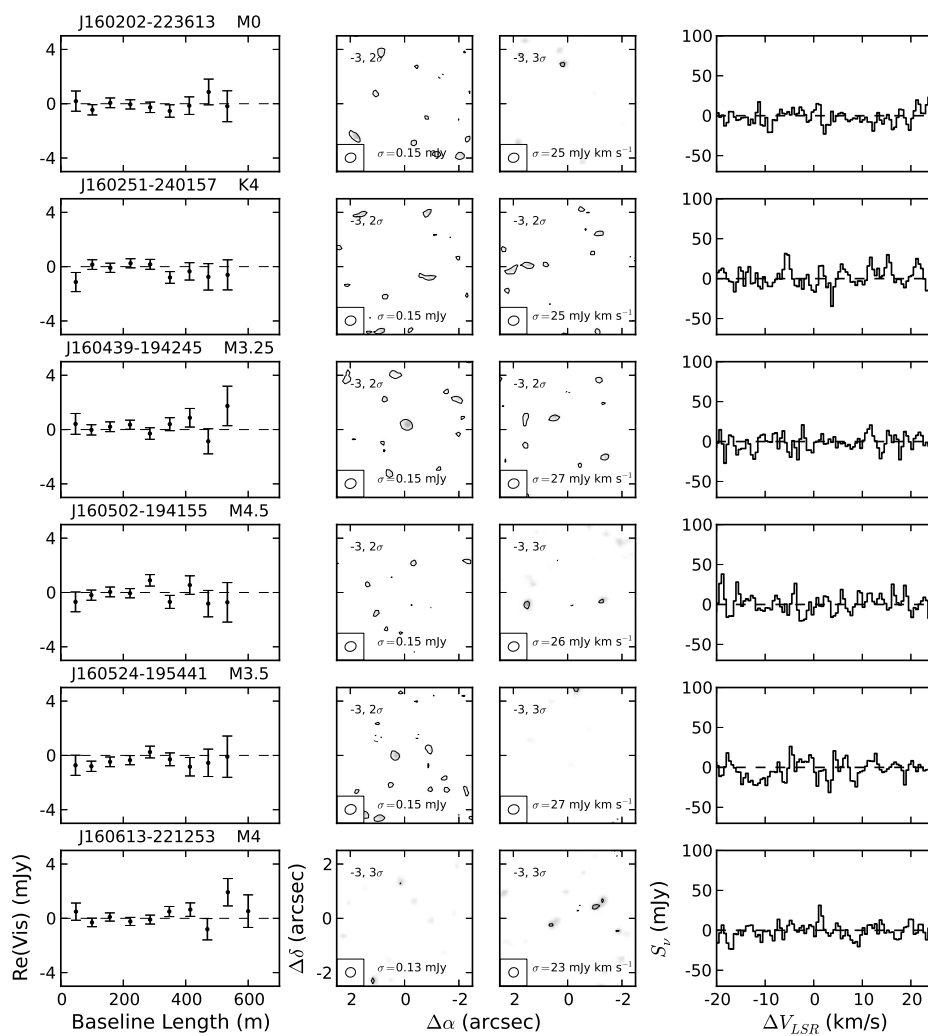


Figure 3.5: Continued.

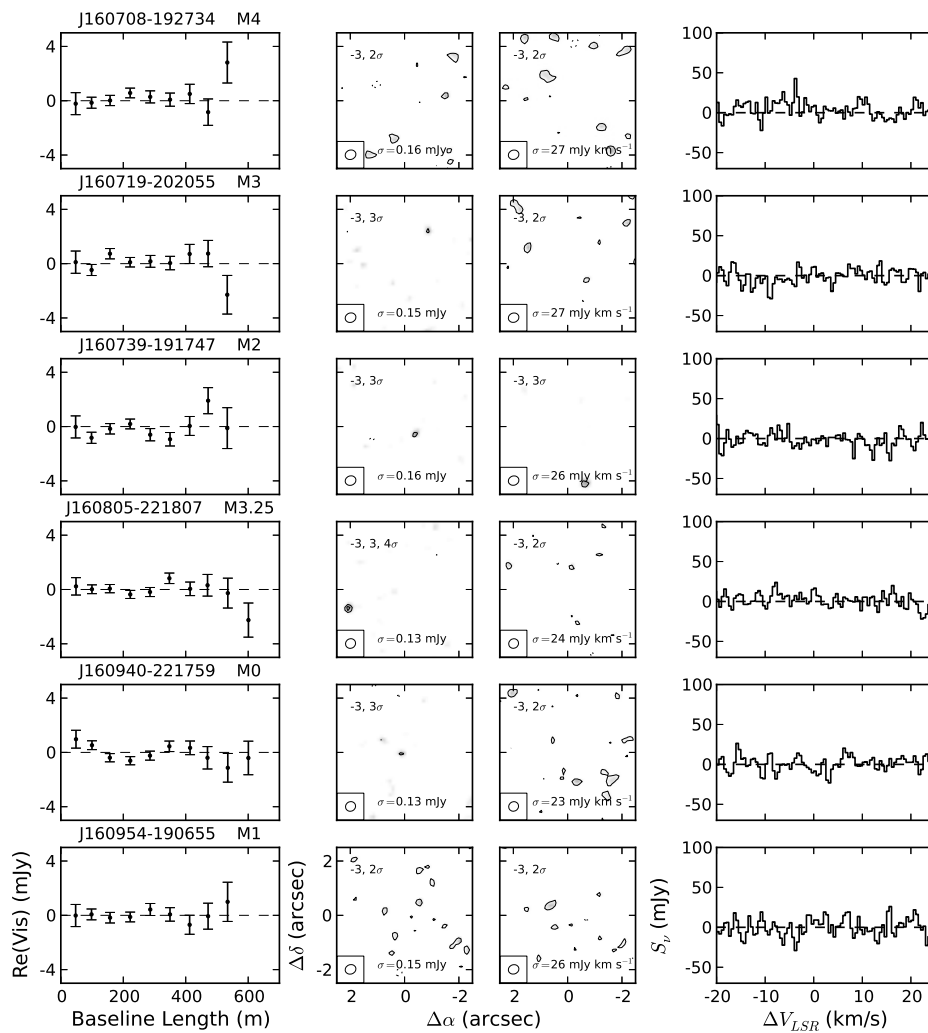


Figure 3.5: Continued.

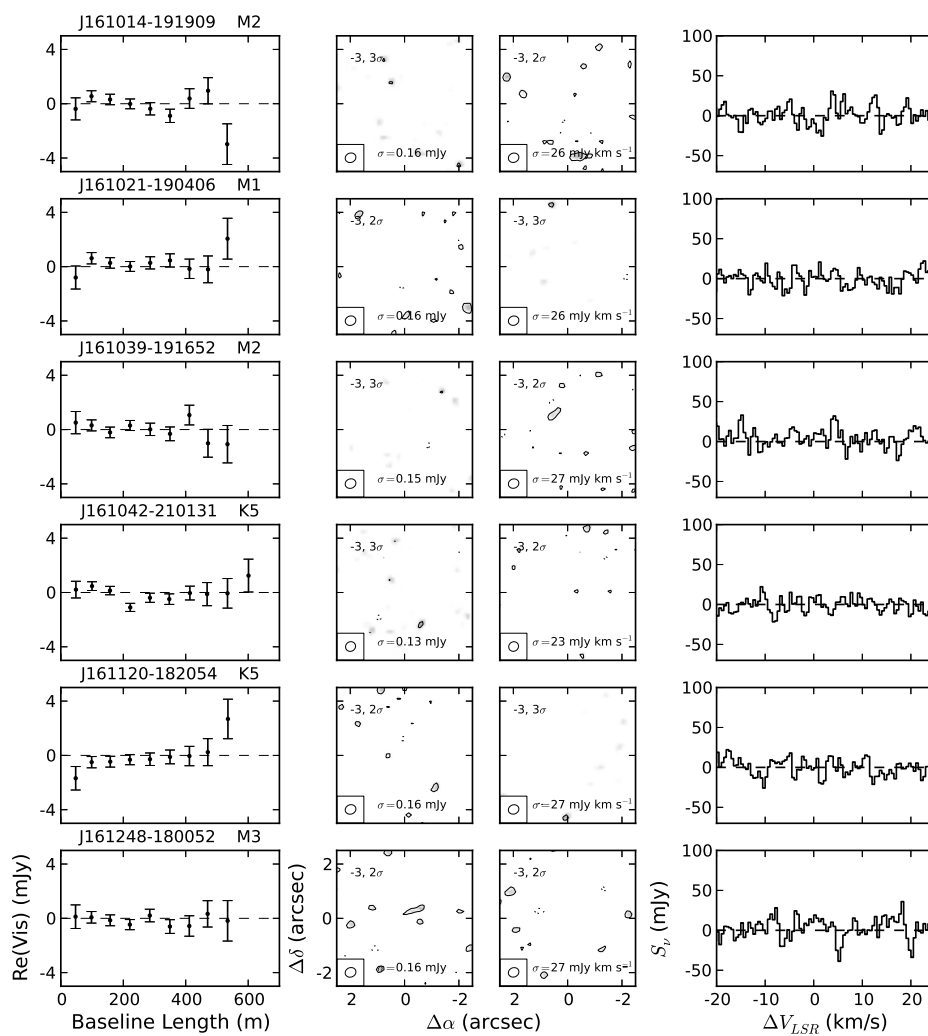


Figure 3.5: Continued.

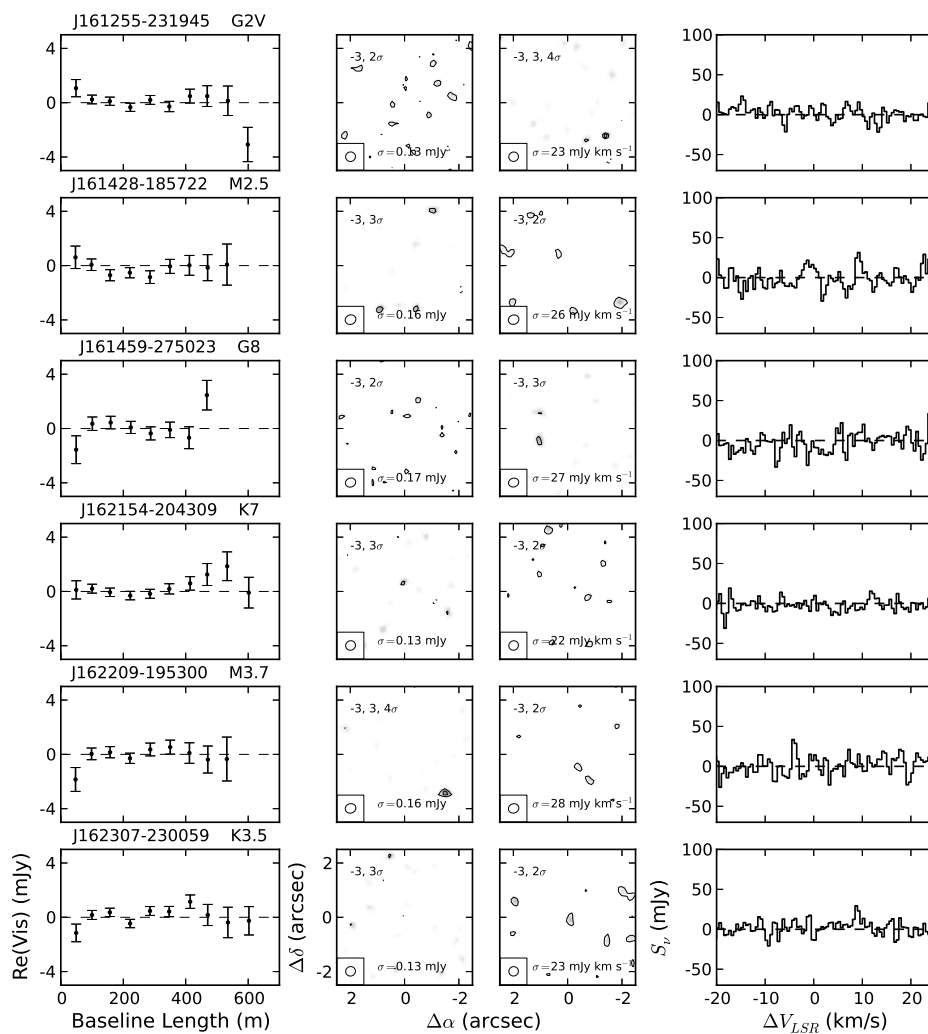


Figure 3.5: Continued.

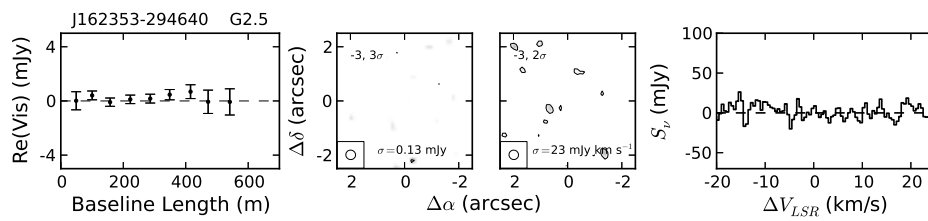


Figure 3.5: Continued.

CO Line Fluxes

CO line fluxes were determined by first subtracting the continuum dust emission using the *uvcontsub* routine in CASA, which removes a linear fit to the continuum in the spectral window containing the CO line. Fluxes were then measured using aperture photometry of the cleaned, continuum subtracted images. Measuring line fluxes in this way can be problematic due to the need to balance simultaneously choosing a velocity range and aperture size that include all emission, but are not so large that they add unnecessary noise to the measurement. On the other hand, it is also possible to select a velocity range too narrow and include only a portion of the spectrum, biasing the flux measurement. To avoid these potential pitfalls, we first identify the appropriate velocity range of the CO emission for each source, and then measure the optimal aperture size that includes all of the CO emission to within the noise.

We started with a circular aperture $0''.5$ in radius (large enough to enclose regions emitting at a range of velocities) centered on the expected stellar position or the center of continuum emission if it is detected. The spectrum within this aperture was computed with 0.5 km s^{-1} velocity sampling. Since the expected host star radial velocity relative to the LSR of our Upper Sco targets is approximately between 0 and 10 km s^{-1} (de Zeeuw et al. 1999; Chen et al. 2011; Dahm, Slesnick, and White 2012), we searched each spectrum between -5 and 15 km s^{-1} for emission exceeding three times the RMS of an emission-free region of the spectrum. If a source had at least two channels in this velocity range exceeding this threshold, we considered the source a candidate detection and selected the velocity range surrounding these channels, bounded by the emission falling to zero. Next, the flux was measured over the appropriate velocity range with increasing aperture size to determine the radius at which the flux becomes constant to within the uncertainty. The field of 2MASS J16113134-1838259 contains two sources with continuum and CO detections; for this star, we used an aperture of $0''.8$ in radius to ensure that only emission from the primary star is included.

This procedure was done using the clean components and residuals directly rather than the clean image to avoid the need to use larger apertures that enclose emission smeared to a larger area by convolution with the clean beam. To estimate the uncertainty in the measured flux, we measured the flux within 20 circular apertures of the same radius and over the same velocity range randomly distributed around the clean component and residual images (with the region containing the source

itself excluded). We adopt the standard deviation of these measurements as the uncertainty.

For all sources analyzed in this way, if the measured line flux exceeds five times its uncertainty, we consider the source a detection. We adopt a higher detection threshold for the CO than the continuum since the procedure to estimate the line flux selects the velocity range and aperture size that maximizes the signal, and thus may produce false detections. To validate our procedure, we repeated our measurements with a $0''.3$ aperture for velocities between 50 and 62 km s^{-1} , a region of the spectrum that should contain no emission. No 5σ detections were identified in this velocity range, but one 3σ detection was made. We therefore expect our 5σ threshold to yield a reliable list of detections.

For sources that were not detected at $\geq 5\sigma$ using the above method, we measured the flux using a $0''.3$ radius aperture between the velocity range of -1.5 km s^{-1} and 10.5 km s^{-1} . These velocities correspond to the median edges of the velocity ranges of the detected sources. For any sources with measured flux greater than five times its uncertainty, either from the initial 5σ cut or from sources measured with a $0''.3$ aperture and median velocity range, we repeated the flux measurement procedure described above, with the aperture centered on the centroid of the CO emission.

We detect 26 of the 75 primordial disks with $> 5\sigma$ significance and an additional 5 primordial disks between 3σ and 5σ . None of the debris/evolved transitional disks are detected. Of the 5σ CO detections, 24 were also detected in the continuum, along with 4 of the CO detections between 3σ and 5σ . Our final CO line flux measurements are listed in Table 3.4. The aperture size and velocity range used is also indicated. Moment 0 (integrated intensity) maps for each source are shown in the third columns of Figures 3.4 and 3.5. Moment 1 (mean velocity) maps are shown for 5σ detections in Figure 3.6. The right columns of Figures 3.4 and 3.5 show the spectrum of each source around the CO line, with the velocity range used indicated for 5σ detections.

The CO spectra show a variety of line shapes. Some sources, such as 2MASS J16142029-1906481, show the characteristic broad, double-peaked emission of an inclined, Keplerian disk. Others, such as 2MASS J16041265-2130284 and 2MASS J16113134-1838259, exhibit narrow, single-peaked lines indicative of face-on disks. 2MASS J16001844-2230114 has a single-peaked line at the expected velocity of Upper Sco, with a tail of weaker emission at higher velocity; this high-velocity tail appears to be coming from just to the northwest of the center of the disk emission.

In the moment 0 map of 2MASS J16001844-2230114, the high-velocity tail region can be seen as a wider extension of the disk on the northwest side relative to the southeastern side.

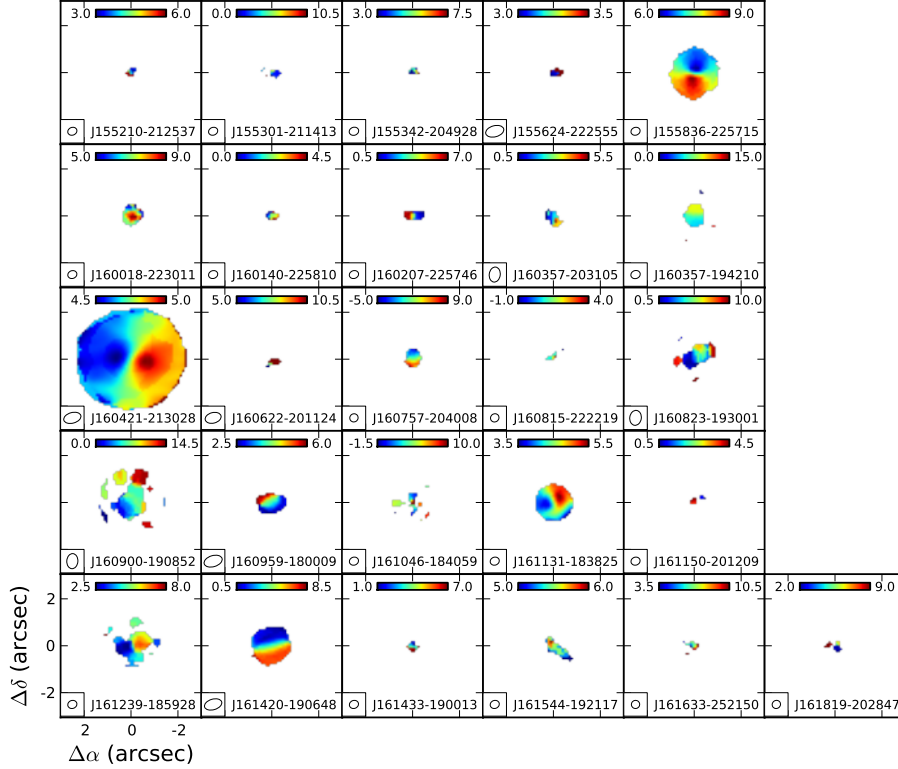


Figure 3.6: Moment 1 maps showing the mean LSRK velocity of the $^{12}\text{CO } J = 3 - 2$ line for all sources detected ($> 5\sigma$) in CO. Each image is centered on the expected stellar position. A color bar indicating the velocity range of each map in km s^{-1} is shown at the top of each map.

3.5 Disk Properties in Upper Sco

In this section, we derive disk dust masses from continuum flux densities. We then investigate the dependence of dust mass on stellar mass for the primordial disks in our sample. Finally, we use a stacking analysis to determine the mean dust mass of the debris/evolved transitional disks.

Primordial Disk Dust Masses

In the present study, we are primarily interested in the bulk dust masses of the disks in our sample. For optically thin, isothermal dust emission, the dust mass is given

by

$$M_d = \frac{S_\nu d^2}{\kappa_\nu B_\nu(T_d)}, \quad (3.1)$$

where S_ν is the continuum flux density, d is the distance, κ_ν is the dust opacity, and $B_\nu(T_d)$ is the Planck function for the dust temperature T_d . We adopt $d = 145$ pc, which is the mean distance to the OB stars of Upper Sco (de Zeeuw et al. 1999). For consistency, we follow the opacity and temperature assumptions of Andrews et al. (2013), assuming a dust opacity of $\kappa_\nu = 2.3 \text{ cm}^2\text{g}^{-1}$ at 230 GHz which scales with frequency as $\nu^{0.4}$. We estimated the dust temperature using the stellar luminosity as $T_d = 25\text{K} \times (L_*/L_\odot)^{0.25}$, which represents the characteristic temperature of the dust in the disk contributing to the continuum emission (see the discussion in Andrews et al. 2013). van der Plas et al. (2016) emphasized that systematic variations in disk size can modify the T_d - L_* relation. However, without direct measurements of disk sizes and how they may vary between Taurus and Upper Sco, we adopt the Andrews et al. (2013) relation. Given the assumptions regarding dust opacity and temperature, relative dust masses within the sample may be more accurate than the absolute dust masses if dust properties are similar within Upper Sco.

The derived dust masses are listed in Table 3.5. For sources not detected in the continuum, dust mass upper limits were estimated using the upper limit of the measured continuum flux density, calculated as three times the uncertainty plus any positive measured flux density. Uncertainties in dust masses include uncertainties in the measured flux density and in the assumed distance uncertainty, which we take to be ± 20 pc (Preibisch and Mamajek 2008, p. 235). Statistical uncertainties in the dust temperature implied from luminosity uncertainties are negligible (of the order of 1 K). Potential systematic uncertainties in dust temperatures and opacities are not included in the dust mass uncertainties. Among the 53 primordial disks detected in the continuum, detected dust masses range from 0.17 to 126 M_\oplus , with a median of 0.52 M_\oplus . The five detected debris/evolved transitional disks have dust masses ranging from 0.10 M_\oplus to 0.27 M_\oplus .

Table 3.5: Derived Dust Masses

Source	M_{dust}/M_\oplus
2MASS J15354856-2958551	0.62 ± 0.16
2MASS J15514032-2146103	0.49 ± 0.15
2MASS J15521088-2125372	< 0.52
2MASS J15530132-2114135	3.34 ± 0.83
2MASS J15534211-2049282	1.18 ± 0.31
2MASS J15551704-2322165	< 0.17
2MASS J15554883-2512240	< 0.07

Table 3.5: Derived Dust Masses

Source	$M_{\text{dust}}/M_{\oplus}$
2MASS J15562477-2225552	< 0.46
2MASS J15570641-2206060	< 0.69
2MASS J15572986-2258438	< 0.40
2MASS J15581270-2328364	< 0.07
2MASS J15582981-2310077	3.77 ± 0.94
2MASS J15583692-2257153	24.30 ± 5.99
2MASS J15584772-1757595	< 0.09
2MASS J16001330-2418106	< 0.16
2MASS J16001730-2236504	< 0.22
2MASS J16001844-2230114	2.08 ± 0.52
2MASS J16014086-2258103	1.48 ± 0.37
2MASS J16014157-2111380	0.56 ± 0.17
2MASS J16020039-2221237	< 0.11
2MASS J16020287-2236139	< 0.35
2MASS J16020757-2257467	2.08 ± 0.52
2MASS J16024152-2138245	7.63 ± 1.89
2MASS J16025123-2401574	< 0.12
2MASS J16030161-2207523	2.48 ± 0.62
2MASS J16031329-2112569	< 0.29
2MASS J16032225-2413111	1.10 ± 0.28
2MASS J16035767-2031055	0.98 ± 0.25
2MASS J16035793-1942108	0.53 ± 0.14
2MASS J16041740-1942287	0.45 ± 0.13
2MASS J16042165-2130284	52.29 ± 12.90
2MASS J16043916-1942459	0.27 ± 0.10
2MASS J16050231-1941554	< 0.39
2MASS J16052459-1954419	< 0.34
2MASS J16052556-2035397	1.05 ± 0.28
2MASS J16052661-1957050	< 0.28
2MASS J16053215-1933159	< 0.75
2MASS J16054540-2023088	3.27 ± 0.81
2MASS J16055863-1949029	< 0.26
2MASS J16060061-1957114	< 0.23
2MASS J16061330-2212537	< 0.12
2MASS J16062196-1928445	0.99 ± 0.27
2MASS J16062277-2011243	0.43 ± 0.14
2MASS J16063539-2516510	1.51 ± 0.39
2MASS J16064102-2455489	3.06 ± 0.76
2MASS J16064115-2517044	< 0.38
2MASS J16064385-1908056	0.23 ± 0.07
2MASS J16070014-2033092	< 0.30
2MASS J16070211-2019387	< 0.49
2MASS J16070873-1927341	< 0.28
2MASS J16071971-2020555	< 0.32
2MASS J16072625-2432079	5.71 ± 1.41
2MASS J16072747-2059442	0.99 ± 0.25
2MASS J16073939-1917472	0.22 ± 0.07
2MASS J16075796-2040087	9.31 ± 2.30
2MASS J16080555-2218070	< 0.15
2MASS J16081566-2222199	0.39 ± 0.11
2MASS J16082324-1930009	13.94 ± 3.45
2MASS J16082751-1949047	0.42 ± 0.12

Table 3.5: Derived Dust Masses

Source	$M_{\text{dust}}/M_{\oplus}$
2MASS J16083455-2211559	< 0.28
2MASS J16084894-2400045	< 0.27
2MASS J16090002-1908368	1.15 ± 0.29
2MASS J16090075-1908526	13.50 ± 3.34
2MASS J16093558-1828232	0.34 ± 0.11
2MASS J16094098-2217594	0.10 ± 0.03
2MASS J16095361-1754474	0.58 ± 0.17
2MASS J16095441-1906551	0.17 ± 0.06
2MASS J16095933-1800090	0.32 ± 0.11
2MASS J16101473-1919095	< 0.20
2MASS J16101888-2502325	< 0.49
2MASS J16102174-1904067	< 0.17
2MASS J16102819-1910444	< 0.48
2MASS J16102857-1904469	0.17 ± 0.06
2MASS J16103956-1916524	< 0.24
2MASS J16104202-2101319	< 0.12
2MASS J16104636-1840598	1.53 ± 0.39
2MASS J16111330-2019029	1.83 ± 0.45
2MASS J16111534-1757214	< 0.19
2MASS J16112057-1820549	< 0.10
2MASS J16113134-1838259	127.28 ± 31.39
2MASS J16115091-2012098	0.32 ± 0.10
2MASS J16122737-2009596	0.39 ± 0.14
2MASS J16123916-1859284	1.79 ± 0.45
2MASS J16124893-1800525	< 0.27
2MASS J16125533-2319456	< 0.05
2MASS J16130996-1904269	< 0.25
2MASS J16133650-2503473	0.41 ± 0.13
2MASS J16135434-2320342	3.81 ± 0.94
2MASS J16141107-2305362	0.68 ± 0.17
2MASS J16142029-1906481	10.52 ± 2.59
2MASS J16142893-1857224	< 0.19
2MASS J16143367-1900133	0.36 ± 0.10
2MASS J16145918-2750230	< 0.11
2MASS J16145928-2459308	< 0.16
2MASS J16151239-2420091	< 0.53
2MASS J16153456-2242421	2.57 ± 0.63
2MASS J16154416-1921171	5.99 ± 1.48
2MASS J16163345-2521505	1.15 ± 0.30
2MASS J16181618-2619080	< 0.22
2MASS J16181904-2028479	3.02 ± 0.75
2MASS J16215466-2043091	0.13 ± 0.04
2MASS J16220961-1953005	< 0.16
2MASS J16230783-2300596	< 0.07
2MASS J16235385-2946401	< 0.06
2MASS J16270942-2148457	2.41 ± 0.60
2MASS J16303390-2428062	0.32 ± 0.09

Stellar Mass Dependence

Derived dust masses are plotted against stellar mass for the primordial disks in Figure 3.7. Visual inspection of this figure shows a spread in dust masses over two orders of magnitude at a given stellar mass. This scatter far exceeds the uncertainties in the individual dust mass measurements and indicates large variations in either the dust opacity or dust mass of the disks in Upper Sco. Despite this scatter, Figure 3.7 reveals a trend that more massive stars tend to have more massive disks. The distribution of upper limits also supports this; only 36 of 57 sources are detected below a stellar mass of $0.35 M_{\odot}$, compared to 17 of 18 above. We used the Cox proportional hazard test for censored data, implemented with the *R Project for Statistical Computing* (R Core Team 2014), to evaluate the significance of this correlation. We find the probability of no correlation to be 2.12×10^{-4} . We thus conclude there is strong evidence that disk dust mass increases with stellar mass in Upper Sco.

Following Andrews et al. (2013), we fit a power law to dust mass as a function of stellar mass using the Bayesian approach of Kelly (2007), which incorporates uncertainties in both parameters, intrinsic scatter about the relation, and observational upper limits. The resulting best-fit relation is $\log(M_{\text{dust}}/M_{\oplus}) = (1.67 \pm 0.37) \log(M_{*}/M_{\odot}) + (0.76 \pm 0.21)$ with an intrinsic scatter of 0.69 ± 0.08 dex in $\log(M_{\text{dust}}/M_{\oplus})$.

Debris/Evolved Transitional Disks

Of the 31 stars classified by Luhman and Mamajek (2012) as debris/evolved transitional disks, 5 were detected in the continuum. For the remaining stars, we performed a stacking analysis to determine their average disk properties. The fields of four of these remaining stars (2MASS J15584772-1757595, 2MASS J16020287-2236139, 2MASS J16025123-2401574, and 2MASS J16071971-2020555) contain a submillimeter continuum source that is offset from the stellar position but within the $6''$ resolution of the $24 \mu\text{m}$ *Spitzer* observations used by Luhman and Mamajek (2012). Thus, it is possible the $24 \mu\text{m}$ excess seen for these stars is due to a background source, and not a disk associated with the star. These four stars were excluded from our stacking analysis.

Images of each source were generated from the visibilities using a circular Gaussian synthesized beam with an FWHM of $0''.4$. Since none of these sources were individually detected, we centered the image of each on the expected stellar position to generate the stacked image. Each pixel of the stacked image was calculated as the

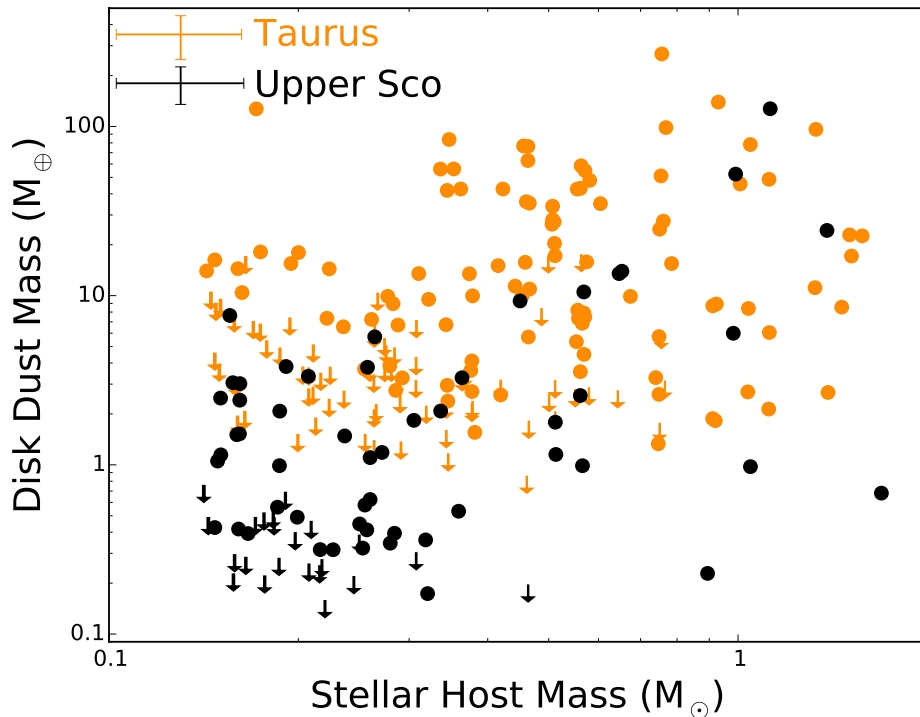


Figure 3.7: Disk dust mass as a function of stellar mass for the Taurus (orange) and Upper Sco (black) primordial disk samples. Upper limits (3σ) are plotted as arrows. Typical error bars are shown in the upper left.

mean of the corresponding pixels of the source images, weighted by the RMS noise of each image. Figure 3.8 shows the resulting mean image. The measured flux density in a $0''.4$ diameter aperture at the center of the stacked image is 0.03 ± 0.05 mJy. We determined the dust mass of the stacked disk in the same way as described in Section 3.5, assuming a median dust temperature of 18 K, and find a 3σ upper limit to the dust mass of $0.06 M_{\oplus}$.

3.6 Comparison Between Upper Sco and Taurus

It has been well established that the statistical properties of the disks in Upper Sco and Taurus are different. While $\sim 65\%$ of low-mass stars in Taurus host an optically thick inner disk (Hartmann et al. 2005), this fraction has decreased to $\sim 19\%$ in Upper Sco (Carpenter et al. 2006). The frequency of disks showing signs of accretion drops even more rapidly, and accretion rates of disks in Upper Sco that still show signs of accretion have dropped by an order of magnitude relative to accreting disks in Taurus (Dahm and Carpenter 2009; Dahm 2010; Fedele et

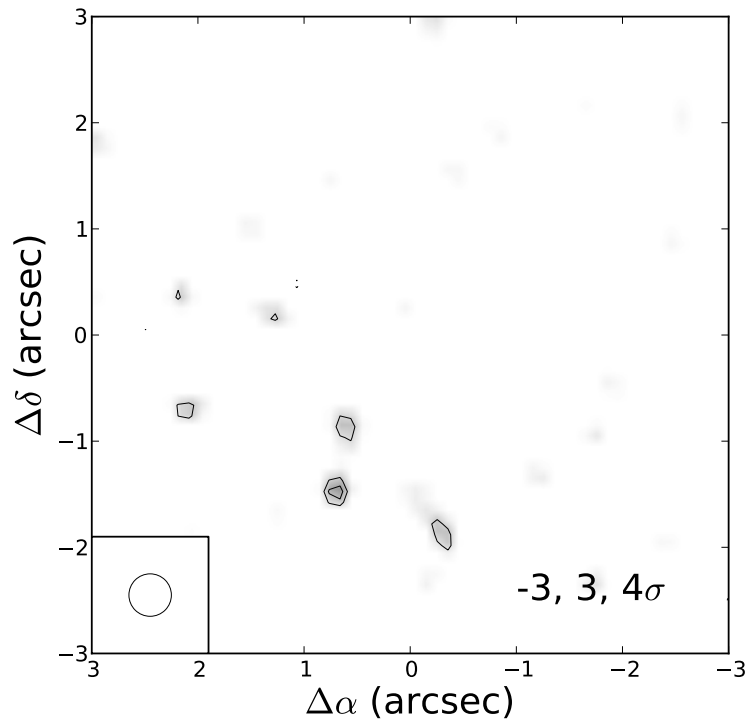


Figure 3.8: Stacked continuum image of the debris/evolved transitional disks which are not detected. Four sources were excluded due to the possibility of being identified as disks due to contamination from background sources (see the text). The flux density inside a 0.4 radius aperture at the center of the image is 0.03 ± 0.05 mJy.

al. 2010). Such observations have been interpreted as evidence for disk evolution between Taurus and Upper Sco. However, for the disks still present in Upper Sco, the question remains whether they differ significantly in dust mass from younger Taurus disks.

The Taurus star-forming region is ideally suited for such a comparison. Decades of study have led to a nearly complete census of the stars with and without disks in the region (see Luhman et al. 2010; Rebull et al. 2010), along with an abundance of stellar data that allow for a comparison with Upper Sco over the same stellar mass range. In addition, the proximity of Taurus provides improved sensitivity of submillimeter observations. Indeed, most disks around stars in Taurus with spectral type M3 or earlier have been detected in the submillimeter continuum (Andrews et al. 2013).

Relative Ages

The age of Upper Sco has become a subject of controversy in the past several years. Pecaat, Mamajek, and Bubar (2012) derived an age of 11 ± 2 Myr through a combination of isochronal ages of B, A, F, and G stars, along with the M supergiant Antares, and a kinematic expansion age. The masses and radii of several eclipsing binaries recently discovered in Upper Sco by the *K2* extended *Kepler* mission (Howell et al. 2014) favor an age of ~ 10 Myr when compared to pre-main-sequence models (David and Hillenbrand 2015; Kraus et al. 2015; Lodieu et al. 2015). This is in conflict with the canonical age of ~ 5 Myr based on the HR diagram positions of lower mass stars (de Geus, de Zeeuw, and Lub 1989; Preibisch et al. 2002; Slesnick, Hillenbrand, and Carpenter 2008). More recently, Herczeg and Hillenbrand (2015) used the latest stellar models of Tognelli, Prada Moroni, and Degl'Innocenti (2011), Baraffe et al. (2015), and Feiden, Jones, and Chaboyer (2015) to find an age of ~ 4 Myr from the HR diagram positions of low-mass stars and brown dwarfs.

In contrast, the mean age of stars in Taurus is $\sim 1-2$ Myr based on HR diagram positions of member stars (Kenyon and Hartmann 1995; Hartmann 2001; Bertout, Siess, and Cabrit 2007; Andrews et al. 2013), indicating that Taurus is younger than Upper Sco. However, ages determined using different methods with different samples of stars are not always comparable. Herczeg and Hillenbrand (2015) showed that isochronal ages depend systematically on not only the evolutionary models used, but also on the stellar mass range observed. These issues are apparent in the differing age estimates for Upper Sco. Ages inferred for Taurus and Upper Sco using the same stellar models and spectral type range indicate that Upper Sco is older than Taurus on a relative basis. Also, the late-type members of Upper Sco have spectral lines indicating stronger surface gravity than stars in Taurus and thus an older age (e.g., Slesnick, Carpenter, and Hillenbrand 2006). Therefore, despite the uncertainties associated with determining the absolute ages of young stars, on a relative basis, it is clear that Upper Sco is older than Taurus.

Relative Dust Masses

The sample of Taurus sources we use for our comparison of disk dust masses was compiled by Luhman et al. (2010) and Rebull et al. (2010). A catalog of submillimeter fluxes of these sources was published by Andrews et al. (2013), who used new observations and literature measurements to estimate the flux density of these sources at 1.3 and 0.89 mm. For our comparison, we use the 0.89 mm flux densities, scaled to our mean wavelength of 0.88 mm assuming $S_\nu \propto \nu^{2.4}$, which is

the frequency dependence adopted by Andrews et al. (2013) to generate the Taurus catalog. Among our Upper Sco sample, we only consider the 75 full, evolved, and transitional disks for this comparison. The debris/evolved transitional disks may represent second-generation systems that are in a different evolutionary phase than the disk sources in Taurus, and thus would not be suitable for a comparison to study *primordial* disk evolution.

Note that our upper limits were not calculated in the same way as those of Andrews et al. (2013). Taurus upper limits are reported as three times the RMS of the measurement, while our Upper Sco upper limits are three times the RMS plus any positive flux density. However, since the dust masses may be expected to be lower in Upper Sco relative to Taurus, the inconsistent treatment of upper limits strengthens our conclusions by bringing the samples closer together.

Figure 3.7 shows disk dust mass as a function of stellar mass for the Upper Sco and Taurus samples. Taurus stellar masses were estimated using the stellar temperatures and luminosities reported by Andrews et al. (2013) and the same interpolation method used for the Upper Sco sample. Taurus disk masses were calculated as described in Section 3.5 using the flux densities from Andrews et al. (2013) scaled to a wavelength of 0.88 mm. Figure 3.7 shows seemingly lower dust masses in Upper Sco than in Taurus, particularly at low stellar masses. Across the entire range of stellar masses, the upper envelope of Upper Sco disk masses is lower than that of Taurus. These differences could in principle be quantified by the cumulative dust mass distributions in Taurus and Upper Sco. However, as emphasized by Andrews et al. (2013), since dust mass is correlated with stellar mass, such a comparison requires that there is no bias in the stellar mass distributions between the two samples. Based on the log-rank and Peto & Peto Generalized Wilcoxon two-sample tests in R , which estimate the probability that two samples have the same parent distribution, we find that the probability that the Taurus and Upper Sco sample have the same stellar mass distribution to be between 3.1×10^{-6} and 3.2×10^{-5} . Thus the dust masses in the two samples cannot be compared without accounting for this bias.

To account for the dependence of disk dust mass on stellar mass, we compare the ratio of dust mass to stellar mass between the Taurus and Upper Sco samples. This ratio is shown as a function of stellar mass in Figure 3.9. To test for a correlation between this ratio and stellar mass, we used the Cox proportional hazard test; we find p values of 0.19 and 0.49 for Taurus and Upper Sco, respectively, consistent with no correlation. Thus, the ratios of disk dust mass to stellar mass in Taurus and

Upper Sco can be safely compared. Using the log-rank and Peto & Peto Generalized Wilcoxon tests, we find a probability between 1.4×10^{-7} and 4.8×10^{-7} that M_{dust}/M_* in Taurus and Upper Sco are drawn from the same distribution, strong evidence that dust masses are different in Upper Sco and Taurus. Figure 3.10 shows the distributions of M_{dust}/M_* in Taurus and Upper Sco found using the Kaplan–Meier estimator for censored data. We find a mean ratio of dust mass to stellar mass of $\langle \log(M_{\text{dust}}/M_*) \rangle = -4.44 \pm 0.05$ in Taurus and $\langle \log(M_{\text{dust}}/M_*) \rangle = -5.08 \pm 0.08$ in Upper Sco. Thus, $\Delta \langle \log(M_{\text{dust}}/M_*) \rangle = 0.64 \pm 0.09$ (Taurus–Upper Sco), such that the M_{dust}/M_* is lower in Upper Sco by a factor of ~ 4.5 .

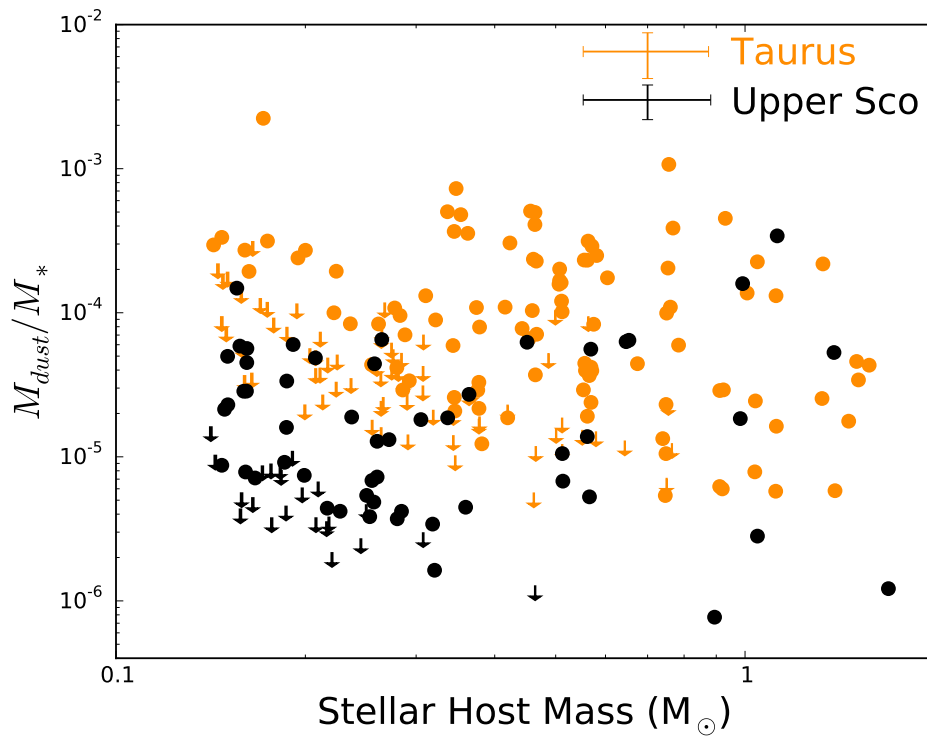


Figure 3.9: Ratio of disk dust mass to stellar mass as a function of stellar mass for the Taurus (orange) and Upper Sco (black) primordial disk samples. Upper limits (3σ) are plotted as arrows. Typical error bars are shown in the upper right. The probability that the dust mass over stellar mass values in each sample are drawn from the same distribution is $p = 1.4 \times 10^{-7} - 4.8 \times 10^{-7}$.

Having shown that the ratio of disk dust mass to stellar mass is lower in Upper Sco than in Taurus, we now examine how this difference depends on stellar mass by comparing the power-law slope of dust mass versus stellar mass in Taurus and Upper Sco. As mentioned above, Andrews et al. (2013) found a significant correlation

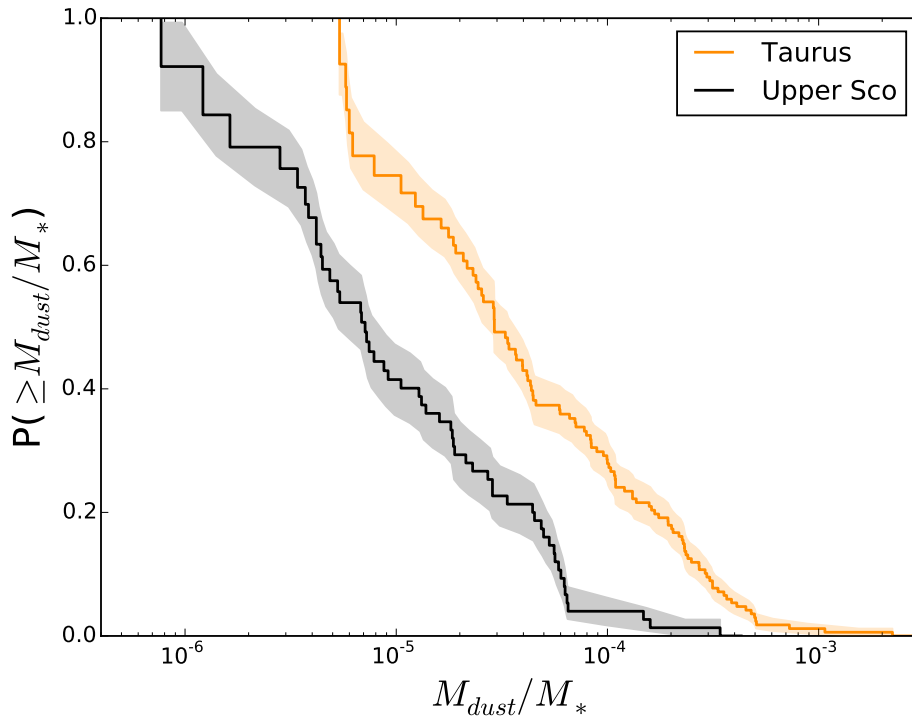


Figure 3.10: Cumulative distribution of the ratio of disk dust mass to stellar mass in Taurus and Upper Sco for the primordial disks. The shaded regions show the 68.3% confidence intervals of the distributions. Using the Kaplan–Meier estimate of the mean of $\log(M_{\text{dust}}/M_*)$ in Taurus and Upper Sco, we find that $\Delta\langle\log(M_{\text{dust}}/M_*)\rangle = 0.64 \pm 0.09$, with (M_{dust}/M_*) a factor of ~ 4.5 lower in Upper Sco than in Taurus.

between dust mass and stellar mass in Taurus. The authors performed a power-law fit using stellar masses from three different stellar models. The weighted mean of the resulting fit parameters gives a power-law slope of 1.2 ± 0.4 and intrinsic scatter of 0.7 ± 0.1 dex for stellar masses between ~ 0.1 and $\sim 10 M_{\odot}$. Our results for Upper Sco are consistent with this slope and scatter. Restricting the Andrews sample over the range of Upper Sco stellar masses, we use our derived Taurus dust and stellar masses to find a power-law slope of 1.45 ± 0.30 and scatter of 0.69 ± 0.06 dex over the range of 0.14 - $1.66 M_{\odot}$, also consistent with our Upper Sco results and the Andrews et al. (2013) result for the full Taurus sample. While disk dust masses in Upper Sco are significantly lower than those in Taurus, the power-law slopes of dust mass versus stellar mass are in agreement. This is consistent with evolution in dust mass between Taurus and Upper Sco being independent of stellar mass within our stellar mass range, though we note that the uncertainties are large.

3.7 Discussion

Dust Mass Evolution

While it has already been established that the fraction of stars with disks is lower in Upper Sco than in Taurus (Carpenter et al. 2006; Luhman and Mamajek 2012), we have shown that for the Upper Sco primordial disks that remain, the ratio of disk dust mass to stellar mass is significantly lower than for disks in Taurus (see also Mathews et al. 2012, 2013; Carpenter, Ricci, and Isella 2014). This conclusion assumes the dust emission is optically thin and the dust opacity is the same between the two regions, such that differences in the measured continuum flux can be interpreted as variations in the disk dust mass. However, from Equation 3.1, the 0.88 mm flux density is proportional to the product of dust mass and dust opacity. Thus, difference in flux density could be due to changes in dust mass, grain size/composition or some combination of the two. For a distribution of dust grain sizes described by $\frac{dn}{da} \propto a^{-p}$, the opacity varies with the maximum grain size as $\kappa \propto (a_{max})^{p-4}$ (Draine 2006). Assuming $p = 3.5$, an increase in maximum grain size by a factor of ~ 20 , for example from 1 mm to 2 cm, could fully explain the apparent decrease in dust mass by a factor of 4.5 between Taurus and Upper Sco. Such a change in the maximum grain size would change the slope of the dust opacity between wavelengths of 1 mm and 7 mm from $\beta = 1.8-1.9$ to $\beta = 1.0-1.5$, depending on the grain composition model assumed (Natta et al. 2004).

No compelling evidence for variations in β with stellar age has been found to date. Ricci et al. (2010c) found no correlation between β and age for individual stars in Taurus. However, much of the apparent age spread within Taurus can be attributed to measurement uncertainties and the effects of binarity (Hartmann 2001). Comparison between clusters with different ages should yield more robust results, but the sample sizes remain limited and no conclusive evidence for variations in β have been found (Ubach et al. 2012; Testi et al. 2014, p. 339) However, none of these results compare β in systems with ages as different as Taurus and Upper Sco. Thus, we cannot exclude the possibility that the disk mass distribution is the same, but the underlying particle size distribution differs. To break this degeneracy, observations at multiple (sub)millimeter wavelengths of both Upper Sco and Taurus are required.

The Relationship between Gas and Dust

Our combination of CO $J = 3 - 2$ and dust continuum observations allows us to probe both the gaseous and solid material in the disks of Upper Sco. Figure 3.11

shows CO line flux plotted against continuum flux density for the 75 primordial disks in our sample. This figure shows that CO flux is correlated with continuum flux over approximately three orders of magnitude. The optically thin continuum flux is proportional to the mass of solid material in the disk, while the CO emission, if it is optically thick, is a proxy for the projected area of the gas in the disk. Thus, the total mass of solids in a disk seems to trace the spatial extent of the gas in the disk. Both continuum and CO flux depend on the temperature of the disk, but this should not vary by a factor of more than a few and not enough to explain the trend between continuum and CO flux over three orders of magnitude. Instead, it appears that in Upper Sco, stars still surrounded by relatively large quantities of dust also maintain extended gas disks. This is consistent with the fact that the six brightest continuum sources are also spatially resolved. In a future paper, we will use the spatial information provided by the high angular resolution of our continuum and CO observations to obtain more quantitative measurements of dust and gas disk sizes in Upper Sco.

While 53 of the 75 primordial disks are detected in the 0.88 mm continuum, only 26 are detected in CO. Similarly, van der Plas et al. (2016) surveyed seven brown dwarfs in the 0.88mm continuum and CO $J = 3 - 2$ with a sensitivity and angular resolution comparable to our survey; while six brown dwarfs were detected in the continuum, only one was detected in CO. Among the non-detections in the present study, the median 5σ sensitivity in the integrated spectra is 72 mJy per channel, which corresponds to a brightness temperature of ~ 9 K. The gas temperature in the disk where the CO is present is expected to be > 20 K, as CO will freeze out onto dust grains at lower temperatures (Collings et al. 2003; Bisschop et al. 2006). Given that the brightness temperature limit of the observations is much less than 20 K, the lack of detectable CO in half of the continuum sources can be attributed to two possibilities: the CO is optically thick but does not fill the aperture, or the CO is optically thin.

If the CO emitting region is smaller than the aperture size, the $\gtrsim 20$ K physical temperature can be diluted to a 9 K observed brightness temperature. This will depend on the projected area of the emitting region, given by

$$A_{CO} = \pi R_{CO}^2 \cos i, \quad (3.2)$$

where R_{CO} is the outer radius of the CO emission and i is the disk inclination. The $0''.3$ radius aperture corresponds to a physical radius of 43.5 au at the distance

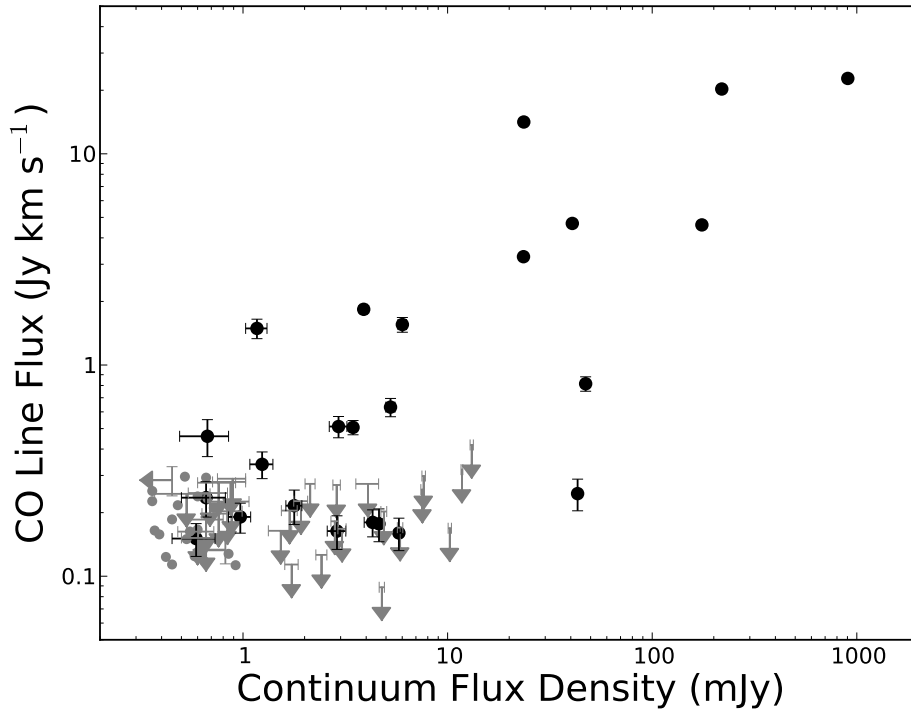


Figure 3.11: $^{12}\text{CO } J = 3 - 2$ flux versus 0.88 mm continuum flux density for the primordial disks in our Upper Sco sample. Upper limits in the CO and continuum flux are shown with arrows. The gray circles are upper limits for both the CO and continuum. Black points show CO and continuum detections.

of Upper Sco. Thus, assuming an inclination of 60 degrees, the 5σ brightness temperature upper limit of 9 K sets an upper limit on R_{CO} of ~ 40 au to dilute the brightness temperature from 20 K. While extensive measurements of CO disk radii of comparably low-mass disks are not available, such small disk sizes are not unprecedented. Woitke et al. (2011) measured a CO disk radius of 10 au for the disk around ET Cha based on analysis of the continuum and the lack of CO $J = 3 - 2$ emission. Piétu et al. (2014) measured CO radii as small as 60 au for a sample of five disks in Taurus, although these disks are at least a factor of five greater in dust mass than our median dust mass of CO non-detections.

An alternative explanation for the lack of CO detections is that gaseous CO in the disk has been depleted or dispersed to the point of becoming optically thin. The upper limit on the CO optical depth (τ_{CO}) can be related to the brightness temperature upper limit (T_b) and the physical CO temperature T_{CO} by the expression

$$B_\nu(T_b) = [B_\nu(T_{\text{CO}}) - B_\nu(T_{\text{CMB}})] (1 - e^{-\tau_{\text{CO}}}), \quad (3.3)$$

where $B_\nu(T)$ is the Planck function and T_{CMB} is the background temperature of the cosmic microwave background Mangum and Shirley (2015). Again assuming a minimum physical temperature of 20 K for the CO, we place a 5σ upper limit on the CO $J = 3 - 2$ optical depth of $\tau_{\text{CO}} = 0.28$ if the CO emission fills the aperture used to measure the flux. Such an optical depth would require substantial CO depletion in these disks. Mangum and Shirley (2015) give an expression for the total column density of a molecule given the integrated intensity of its spectrum, assuming optically thin emission:

$$N_{\text{tot}} = \left(\frac{8\pi\nu^3}{c^3 A_{\text{ul}}} \right) \left(\frac{Q_{\text{rot}}}{2J+1} \right) \frac{\exp\left(\frac{E_u}{kT_{\text{ex}}}\right)}{\exp\left(\frac{h\nu}{kT_{\text{ex}}}\right) - 1} \frac{1}{(J_\nu(T_{\text{ex}}) - J_\nu(T_{\text{CMB}}))} \int T_b \, d\nu. \quad (3.4)$$

In this expression, ν is the frequency of the transition (345.79599 GHz for ^{12}CO $J = 3 - 2$), c is the speed of light, k is Boltzmann's constant, h is Planck's constant, T_{ex} is the excitation temperature of the gas, and T_{CMB} is the temperature of the cosmic microwave background radiation. A_{ul} is the Einstein A coefficient and E_u is the energy of the upper level of the transition ($A_{\text{ul}} = 2.497 \times 10^{-6} \text{ s}^{-1}$ and $\frac{E_u}{k} = 33.19 \text{ K}$ for ^{12}CO $J = 3 - 2$, Müller et al. 2001, 2005). Q_{rot} is the partition function, which can be approximated as

$$Q_{\text{rot}} = \frac{kT}{hB_0} \exp\left(\frac{hB_0}{3kT}\right), \quad (3.5)$$

where $B_0 = 5.8 \times 10^{10} \text{ s}^{-1}$ (Huber and Herzberg 1979). J_ν is defined as

$$J_\nu \equiv \frac{\frac{h\nu}{k}}{\exp\left(\frac{h\nu}{kT}\right) - 1}. \quad (3.6)$$

Finally the integral in Equation 3.4 is simply the integrated line flux in terms of brightness temperature.

To estimate an upper limit on the ^{12}CO column density if it is optically thin, we assume an excitation temperature of 20 K. For the CO non-detections, our median 5σ upper limit on the integrated flux density is $202 \text{ mJy km s}^{-1}$. This corresponds to a CO column density upper limit of $3.5 \times 10^{15} \text{ cm}^{-2}$. This value can be compared to that expected for a typical disk in our sample given our measured dust masses. Assuming a gas to dust mass ratio of 100, a disk radius of 43.5 au to fill the measurement aperture, and the median dust mass of our CO non-detections of $0.4 M_\oplus$, the column density of molecular hydrogen would be $5.3 \times 10^{22} \text{ cm}^{-2}$. For a ^{12}CO abundance relative to H_2 of 7×10^{-5} (Beckwith and Sargent 1993; Dutrey et al. 1996, and references therein), the CO column density would be $3.7 \times 10^{18} \text{ cm}^{-2}$, a

factor of ~ 1000 higher than the limit we observe. For the disks in our sample to have spatially extended CO that fills the aperture and not be detected, the abundance of gaseous CO relative dust must be drastically reduced by depletion of CO specifically (for example, through freeze out onto dust grains) or of the gas as a whole.

Previous observations (Dutrey, Guilloteau, and Simon 2003; Chapillon et al. 2008; Williams and Best 2014, e.g.,) have found evidence for CO depletion in Taurus disks by factors of up to ~ 100 relative to the interstellar medium. Based on a lack of CI emission toward the disk around CQ Tau, Chapillon et al. (2010) concluded that the weak CO emission previously observed for this disk is due to depletion of the gas as a whole, not just of CO. Focusing on disks later in their evolution, Hardy et al. (2015) observe 24 sources with ALMA lacking signs of ongoing accretion, but still showing infrared excesses indicative of dust. While four of these sources are detected in the 1.3mm continuum, none are detected in $^{12}\text{CO } J = 2 - 1$. Assuming interstellar medium gas to dust ratios and CO abundances, the CO in the four continuum-detected disks should have been easily detected, again implying substantial depletion of CO. Given that the Upper Sco disks in the present study represent the final phase of primordial disk evolution, similar or greater levels of CO depletion may be plausible.

3.8 Summary

We have presented the results of ALMA observations of 106 stars in the Upper Scorpius OB association classified as circumstellar disk hosts based on infrared excess. We constructed a catalog of the 0.88 mm continuum and $^{12}\text{CO } J = 3 - 2$ fluxes of these stars. Continuum emission was detected toward 53 of 75 primordial disks and 5 of 31 debris/evolved transitional disks, while CO was detected in 26 of the primordial disks and none of the debris/evolved transitional disks. The continuum observations were used to measure the dust mass in the disks assuming the emission is optically thin and isothermal. We compared these masses to dust masses of disks in Taurus measured using the flux catalog compiled by Andrews et al. (2013) in order to investigate the evolution of disk dust mass and how this evolution depends on stellar mass. Within Upper Sco itself, we analyzed the dependence of disk mass on stellar host mass and the relationship between gas and dust in primordial disks. The key conclusions of this paper are as follows.

1. There is strong evidence for systematically lower dust masses in Upper Sco relative to Taurus. For the stellar mass range of $0.14 - 1.66 M_{\odot}$, we find that

the ratio of disk dust masses to stellar masses in Upper Sco are a factor of ~ 4.5 lower than in Taurus, with a probability between 1.4×10^{-7} and 4.8×10^{-7} that the dust masses in Taurus and Upper Sco are drawn from the same distribution.

2. There is a statistically significant correlation between disk dust mass and stellar host mass for primordial disks in Upper Sco. Fitting a power law, we find $M_{\text{dust}} \propto M_*^{1.67 \pm 0.37}$. Within uncertainties, the power-law slope of this relation is in agreement with the slope of the power-law relation found for Taurus dust and stellar masses by Andrews et al. (2013), indicating that dust mass evolution is consistent with being independent of stellar mass.
3. Only about half of the primordial disks detected in the continuum were detected in CO. The lack of CO detections could be explained if the CO is optically thick and has an emitting area with a radius of $\lesssim 40$ au, or if the CO has an optical depth of $\lesssim 0.28$ and is more extended. Continuum flux and ^{12}CO flux are correlated over approximately three orders of magnitude for primordial disks in Upper Sco, suggesting that the same stars have maintained relatively large gas and dust disks.

ACKNOWLEDGEMENTS

We thank the referee for their useful comments, which improved this manuscript. We are grateful to Sean Andrews for his advice on the comparison of Upper Sco and Taurus disk masses, to Trevor David for valuable input on the age of Upper Sco, to Ivan Marti-Vidal for clarification regarding the use of *uvmultifit*, and to Nick Scoville for providing an original version of the aperture photometry code that was adapted for use in this work. We also thank the ALMA staff for their assistance in the data reduction. The National Radio Astronomy Observatory is a facility of the National Science Foundation operated under cooperative agreement by Associated Universities, Inc. This paper makes use of the following ALMA data: ADS/JAO.ALMA#2011.0.00966.S and ADS/JAO.ALMA#2013.1.00395.S. ALMA is a partnership of ESO (representing its member states), NSF (USA) and NINS (Japan), together with NRC (Canada) and NSC and ASIAA (Taiwan), in cooperation with the Republic of Chile. The Joint ALMA Observatory is operated by ESO, AUI/NRAO, and NAOJ. A.I. and J.M.C. acknowledge support from NSF awards AST-1109334 and AST-1140063. This publication makes use of data products from the Two Micron All Sky Survey, which is a joint project of the University of Massachusetts and the Infrared Processing and Analysis Center/California Institute of Technology, funded by the National Aeronautics and Space Administration and the National Science Foundation. This publication makes use of data products from the *Wide-field Infrared Survey Explorer*, which is a joint project of the University of California, Los Angeles, and the Jet Propulsion Laboratory/California Institute of Technology, funded by the National Aeronautics and Space Administration. This research has made use of the NASA/IPAC Extragalactic Database (NED) which is operated by the Jet Propulsion Laboratory, California Institute of Technology, under contract with the National Aeronautics and Space Administration. This work is based [in part] on observations made with the Spitzer Space Telescope, which is operated by the Jet Propulsion Laboratory, California Institute of Technology under a contract with NASA.

*Chapter 4***MEASUREMENT OF CIRCUMSTELLAR DISK SIZES IN THE
UPPER SCORPIUS OB ASSOCIATION WITH ALMA**

ABSTRACT

We present detailed modeling of the spatial distributions of gas and dust in 57 circumstellar disks in the Upper Scorpius OB Association observed with ALMA at submillimeter wavelengths. We fit power-law models to the dust surface density and CO $J = 3 - 2$ surface brightness to measure the radial extent of dust and gas in these disks. We found that these disks are extremely compact: the 25 highest signal-to-noise disks have a median dust outer radius of 21 au, assuming an R^{-1} dust surface density profile. Our lack of CO detections in the majority of our sample is consistent with these small disk sizes assuming the dust and CO share the same spatial distribution. Of seven disks in our sample with well-constrained dust and CO radii, four appear to be more extended in CO, although this may simply be due to the higher optical depth of the CO. Comparison of the Upper Sco results with recent analyses of disks in Taurus, Ophiuchus, and Lupus suggests that the dust disks in Upper Sco may be approximately three times smaller in size than their younger counterparts, although we caution that a more uniform analysis of the data across all regions is needed. We discuss the implications of these results for disk evolution.

4.1 Introduction

The past two decades have seen tremendous progress in our understanding of protoplanetary disks (see the recent reviews by Williams and Cieza 2011; Alexander et al. 2014; Dutrey et al. 2014; Espaillat et al. 2014; Pontoppidan et al. 2014; Testi et al. 2014; Andrews 2015). Submillimeter interferometry has played a crucial role, allowing the gas and dust throughout disks to be studied at high spatial resolution. At submillimeter wavelengths, the dust continuum emission from disks is mostly optically thin, making it possible to measure dust masses and surface densities. Additionally, a number of molecular species present in disks have rotational lines observable in the submillimeter that can be used to study disk temperature, chemistry, kinematics, and mass.

Early submillimeter observations with interferometers focused on young, bright disks, revealing objects that were hundreds of astronomical units in size with masses of a few percent of their host stars (e.g., Kitamura et al. 2002; Andrews and Williams 2007; Isella et al. 2007; Andrews et al. 2009; Isella, Carpenter, and Sargent 2009, 2010; Isella et al. 2010; Guilloteau et al. 2011). Subsequent observations of fainter disks indicated that smaller sizes and masses may be more typical (Andrews et al. 2013; Piétu et al. 2014; Testi et al. 2016; Hendlar et al. 2017b; Tazzari et al. 2017). More recently, a number of studies targeted older protoplanetary disks, which are crucial to our understanding of how disks evolve and dissipate. Pre-ALMA surveys of IC348 (Lee, Williams, and Cieza 2011), the Upper Scorpius OB Association (hereafter Upper Sco, Mathews et al. 2012), and σ Orionis (Williams et al. 2013), revealed a dearth of evolved disks comparable to the brightest objects in younger regions, suggesting that older disks are intrinsically fainter than their younger counterparts.

With ALMA, it is possible to conduct large surveys of disks at an unprecedented level of sensitivity, revealing the properties of unbiased samples within individual stellar populations. Thus, Ansdell et al. (2016) surveyed the 1-3 Myr old Lupus star-forming region and, from separate measurements of dust and gas masses in 89 disks, found evidence that CO is depleted relative to dust compared to interstellar medium (ISM) values (see also Miotello et al. 2017). Eisner et al. (2016) and Ansdell et al. (2017) found evidence for similar depletion in the < 1 Myr old Orion Nebula cluster and the 3-5 Myr old σ Orionis region. In a survey of 93 disks in the 2-3 Myr old Chamaeleon star-forming region, Pascucci et al. (2016) found a relationship between disk dust mass and stellar mass consistent with other 1-3 Myr

old regions, but with a shallower slope than is seen for older disks.

Crucially, the sensitivity of ALMA enables disk surveys to be extended to more evolved stellar populations (e.g., Carpenter, Ricci, and Isella 2014; Hardy et al. 2015; van der Plas et al. 2016; Barenfeld et al. 2016, hereafter Paper I). In particular, Upper Sco provides an ideal target for such studies. The 5-11 Myr age of this association (Preibisch et al. 2002; Pecaut, Mamajek, and Bubar 2012) implies that its protoplanetary disks are in the last stage of evolution before dissipation (Hernández et al. 2008). Based on ALMA observations of 20 disk-bearing stars in Upper Sco, Carpenter, Ricci, and Isella (2014) found tentative evidence that disk dust masses are lower than in the younger Taurus star-forming region. Paper I expanded this sample to include ALMA observations of 106 Upper Sco disks and found that the dust masses are on average a factor of 4.5 lower than those in Taurus with high statistical significance. Of the 58 sources detected in the continuum in this survey, the majority were not spatially resolved, implying dust disk radii of a few tens of astronomical units or less. Only 26 sources were detected in CO, suggesting that the CO is also confined to a compact emitting area or is heavily depleted relative to the dust.

Here we present a more detailed study of the gas and dust for the disks in the Paper I sample and build on our previous results by measuring disk sizes, modeling CO emission, and determining the relative distributions of gas and dust. In Section 4.2, we describe our disk sample and ALMA observations. In Section 4.3, we detail our methodology for modeling the continuum emission, while our modeling of the CO emission is described in Section 4.4. We then discuss the implications of the gas and dust properties of these disks in Section 4.5. Our conclusions are summarized in Section 4.6.

4.2 Sample and Observations

Our stellar sample for the current work is a subset of the parent sample described in detail in Paper I. Briefly, our parent sample consisted of 106 stars in Upper Sco with spectral types between G2 and M5 (inclusive) and included all 100 candidate G2-M4.75 disk-host stars in Upper Sco identified by Luhman and Mamajek (2012) using *Spitzer* and *WISE* observations, as well as six M5 disk-host candidates from Carpenter et al. (2006) found using *Spitzer* observations.

In this work, we analyzed 57 sources detected in Paper I, listed in Tables 4.1 and 4.3. Of these sources, 21 were detected in both the 0.88 mm continuum and the

CO $J = 3 - 2$ line at 345.79599 GHz, 34 were only detected in the continuum, and two were detected only in CO. Five of the sources analyzed are classified as debris/evolved transitional disks by Luhman and Mamajek (2012). We consider the remaining sources to be primordial disks (see Paper I).

Three extremely bright continuum sources were identified in Paper I, 2MASS J15583692-2257153, 2MASS J16042165-2130284, and 2MASS J16113134-1838259, which have continuum flux densities of 174.92 ± 0.27 mJy, 218.76 ± 0.81 mJy, and 903.56 ± 0.85 mJy at 0.88mm, respectively. 2MASS J15583692-2257153 exhibits an azimuthal asymmetry in the continuum, while 2MASS J16042165-2130284 shows the large inner cavity of a transitional disk. 2MASS J16113134-1838259 is more than 20 times brighter in the continuum than any of the sources we are including in this paper and exhibits possible disk winds and tidal interactions with a stellar companion (Salyk et al. 2014). Since these systems are not representative of typical disks in Upper Sco, we excluded them from the present analysis and focused instead on understanding the broader population of ordinary disks. Zhang et al. (2014) presented a detailed analysis of 2MASS J16042165-2130284 (see also Mayama et al. 2012; van der Marel et al. 2015; Pinilla et al. 2015; Dong et al. 2017).

The ALMA observations were obtained in Cycle 0 and Cycle 2 using the 12 m array (see Paper I). All observations used band 7, with a mean frequency of 340.7 GHz for Cycle 0 and 341.1 GHz for Cycle 2 (0.88 mm) and a total bandwidth of 7.5 GHz. One spectral window was configured with channel widths of 0.488 MHz (0.429 km s^{-1} , the spectral resolution is twice the channel width) to observe the CO $J = 3 - 2$ line at 345.79599 GHz. The observations had angular resolution between $0''.35$ and $0''.73$ with a median of $0''.37$ and a continuum rms ranging from 0.13 mJy/beam to 0.26 mJy/beam, with a median of 0.15 mJy/beam.

4.3 Continuum Modeling

Our goal in modeling the continuum data was to determine the radial extent of the dust for the 55 continuum-detected disks in our sample. To accomplish this, we compared our observed visibilities to the synthetic visibilities of a model disk, deriving the model visibilities from an assumed dust density distribution in a self-consistent way.

For our model disk, we parameterized the dust surface density as a function of radius

using a truncated power law:

$$\Sigma(R) = \Sigma_0 \left(\frac{R}{10\text{au}} \right)^{-1}, \quad (4.1)$$

for R between the dust inner and outer radii, R_{in} and R_{dust} , with $\Sigma = 0$ outside of this range. We fixed R_{in} at the values found by the SED fitting of Mathews et al. (2013) for the 24 sources we share with their survey. For our remaining sources, we set R_{in} to be equal to the dust sublimation radius, calculated based on the stellar luminosities from Paper I. The choice of R_{in} does not impact our results.

The continuum signal-to-noise ratio for the majority of our sample is too low to simultaneously constrain the dust outer radius and the slope of the surface density power law. We therefore adopted a fixed R^{-1} parameterization for the surface density, which is fairly typical for disks (e.g., Kitamura et al. 2002; Andrews and Williams 2007; Isella et al. 2007; Isella, Carpenter, and Sargent 2010; Guilloteau et al. 2011). Assuming $\Sigma \propto R^{-0.5}$ and $\Sigma \propto R^{-1.5}$ power laws resulted in slightly smaller or larger disk sizes, respectively, but did not qualitatively impact our results or conclusions.

Some authors (e.g., Hughes et al. 2008; Andrews et al. 2009; Isella, Carpenter, and Sargent 2009; Andrews et al. 2010c, 2010b; Hughes et al. 2010; Isella, Carpenter, and Sargent 2010; Isella et al. 2010; Andrews et al. 2011; Guilloteau et al. 2011; Andrews et al. 2012) have parameterized the disk surface density using the self-similar solution for a viscously evolving disk, which can be approximated as a power law with an exponential tail. However, given the evolutionary state of the Upper Sco disks, it is not clear that this description is appropriate. Other effects, such as the inward radial migration of dust grains (e.g., Weidenschilling 1977), may also change the surface density profile. Birnstiel and Andrews (2014) modeled dust transport in a viscously evolving disk and found that grain migration results in a dust surface density well-described by a power law with a sharp outer edge. We therefore adopted a power-law surface density for our analysis. Broken power-law models have also been used to model dust surface density (e.g., Hogerheijde et al. 2016) but given the low signal-to-noise of the majority of our detections, we opted for a single power-law model with fewer free parameters.

The vertical disk structure was parameterized using the commonly assumed Gaussian vertical density structure of an isothermal disk (e.g., Isella et al. 2007):

$$\rho(R, z) = \frac{\Sigma(R)}{h\sqrt{2\pi}} \exp\left(\frac{-z^2}{2h^2}\right), \quad (4.2)$$

The disk scale height, h , was assumed to be a power-law function of radius

$$h = h_0 \left(\frac{R}{100\text{au}} \right)^p. \quad (4.3)$$

We allowed h_0 and p to vary with priors based on the SED fits of Mathews et al. (2013). Our choice of these priors does not affect our conclusions. Thus, if a disk was included in the Mathews et al. (2013) sample, we used their best-fit values for h_0 and p with uncertainties of 1 au and 0.05 to create normally distributed priors. If a disk was not in the Mathews et al. (2013) sample, we assumed a normally distributed prior for p , with a mean of 1.13 (the median value of p for their sample of 45 disks) and standard deviation of 0.05. For h_0 , three-quarters of the Mathews et al. (2013) disks had $h_0 < 10$ au, so we assumed uniform priors from 0-10 au and 10-20 au, with the probability of $h_0 > 10$ au equal to one-third of the probability of $h_0 < 10$ au.

We also assumed a constant dust opacity throughout the disk. Previous multi-wavelength studies of disks at millimeter and centimeter wavelengths suggested radial variations in dust opacity due to grain growth (Isella, Carpenter, and Sargent 2010; Banzatti et al. 2011; Guilloteau et al. 2011; Pérez et al. 2012, 2015; Trotta et al. 2013; Menu et al. 2014; ALMA Partnership et al. 2015; Guidi et al. 2016; Tazzari et al. 2016). Similar radial variations may be present in our Upper Sco disks, and, in fact, are predicted by models of dust transport and evolution (e.g., Dullemond and Dominik 2005; Birnstiel, Dullemond, and Brauer 2010). However, there is no way to constrain the dust opacity based on our single-wavelength data. Thus, we used a uniform dust opacity, calculated as a function of wavelength using Mie theory for dust grains composed of a mix of carbons, ices, and silicates (e.g., Pollack et al. 1994), with a grain size distribution of $n(a) \propto a^{-3.5}$ and a maximum grain size of 1 cm. Only Σ_0 , which is inversely proportional to opacity for a given flux density, was sensitive to our choice of maximum grain size.

The Monte Carlo radiative transfer code RADMC-3D (Dullemond et al. 2012) was used to determine the temperature throughout the model dust disk due to stellar irradiation. We adopted the stellar parameters derived in Paper I. We assumed a minimum temperature of 10 K at any location in the disk to account for other heat sources such as radioactive decay and cosmic rays (e.g., D'Alessio, Calvet, and Hartmann 2001; Woitke 2015). RADMC-3D was then used to generate an image of the model disk for a given inclination and position angle. The Fourier transform of this image provided a grid of model visibilities, which was interpolated at our

observational uv points. We used the χ^2 difference between the model and observed visibilities (real and imaginary) to calculate the likelihood of the current set of model parameters:

$$L = \sum \exp \left[-\frac{(\text{Re}_{mod} - \text{Re}_{obs})^2}{2\sigma_{vis}^2} - \frac{(\text{Im}_{mod} - \text{Im}_{obs})^2}{2\sigma_{vis}^2} \right], \quad (4.4)$$

where $\frac{1}{\sigma_{vis}^2}$ is the visibility weight. The observed visibilities were corrected to center the disk at the phase center of observations using the disk positions determined in Paper I. The Markov chain Monte Carlo implementation *emcee* (Foreman-Mackey et al. 2013) was used to constrain Σ_0 , R_{dust} , h_0 , p , inclination, and position angle.

Table 4.1 contains the most likely values for Σ_0 , R_{dust} , h_0 , p , inclination, and position angle from the continuum fitting, together with their uncertainties. The values of each parameter sampled by the MCMC in the fitting of each source gave the final probability distribution of that parameter. The reported values in Table 4.1 were taken from the peak of these distributions. The uncertainties were defined as the bounds of the range around the peak containing 68.3% of the integrated probability. The dust disks range from 4 to 173 au in radius, although 82% of the disks have radii less than 50 au. Figure 4.1 shows an image of the best-fit model of each source, along with the observed image and residuals. This figure also shows the deprojected observed and best-fit model visibilities as a function of baseline length.

Five sources, 2MASS J16032225-2413111, 2MASS J16054540-2023088, 2MASS J16111330-2019029, 2MASS J16123916-1859284, and 2MASS J16135434-2320342, exhibited 5σ emission in the residual images of their best-fit models. We fit point-source models to the residual visibilities of these sources; their continuum flux densities and positions relative to the primary disks are listed in Table 4.2. The NASA/IPAC Extragalactic Database lists no known background galaxies at the positions of these secondary sources. 2MASS J16054540-2023088 was identified as a double line spectroscopic binary by Dahm, Slesnick, and White (2012), while none of the other sources with secondary emission are known binaries.

The secondary sources of 2MASS J16032225-2413111, 2MASS J16123916-1859284, and 2MASS J16135434-2320342 were also identified in Paper I. The secondary sources of 2MASS J16054540-2023088 and 2MASS J16111330-2019029 were too close to their respective primary sources to have been identified in Paper I, but can be seen in Figure 4.1 as non-axisymmetric extended emission on the eastern side of the primaries. The secondary source to 2MASS J16135434-2320342, by

far the brightest in our sample, is clearly visible as a second disk to the east of the primary. We used the MCMC fitting method described above to determine the dust properties of this source after subtracting our best-fit model for the primary disk from the observed visibilities and shifting the phase center to the secondary disk. The best-fit parameters are given in Table 4.1 for both components of 2MASS J16135434-2320342.

Table 4.1: Continuum Fitting Results

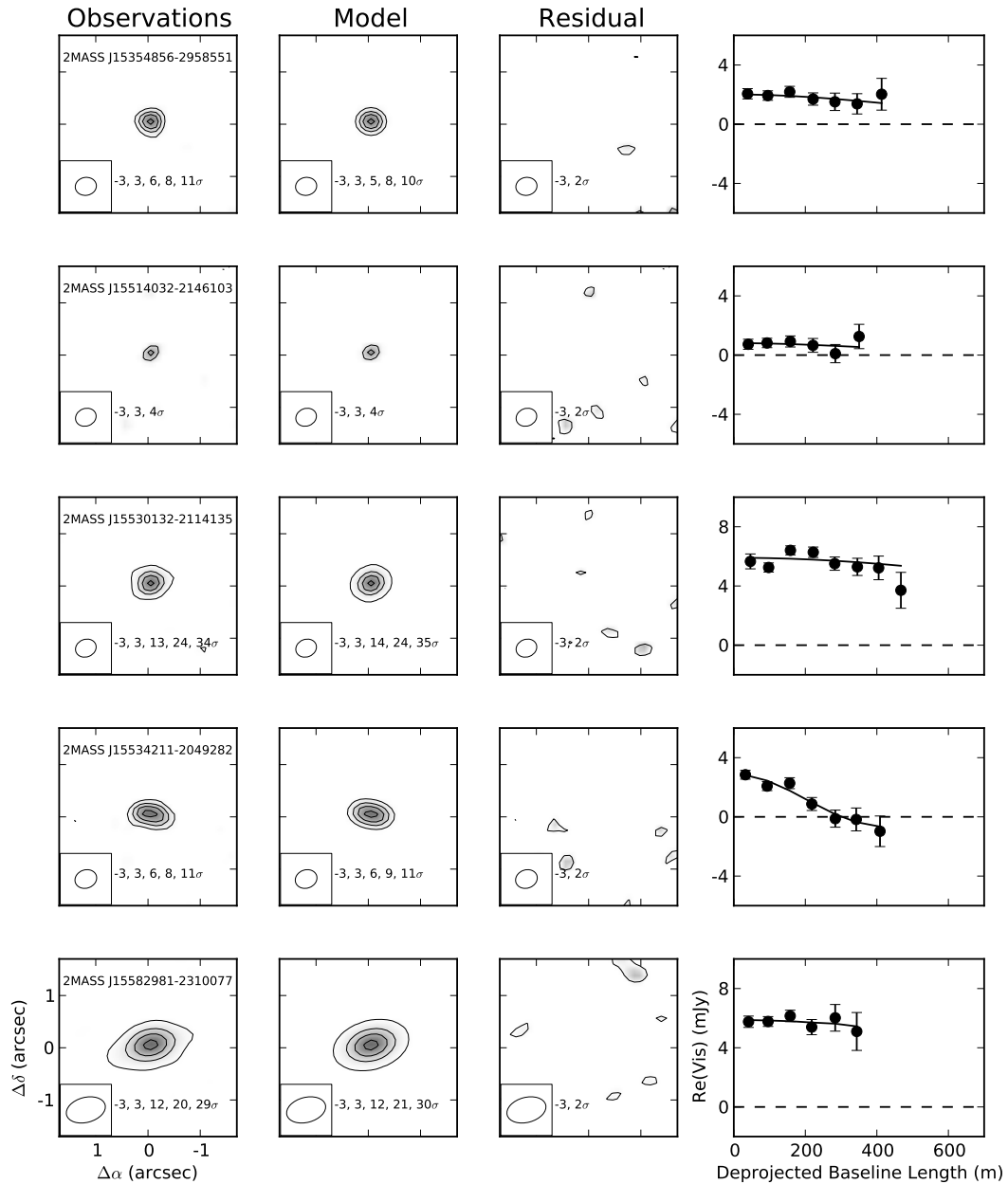
Source	$\log \frac{\Sigma_0}{\text{gcm}^{-2}}$	R_{dust} (au)	p	h_0 (au)	Inclination (deg)	Position Angle (deg)
2MASS J15354856-2958551	-2.45 (-0.19,+0.24)	14 (-10,+18)	1.12 (-0.04,+0.06)	3 (-3,+7)	46 (-34,+17)	25 (-25,+121)
2MASS J15514032-2146103	-2.78 (-0.25,+0.29)	13 (-10,+35)	1.12 (-0.04,+0.06)	8 (-8,+1)	84 (-59,+4)	130 (-95,+46)
2MASS J15530132-2114135	-1.41 (-0.20,+0.32)	8 (-2,+5)	1.12 (-0.04,+0.05)	8 (-4,+6)	47 (-40,+14)	28 (-25,+117)
2MASS J15534211-2049282	-2.01 (-0.61,+1.07)	45 (-7,+21)	1.13 (-0.06,+0.04)	1 (-1,+1)	89 (-2,+1)	73 (-6,+5)
2MASS J15582981-2310077	-1.58 (-0.14,+0.21)	13 (-3,+10)	1.13 (-0.07,+0.04)	6 (-1,+1)	32 (-21,+18)	47 (-32,+115)
2MASS J16001844-2230114	-1.98 (-0.13,+0.16)	30 (-9,+5)	1.13 (-0.05,+0.05)	5 (-3,+6)	45 (-21,+35)	6 (-48,+36)
2MASS J16014086-2258103	-2.12 (-0.17,+0.14)	36 (-9,+9)	1.12 (-0.06,+0.05)	8 (-3,+10)	74 (-31,+10)	26 (-23,+22)
2MASS J16014157-2111380	-2.60 (-0.36,+0.38)	9 (-9,+18)	1.13 (-0.05,+0.05)	3 (-3,+6)	80 (-58,+5)	160 (-105,+20)
2MASS J16020757-2257467	-2.17 (-0.12,+0.21)	47 (-7,+8)	1.12 (-0.03,+0.07)	1 (-1,+16)	57 (-19,+14)	80 (-15,+17)
2MASS J16024152-2138245	-1.37 (-0.17,+0.14)	24 (-3,+3)	1.13 (-0.04,+0.05)	8 (-3,+7)	41 (-21,+14)	63 (-21,+28)
2MASS J16030161-2207523	-1.86 (-0.19,+0.24)	19 (-8,+7)	1.13 (-0.04,+0.05)	7 (-4,+8)	52 (-42,+22)	62 (-50,+46)
2MASS J16032225-2413111	-2.20 (-0.19,+0.30)	15 (-11,+13)	1.12 (-0.04,+0.04)	6 (-3,+12)	64 (-36,+16)	72 (-43,+56)
2MASS J16035767-2031055	-2.51 (-0.10,+0.10)	115 (-46,+88)	1.11 (-0.05,+0.05)	10 (-1,+1)	69 (-27,+21)	5 (-26,+22)
2MASS J16035793-1942108	-2.75 (-0.09,+0.10)	173 (-60,+46)	1.14 (-0.05,+0.05)	9 (-1,+1)	56 (-34,+14)	42 (-42,+34)
2MASS J16041740-1942287	-2.62 (-0.24,+0.34)	9 (-8,+14)	1.12 (-0.05,+0.05)	4 (-3,+6)	80 (-50,+7)	100 (-79,+60)
2MASS J16043916-1942459	-2.53 (-1.36,+1.10)	46 (-42,+21)	1.13 (-0.05,+0.05)	4 (-4,+7)	77 (-54,+9)	22 (-18,+123)
2MASS J16052556-2035397	-2.46 (-0.19,+0.28)	16 (-12,+38)	1.21 (-0.05,+0.05)	3 (-1,+1)	74 (-23,+16)	91 (-68,+72)
2MASS J16054540-2023088	-1.72 (-0.08,+0.07)	19 (-2,+5)	1.22 (-0.04,+0.06)	9 (-1,+1)	67 (-29,+9)	10 (-10,+36)
2MASS J16062196-1928445	-2.77 (-0.13,+0.13)	46 (-16,+32)	1.13 (-0.05,+0.05)	13 (-1,+1)	85 (-68,+5)	121 (-52,+39)
2MASS J16062277-2011243	-2.99 (-0.34,+0.33)	9 (-8,+33)	1.22 (-0.05,+0.05)	6 (-1,+1)	85 (-50,+5)	161 (-127,+13)
2MASS J16063539-2516510	-2.28 (-0.20,+0.16)	43 (-19,+17)	1.14 (-0.06,+0.04)	8 (-3,+8)	74 (-43,+13)	11 (-11,+70)
2MASS J16064102-2455489	-1.96 (-0.12,+0.24)	29 (-8,+8)	1.13 (-0.05,+0.05)	6 (-4,+8)	40 (-36,+14)	81 (-41,+48)
2MASS J16064385-1908056	-3.04 (-0.20,+0.23)	17 (-16,+62)	1.19 (-0.05,+0.05)	3 (-1,+1)	48 (-39,+38)	81 (-36,+81)
2MASS J16072625-2432079	-1.50 (-0.13,+0.20)	29 (-2,+2)	1.13 (-0.05,+0.04)	6 (-4,+4)	43 (-17,+10)	2 (-14,+19)
2MASS J16072747-2059442	-2.19 (-0.17,+0.26)	11 (-5,+9)	1.12 (-0.04,+0.06)	4 (-4,+6)	68 (-49,+10)	20 (-20,+106)
2MASS J16073939-1917472	-3.10 (-0.34,+0.33)	9 (-9,+73)	1.13 (-0.05,+0.05)	2 (-1,+8)	83 (-75,+7)	148 (-117,+31)
2MASS J16075796-2040087	-0.64 (-0.22,+0.13)	11 (-1,+1)	1.18 (-0.04,+0.04)	18 (-4,+1)	47 (-14,+8)	0 (-14,+15)
2MASS J16081566-2222199	-2.89 (-0.16,+0.19)	80 (-41,+59)	1.13 (-0.05,+0.05)	8 (-6,+5)	86 (-26,+4)	173 (-18,+24)
2MASS J16082324-1930009	-1.10 (-0.15,+0.18)	65 (-5,+5)	1.16 (-0.07,+0.04)	8 (-1,+1)	74 (-4,+5)	123 (-2,+3)
2MASS J16082751-1949047	-2.72 (-0.19,+0.21)	44 (-35,+21)	1.11 (-0.05,+0.05)	2 (-1,+1)	41 (-34,+34)	17 (-11,+132)
2MASS J16090002-1908368	-2.57 (-0.14,+0.31)	9 (-7,+18)	1.24 (-0.05,+0.06)	19 (-1,+1)	63 (-45,+18)	84 (-38,+81)
2MASS J16090075-1908526	-1.27 (-0.06,+0.07)	58 (-4,+5)	1.13 (-0.05,+0.05)	6 (-1,+1)	56 (-5,+5)	149 (-9,+9)
2MASS J16093558-1828232	-2.87 (-0.31,+0.36)	7 (-7,+28)	1.13 (-0.05,+0.05)	3 (-3,+6)	83 (-59,+6)	104 (-81,+40)
2MASS J16094098-2217594	-3.58 (-0.35,+0.36)	12 (-10,+62)	1.13 (-0.05,+0.05)	1 (-1,+13)	82 (-61,+6)	74 (-53,+65)
2MASS J16095361-1754474	-2.76 (-0.21,+0.31)	6 (-6,+28)	1.18 (-0.05,+0.05)	9 (-1,+1)	86 (-60,+4)	154 (-131,+16)
2MASS J16095441-1906551	-3.11 (-0.58,+0.52)	7 (-7,+41)	1.13 (-0.05,+0.05)	2 (-2,+7)	83 (-72,+5)	177 (-42,+48)
2MASS J16095933-1800090	-3.56 (-0.30,+0.34)	8 (-6,+63)	1.14 (-0.04,+0.06)	16 (-1,+1)	86 (-66,+4)	105 (-64,+59)
2MASS J16102857-1904469	-3.02 (-0.44,+0.40)	9 (-9,+28)	1.14 (-0.06,+0.05)	2 (-2,+12)	84 (-51,+6)	98 (-74,+43)
2MASS J16104636-1840598	-2.13 (-0.25,+0.36)	10 (-8,+15)	1.12 (-0.04,+0.06)	8 (-5,+8)	71 (-63,+8)	84 (-38,+78)
2MASS J16111330-2019029	-1.69 (-0.27,+0.15)	8 (-2,+8)	1.14 (-0.06,+0.04)	6 (-3,+12)	17 (-13,+40)	141 (-78,+35)
2MASS J16115091-2012098	-2.94 (-0.25,+0.24)	95 (-53,+6)	1.13 (-0.04,+0.06)	1 (-1,+8)	86 (-42,+4)	144 (-44,+32)
2MASS J16122737-2009596	-2.98 (-0.30,+0.35)	86 (-43,+15)	1.13 (-0.05,+0.05)	1 (-1,+8)	26 (-14,+50)	159 (-112,+18)

Table 4.1: Continuum Fitting Results

Source	$\log \frac{\Sigma_0}{\text{gcm}^{-2}}$	R_{dust} (au)	p	h_0 (au)	Inclination (deg)	Position Angle (deg)
2MASS J16123916-1859284	-2.21 (-0.10,+0.20)	48 (-7,+8)	1.12 (-0.05,+0.05)	8 (-5,+8)	51 (-36,+14)	46 (-27,+22)
2MASS J16133650-2503473	-2.82 (-0.26,+0.26)	45 (-33,+48)	1.14 (-0.06,+0.04)	4 (-2,+12)	86 (-52,+4)	23 (-29,+105)
2MASS J16135434-2320342	-1.18 (-0.59,+0.86)	10 (-3,+3)	1.14 (-0.05,+0.05)	6 (-5,+5)	52 (-44,+14)	75 (-49,+52)
2MASS J16135434-2320342B	-1.60 (-0.17,+0.25)	13 (-3,+5)	1.14 (-0.05,+0.04)	6 (-1,+12)	40 (-34,+10)	154 (-88,+29)
2MASS J16141107-2305362	-2.28 (-0.07,+0.12)	30 (-8,+9)	1.04 (-0.04,+0.04)	3 (-1,+1)	4 (-3,+48)	46 (-40,+104)
2MASS J16142029-1906481	-1.03 (-0.12,+0.17)	29 (-2,+1)	1.10 (-0.02,+0.06)	9 (-5,+1)	27 (-23,+10)	19 (-19,+32)
2MASS J16143367-1900133	-2.69 (-0.18,+0.29)	11 (-9,+13)	1.14 (-0.06,+0.05)	8 (-6,+5)	69 (-43,+18)	51 (-38,+109)
2MASS J16153456-2242421	-1.63 (-0.18,+0.11)	21 (-2,+2)	1.12 (-0.04,+0.06)	3 (-2,+16)	46 (-21,+12)	170 (-31,+10)
2MASS J16154416-1921171	-0.88 (-0.21,+0.25)	10 (-1,+2)	1.15 (-0.05,+0.05)	9 (-1,+8)	40 (-17,+24)	117 (-54,+26)
2MASS J16163345-2521505	-2.33 (-0.57,+0.53)	72 (-23,+25)	1.12 (-0.05,+0.06)	1 (-1,+2)	88 (-9,+2)	64 (-9,+9)
2MASS J16181904-2028479	-1.62 (-0.18,+0.29)	11 (-3,+6)	1.13 (-0.05,+0.06)	8 (-5,+5)	56 (-46,+7)	90 (-56,+42)
2MASS J16215466-2043091	-3.08 (-0.55,+0.48)	8 (-8,+29)	1.13 (-0.05,+0.05)	1 (-1,+8)	82 (-53,+8)	127 (-110,+41)
2MASS J16270942-2148457	-1.96 (-0.13,+0.25)	22 (-6,+10)	1.13 (-0.05,+0.05)	8 (-6,+7)	70 (-33,+15)	176 (-29,+25)
2MASS J16303390-2428062	-2.98 (-0.23,+0.27)	96 (-66,+3)	1.13 (-0.05,+0.05)	1 (-1,+8)	74 (-25,+16)	76 (-47,+75)

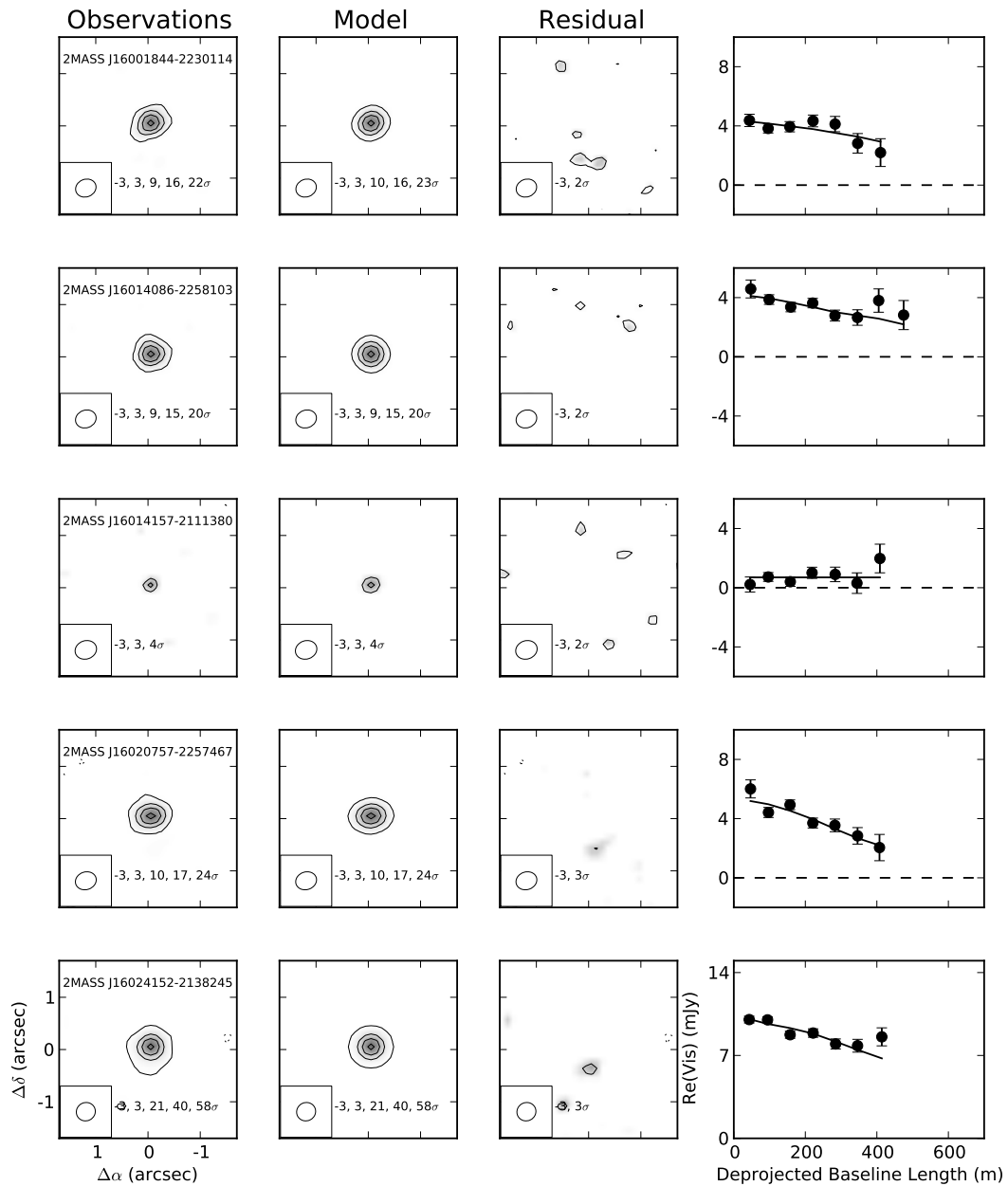
Table 4.2: Secondary Source Properties

Field	S_{tot} (mJy)	$\Delta\alpha$ (arcsec)	$\Delta\delta$ (arcsec)
2MASS J16032225-2413111	0.85 ± 0.14	0.80 ± 0.04	0.06 ± 0.04
2MASS J16054540-2023088	1.00 ± 0.15	0.39 ± 0.04	-0.01 ± 0.04
2MASS J16111330-2019029	1.00 ± 0.16	0.48 ± 0.04	-0.19 ± 0.04
2MASS J16123916-1859284	1.09 ± 0.16	0.75 ± 0.04	-0.15 ± 0.04
2MASS J16135434-2320342	5.83 ± 0.12	0.59 ± 0.03	-0.18 ± 0.03



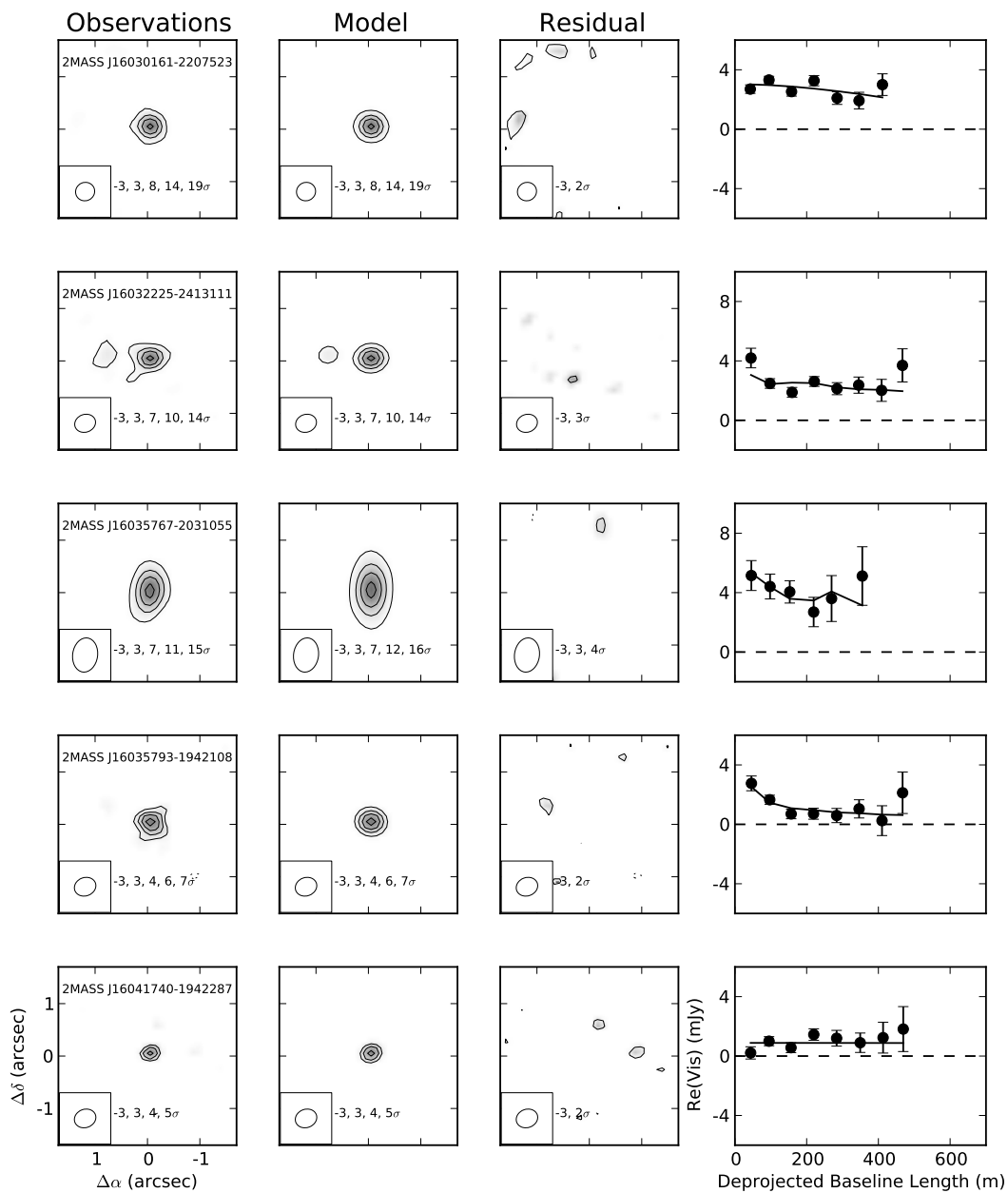
(a)

Figure 4.1: ALMA 0.88 mm observed, model, and residual images corresponding to the best-fit dust model parameters for each source. The real part of the deprojected visibilities for the observations (solid points) and best-fit model (solid curve) are also shown as a function of baseline length.



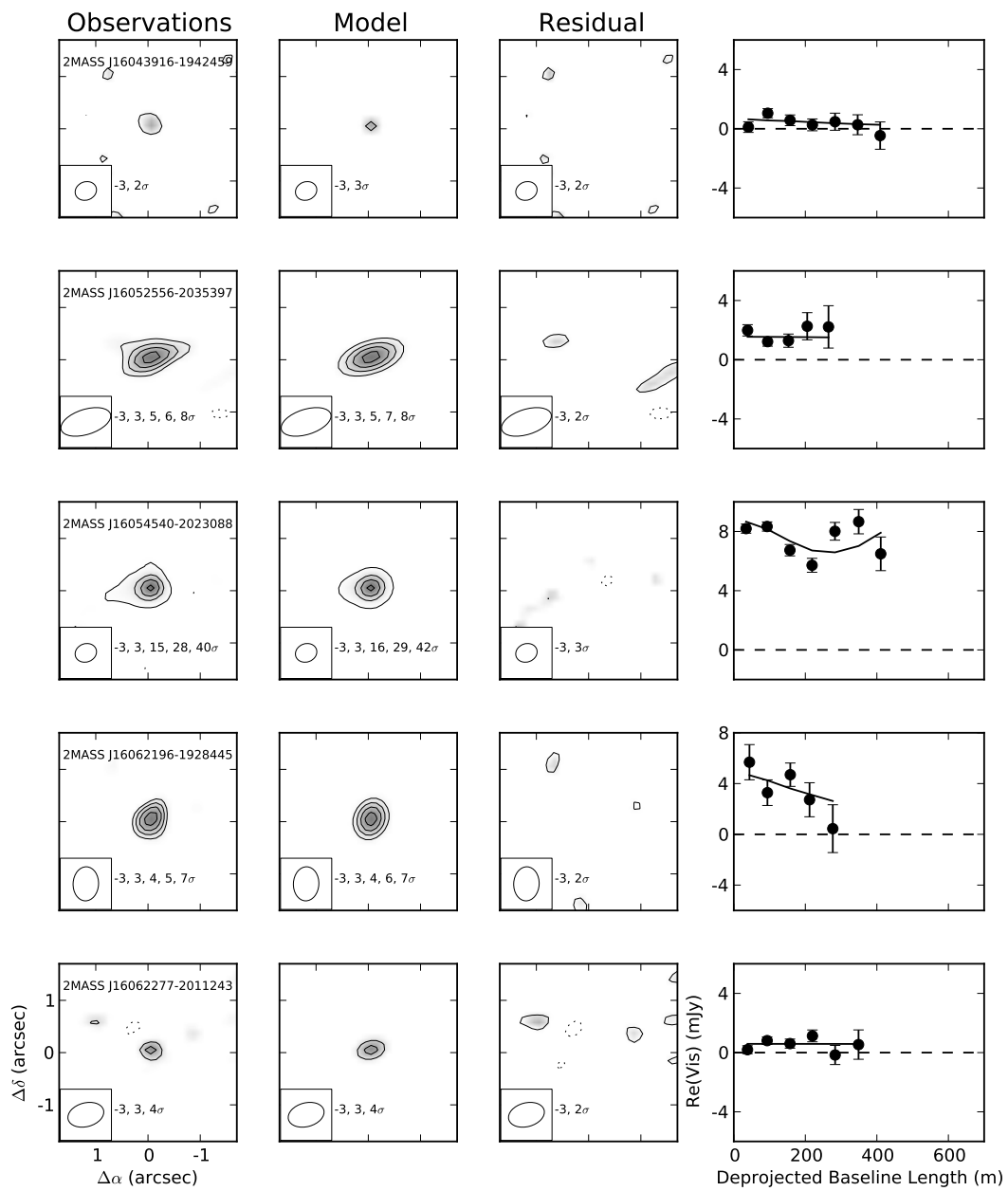
(b)

Figure 4.1: Continued.



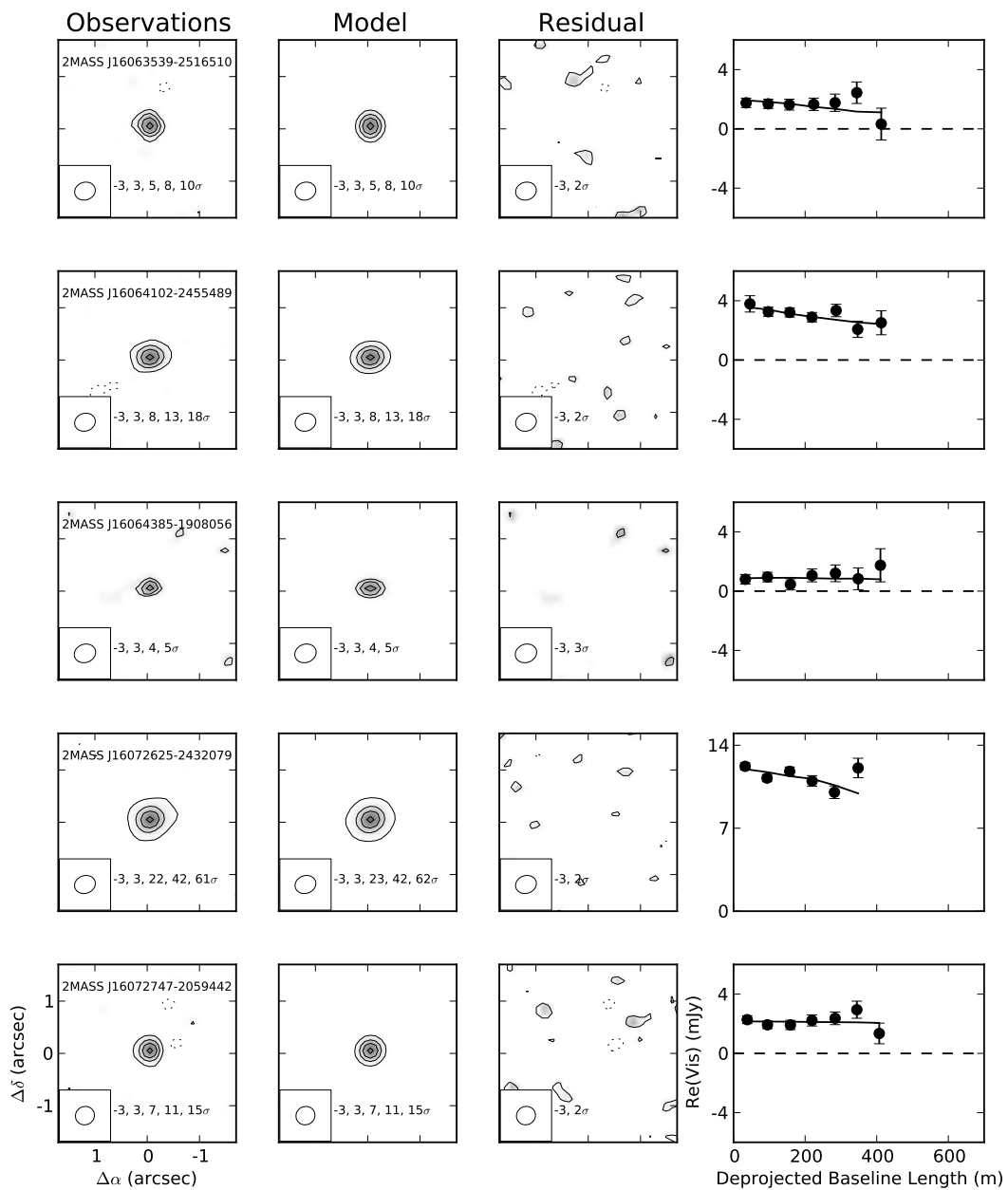
(c)

Figure 4.1: Continued



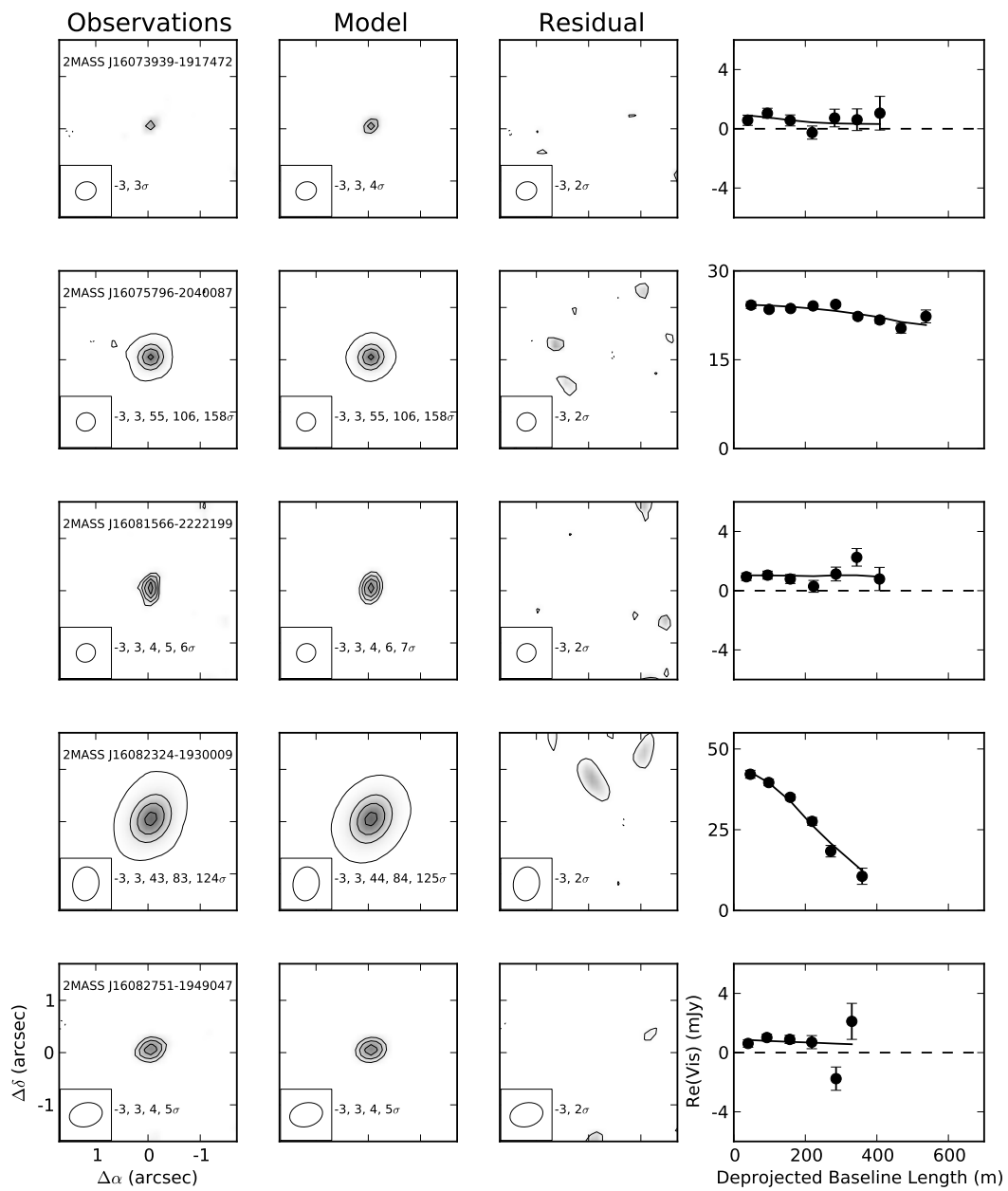
(d)

Figure 4.1: Continued



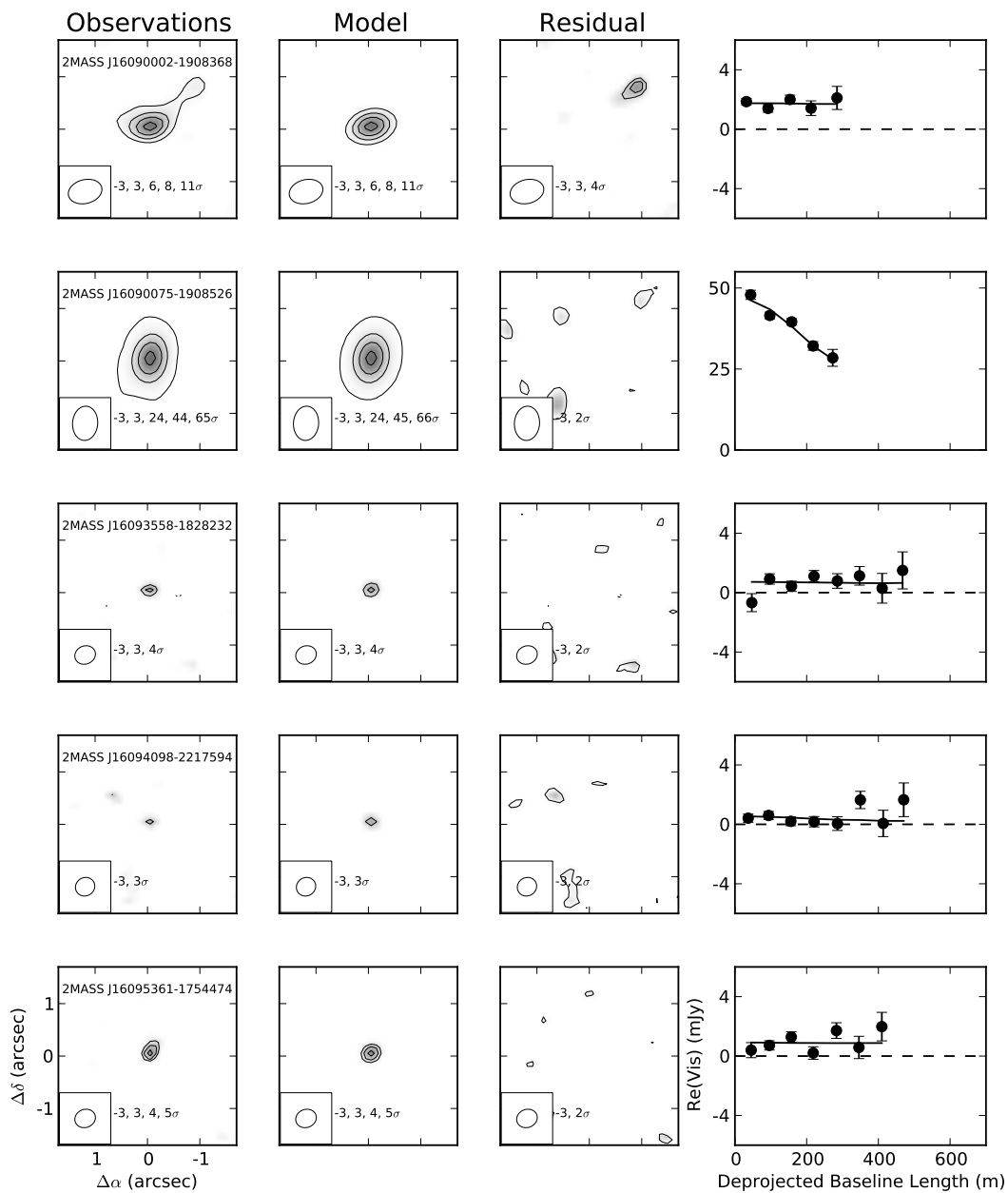
(e)

Figure 4.1: Continued



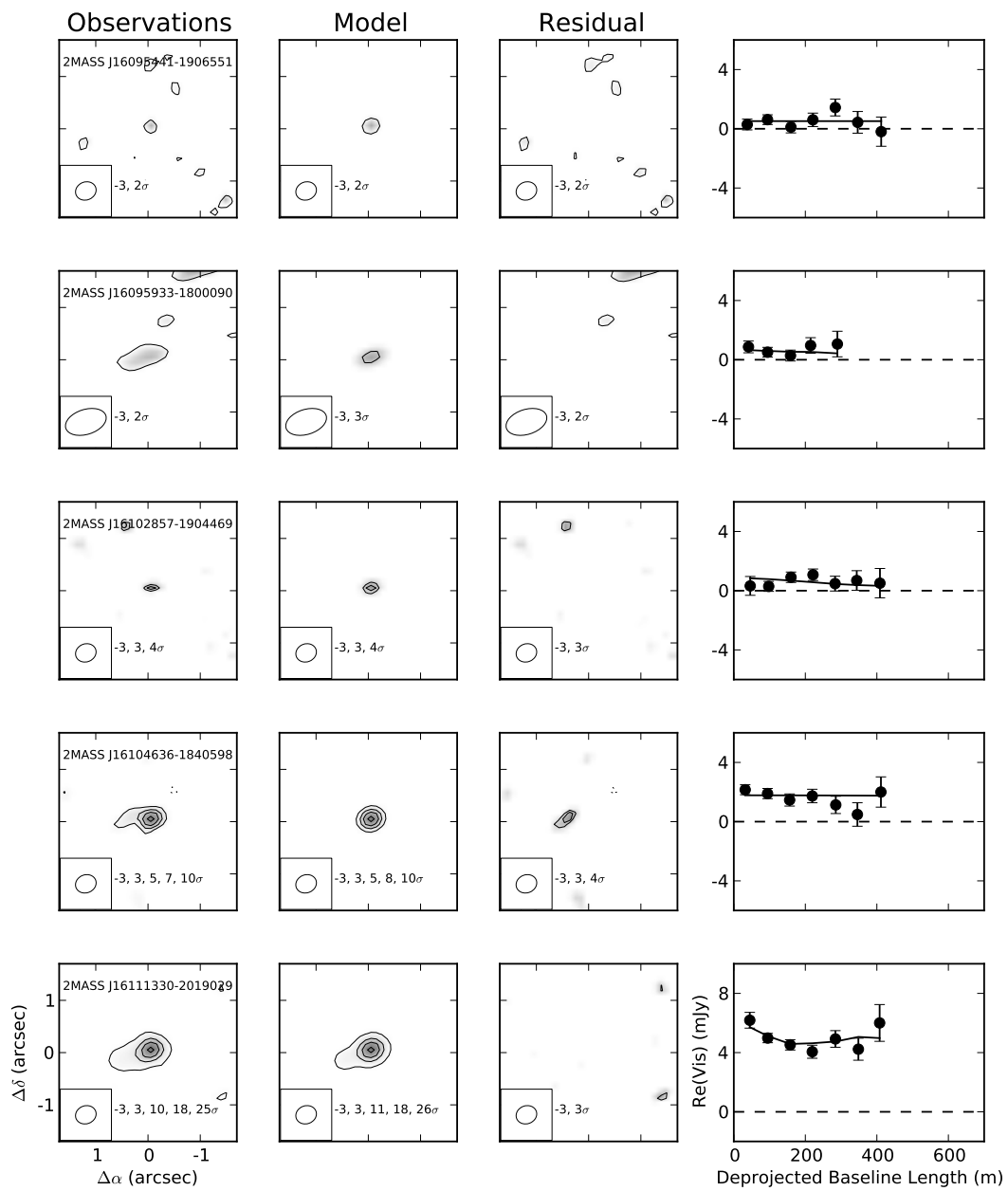
(f)

Figure 4.1: Continued



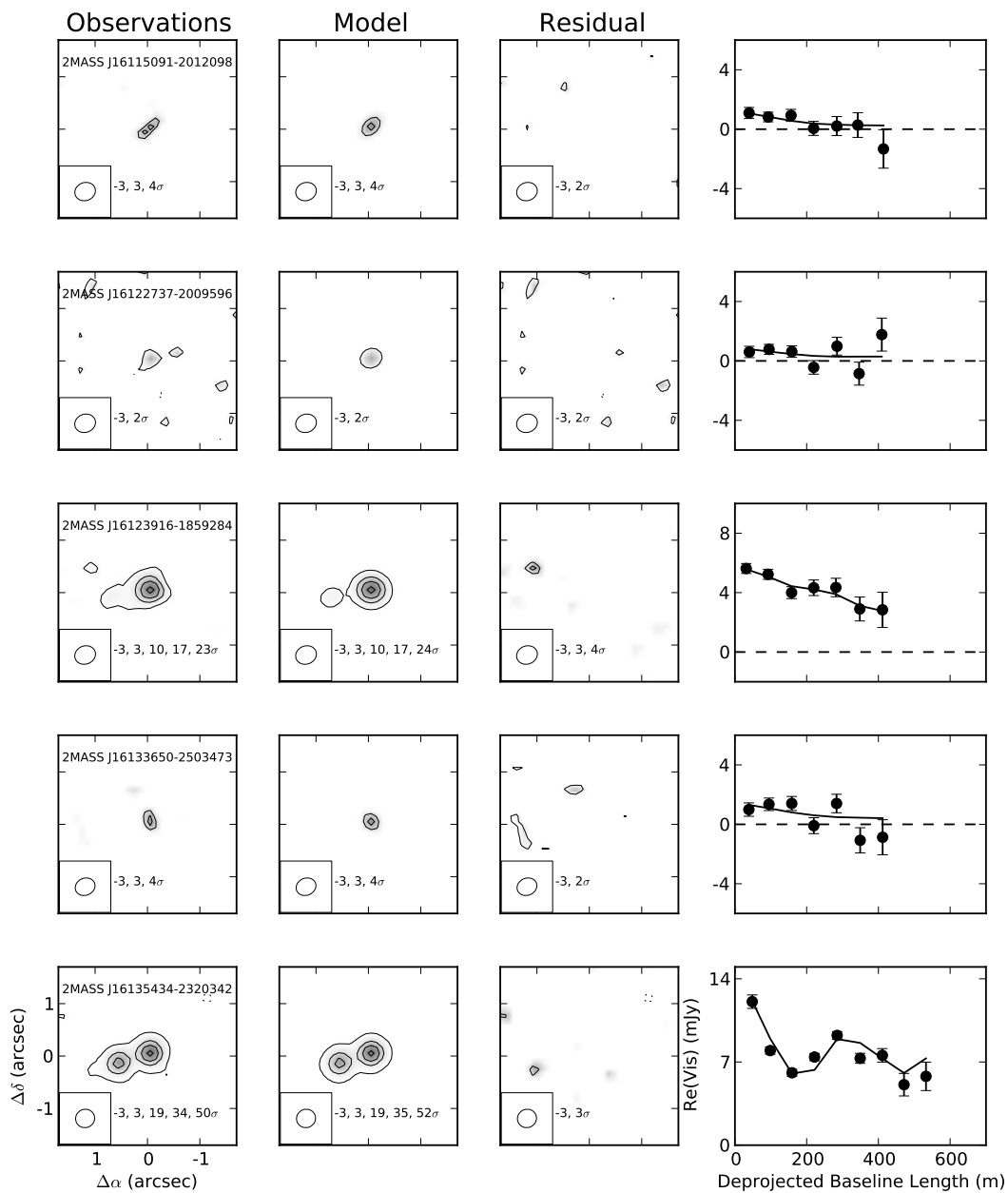
(g)

Figure 4.1: Continued



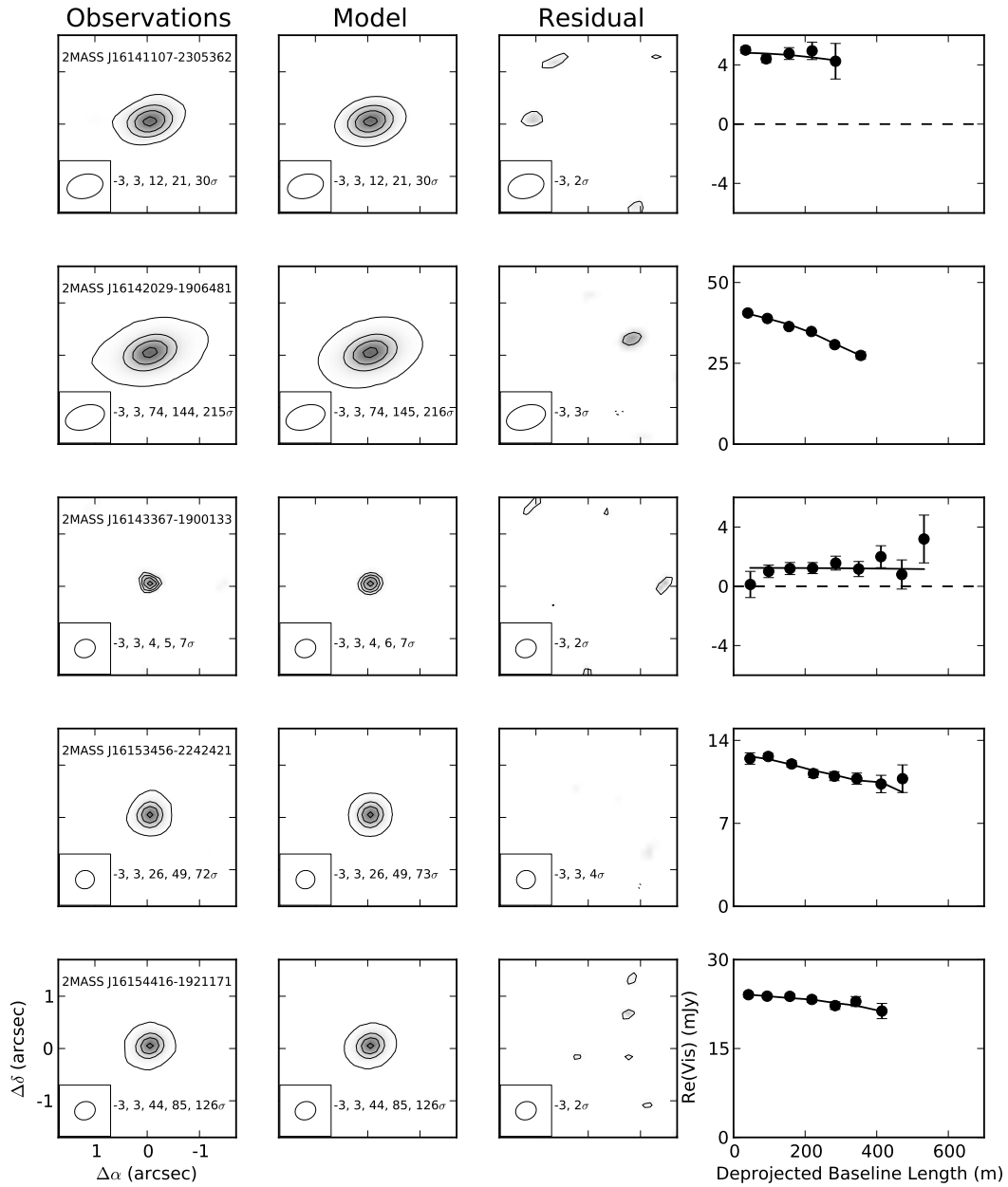
(h)

Figure 4.1: Continued



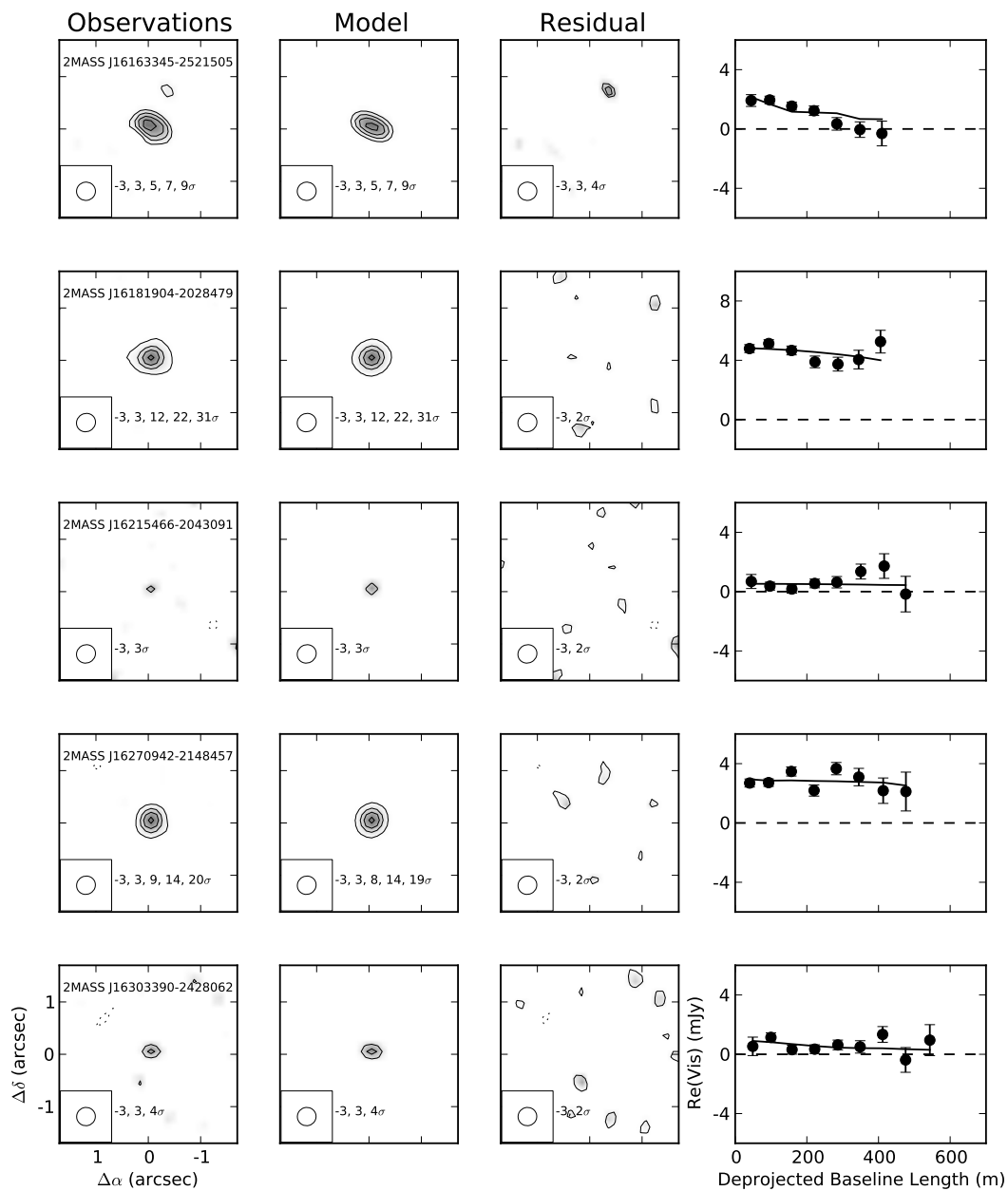
(i)

Figure 4.1: Continued



(j)

Figure 4.1: Continued



(k)

Figure 4.1: Continued

4.4 CO Modeling

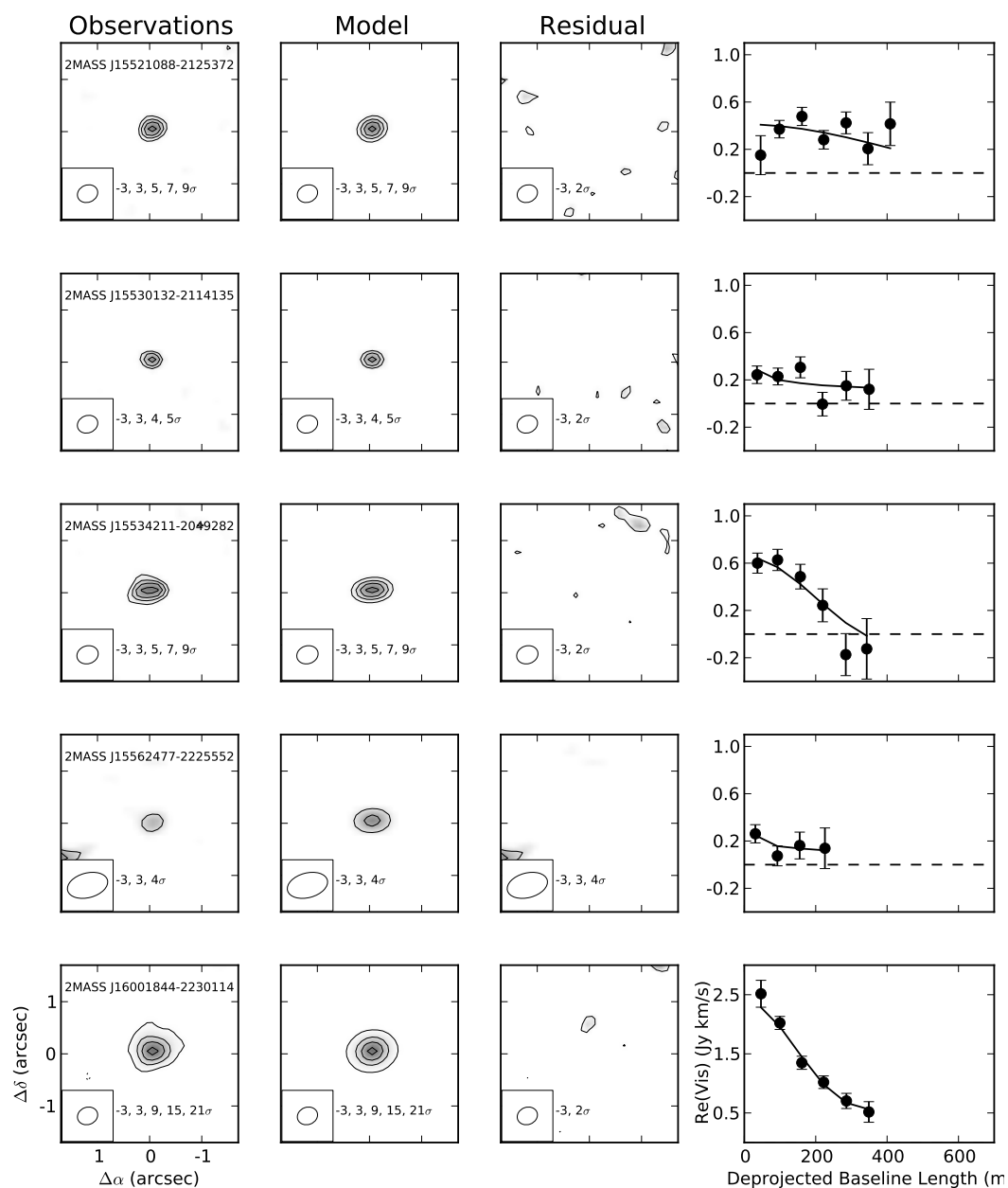
CO Surface Brightness Fitting

Our modeling approach for the CO data was similar to that for the continuum. We used the continuum-subtracted visibilities for each of the 23 CO detections to measure the radial extent of gas. Due to the likelihood of optically thick CO emission, we fit the CO surface brightness of the disks instead of a physical surface density. For each source, we used the velocity range corresponding to the $J = 3 - 2$ emission line, as determined by Paper I, to generate integrated “moment 0 visibilities.” We then fit to the real and imaginary part of these visibilities as described in Section 4.3. For consistency with our continuum fitting, we assumed an azimuthally symmetric disk with surface brightness described by a truncated power law,

$$S(R) = S_0 \left(\frac{R}{10\text{au}} \right)^{-\gamma} \quad (4.5)$$

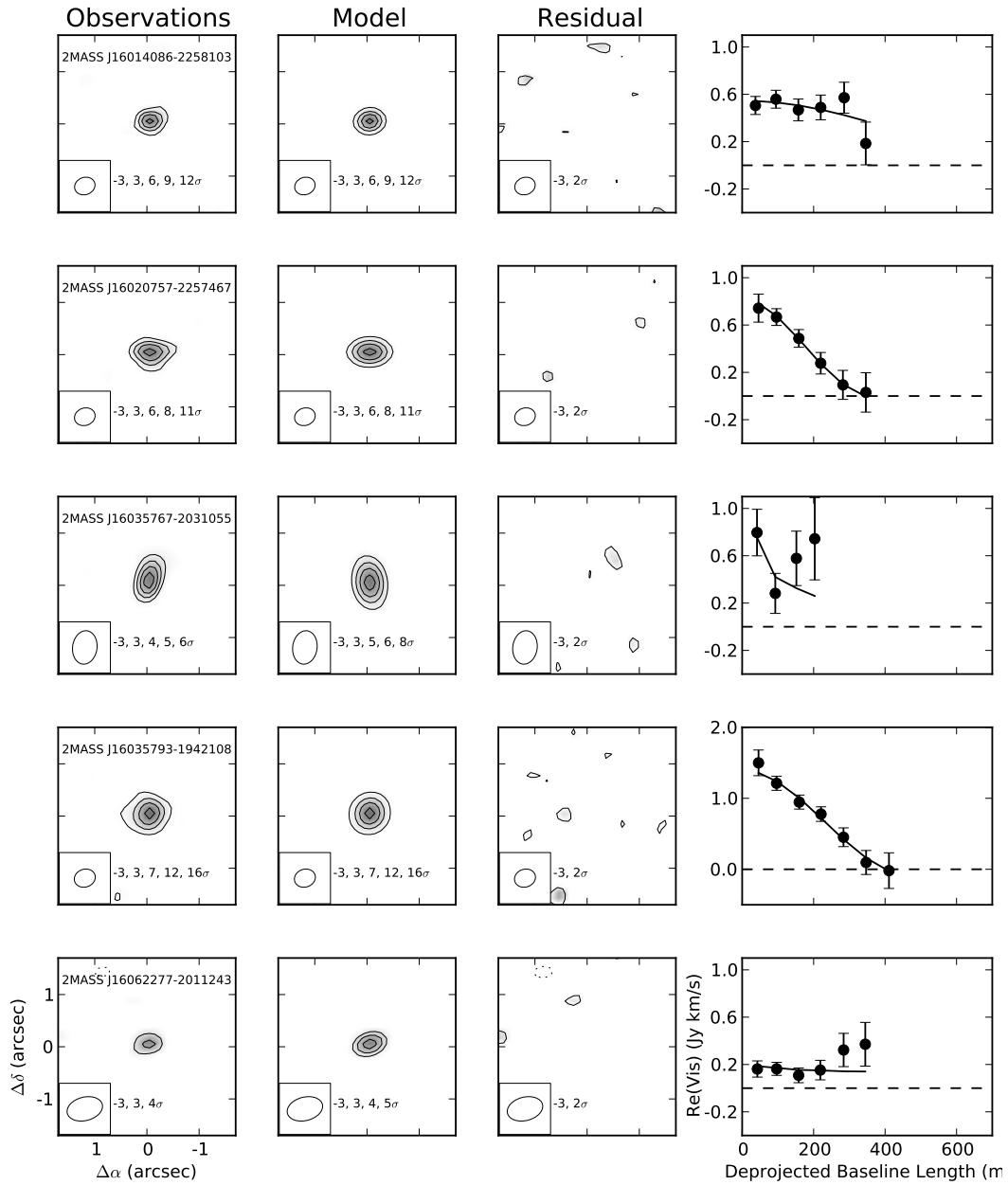
for $R \leq R_{\text{CO}}$ and $S = 0$ beyond R_{CO} . We used *emcee* to fit for the surface brightness normalization, S_0 , the power-law slope, γ , the outer radius, R_{CO} , the inclination, and position angle.

Table 4.3 presents the best-fit parameters of our CO model fitting. Best-fit values and uncertainties were defined as described in Section 4.3 for the dust modeling. Observed, model, and residual images for the CO are shown in Figure 4.2, along with the deprojected observed and best-fit visibilities of each source. We found CO outer radii ranging from 6 to 430 au. 2MASS J16154416-1921171 was the largest CO disk in our sample, with a radius of 430 au. Examination of the CO channel maps suggested contamination by a surrounding molecular cloud and we therefore excluded this source from further CO analysis. With this source excluded, our largest CO outer radius is 169 au. It is worth noting that the gaseous disks may extend beyond our measured CO outer radii; CO will be subject to freeze-out and photodissociation in the outer parts of disks (though some CO will return to the gas phase through non-thermal desorption, e.g., Öberg 2016), while H_2 and other gaseous molecules can survive out to these regions.



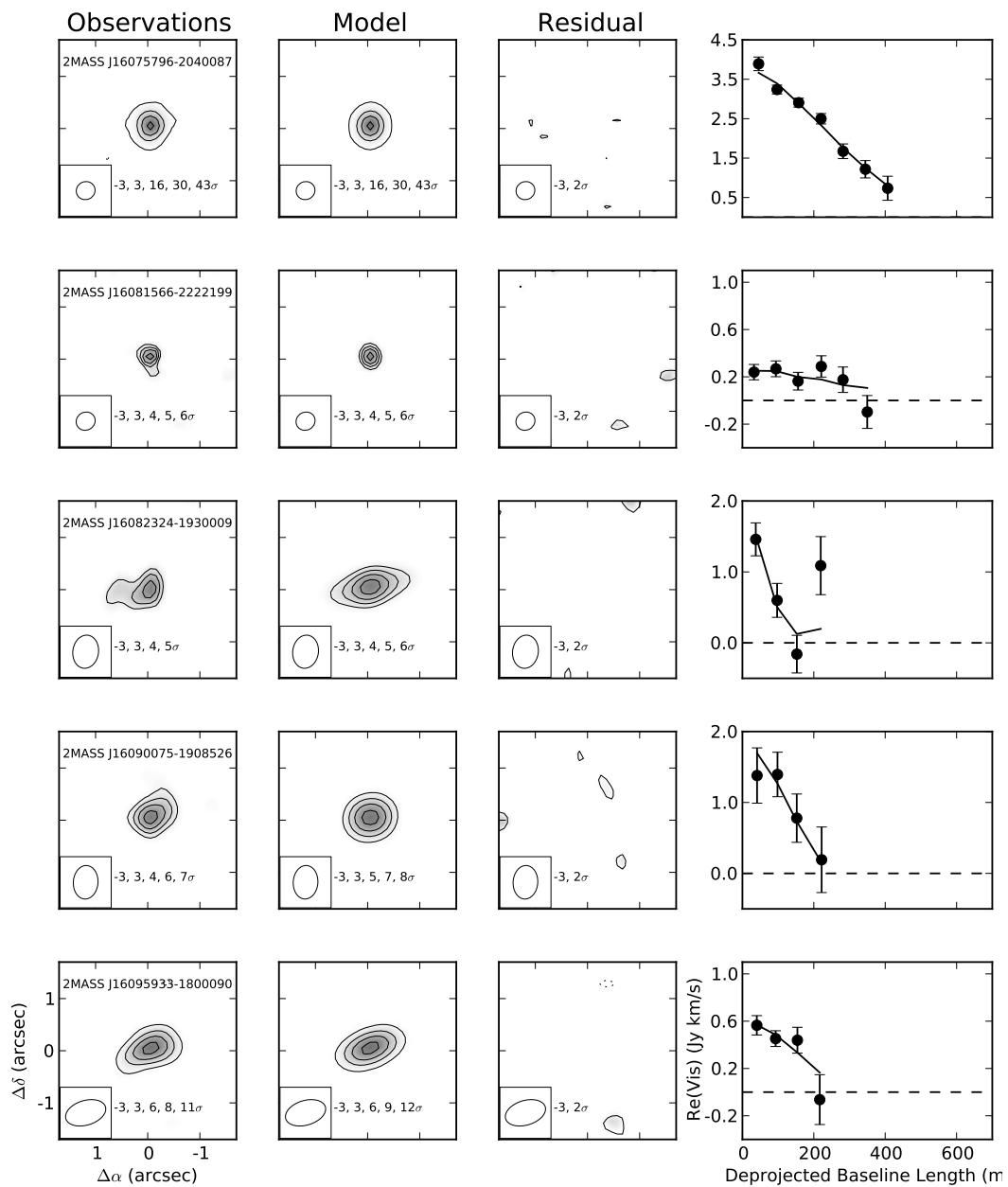
(a)

Figure 4.2: Observed, model, and residual images corresponding to the best-fit CO model parameters for each source. The real part of the deprojected visibilities for the observations (solid points) and best-fit model (solid curve) are also shown as a function of baseline length.



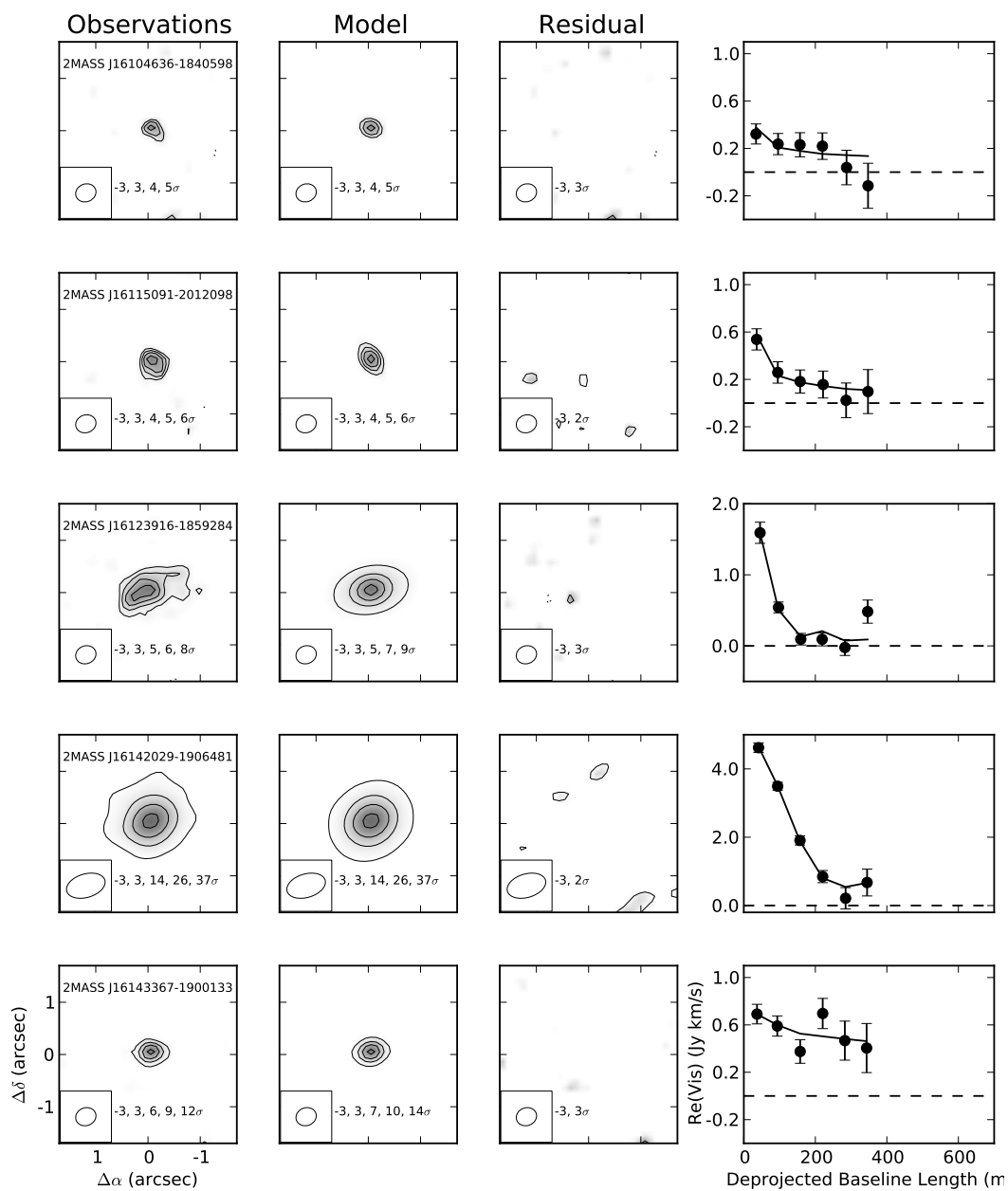
(b)

Figure 4.2: Continued.



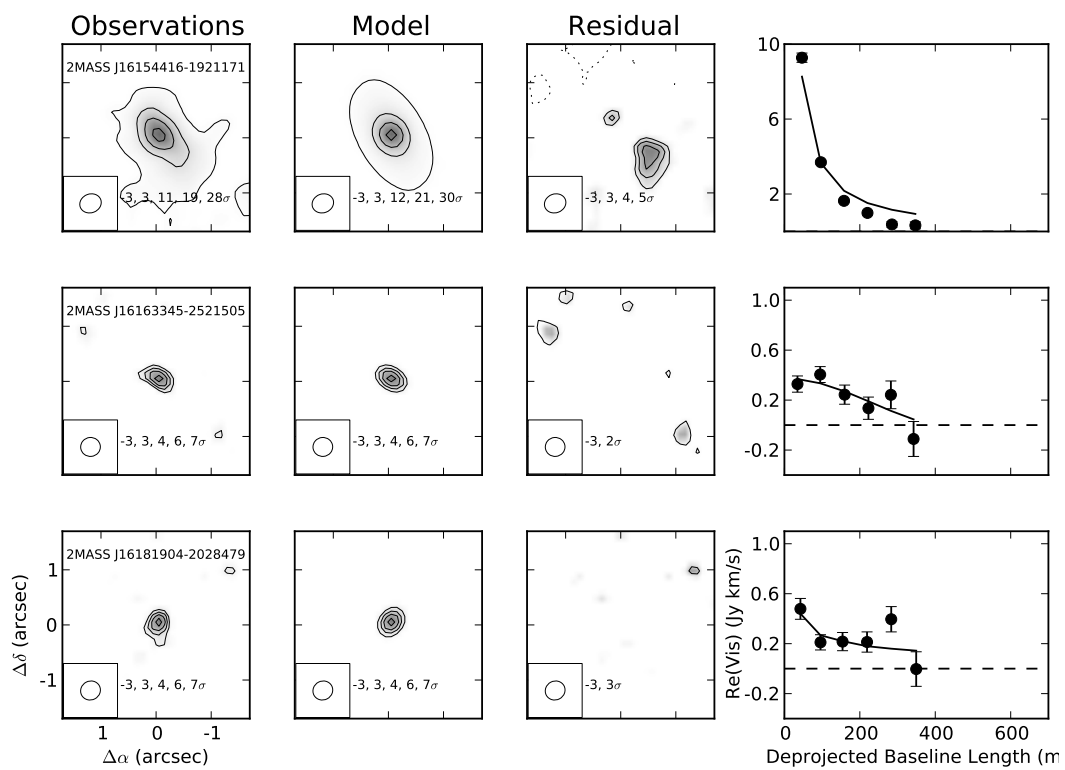
(c)

Figure 4.2: Continued



(d)

Figure 4.2: Continued



(e)

Figure 4.2: Continued

Table 4.3: CO Fitting Results

Source	$\log \frac{S_0}{Jykm/s/arcsecond^2}$	γ	R_{CO} (au)	Inclination (deg)	Position Angle (deg)
2MASS J15521088-2125372	0.77 (-0.18,+0.32)	1.71 (-1.32,+0.05)	24 (-13,+11)	24 (-17,+39)	89 (-61,+57)
2MASS J15530132-2114135	0.47 (-0.23,+0.51)	1.70 (-0.82,+0.08)	17 (-17,+37)	88 (-61,+2)	70 (-64,+47)
2MASS J15534211-2049282	0.96 (-0.21,+0.26)	0.05 (-0.05,+0.63)	51 (-10,+10)	77 (-10,+8)	95 (-13,+11)
2MASS J15562477-2225552	0.26 (-0.39,+0.56)	1.67 (-0.77,+0.12)	16 (-16,+104)	85 (-67,+5)	53 (-27,+79)
2MASS J16001844-2230114	1.20 (-0.03,+0.04)	1.32 (-0.18,+0.11)	68 (-14,+16)	24 (-10,+27)	90 (-39,+41)
2MASS J16014086-2258103	1.17 (-0.31,+0.53)	1.71 (-1.19,+0.06)	12 (-11,+13)	87 (-50,+3)	72 (-42,+55)
2MASS J16020757-2257467	0.77 (-0.09,+0.14)	0.94 (-0.63,+0.26)	54 (-11,+13)	59 (-18,+12)	82 (-15,+16)
2MASS J16035767-2031055	0.71 (-0.19,+0.33)	1.69 (-0.51,+0.07)	37 (-7,+182)	55 (-38,+23)	22 (-95,+30)
2MASS J16035793-1942108	1.00 (-0.08,+0.06)	0.79 (-0.58,+0.19)	43 (-6,+7)	43 (-24,+10)	3 (-28,+23)
2MASS J16062277-2011243	0.35 (-0.27,+0.78)	1.70 (-1.33,+0.07)	6 (-6,+37)	88 (-58,+2)	160 (-131,+12)
2MASS J16075796-2040087	1.67 (-0.04,+0.04)	0.74 (-0.50,+0.31)	34 (-2,+6)	52 (-5,+4)	1 (-5,+5)
2MASS J16081566-2222199	0.43 (-0.12,+0.18)	1.67 (-0.34,+0.09)	30 (-14,+129)	3 (-2,+52)	15 (-88,+50)
2MASS J16082324-1930009	0.87 (-0.22,+0.34)	0.95 (-0.38,+0.37)	156 (-32,+29)	72 (-11,+12)	101 (-12,+14)
2MASS J16090075-1908526	0.97 (-0.23,+0.17)	1.30 (-0.91,+0.26)	72 (-22,+42)	50 (-41,+10)	95 (-40,+62)
2MASS J16095933-1800090	0.65 (-0.13,+0.23)	1.69 (-0.96,+0.08)	52 (-23,+33)	63 (-42,+16)	119 (-42,+40)
2MASS J16104636-1840598	0.45 (-0.16,+0.36)	1.70 (-0.40,+0.08)	22 (-22,+148)	54 (-33,+25)	50 (-43,+68)
2MASS J16115091-2012098	0.54 (-0.14,+0.56)	1.30 (-0.26,+0.26)	75 (-29,+241)	86 (-36,+4)	26 (-13,+13)
2MASS J16123916-1859284	0.70 (-0.07,+0.07)	0.85 (-0.13,+0.09)	169 (-26,+24)	53 (-8,+6)	104 (-11,+14)
2MASS J16142029-1906481	1.52 (-0.05,+0.07)	0.97 (-0.12,+0.09)	88 (-6,+6)	58 (-4,+4)	5 (-4,+4)
2MASS J16143367-1900133	1.32 (-0.36,+0.35)	1.71 (-0.96,+0.07)	14 (-12,+12)	83 (-51,+5)	88 (-50,+76)
2MASS J16154416-1921171	1.73 (-0.01,+0.01)	1.01 (-0.01,+0.01)	430 (-10,+10)	61 (-1,+1)	28 (-1,+1)
2MASS J16163345-2521505	0.79 (-0.23,+0.36)	1.31 (-0.90,+0.27)	45 (-19,+22)	81 (-17,+7)	59 (-19,+16)
2MASS J16181904-2028479	0.48 (-0.11,+0.28)	1.69 (-0.26,+0.07)	26 (-11,+176)	69 (-60,+5)	155 (-28,+59)

Expected CO Fluxes

Only 21 of the 55 continuum-detected sources in our sample were also detected in CO. The relatively low number of CO detections suggested that the CO is either heavily depleted relative to the dust or has a compact emitting area due to small disk sizes. In this section, we test the latter possibility. We used the results of our continuum modeling to predict the CO $J = 3 - 2$ line flux from our continuum-detected disks, assuming the gas and dust share the same spatial distribution.

To estimate the expected CO $J = 3 - 2$ line fluxes for our continuum-detected disks, we used the posterior distributions of Σ_0 , R_{dust} , h_0 , p , inclination, and position angle from our MCMC continuum fits to generate a sample of model dust disks for each source. We then added CO to these disks by assuming that the CO and dust share the same temperature structure and spatial distribution with a gas-to-dust ratio of 100 and a CO to H_2 ratio of 7×10^{-5} by number (Beckwith and Sargent 1993; Dutrey et al. 1996, and references therein). If a source was detected in CO, we sampled CO outer radii (R_{CO}) from the posterior distribution of our surface brightness fitting and

extended the model CO disk out to these radii. If R_{CO} is larger than R_{dust} , we used our 3σ upper limits on the total continuum flux between R_{dust} and R_{CO} to calculate an upper limit on the dust mass in this annulus, assuming optically thin emission and a dust temperature of 10 K. This dust mass upper limit was then converted into a uniform dust surface density between R_{dust} and R_{CO} , and the disk was populated with CO as described above.

We took into account the removal of CO from the gas phase by freeze-out and photodissociation. At any location in a model disk where the temperature was less than 20 K, we assumed the CO was frozen onto dust grains and had an abundance of zero (Collings et al. 2003; Bisschop et al. 2006). While a small fraction of this CO will re-enter the gas phase through UV photodesorption (Öberg, Bottinelli, and van Dishoeck 2009; Öberg, van Dishoeck, and Linnartz 2009; Fayolle et al. 2011; Chen et al. 2014) and cosmic-ray heating (Hasegawa and Herbst 1993), modeling of these processes has shown the effects on CO observations to be negligible (Öberg et al. 2015). A common method for treating photodissociation in disks is to assume a minimum column density of H_2 that will shield CO from destruction by stellar and interstellar ultraviolet and X-ray radiation. Visser, van Dishoeck, and Black (2009) modeled a molecular cloud exposed to the interstellar radiation field and found that an H_2 column density of $10^{21} \text{ g cm}^{-2}$ would shield CO. Detailed modeling (Aikawa and Nomura 2006; Gorti and Hollenbach 2008) and observations (Qi et al. 2011) of photodissociation in disks around accreting young stars found similar results. Thus, it is often assumed that CO in disks will only survive below a vertical column density of $10^{21} \text{ g cm}^{-2}$ of H_2 (Williams and Best 2014; Walsh et al. 2016).

In the young circumstellar disks modeled in this way, high energy radiation produced by stellar accretion dominated over the interstellar radiation field (van Zadelhoff et al. 2003; Visser, van Dishoeck, and Black 2009), providing an abundant source of UV and X-ray photons. This may not be the case for the more evolved disks in Upper Sco, however. Dahm and Carpenter (2009) found that only 7 out of a sample of 35 disk-bearing Upper Sco sources showed signs of accretion, and that the median accretion rate of these 7 sources was an order of magnitude lower than that of younger disks in Taurus. Therefore, the disks in the present sample are likely to be exposed to much weaker radiation fields than younger, more strongly accreting disks, and will require less material to shield CO. To reflect this uncertainty in the minimum shielding column density required, we treated photodissociation in two ways. First, we followed the typical assumption for younger disks and assumed that

if the vertical column density of H_2 above any location in the disk was below 10^{21} cm^{-2} , CO would be photodissociated to a density of zero. As an alternative, we also calculated the expected CO flux without any photodissociation, which we consider a conservative upper limit on the amount of gaseous CO that survives and therefore on the model CO flux. We note that once enough CO survives to become optically thick, the shielding column density and precise amount that survives has little impact on the expected flux. Ignoring photodissociation entirely is an approximation of this scenario.

With these model CO disks, we used RADMC3D to calculate the CO $J = 3 - 2$ flux over the velocity range determined for each source in Paper I. We repeated this process for every continuum-detected source in our sample, generating a distribution of model CO fluxes for each. Figure 4.3 shows a comparison of our model CO fluxes with our observed fluxes from Paper I for the two treatments of photodissociation described above. Among the sources detected in CO, there was considerable scatter in the observed fluxes relative to the model fluxes. This reflects the uncertainties of our modeling procedure, both statistical from our uncertain dust model parameters and systematic relating to our assumptions regarding gas temperature and gas-to-dust ratio, as well as our treatments of freeze-out and photodissociation. Without photodissociation, CO fluxes increased by as much as an order of magnitude. This was due to cases where the combination of freeze-out and photodissociation truncated the CO disk inside of the observed R_{CO} , reducing the emitting area of the disk. For the sources not detected in CO, the model fluxes were consistent with observational upper limits.

4.5 Discussion

Dust Disk Sizes

Based on our derived dust outer radii, the majority of the continuum-detected dust disks in our sample are quite compact. Empirically, we determined that to constrain the dust outer radius (R_{dust}) to better than a factor of 2 required a signal-to-noise of at least 15. The 25 disks that meet this threshold have dust outer radii ranging from 8 to 65 au, with a median of 21 au. Only two disks, 2MASS J16082324-1930009 and 2MASS J16090007-1908526, have radii larger than 50 au. Note that this excludes 2MASS J15583692-2257153, 2MASS J16042165-2130284, and 2MASS J16113134-1838259 (see Section 4.2), all of which appear to be larger than 65 au in radius based on visual inspection of their continuum images (see Paper I). Figure 4.4 shows the posterior probability distributions of the outer radius for the 25 high

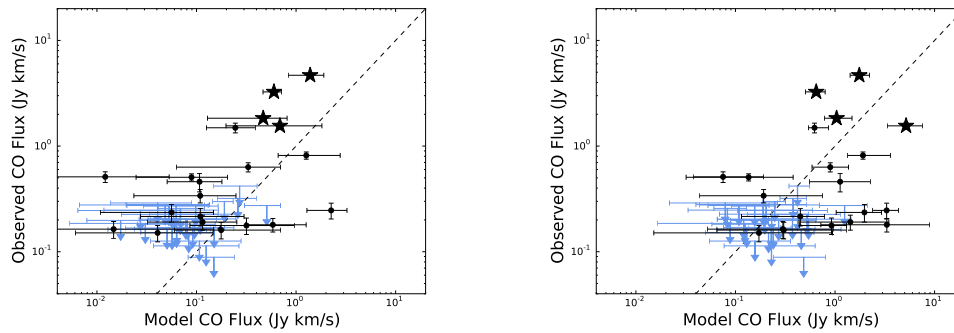


Figure 4.3: Observational and model fluxes for CO $J = 3 - 2$ emission for sources detected in the continuum, for models with (left panel) and without (right panel) photodissociation. Model fluxes were calculated based on the expected CO emission given the disk dust properties, as discussed in Section 4.4. CO detections are shown as black points, while upper limits are shown with blue arrows. The four well-constrained sources with larger CO outer radii than dust outer radii are shown as stars. Horizontal error bars represent the 68.3% confidence range for the model fluxes. The dashed line represents agreement between the model and observed fluxes.

signal-to-noise disks. The distributions are sharply peaked around the best-fit value, with no significant probability tails extending out to larger radii. Thus, while we cannot rule out that the dust surface density follows a different distribution than R^{-1} , such as a power law with a different slope or with an exponential tail, any such distribution must fall off rapidly at or near our best-fit outer radii.

While we lack a sample of younger disks analyzed in the same way to compare with our 5 – 11 Myr old Upper Sco sample, we do see evidence that the dust disks in Upper Sco are more compact than younger disks. Tripathi et al. (2017) measured the sizes of 50 disks primarily located in the 1-2 Myr old Taurus and Ophiuchus star-forming regions by fitting “Nuker” profiles (Lauer et al. 1995) to the continuum emission. More than half of the stars in this sample have spectral types earlier than K9, compared to only 2 of 25 stars in our high signal-to-noise sample, J16141107-2305362 and 2MASS J16154416-1921171. We therefore include only spectral types K9-M5 when comparing the present Upper Sco sample to these younger disks. Pre-main-sequence stars of these spectral types are fully convective and evolve at approximately constant temperature (e.g., Siess, Dufour, and Forestini 2000), making spectral type a good proxy for stellar mass even when comparing stars of different ages. For this spectral type range, Tripathi et al. (2017) found effective radii, defined as the radius containing 68% of the disk continuum flux,

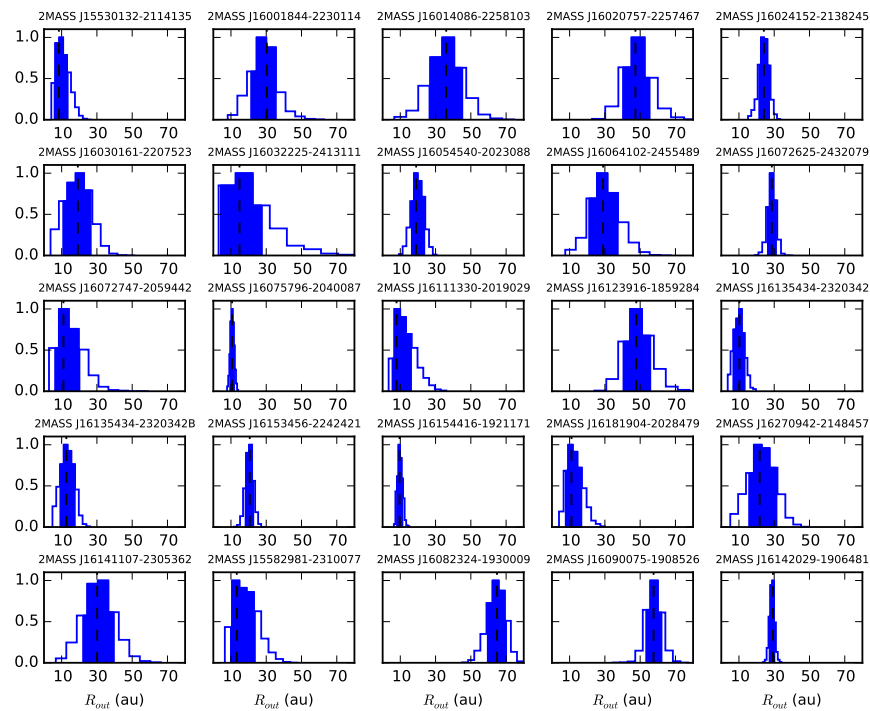


Figure 4.4: Posterior distributions of dust outer radius for the 25 disks with continuum signal-to-noise of at least 15. The distributions are sharply peaked around the best-fit values (dashed lines), indicating that these disks are well-constrained to be compact. The blue shaded regions show the 68.3% confidence range for the outer radii.

ranging from 19 to 182 au, with a median of 48 au. Assuming optically thin dust emission and constant midplane dust temperature in the outer regions of our Upper Sco disks, where most of the dust mass resides, we can define an effective radius for our sample as containing 68% of the total dust mass, which will be approximately equivalent to the radius containing 68% of the continuum flux. With this definition, the effective radii of our high signal-to-noise sources with spectral types K9-M5 range from 5 au to 44 au, with a median of 14 au. These effective radii may in fact be overestimated for the Upper Sco disks, as the innermost region of the disks will have higher dust temperatures than the outer regions, causing the disk continuum flux to be slightly more concentrated at small radii than the dust mass. However, since we found that the disks in Upper Sco appear to be smaller than the younger disks of Tripathi et al. (2017), this effect strengthens our conclusions.

In a separate study of young disks, Tazzari et al. (2017) fit for the outer radii

of 22 disks in the 1-3 Myr old Lupus star-forming region. The authors used a power law with an exponential cutoff to parameterize the dust surface density, defining the effective radius as that which contains 95% of the dust mass. We again exclude 2MASS J16141107-2305362 and 2MASS J16154416-1921171, restricting our comparison to stars between 0.15 and 0.7 M_{\odot} . For this stellar mass range, Tazzari et al. (2017) measure effective radii ranging from 18 to 129 au, with a median of 55 au. Calculating the radii of our disks containing 95% of the dust mass, we find a range of 7 to 62 au, with a median of 20 au. Taken at face-value, these results suggest that the disks in Upper Sco are smaller than those found in Taurus, Ophiuchus, and Lupus by a factor of approximately three. However, we caution however that a self-consistent analysis of all these disks needs to be performed to confirm this trend.

Finally, we note that Hendler et al. (2017b) measured dust outer radii from the spectral energy distributions of 11 young disks around very low mass stars and brown dwarfs in the Taurus and Chamaeleon I star-forming regions, finding disk sizes similar to those we see in Upper Sco. This younger sample probes lower stellar masses than the present Upper Sco sample, and is therefore not directly comparable. However, van der Plas et al. (2016) used ALMA to image the disks around seven very low mass stars and brown dwarfs in Upper Sco. None of these objects were spatially resolved, constraining them to also be compact ($\lesssim 40$ au). Follow-up studies of these low mass stellar and substellar systems can be used to determine if the reduction in dust disk sizes with age observed here extends to lower stellar masses.

Comparing Dust and CO

Empirically, we found that to measure R_{CO} to better than a factor of 2 required a CO signal-to-noise of at least 8, as measured from the moment 0 maps in Paper I. This threshold is lower than that of continuum data due to the CO model fitting having one less free parameter than the continuum fitting. Also, the CO emission tends to be more extended than the continuum emission, allowing for a smaller fractional uncertainty on the outer radius for a given signal-to-noise. For the nine disks with well-constrained CO outer radii we measured radii ranging from 12 to 169 au, with a median of 54 au, excluding 2MASS J16154416-1921171 (see Section 4.4). Only three of these nine sources have CO radii less than 50 au. Figure 4.5 displays the continuum and CO deprojected visibilities, with their best-fit models, for the seven sources with well-constrained dust and CO outer radii. Figure

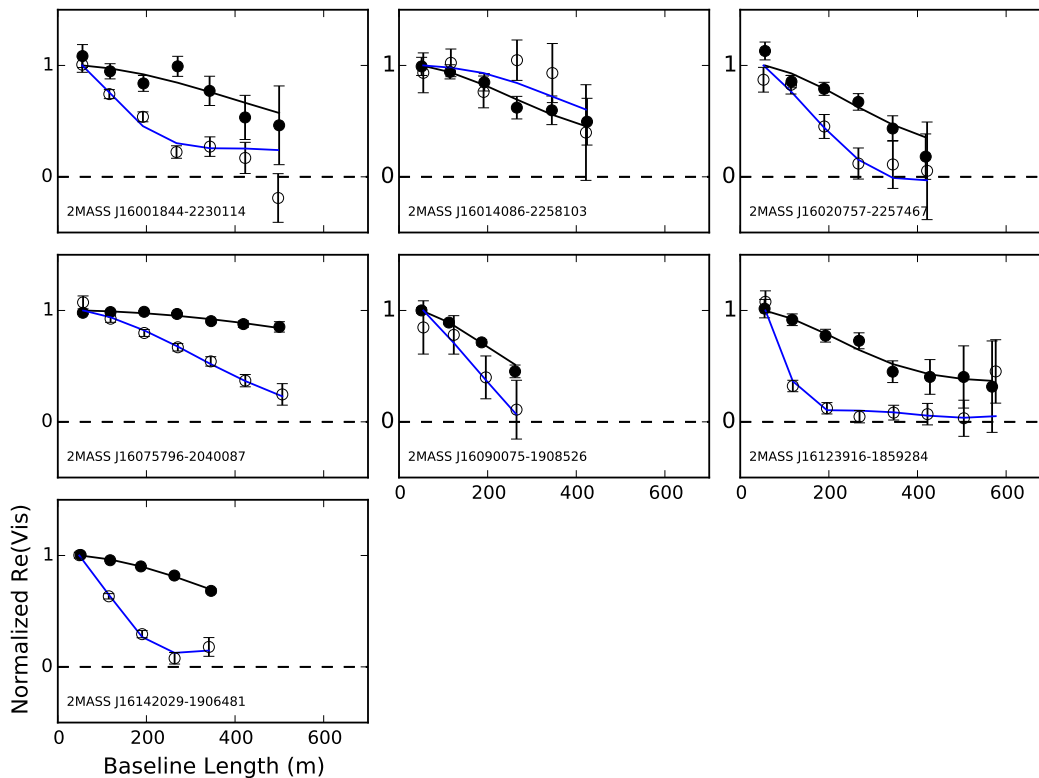


Figure 4.5: Continuum (black circles) and CO (open circles) deprojected visibilities for the sources with well-constrained dust and CO outer radii. The black and blue curves show the best-fit models for the dust and CO, respectively. Four sources, 2MASS J16001844-2230114, 2MASS J16075796-2040087, 2MASS J16123916-1859284, and 2MASS J16142029-1906481, exhibited detectable CO emission extending beyond their dust emission.

4.6 shows the outer radii for these sources. Four sources, 2MASS J16001844-2230114, 2MASS J16075796-2040087, 2MASS J16123916-1859284, and 2MASS J16142029-1906481, have detectable CO emission extending to larger radii than the detectable dust emission. Previous observations of younger disks also revealed CO emission extending beyond any detectable continuum emission (e.g., Piétu, Guilloteau, and Dutrey 2005; Isella et al. 2007; Panić et al. 2009; Andrews et al. 2012) and enhanced gas-to-dust ratios at large radii (Isella et al. 2016).

However, optical depth effects must be taken into account (Hughes et al. 2008; Facchini et al. 2017). A low surface density tail of dust may extend beyond the apparent dust outer radius, with its optically thin emission undetected. Emission from CO, on the other hand, is optically thick down to low surface densities, and therefore is more likely to be detected in the outer parts of a disk even if the dust

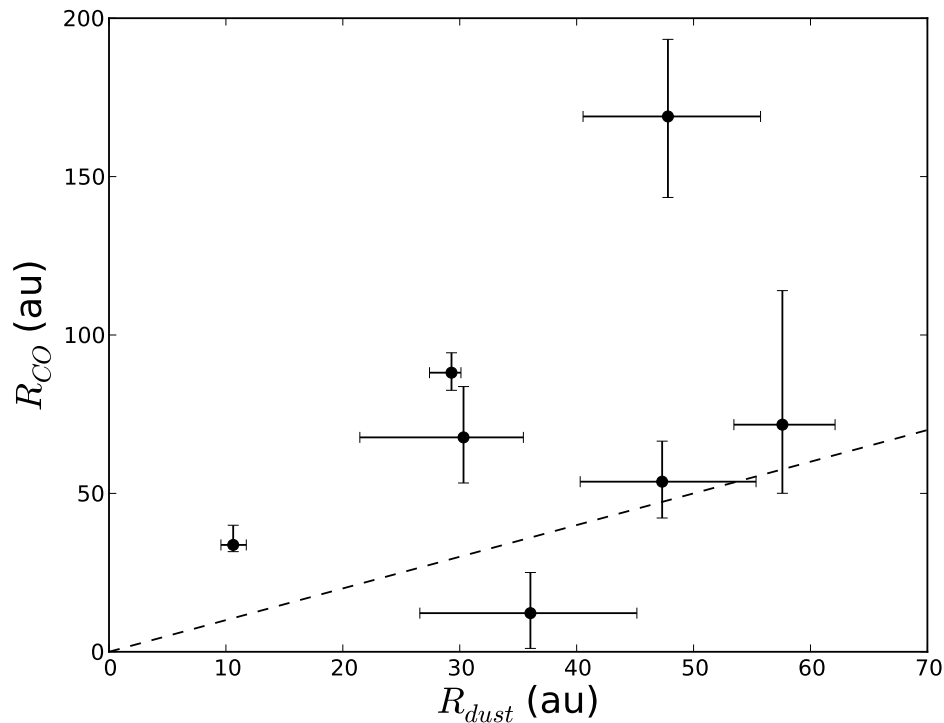


Figure 4.6: best-fit CO and dust outer radii for sources where both are well constrained. Four sources, 2MASS J16001844-2230114, 2MASS J16075796-2040087, 2MASS J16123916-1859284, and 2MASS J16142029-1906481, have CO outer radii larger than their dust outer radii.

emission is weak. To test this possibility for the four sources with CO potentially extending beyond the dust, we used the predicted CO fluxes of Section 4.4 and Figure 4.3, where these four sources are shown as stars. These models assumed a low surface density tail of dust, consistent with our upper limits, between the apparent dust and CO outer radii, with standard CO abundances relative to the dust. We found that the predicted CO line fluxes of these sources were consistent with the observed fluxes, although this was dependent on the assumed photodissociation prescription. Therefore, while these disks may in fact have an enhanced gas-to-dust ratio in the outer disk due to inward grain migration (e.g., Birnstiel and Andrews 2014), we could not rule out a standard gas-to-dust ratio, with a drop in surface density of both gas and dust beyond the apparent dust outer radius. Further observations that place deeper limits on the dust surface density in the outer disk and/or include the optically thin isotopologues of CO to estimate gas surface densities can be used to distinguish between these two cases.

Previous studies of 1-3 Myr old disks have found evidence for a low CO abundance relative to dust throughout the disk (Dutrey, Guilloteau, and Simon 2003; Chapillon et al. 2008; Williams and Best 2014; Hardy et al. 2015; Long et al. 2017). Ansdell et al. (2016) used observations of optically thin ^{13}CO and C^{18}O emission to measure the gas-to-dust ratios of 62 disks in 1-3 Myr old Lupus complex, finding that the majority of sources had a gas-to-dust ratio below the ISM value of 100 assuming an ISM abundance of CO relative to H_2 (see also Miotello et al. 2017). Ansdell et al. (2017) found similar results for the 3-5 Myr old σ Orionis region. To the extent that CO traces the total gas mass, this has important implications for disk evolution and the relative timescales of gas and dust dissipation in disks. However, chemical processing of the gas in disks is expected to lower the CO to H_2 ratio (Kama et al. 2016; Yu et al. 2017). Gas mass measurements using the HD 112 μm line showed that CO in disks may be depleted relative to hydrogen by up to two orders of magnitude (Bergin et al. 2013; McClure et al. 2016).

If the processes causing these low CO abundances continue to the age of Upper Sco, this could explain the lack of CO detections in over half of our continuum-detected disks. However, as our analysis in Section 4.4 shows, CO depletion is not required to explain these non-detections, given the signal-to-noise of the data. The small sizes of these disks alone are sufficient to explain the lack of detectable CO emission. For the sources where we do see CO emission, we could not constrain the total mass in CO due to the likelihood that the emission is optically thick. Upper Sco represents a crucial data point to study the relative evolution of gas and dust in disks, but to do so requires additional sensitivity and/or observations of ^{13}CO and C^{18}O to constrain the gaseous CO mass.

Implications for Disk Evolution

The evolved nature of the disks in our Upper Sco sample presents an opportunity to use the properties of these disks to improve our understanding of disk evolution. Paper I and Ansdell et al. (2016) showed that the dust disks in Upper Sco are on average a factor of 3-4.5 less massive than those in Taurus and Lupus (see also Pascucci et al. 2016). Taken at face-value, the indication of dust disks being more compact as well in Upper Sco (Section 4.5) implies that at least some of this mass is lost through the disappearance of millimeter grains in the outer disk. These grains may be completely removed from the millimeter grain population of the system, either through photoevaporation of the outer disk (e.g., Owen, Clarke, and Ercolano 2012; Alexander et al. 2014; Gorti, Hollenbach, and Dullemond 2015) or through

growth into larger bodies (Testi et al. 2014, and references therein). On the other hand, inward migration of grains from the outer disk (e.g., Weidenschilling 1977; Birnstiel and Andrews 2014) may cause the inner disk to become optically thick, in effect hiding the dust mass of the outer disk and making the disk appear to be less massive.

We tested these scenarios by comparing the dust surface densities of the Upper Sco disks in this work and of the Lupus disks measured by Tazzari et al. (2017) to determine if the amount of inner disk dust has increased by the age of Upper Sco. We used the best-fit surface density normalizations of both studies, Σ_0 , representing the surface density at the normalization radius of 10 au, as a proxy for inner disk surface density. The Σ_0 values of Tazzari et al. (2017) are measured assuming a dust opacity at $890\mu\text{m}$ of $3.37\text{ cm}^2\text{ g}^{-1}$ so we scaled their surface densities to match our assumed dust opacity of $4.94\text{ cm}^2\text{ g}^{-1}$. In addition, the authors report the inferred *gas* surface density at 10 au assuming a gas-to-dust ratio of 100. We therefore divided by their assumed gas-to-dust ratio to recover the dust surface density. Applying these corrections and restricting our comparison to stars between 0.15 and $0.7 M_\odot$ as in Section 4.5, we found Σ_0 values ranging from $4.9 \times 10^{-3}\text{ g cm}^{-2}$ to 0.71 g cm^{-2} for Lupus and $6.2 \times 10^{-3}\text{ g cm}^{-2}$ to 0.23 g cm^{-2} for the high signal-to-noise Upper Sco disks. The mean of $\log \Sigma_0$ is -1.04 for Lupus, with a standard deviation of 0.64 , while Upper Sco has a mean $\log \Sigma_0$ of -1.65 , with a standard deviation of 0.42 . In addition, the mean $\log \Sigma_0$ value we find for Upper Sco implies an inner disk that only becomes optically thick inside of ~ 1 au, assuming $\Sigma \propto R^{-1}$. We therefore see no evidence of inner disks increasing in dust surface density between Lupus and Upper Sco.

However, our modeling assumes that the dust in these disks is distributed smoothly in radius following a simple parameterization, which may not be the case. Tripathi et al. (2017) suggested that disks may be composed of optically thick substructures with a filling factor of a few tens of percent to explain an observed correlation between disk size and luminosity in 1-2 Myr old disks in Taurus and Ophiuchus. This idea is supported by theoretical models of gas and dust interactions in disks, which predict that small-scale gas pressure maxima can trap dust grains and create concentrations of optically thick continuum emission (e.g., Whipple 1972; Pinilla et al. 2012). Recent high resolution observations with ALMA have revealed a number of disks exhibiting such substructure (ALMA Partnership et al. 2015; Andrews et al. 2016; Cieza et al. 2016; Isella et al. 2016; Pérez et al. 2016; Zhang et al. 2016;

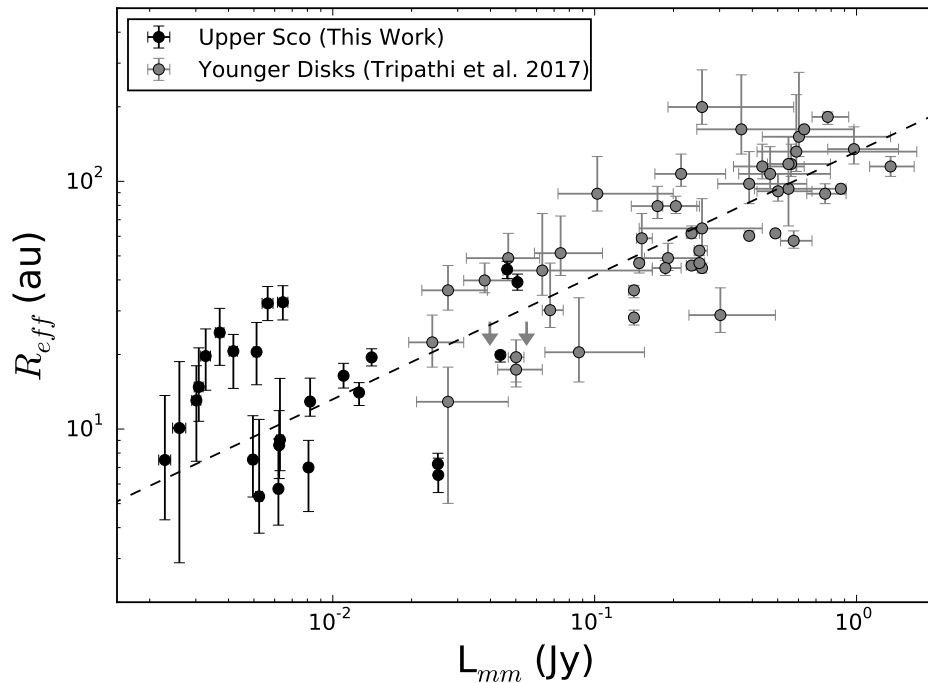


Figure 4.7: Dust effective radius versus continuum flux density at 0.88 mm for circumstellar disks in Taurus and Ophiuchus (gray points, Tripathi et al. 2017) and Upper Sco (black points, this work). Flux densities have been scaled to a distance of 140 pc. The dashed line shows the disk size-luminosity relation from Tripathi et al. (2017), which has been extrapolated to the flux densities of the Upper Sco disks. The Upper Sco sources shown are those with a continuum signal-to-noise of at least 15.

Loomis et al. 2017). If young disks such as those in Lupus and Taurus are in general composed of optically thick substructures with filling factors less than 1, appearing optically thin to lower resolution observations, this could provide a way to hide dust grains migrating from the outer disk and cause the disk to appear less massive as it decreases in size. As long as the filling factor of the substructure does not increase, lower resolution observations such as those presented here and in Tazzari et al. (2017) would not detect the increase in dust surface density.

Figure 4.7 compares the effective radii (R_{eff}) and continuum fluxes scaled to 140 pc (L_{mm}) for Upper Sco and the young stars analyzed by Tripathi et al. (2017). The Tripathi et al. (2017) disk size-luminosity relation, $R_{\text{eff}} \propto L_{\text{mm}}^{0.50 \pm 0.07}$, is also shown, extrapolated to the scaled flux densities of Upper Sco. Despite the difference in age and luminosity, our disks lie approximately along this extrapolation. We therefore

conclude that our data is qualitatively consistent with the Tripathi et al. (2017) disk size-luminosity relation. Thus, if the disk size-luminosity correlation is caused by optically thick substructures, the filling factor of these substructures will be roughly the same in Upper Sco as in Taurus and Ophiuchus. Higher resolution observations of samples of disks of different ages can help to further constrain the evolution of inner disks, allowing the dust surface density and optical depth to be more precisely measured as a function of radius and possibly detecting substructure.

4.6 Summary

We have presented detailed modeling of 57 circumstellar disks in the Upper Scorpius OB Association observed with ALMA. Our sample excludes the three brightest continuum disks observed in Paper I, 2MASS J15583692-2257153, 2MASS J16042165-2130284, and 2MASS J16113134-1838259, instead focusing on more typical Upper Sco disks. Power-law model fits of the dust surface density to the continuum observations yielded the radial extent of dust in these disks. Similar model fits to the CO surface brightness of the disks measured the extent of CO. Using our modeling results, we compared the spatial extents of dust and CO Upper Sco disks and calculated a range of expected CO fluxes, comparing these model fluxes to our observed values from Paper I. The key conclusions of this paper are as follows.

1. Of the 25 analyzed disks with a continuum signal-to-noise of at least 15, we find a median dust outer radius of 21 au. Only two of these disks had dust outer radii larger than 50 au, with none greater than 65 au, assuming an R^{-1} power-law dust surface density. While this excludes the three brightest continuum sources in our sample, which appear to be more extended, it is clear that the majority of the high signal-to-noise dust disks in Upper Sco are extremely compact.
2. Among our seven disks with well-constrained dust and CO outer radii, four exhibited CO radii significantly larger than their dust radii. Given the signal-to-noise of the continuum and CO data, this may simply be a result of higher optical depths of the CO line. More sensitive observations, especially of ^{13}CO and C^{18}O , are needed to determine whether there is a true deficit of dust in the outer regions of these disks.
3. Assuming that the CO and dust share the same spatial distribution, the lack

of CO detections in most of the disks is consistent with the small disk sizes inferred from the continuum.

4. Dust disks in Upper Sco are a factor of approximately three times more compact than those in Taurus, Ophiuchus, and Lupus. Assuming that the continuum emission is optically thin, the lower disk masses in Upper Sco relative to Taurus and Lupus (Paper I; Ansdell et al. 2016) appear to be primarily due to the removal of material in the outer disk. We caution, however, that a more uniform analysis between samples is needed.
5. The disks in Upper Sco fall along the same size-luminosity correlation found by Tripathi et al. (2017). If the origin of this correlation is caused by the presence of optically thick substructures, the filling factor of such structures is similar between Upper Sco and the young disks studied by Tripathi et al. (2017).

ACKNOWLEDGEMENTS

We thank the referee and statistics editor for their useful comments, which improved this manuscript. We are grateful to the ALMA staff for their assistance in the data reduction. The National Radio Astronomy Observatory is a facility of the National Science Foundation operated under cooperative agreement by Associated Universities, Inc. This paper makes use of the following ALMA data: ADS/JAO.ALMA#2011.0.00966.S and ADS/JAO.ALMA#2013.1.00395.S. ALMA is a partnership of ESO (representing its member states), NSF (USA) and NINS (Japan), together with NRC (Canada) and NSC and ASIAA (Taiwan), in cooperation with the Republic of Chile. The Joint ALMA Observatory is operated by ESO, AUI/NRAO, and NAOJ. This material is based upon work supported by the National Science Foundation Graduate Research Fellowship under grant No. DGE-1144469. S.A.B. acknowledges support from the NSF grant No. AST-1140063. J.M.C. acknowledges support from the National Aeronautics and Space Administration under grant No. 15XRP15_20140 issued through the Exoplanets Research Program. A.I. acknowledges support from the NSF grant No. AST-1535809 and the National Aeronautics and Space Administration grant No. NNX15AB06G. This publication makes use of data products from the Two Micron All Sky Survey, which is a joint project of the University of Massachusetts and the Infrared Processing and Analysis Center/California Institute of Technology, funded by the National Aeronautics and Space Administration and the National Science Foundation. This publication makes use of data products from the *Wide-field Infrared Survey Explorer*, which is a joint project of the University of California, Los Angeles, and the Jet Propulsion Laboratory/California Institute of Technology, funded by the National Aeronautics and Space Administration. This research has made use of the NASA/IPAC Extragalactic Database (NED) which is operated by the Jet Propulsion Laboratory, California Institute of Technology, under contract with the National Aeronautics and Space Administration. This work is based [in part] on observations made with the Spitzer Space Telescope, which is operated by the Jet Propulsion Laboratory, California Institute of Technology under a contract with NASA.

*Chapter 5*THE EFFECT OF BINARITY ON CIRCUMSTELLAR DISK
EVOLUTION

ABSTRACT

We present new results on how the presence of stellar companions affects disk evolution based on a study of the 5-11 Myr old Upper Scorpius OB Association. Of the 50 G0-M3 Upper Sco members with disks in our sample, only seven host a stellar companion within $2''$ and brighter than $K = 15$, compared to 35 of 75 members without disks. This matches a trend seen in the 1-2 Myr old Taurus region, where systems with a stellar companion within 40 au have a lower fraction of infrared-identified disks than those without such companions, indicating shorter disk lifetimes in close multiple systems. However, the fractions of disk systems with a stellar companion within 40 au match in Upper Sco and Taurus. Additionally, we see no difference in the millimeter brightnesses of disks in Upper Sco systems with and without companions, in contrast to Taurus where systems with a companion within 300 au are significantly fainter than wider and single systems. These results suggest that the effects of stellar companions on disk lifetimes occur within the first 1-2 Myr of disk evolution, after which companions play little further role. By contrast, disks around single stars lose the millimeter-sized dust grains in their outer regions between ages of 1-2 Myr and 5-11 Myr. The end result of small dust disk sizes and faint millimeter luminosities is the same whether the disk has been truncated by a companion or has evolved through internal processes.

5.1 Introduction

The formation and evolution of circumstellar disks is fundamental to our understanding of planet formation. This process begins with the collapse of a dense molecular cloud core and the subsequent formation of a protostar surrounded by an infalling envelope. Over a period of about 1 Myr, conservation of angular momentum causes the infalling material to form a circumstellar disk that remains around the star after the surrounding envelope is lost (Li et al. 2014, and references therein). This disk can provide the material for planet formation, a process that is not fully understood but likely involves direct collapse of disk material into a planet through gravitational instability and/or the slower growth of planetesimals and planets through core accretion (e.g., Chabrier et al. 2014; Helled et al. 2014). As the disk evolves, material will continue to viscously accrete onto the central star (e.g., Hartmann et al. 1998). At the same time, photoevaporation from the disk surface by high energy stellar radiation dissipates disk material (Owen, Clarke, and Ercolano 2012; Alexander et al. 2014; Gorti, Hollenbach, and Dullemond 2015). Simultaneously, dust grains migrate inwards due to gas drag and grow to form larger bodies, depleting the small grain population (Whipple 1972; Weidenschilling 1977; Brauer et al. 2007; Birnstiel and Andrews 2014; Testi et al. 2014). By an age of 5-10 Myr, the majority of disks have dissipated (Hernández et al. 2008), leaving behind a young star surrounded by any planets and associated debris that have formed.

Even for single stars, there are many uncertainties associated with the processes of disk evolution and planet formation. Additional complications arise from the fact that most stars are born in multiple systems. Studies of field stars show that the fraction of multiple systems is $\sim 50\%$ among solar-type stars (Raghavan et al. 2010) and $\sim 30 - 40\%$ for later-type stars (Fischer and Marcy 1992; Bergfors et al. 2010). In the pre-main sequence phase, multiplicity is at least as common (Ratzka, Köhler, and Leinert 2005; Kraus et al. 2008; Lafrenière et al. 2008; Kraus et al. 2011; Cheetham et al. 2015). Indeed, surveys of the earliest protostars indicate that a high binary fraction is intrinsic to the star formation process (Chen et al. 2013). Results from the *Kepler* survey (Borucki et al. 2010) show that while planet formation is suppressed in binary systems (Wang et al. 2014a, 2014b, 2015a, 2015b; Kraus et al. 2016), it is possible for such planets to form (e.g., Holman and Wiegert 1999; Dupuy et al. 2016; Hirsch et al. 2017). A complete understanding of the formation and evolution of stars and planets must therefore take the effects of stellar companions into account.

Theoretical calculations have long predicted that the presence of a stellar companion will have an important influence on disk evolution (Papaloizou and Pringle 1977). A disk around a single component of a binary system will be tidally truncated at approximately one-third to one-half of the binary separation and the resulting smaller disk will dissipate on a more rapid timescale than an unperturbed disk around a single star (e.g., Artymowicz and Lubow 1994; Pichardo, Sparke, and Aguilar 2005; Jang-Condell 2015). In fact, some initial surveys found that the fraction of binaries is lower in systems with disks and, in particular, accreting disks (Ghez, Neugebauer, and Matthews 1993; Ratzka, Köhler, and Leinert 2005), although other studies found no difference between accreting and non-accreting systems (Leinert et al. 1993; Köhler and Leinert 1998). Most recently, catalogs of much larger samples of disks identified with the *Spitzer Space Telescope* (Werner et al. 2004) and the *Wide-field Infrared Survey Explorer (WISE)* (Wright et al. 2010) have provided more convincing evidence that the presence of stellar companions leads to shorter disk lifetimes (Bouwman et al. 2006; Daemgen et al. 2016; Long et al. 2018), with the disk fraction in 1-3 Myr old close binary systems (≤ 40 au separation) less than half that of wider binaries and single stars (Cieza et al. 2009; Kraus et al. 2012; Cheetham et al. 2015).

Submillimeter interferometric observations are now providing high-resolution images of the outer regions of disks, where most of the material resides, so that the effects of binarity on the entire disk, beyond the central regions probed by infrared observations, can be studied. In a millimeter study of 1-2 Myr old disks in Taurus, Harris et al. (2012) detected only one-third of disks in binary systems compared to two-thirds of single-star disks. In addition, the authors observed a positive correlation between binary separation and disk millimeter luminosity. While disks in binary systems with separations greater than 300 au had luminosities indistinguishable from single stars, disks in systems with a companion between 30 and 300 au were fainter by a factor of five. Disks in systems with a companion within 30 au were an additional factor of five fainter, implying that even in Taurus binary systems that maintain their disks, a substantial fraction of the millimeter-wavelength-emitting grains are lost due to the companion (see also Jensen, Mathieu, and Fuller 1994, 1996).

Understanding how stellar companions affect later stages of disk evolution requires observations of older systems. Since these older disks are significantly fainter than their younger counterparts (Nuernberger, Chini, and Zinnecker 1997; Carpenter

2002; Lee, Williams, and Cieza 2011; Mathews et al. 2012; Williams et al. 2013; Carpenter, Ricci, and Isella 2014; Ansdell, Williams, and Cieza 2015; Barenfeld et al. 2016), detailed studies require the sensitivity of the Atacama Large Millimeter/submillimeter Array (ALMA). To this end, we measured the properties of over 100 disks in the 5-11 Myr old Upper Scorpius OB Association (hereafter Upper Sco) using ALMA and found that these disks are a factor of ~ 4.5 less massive (Barenfeld et al. 2016) and a factor of ~ 3 smaller (Barenfeld et al. 2017) than their younger counterparts. In this paper, we consider how the influence of stellar companions has impacted the evolution of these disks to their current state. To investigate this, we searched for companions to the stars in our Upper Sco disk sample using adaptive optics (AO) imaging and aperture masking. We describe our sample, observations, and data reduction in Section 5.2. Section 5.3 specifies how companions were identified. In Section 5.4, we describe our detected companions and compare the companion frequency of systems with and without disks in Upper Sco. Finally, in Section 5.5, we discuss how the effects of stellar multiplicity on disk properties vary with age in the context of disk evolution. Our conclusions are summarized in Section 5.6.

5.2 Sample and Observations

Our sample contains all 100 Upper Sco stars with spectral types between G2 and M4.75 (inclusive) as well as 13 M5 stars in Upper Sco identified as hosting disks by Carpenter et al. (2006) and Luhman and Mamajek (2012).¹ These disks were discovered based on excess infrared emission observed by *Spitzer* and *WISE* and include 82 disks classified as “full,” “evolved,” or “transitional” by Luhman and Mamajek (2012) based on their infrared colors. We consider these disks to be “primordial,” i.e., a direct evolution of younger protoplanetary disks such as those in Taurus. The remaining 31 disks in the sample are characterized as “debris/evolved transitional” (Luhman and Mamajek 2012). These disks may represent the final phase of primordial disk evolution or be second-generation objects composed of dust created by the collision of planetesimals, with only an indirect evolutionary link to younger disks. The full sample is listed in Table 5.1 and receives a more detailed description in Barenfeld et al. (2016). Distances to the stars in the sample are taken from the catalog of Bailer-Jones et al. (2018), inferred from Gaia parallaxes using a Bayesian distance prior.

¹Recent surveys, published after the present observations were obtained, have since expanded the known population of stars and disks in Upper Sco (Luhman et al. 2018; Esplin et al. 2018).

Table 5.1: Upper Sco Disk Sample

Source	Disk Type	Spectral Type	K (mag)	Distance ^a (pc)	$S_{0.88\text{mm}}$ ^b (mJy)	Observation Epoch ^c	Total Int. Time (s)		Coronagraph?
							Imaging	Masking ^d	
2MASS J15354856-2958551	primordial	M4	9.46 ± 0.03	145 (-11, +11)	1.92 ± 0.15
2MASS J15514032-2146103	primordial	M4	11.00 ± 0.02	142 (-2, +2)	0.76 ± 0.16	2013 May 30	60	120	no
2MASS J15521088-2125372	primordial	M4	12.08 ± 0.03	167 (-7, +8)	-0.10 ± 0.15	2015 May 27	40	160	no
2MASS J15530132-2114135	primordial	M4	11.02 ± 0.02	146 (-2, +3)	5.78 ± 0.14	2013 May 30	60	120	no
2MASS J15534211-2049282	primordial	M3.4	9.62 ± 0.03	135 (-3, +3)	2.93 ± 0.29	2013 May 30	30	...	no
2MASS J15551704-2322165	debris/ev. trans.	M2.5	9.33 ± 0.02	124 (-2, +2)	0.11 ± 0.15	2015 May 27	40	160	yes
2MASS J15554883-2512240	debris/ev. trans.	G3	8.29 ± 0.02	143 (-1, +1)	-0.14 ± 0.15	2015 May 27	40	320	yes
2MASS J15562477-2225552	primordial	M4	10.79 ± 0.02	141 (-2, +2)	0.28 ± 0.18	2013 May 30	60	120	no
2MASS J15570641-2206060	primordial	M4	11.29 ± 0.03	157 (-3, +3)	0.32 ± 0.20	2013 May 30	60	120	no
2MASS J15572986-2258438	primordial	M4	11.19 ± 0.02	145 (-11, +11)	-0.04 ± 0.20	2013 May 30	30	...	no
2MASS J15581270-2328364	debris/ev. trans.	G6	8.02 ± 0.02	143 (-1, +1)	0.00 ± 0.15	2015 May 27	40	160	yes
2MASS J15582981-2310077	primordial	M3	11.30 ± 0.02	147 (-3, +3)	5.86 ± 0.18	2013 May 30	60	120	no
2MASS J15583692-2257153	primordial	G7	7.05 ± 0.03	165 (-4, +4)	174.92 ± 0.27
2MASS J15584772-1757595	debris/ev. trans.	K4	8.32 ± 0.02	138 (-1, +1)	-0.20 ± 0.15	2015 May 27	40	320	yes
2MASS J16001330-2418106	debris/ev. trans.	M0	9.51 ± 0.02	146 (-1, +1)	0.05 ± 0.15
2MASS J16001730-2236504	primordial	M4	9.94 ± 0.02	148 (-2, +2)	0.10 ± 0.15	2015 May 27	40	160	yes
2MASS J16001844-2230114	primordial	M4.5	10.41 ± 0.02	138 (-8, +9)	3.89 ± 0.15	2015 May 27	40	160	yes
2MASS J16014086-2258103	primordial	M4	9.85 ± 0.02	124 (-2, +2)	3.45 ± 0.14
2MASS J16014157-2111380	primordial	M4	11.68 ± 0.03	144 (-2, +3)	0.66 ± 0.14	2013 May 31	60	120	no
2MASS J16020039-2221237	debris/ev. trans.	M1	8.84 ± 0.02	144 (-2, +3)	-0.08 ± 0.14
2MASS J16020287-2236139	debris/ev. trans.	M0	11.61 ± 0.03	145 (-11, +11)	0.04 ± 0.15	2015 May 28	60	...	no
2MASS J16020757-2257467	primordial	M2.5	9.86 ± 0.02	140 (-1, +1)	5.26 ± 0.27	2013 May 31	40	120	yes
2MASS J16024152-2138245	primordial	M4.75	11.18 ± 0.02	141 (-2, +3)	10.25 ± 0.19	2013 May 31	60	120	no
2MASS J16025123-2401574	debris/ev. trans.	K4	8.93 ± 0.02	143 (-1, +1)	0.07 ± 0.15
2MASS J16030161-2207523	primordial	M4.75	11.73 ± 0.02	144 (-3, +4)	2.81 ± 0.12	2015 May 27	40	160	no
2MASS J16031329-2112569	primordial	M4.75	11.16 ± 0.02	143 (-2, +2)	0.06 ± 0.12	2015 May 27	40	160	no
2MASS J16032225-2413111	primordial	M3.5	10.01 ± 0.02	144 (-3, +3)	2.42 ± 0.15	2013 May 30	40	120	yes
2MASS J16033471-1829303	primordial	M5	11.48 ± 0.02	146 (-7, +8)	...	2013 May 30	30	...	no
2MASS J16035767-2031055	primordial	K5	8.37 ± 0.03	142 (-1, +1)	4.30 ± 0.39
2MASS J16035793-1942108	primordial	M2	10.32 ± 0.02	157 (-2, +2)	1.17 ± 0.14	2013 May 30	40	120	yes
2MASS J16041740-1942287	primordial	M3.5	10.42 ± 0.05	161 (-2, +2)	0.89 ± 0.14	2013 May 31	30	...	no
2MASS J16042165-2130284	primordial	K2	8.51 ± 0.02	149 (-1, +1)	218.76 ± 0.81
2MASS J16043916-1942459	debris/ev. trans.	M3.25	10.79 ± 0.02	151 (-2, +2)	0.49 ± 0.15	2015 May 28	40	160	yes
2MASS J16050231-1941554	debris/ev. trans.	M4.5	11.54 ± 0.02	157 (-3, +3)	-0.16 ± 0.15	2015 May 28	40	160	no
2MASS J16052459-1954419	debris/ev. trans.	M3.5	10.48 ± 0.02	152 (-2, +2)	0.22 ± 0.15	2015 May 28	40	160	no
2MASS J16052556-2035397	primordial	M5	11.05 ± 0.02	142 (-3, +3)	1.53 ± 0.20	2013 May 30	30	...	no
2MASS J16052661-1957050	primordial	M4.5	10.69 ± 0.02	145 (-11, +11)	0.07 ± 0.15	2013 May 31	30	...	no
2MASS J16053215-1933159	primordial	M5	11.36 ± 0.02	154 (-2, +3)	0.25 ± 0.20	2013 May 30	60	120	no
2MASS J16054540-2023088	primordial	M2	10.41 ± 0.02	145 (-2, +2)	7.64 ± 0.15	2013 May 30	30	...	no
2MASS J16055863-1949029	primordial	M4	10.74 ± 0.02	148 (-2, +2)	-0.08 ± 0.15	2015 May 28	40	160	yes
2MASS J16060061-1957114	primordial	M5	10.44 ± 0.03	145 (-11, +11)	0.00 ± 0.13	2013 May 30	30	...	no
2MASS J16061144-1935405	primordial	M5	11.78 ± 0.02	139 (-3, +3)	...	2013 May 30	60	...	no
2MASS J16061330-2212537	debris/ev. trans.	M4	9.59 ± 0.02	139 (-2, +2)	-0.20 ± 0.12	2015 May 28	40	160	yes
2MASS J16062196-1928445	primordial	M0	8.62 ± 0.03	145 (-11, +11)	4.08 ± 0.52
2MASS J16062277-2011243	primordial	M5	11.00 ± 0.02	151 (-2, +2)	0.59 ± 0.14	2013 May 30	60	...	no
2MASS J16063539-2516510	primordial	M4.5	11.71 ± 0.03	139 (-3, +3)	1.69 ± 0.15	2013 May 30	60	...	no
2MASS J16064102-2455489 ^e	primordial	M4.5	12.07 ± 0.02	152 (-3, +3)	3.05 ± 0.14	2015 May 28	40	160	no
2MASS J16064115-2517044	primordial	M3.25	10.92 ± 0.02	149 (-2, +2)	0.20 ± 0.15	2013 May 31	60	120	no
2MASS J16064385-1908056	primordial	K6	9.20 ± 0.02	144 (-6, +7)	0.84 ± 0.15
2MASS J16070014-2033092	primordial	M2.75	9.94 ± 0.02	139 (-2, +2)	0.22 ± 0.15	2013 May 31	40	...	yes
2MASS J16070211-2019387	primordial	M5	11.40 ± 0.03	149 (-5, +5)	-0.09 ± 0.20

Table 5.1: Upper Sco Disk Sample

Source	Disk Type	Spectral Type	K (mag)	Distance ^a (pc)	$S_{0.88\text{mm}}$ ^b (mJy)	Observation Epoch ^c	Total Int. Time (s)		Coronagraph?
							Imaging	Masking ^d	
2MASS J16070873-1927341	debris/ev. trans.	M4	11.17 ± 0.02	146 (-2, +2)	-0.09 ± 0.15	2011 May 15	90	940	no
2MASS J16071971-2020555	debris/ev. trans.	M3	10.72 ± 0.02	164 (-3, +3)	0.16 ± 0.16	2011 May 15	90	1200	no
2MASS J16072625-2432079	primordial	M3.5	9.88 ± 0.02	142 (-2, +2)	13.12 ± 0.24	2013 May 30	40	...	yes
2MASS J16072747-2059442	primordial	M4.75	10.22 ± 0.02	145 (-11, +11)	2.13 ± 0.12	2013 May 31	30	...	no
2MASS J16073939-1917472	debris/ev. trans.	M2	9.80 ± 0.02	137 (-1, +1)	0.58 ± 0.16	2011 May 15	90	800	no
2MASS J16075796-2040087	primordial	M1	7.81 ± 0.02	198 (-8, +8)	23.49 ± 0.12	2015 May 28	40	160	yes
2MASS J16080555-2218070	debris/ev. trans.	M3.25	9.85 ± 0.02	142 (-1, +1)	0.02 ± 0.12	2015 May 28	40	160	yes
2MASS J16081566-2222199	primordial	M3.25	9.95 ± 0.02	140 (-2, +2)	0.97 ± 0.12	2013 May 31	40	120	yes
2MASS J16082324-1930009	primordial	K9	9.47 ± 0.02	137 (-1, +1)	43.19 ± 0.81
2MASS J16082733-2217292	primordial	M5	10.45 ± 0.02	146 (-3, +3)	...	2013 May 31	40	120	yes
2MASS J16082751-1949047	primordial	M5	10.59 ± 0.02	145 (-11, +11)	0.76 ± 0.13	2013 May 30	30	...	no
2MASS J16082870-2137198	primordial	M5	10.76 ± 0.02	139 (-2, +2)	...	2013 May 31	60	120	no
2MASS J16083455-2211559	primordial	M4.5	11.53 ± 0.02	135 (-3, +3)	0.01 ± 0.12	2013 May 31	60	120	no
2MASS J16084894-2400045	primordial	M3.75	10.94 ± 0.02	144 (-2, +2)	-0.06 ± 0.15	2013 May 30	60	...	no
2MASS J16090002-1908368	primordial	M5	10.96 ± 0.02	139 (-3, +3)	1.73 ± 0.13	2013 May 30	60	120	no
2MASS J16090075-1908526	primordial	K9	9.15 ± 0.03	137 (-1, +1)	47.28 ± 0.91
2MASS J16093558-1828232	primordial	M3	10.70 ± 0.02	165 (-3, +3)	0.69 ± 0.15	2013 May 31	60	120	no
2MASS J16094098-2217594	debris/ev. trans.	M0	8.44 ± 0.03	146 (-1, +1)	0.44 ± 0.12
2MASS J16095361-1754474	primordial	M3	11.53 ± 0.02	157 (-5, +6)	0.87 ± 0.16	2013 May 30	60	120	no
2MASS J16095441-1906551	debris/ev. trans.	M1	9.60 ± 0.02	136 (-1, +1)	0.50 ± 0.16
2MASS J16095933-1800090	primordial	M4	10.34 ± 0.02	136 (-2, +2)	0.67 ± 0.18	2013 May 30	40	120	yes
2MASS J16101473-1919095	debris/ev. trans.	M2	10.03 ± 0.02	139 (-1, +2)	0.01 ± 0.16	2011 May 15	90	1400	no
2MASS J16101888-2502325	primordial	M4.5	11.26 ± 0.05	155 (-4, +4)	0.30 ± 0.14	2015 May 28	40	160	no
2MASS J16102174-1904067	debris/ev. trans.	M1	9.62 ± 0.02	133 (-1, +1)	-0.05 ± 0.16
2MASS J16102819-1910444 ^f	primordial	M4	11.79 ± 0.02	150 (-2, +3)	0.05 ± 0.16	2013 May 31	40	120	yes
2MASS J16102857-1904469	primordial	M3	8.71 ± 0.02	145 (-11, +11)	0.66 ± 0.16
2MASS J16103956-1916524 ^g	debris/ev. trans.	M2	10.27 ± 0.03	158 (-2, +2)	0.07 ± 0.16	2015 May 28	40	160	yes
2MASS J16104202-2101319	debris/ev. trans.	K5	8.56 ± 0.03	139 (-1, +1)	0.17 ± 0.12
2MASS J16104636-1840598	primordial	M4.5	11.27 ± 0.02	143 (-3, +3)	1.78 ± 0.16	2015 May 28	40	160	no
2MASS J16111330-2019029	primordial	M3	9.56 ± 0.03	155 (-1, +2)	4.88 ± 0.16	2013 May 31	40	120	yes
2MASS J16111534-1757214	primordial	M1	9.20 ± 0.02	136 (-1, +1)	0.18 ± 0.16
2MASS J16111705-2213085	primordial	M5	10.58 ± 0.02	146 (-3, +3)	...	2013 May 31	60	120	no
2MASS J16112057-1820549	debris/ev. trans.	K5	8.56 ± 0.02	136 (-1, +1)	-0.06 ± 0.16
2MASS J16113134-1838259	primordial	K5	5.78 ± 0.02	127 (-2, +2)	903.56 ± 0.85
2MASS J16115091-2012098	primordial	M3.5	10.40 ± 0.02	152 (-4, +4)	0.66 ± 0.16	2013 May 31	40	120	yes
2MASS J16122737-2009596	primordial	M4.5	11.54 ± 0.02	147 (-4, +4)	0.53 ± 0.16	2015 May 28	40	160	no
2MASS J16123916-1859284	primordial	M0.5	9.11 ± 0.03	139 (-2, +2)	6.01 ± 0.29	2013 May 31	40	120	yes
2MASS J16124893-1800525 ^h	debris/ev. trans.	M3	10.36 ± 0.02	158 (-2, +2)	0.11 ± 0.16	2015 May 28	60	160	no
2MASS J16125533-2319456	debris/ev. trans.	G2	7.29 ± 0.02	151 (-1, +1)	0.08 ± 0.13	2015 May 28	40	160	yes
2MASS J16130996-1904269	primordial	M4	10.58 ± 0.02	137 (-2, +2)	-0.05 ± 0.16	2013 May 31	60	120	no
2MASS J16133650-2503473	primordial	M3.5	10.26 ± 0.02	145 (-11, +11)	0.88 ± 0.19	2013 May 30	30	...	no
2MASS J16135434-2320342	primordial	M4.5	10.06 ± 0.02	145 (-11, +11)	7.53 ± 0.13	2013 May 31	30	...	no
2MASS J16141107-2305362	primordial	K2	7.46 ± 0.03	145 (-11, +11)	4.77 ± 0.14
2MASS J16142029-1906481	primordial	M0	7.81 ± 0.03	142 (-2, +3)	40.69 ± 0.22
2MASS J16142893-1857224	debris/ev. trans.	M2.5	9.47 ± 0.02	141 (-2, +2)	0.10 ± 0.16	2015 May 28	40	160	yes
2MASS J16143367-1900133	primordial	M3	8.26 ± 0.02	141 (-2, +2)	1.24 ± 0.16	2013 May 31	40	120	yes
2MASS J16145918-2750230	debris/ev. trans.	G8	8.69 ± 0.02	145 (-11, +11)	0.03 ± 0.19	2015 May 28	40	160	yes
2MASS J16145928-2459308	primordial	M4.25	11.09 ± 0.02	158 (-3, +3)	-0.03 ± 0.12	2013 May 30	100	...	no
2MASS J16151239-2420091	primordial	M4	12.13 ± 0.02	153 (-3, +3)	0.22 ± 0.12	2013 May 30	60	...	no
2MASS J16153456-2242421	primordial	M0	7.91 ± 0.02	139 (-1, +1)	11.75 ± 0.12
2MASS J16154416-1921171	primordial	K5	8.40 ± 0.02	131 (-2, +2)	23.57 ± 0.16	2013 May 31	40	120	yes

Table 5.1: Upper Sco Disk Sample

Source	Disk Type	Spectral Type	K (mag)	Distance ^a (pc)	$S_{0.88\text{mm}}$ ^b (mJy)	Observation Epoch ^c	Total Int. Time (s)		Coronagraph?
							Imaging	Masking ^d	
2MASS J16163345-2521505	primordial	M0.5	10.13 ± 0.02	162 (-1, +1)	2.88 ± 0.30	2013 May 31	40	120	yes
2MASS J16181618-2619080	primordial	M4.5	10.94 ± 0.02	145 (-11, +11)	-0.07 ± 0.12
2MASS J16181904-2028479	primordial	M4.75	10.96 ± 0.02	137 (-2, +2)	4.62 ± 0.12	2013 May 30	60	...	no
2MASS J16215466-2043091	debris/ev. trans.	K7	9.15 ± 0.02	109 (-1, +1)	0.49 ± 0.12
2MASS J16220961-1953005	debris/ev. trans.	M3.7	8.90 ± 0.02	138 (-2, +2)	0.07 ± 0.16	2015 May 28	60	...	no
2MASS J16230783-2300596	debris/ev. trans.	K3.5	8.18 ± 0.02	139 (-1, +1)	-0.35 ± 0.12
2MASS J16235385-2946401	debris/ev. trans.	G2.5	7.65 ± 0.02	134 (-1, +1)	0.11 ± 0.12	2015 May 28	40	160	yes
2MASS J16270942-2148457	primordial	M4.5	11.71 ± 0.02	140 (-3, +3)	2.87 ± 0.12	2015 May 27	20	160	no
2MASS J16294879-2137086	primordial	M5	11.52 ± 0.02	131 (-7, +7)	...	2013 May 31	60	120	no
2MASS J16303390-2428062	primordial	M4	10.36 ± 0.02	150 (-3, +3)	0.60 ± 0.12	2013 May 30	40	...	yes
2MASS J16310240-2408431	primordial	M5	10.79 ± 0.03	136 (-2, +2)	...	2013 May 30	60	...	no

^a Distances from Bailer-Jones et al. (2018). When no such distance was available, the mean and standard deviation of the rest of the sample, 145 ± 11 pc, were used.

^b 0.88 mm continuum flux density measured by Barenfeld et al. (2016). Ellipses indicate sources not observed with ALMA.

^c Ellipses indicate source with previous observation, summarized in Table 5.2.

^d Ellipses in only this column indicate sources for which masking observations were not obtained due to the presence of a visual companion seen during observations.

^e Poor tip-tilt correction as discussed in Section 5.2.

^f Target not visible in images as discussed in Section 5.2.

Twenty-seven systems in our sample have already been surveyed for stellar companions. These systems are listed in Table 5.2, along with the properties of any known companions. We obtained adaptive optics (AO) imaging and aperture masking observations of the remaining 86 stars using the NIRC2 AO imager (instrument PI: Keith Matthews) on the 10 m Keck II telescope. Targets were observed on the nights of 2011 May 15, 2013 May 30-31, 2015 May 27-28. Sources brighter than $R = 13.5$ were observed using natural guide star tip-tilt correction. Otherwise, a laser guide star was used (Wizinowich et al. 2006).

Based on the Kraus et al. (2008) multiplicity survey of Upper Sco systems without disks identified by Luhman and Mamajek (2012), we expected to detect stellar companions at separations ranging from tens of milliarcseconds to several arcseconds. This range of separations can be probed using a combination of AO imaging, able to detect medium and wide separation companions, and nonredundant aperture masking, which achieves deeper contrast limits than AO imaging within a few hundred milliarcseconds. We thus observed our sample with both techniques using NIRC2. Our observing procedure for each of these techniques is described below.

Table 5.2: Results from Previous Surveys

Primary	Separation ^a (mas)	ΔK ^b (mag)	K_{comp} ^c (mag)	Position Angle ^d (deg)	Reference
2MASS J15354856-2958551	844 ± 3	0.09 ± 0.08	9.55 ± 0.10	254.40 ± 0.03	Köhler et al. (2000)
2MASS J15583692-2257153	Kraus et al. (2008)
2MASS J16001330-2418106	Kraus et al. (2008)
2MASS J16014086-2258103	706 ± 1	0.84 ± 0.03	10.68 ± 0.06	357.5 ^e	Bouy et al. (2006)
2MASS J16020039-2221237	Kraus et al. (2008)
2MASS J16025123-2401574	7198 ± 13	2.91 ± 0.02	11.84 ± 0.06	352.22 ± 0.04	Kraus et al. (2008)
2MASS J16035767-2031055	Kraus et al. (2008)
2MASS J16042165-2130284	Kraus et al. (2008)
2MASS J16062196-1928445	578 ± 3	0.64 ± 0.01	9.26 ± 0.06	148.20 ± 0.03	Köhler et al. (2000)
2MASS J16064385-1908056	Kraus et al. (2008)
2MASS J16070211-2019387	55 ± 2	0.14 ± 0.05	11.54 ± 0.08	271.63 ± 1.08	Kraus and Hillenbrand (2012)
2MASS J16070211-2019387	1483 ± 2	0.85 ± 0.03	12.25 ± 0.07	242.05 ± 0.05	Kraus and Hillenbrand (2012)
2MASS J16082324-1930009	Kraus et al. (2008)
2MASS J16090075-1908526	Kraus et al. (2008)
2MASS J16094098-2217594	Kraus et al. (2008)
2MASS J16095441-1906551	Kraus et al. (2008)
2MASS J16102174-1904067	4606 ± 2	2.48 ± 0.03	12.10 ± 0.06	6.71 ± 0.03	Kraus et al. (2008)
2MASS J16102857-1904469	299 ± 3	0.42 ± 0.04	9.13 ± 0.07	84.1 ± 0.3	Köhler et al. (2000)
2MASS J16104202-2101319	Kraus et al. (2008)
2MASS J16111534-1757214	Kraus et al. (2008)
2MASS J16112057-1820549	Kraus et al. (2008)
2MASS J16113134-1838259	1310 ^e	0.91 ± 0.12	6.72 ± 0.13	213 ^e	Eisner et al. (2005)
2MASS J16141107-2305362	222 ± 3	0.21 ± 0.10	7.67 ± 0.12	304.76 ± 0.41	Metchev and Hillenbrand (2009)
2MASS J16142029-1906481	Lafrenière et al. (2014)
2MASS J16153456-2242421	1907 ± 3	1.19 ± 0.01	9.09 ± 0.05	338.81 ± 0.03	Kraus et al. (2008)
2MASS J16181618-2619080	147 ± 3	0.12 ± 0.03	11.08 ± 0.06	192.3 ^e	Bouy et al. (2006)
2MASS J16215466-2043091	Kraus et al. (2008)
2MASS J16230783-2300596	Kraus et al. (2008)

^a Ellipses indicate single stars. Contrast limits quoted by the previous studies, shown in Figure 5.8 and listed in Table 5.4, are comparable to the current survey.

^b Difference in K magnitude between primary and companion.

^c K magnitude of companion.

^d Position angle is defined east of north.

^e Uncertainties not provided by authors.

Imaging Observations

Our imaging observations are summarized in Table 5.1. For targets observed in 2013 and 2015, we acquired two 10 s AO images using either the K' or K_c filter on NIRC2. Targets with a Two Micron All Sky Survey (2MASS, Cutri et al. 2003; Skrutskie et al. 2006) magnitude brighter than $K_s = 8.3$ were observed using the K_c filter to prevent saturation. A third 10 s image was obtained of targets with a visually identifiable companion. If no such companion was seen, we obtained two further frames of 20 s AO images with the K' filter. These additional frames used a 600 mas diameter coronagraph for targets brighter than 2MASS $K_s = 10.6$ that would be partially visible behind the semi-transparent coronagraph. Fainter targets

were observed without the coronagraph, allowing us to easily determine primary positions when calculating companion separations. Due to unknown errors during observations, the two initial 10 s images were not saved on the nights of 2015 May 27-28, reducing the total integration times shown in Table 5.1. To avoid saturation in the initial and follow-up frames, we used shorter exposure times that were coadded to give the final 10 and 20 s frames. The exposure time per coadd was set based on the 2MASS K_s magnitude of the target and the number of coadds was chosen to give total integration times of 10 or 20 s, respectively. Four targets, 2MASS J16070873-1927341, 2MASS J16071971-2020555, 2MASS J16073939-1917472, and 2MASS J16101473-1919095, were observed on 2011 May 15 as part of a separate program. For these targets, ten frames of nine seconds each were obtained using the K' filter without a coronagraph in place.

On the observing night of 2015 May 28, tip-tilt errors caused a number of targets to appear blurred in the images. For five of these sources, good quality observations from the previous night were available. For six sources, 2MASS J16020287-2236139, 2MASS J16050231-1941554, 2MASS J16052459-1954419, 2MASS J16064102-2455489, 2MASS J16103956-1916524, and 2MASS J16124893-1800525, there is only data with poor tip-tilt correction. Despite these lower-quality data, we were still able to obtain useful detection limits for these systems in our comparison with other surveys (see Section 5.4). For unknown reasons, 2MASS J16102819-1910444 was not visible in our images during observations. We exclude this source from our sample in the remainder of our analysis.

The NIRC2 Preprocessing and Vortex Image Processing (VIP) packages² (Gomez Gonzalez et al. 2017) were used to reduce the imaging observations. This included flat fielding, dark subtraction, and bad pixel removal, as well as centering and de-rotation to align and stack individual frames for each target. High-order distortion corrections were applied using the solutions of Yelda et al. (2010) for the 2011 and 2013 data and the updated solutions of Service et al. (2016) for the 2015 data.

Nonredundant Aperture Masking Observations

Nonredundant aperture masking observations were obtained if no obvious companion was revealed in the initial 10 s images. We used a nine-hole mask with baselines ranging from 1.67-8.27 m. Images were read from a 512×512 pixel sub-array of the ALADDIN detector using multiple-correlated double sampling. We obtained

²<https://github.com/vortex-exoplanet/VIP>

six 20 s frames for each target observed in 2013, eight such frames for each target in 2015, and between 40 and 70 frames in 2011. Total integration times are given for each source in Table 5.1. Depending on the brightness of the target, either 8, 16, or 64 endpoint reads were used along with coadds with shorter integration times in order to avoid saturation.

Reduction of the aperture masking observations followed the procedure described in Kraus et al. (2008; see also Pravdo et al. 2006, Lloyd et al. 2006, Martinache et al. 2007, Kraus et al. 2011).³ After dark-subtracting and flat-fielding, remaining bad pixels were removed from each frame. Frames were then spatially filtered using a super-Gaussian function of the form $\exp(-kx^4)$ to further reduce read noise. Complex visibilities were extracted from Fourier transforms of the filtered frames. To remove non-common path errors within the telescope and instrument, the data were calibrated using frames of Upper Sco targets that we determined were single. Observations on the night of 2015 May 27 were taken with the telescope in position angle mode rather than vertical angle mode, causing the orientation of the nine-hole mask to change throughout the night and making this calibration more difficult. This led to shallower detection limits for these targets than those observed in vertical angle mode on other nights.

5.3 Candidate Companion Identification

In this section we present how candidate companions were identified. We first describe the identification of astrophysical sources in our imaging and aperture masking data. We then discuss how the brightnesses and separations of these sources were used to determine whether or not they are likely to be physically-associated companions. Finally, we identify potential wide-separation companions using Gaia.

Imaging

Stacked images of each of the 85 Upper Sco targets (excluding 2MASS J16102819-1910444) were searched for potential companions using VIP’s *detection* routine. These images were first convolved with the point spread function (PSF) of the primary star to enhance the signal of any potential companions. A two-dimensional Gaussian was then fit to local maxima of the unsmoothed image to compare the shape of the emission around each maximum to the expected PSF. For fits that

³Reduction and analysis of the masking data were performed using the Sydney code (<https://github.com/mikeireland/idlnrm>).

displayed positive amplitude, had a center within two pixels of the location of the maximum, and had a full width at half maximum (FWHM) within three pixels of the PSF FWHM, the significance of the detection was determined by measuring its signal-to-noise ratio in the unsmoothed image. The signal-to-noise ratio was defined as

$$S/N = \frac{F_{source} - F_{bkg}}{\sigma_{bkg} \sqrt{1 + \frac{1}{n}}}, \quad (5.1)$$

where F_{source} is the integrated flux of the source within one resolution element equal in diameter to the FWHM of the PSF. F_{bkg} and σ_{bkg} are the mean and standard deviation, respectively, of the integrated flux measured in resolution elements around an annulus at the radius of the potential source from the primary star. The number of these resolution elements within the annulus, n , corrects for the small sample statistics introduced by the low number used (Mawet et al. 2014). Using this technique, we found 170 potential sources with a signal-to-noise ratio greater than or equal to five.

Subsequently, each image was inspected by eye to identify any speckles or other artifacts among detected sources that appeared at the same location in images of multiple targets. This inspection also located faint potential sources that the search algorithm missed due to, for example, another bright source or artifact at the same separation from the primary, which would increase the RMS noise at that separation. A total of 119 sources were rejected by this inspection, while ten additional sources were identified.

Principal component analysis (PCA) using VIP was performed to subtract the stellar PSF and speckles from our images and improve our contrast limits (e.g., Amara and Quanz 2012; Soummer, Pueyo, and Larkin 2012). Principal components were constructed from a PSF library composed of frames of other target stars found to be single by the above procedure. PCA was then applied to each target star, with the star itself excluded from the PSF library. We used 13 principal components and a library of 48 reference frames for images taken without the coronagraph. For images taken with the coronagraph, we used seven principal components and a library of 14 reference frames. The above companion detection procedure was then repeated on the PSF-subtracted images.

In all, we identified 61 new sources from direct imaging that appear to be astrophysical but may or may not be physically bound to the primaries. These detections are listed in Table 5.3. Relative photometry and astrometry of the sources in these

systems were measured using the Python package *photutils* (Bradley et al. 2016). The relative positions of primary stars and additional sources were derived from two-dimensional Gaussian fits. For targets with poor AO correction, centroids were estimated using a “center of mass” technique that relied on the moments of a subimage around the source or primary. Uncertainties on positions were estimated by measuring source locations in individual frames for each target and taking the maximum difference between any two frames.

Aperture photometry provided the relative fluxes of the primaries and additional sources with an aperture diameter equal to twice the FWHM of the primary. For systems with a detected source within $0''.3$ of the primary, we used PSF-fitting photometry to measure the positions and relative fluxes. PSFs were constructed with the algorithm described in Kraus et al. (2016), which iteratively uses a library of single-star PSFs to generate template binary PSFs.

We estimated backgrounds and uncertainties in our aperture photometry using the mean and standard deviation of 20 apertures around an annulus at the same distance from the target source as the newly detected source. This accounts for both read noise and speckle noise, as well as any light from the primary that is included in our aperture photometry, as any such contamination will be incorporated into our background subtraction and uncertainties. To measure background and uncertainties in the photometry of the primary stars, apertures were randomly positioned in annuli between $2''$ and $2''.5$ from the primary. For 2MASS J15562477-2225552, 2MASS J16020287-2236139, 2MASS J16020757-2257467, 2MASS J16041740-1942287, 2MASS J16054540-2023088, 2MASS J16093558-1828232, and 2MASS J16220961-1953005, where sources lie within this separation range, annuli from $3''.5$ to $4''$ were used.

For our detected sources, photometric calibrations used the 2MASS K_s magnitude of the primary and the ratio of integrated counts between each source and primary. For systems with a source located within the $2''.6$ FWHM of the 2MASS PSF (Skrutskie et al. 2006), we separated out the K_s magnitude attributable only to the primary. In addition to the photometric uncertainties described above, the uncertainties in new source magnitudes include the statistical uncertainty in the 2MASS magnitude of the primary and an assumed uncertainty of 0.05 magnitudes due to K -band variability of the primary (Carpenter, Hillenbrand, and Skrutskie 2001). Since the primary star is saturated in our images of 2MASS J16041740-1942287, 2MASS J16101888-2502325, and 2MASS J16154416-1921171, the K magnitudes of the

additional sources in these systems were determined using other targets observed during the same two-night runs to convert counts to K magnitude. The separations and magnitudes of our newly detected sources are listed in Table 5.3.

Contrast limits are calculated for single stars using VIP's *contrast curve* routine. This routine injects fake companions with a range of separations and contrasts relative to the primary into the stacked, PSF-subtracted frames for each target. The 5σ contrast limit is measured as the contrast of the brightest companion that is recovered with a signal-to-noise ratio of less than five. As above, noise is measured in the annulus at the angular separation of the fake companion using Equation 5.1. Our imaging contrast limits for sources without candidate companions (see Section 5.3) are listed in Table 5.4.

Nonredundant Aperture Masking

Nonredundant aperture masking achieves deeper contrast limits than traditional AO imaging at separations within a few hundred milliarcseconds using closure phases. At these separations, imaging contrast is limited by speckle noise created by atmospheric turbulence. This same turbulence introduces errors in the relative phases of the light reaching pairs of holes in the aperture mask. However, if these relative phases are summed around a triangle of the baselines connecting each pair, phase errors specific to individual holes, such as those due to atmospheric effects, will cancel out (e.g., Lohmann, Weigelt, and Wirtitzer 1983; Readhead et al. 1988). The resulting closure phases can then be used to search for close companions.

To locate companions in the aperture masking data, we adopted the technique used by Kraus et al. (2008). Briefly, χ^2 minimization was used to find the best-fit separation, contrast, and position angle of a potential companion for the closure phases of each target, along with the uncertainties in each of these parameters. The detection sensitivity to companions as a function of separation from the primary star was determined using 10,000 simulated data sets of a single star observed with the same (u,v)-sampling and closure phase errors as the observed data. The same fitting procedure was used to find the brightest detected companion in different annuli in each simulated data set. The detection threshold for each annulus was defined as the contrast ratio above which no potential companions were detected in 99.9% of the simulated data sets. Table 5.3 lists the six companions identified above this threshold. Table 5.4 provides the contrast limits of the remaining targets.

Table 5.3: Newly Detected Sources

Primary Star	Detection Technique	Separation (mas)	ΔK^a (mag)	K_{comp}^a (mag)	Position Angle ^a (deg)	Candidate Companion? ^b
2MASS J15530132-2114135	Imaging	1690.2 ± 11.4	7.13 ± 0.10	18.15 ± 0.11	249.50 ± 0.39	no
2MASS J15534211-2049282	Imaging	321.8 ± 0.1	1.47 ± 0.01	11.55 ± 0.06	254.59 ± 0.02	yes
2MASS J15534211-2049282	Imaging	1097.1 ± 0.1	1.47 ± 0.01	11.55 ± 0.06	68.44 ± 0.01	yes
2MASS J15554883-2512240	Imaging	2306.2 ± 0.8	5.87 ± 0.01	14.17 ± 0.06	353.85 ± 0.02	no
2MASS J15562477-2225552	Imaging	2129.8 ± 18.9	7.79 ± 0.17	18.58 ± 0.18	59.77 ± 0.51	no
2MASS J15570641-2206060	Imaging	4381.7 ± 39.1	6.90 ± 0.08	18.19 ± 0.10	181.63 ± 0.51	no
2MASS J15572986-2258438	Imaging	194.4 ± 1.5	0.26 ± 0.06	12.04 ± 0.08	145.32 ± 0.44	yes
2MASS J16001730-2236504	Masking	43.1 ± 1.4	1.70 ± 0.06	11.64 ± 0.08	290.74 ± 1.22	yes
2MASS J16001730-2236504	Imaging	5347.8 ± 0.2	8.43 ± 0.05	18.37 ± 0.07	140.83 ± 0.01	no
2MASS J16001730-2236504	Imaging	4209.9 ± 0.7	8.73 ± 0.06	18.67 ± 0.08	186.04 ± 0.01	no
2MASS J16001844-2230114	Imaging	142.5 ± 1.5	0.88 ± 0.04	11.68 ± 0.07	251.25 ± 0.60	yes
2MASS J16001844-2230114	Imaging	6173.4 ± 0.4	7.19 ± 0.03	17.99 ± 0.06	317.23 ± 0.01	no
2MASS J16014157-2111380	Imaging	2435.5 ± 29.7	6.70 ± 0.21	18.38 ± 0.22	334.91 ± 0.70	no
2MASS J16020287-2236139	Imaging	2438.1 ± 2.7	0.90 ± 0.01	12.91 ± 0.06	94.21 ± 0.06	no
2MASS J16020757-2257467	Imaging	3280.4 ± 0.5	6.57 ± 0.01	16.43 ± 0.06	343.01 ± 0.01	no
2MASS J16020757-2257467	Imaging	2483.0 ± 0.9	7.45 ± 0.02	17.31 ± 0.06	163.85 ± 0.02	no
2MASS J16030161-2207523	Imaging	5378.5 ± 0.6	4.61 ± 0.02	16.34 ± 0.06	49.60 ± 0.01	no
2MASS J16032225-2413111	Imaging	5048.7 ± 0.6	6.21 ± 0.01	16.22 ± 0.05	58.11 ± 0.01	no
2MASS J16032225-2413111	Imaging	3145.3 ± 7.2	10.12 ± 0.25	20.13 ± 0.26	231.83 ± 0.13	no
2MASS J16033471-1829303	Imaging	62.7 ± 1.6	0.08 ± 0.05	12.11 ± 0.08	158.64 ± 1.35	yes
2MASS J16035793-1942108	Imaging	6034.5 ± 16.3	9.17 ± 0.16	19.49 ± 0.17	251.75 ± 0.15	no
2MASS J16041740-1942287	Imaging	4978.9 ± 17.2	1.03 ± 0.24	11.45 ± 0.23	353.22 ± 0.20	no
2MASS J16041740-1942287	Imaging	2158.9 ± 3.1	8.42 ± 0.27	18.84 ± 0.26	114.32 ± 0.08	no
2MASS J16043916-1942459	Masking	25.4 ± 0.4	0.15 ± 0.04	10.94 ± 0.07	42.10 ± 1.40	yes
2MASS J16052556-2035397	Imaging	534.9 ± 1.6	0.97 ± 0.01	12.63 ± 0.06	350.02 ± 0.16	yes
2MASS J16052556-2035397	Imaging	94.5 ± 1.9	1.13 ± 0.02	12.80 ± 0.06	81.65 ± 1.77	yes
2MASS J16052661-1957050	Imaging	356.6 ± 0.3	0.19 ± 0.01	11.54 ± 0.06	88.77 ± 0.05	yes
2MASS J16054540-2023088	Imaging	2038.9 ± 1.0	3.03 ± 0.01	13.51 ± 0.06	48.24 ± 0.03	no
2MASS J16054540-2023088	Imaging	1529.2 ± 1.9	7.05 ± 0.09	17.53 ± 0.10	143.01 ± 0.07	no
2MASS J16060061-1957114	Imaging	1079.9 ± 0.4	0.05 ± 0.01	11.22 ± 0.06	139.76 ± 0.02	yes
2MASS J16062277-2011243	Imaging	5712.0 ± 51.8	5.74 ± 0.02	16.74 ± 0.06	7.54 ± 0.52	no
2MASS J16063539-2516510	Imaging	4995.5 ± 6.3	5.95 ± 0.04	17.66 ± 0.07	152.29 ± 0.07	no
2MASS J16070014-2033092	Imaging	3055.1 ± 1.7	8.15 ± 0.03	18.09 ± 0.06	28.96 ± 0.03	no
2MASS J16070873-1927341	Masking	19.3 ± 0.7	0.27 ± 0.10	11.44 ± 0.11	289.13 ± 2.73	yes
2MASS J16072747-2059442	Imaging	566.6 ± 1.2	0.12 ± 0.01	11.03 ± 0.05	112.56 ± 0.12	yes
2MASS J16075796-2040087	Masking	31.9 ± 3.7	2.14 ± 0.24	9.95 ± 0.25	357.53 ± 2.65	yes
2MASS J16080555-2218070	Masking	25.5 ± 1.3	1.20 ± 0.20	11.05 ± 0.21	24.40 ± 2.20	yes
2MASS J16080555-2218070	Imaging	4770.1 ± 1.5	6.33 ± 0.01	16.19 ± 0.05	291.05 ± 0.02	no
2MASS J16082733-2217292	Imaging	3119.5 ± 2.5	7.28 ± 0.02	17.86 ± 0.06	315.01 ± 0.05	no
2MASS J16082751-1949047	Imaging	183.0 ± 1.6	0.02 ± 0.01	11.36 ± 0.05	20.25 ± 0.47	yes
2MASS J16082870-2137198	Imaging	2665.3 ± 22.8	8.27 ± 0.21	19.03 ± 0.22	350.28 ± 0.49	no
2MASS J16093558-1828232	Imaging	2130.7 ± 6.4	8.08 ± 0.10	18.78 ± 0.11	81.59 ± 0.17	no
2MASS J16095361-1754474	Imaging	4321.0 ± 53.2	7.99 ± 0.22	19.52 ± 0.22	156.51 ± 0.70	no
2MASS J16095933-1800090	Imaging	3691.8 ± 0.2	7.44 ± 0.02	17.78 ± 0.06	150.03 ± 0.01	no
2MASS J16101888-2502325	Imaging	4896.5 ± 2.0	0.11 ± 0.13	11.38 ± 0.11	241.10 ± 0.02	no
2MASS J16103956-1916524	Imaging	1026.7 ± 0.6	5.42 ± 0.14	15.69 ± 0.15	168.04 ± 0.03	no
2MASS J16111330-2019029	Imaging	3790.7 ± 0.8	7.52 ± 0.01	17.07 ± 0.06	4.38 ± 0.01	no
2MASS J16115091-2012098	Imaging	1094.2 ± 0.1	5.67 ± 0.01	16.07 ± 0.06	230.79 ± 0.01	no
2MASS J16115091-2012098	Imaging	2112.6 ± 1.7	9.05 ± 0.14	19.45 ± 0.15	169.89 ± 0.05	no
2MASS J16122737-2009596	Imaging	4285.3 ± 0.3	3.25 ± 0.01	14.78 ± 0.06	9.98 ± 0.01	no
2MASS J16124893-1800525	Imaging	3161.9 ± 2.2	2.99 ± 0.02	13.35 ± 0.06	10.82 ± 0.04	no

Table 5.3: Newly Detected Sources

Primary Star	Detection Technique	Separation (mas)	ΔK^a (mag)	K_{comp}^a (mag)	Position Angle ^a (deg)	Candidate Companion? ^b
2MASS J16133650-2503473	Imaging	138.4 ± 1.8	0.26 ± 0.01	11.14 ± 0.05	29.53 ± 0.66	yes
2MASS J16135434-2320342	Imaging	617.7 ± 0.1	0.54 ± 0.01	11.11 ± 0.06	108.26 ± 0.01	yes
2MASS J16142893-1857224	Masking	37.0 ± 1.3	1.69 ± 0.06	11.16 ± 0.08	256.50 ± 1.20	yes
2MASS J16145918-2750230	Imaging	3803.2 ± 2.1	9.73 ± 0.06	18.41 ± 0.08	151.08 ± 0.03	no
2MASS J16145928-2459308	Imaging	4283.6 ± 19.8	5.91 ± 0.02	16.99 ± 0.06	16.20 ± 0.50	no
2MASS J16145928-2459308	Imaging	4682.2 ± 40.9	7.39 ± 0.07	18.48 ± 0.09	151.41 ± 0.26	no
2MASS J16154416-1921171	Imaging	2993.7 ± 0.7	9.98 ± 0.16	18.38 ± 0.15	176.20 ± 0.01	no
2MASS J16220961-1953005	Imaging	1790.9 ± 0.8	2.90 ± 0.01	11.87 ± 0.06	225.30 ± 0.12	yes
2MASS J16220961-1953005	Imaging	2880.5 ± 0.1	4.48 ± 0.01	13.45 ± 0.06	359.90 ± 0.01	no
2MASS J16220961-1953005	Imaging	1572.4 ± 3.2	7.28 ± 0.14	16.25 ± 0.15	112.99 ± 0.03	no
2MASS J16235385-2946401	Imaging	5890.3 ± 5.5	7.07 ± 0.34	14.73 ± 0.34	9.68 ± 0.05	no
2MASS J16235385-2946401	Imaging	4888.5 ± 11.9	7.13 ± 0.37	14.78 ± 0.38	13.83 ± 0.14	no
2MASS J16303390-2428062	Imaging	3409.2 ± 0.4	7.00 ± 0.03	17.36 ± 0.06	234.41 ± 0.01	no
2MASS J16303390-2428062	Imaging	4290.7 ± 4.4	7.47 ± 0.05	17.83 ± 0.08	146.75 ± 0.06	no
2MASS J16303390-2428062	Imaging	5177.7 ± 1.6	8.53 ± 0.16	18.89 ± 0.17	120.86 ± 0.02	no
2MASS J16310240-2408431	Imaging	3347.8 ± 11.0	6.45 ± 0.05	17.24 ± 0.08	318.22 ± 0.19	no

^a ΔK , K_{comp} , and Position Angle are defined as in Table 5.2.

^b Sources are considered to be candidate companions if they satisfy $K_{\text{comp}} < 15$ and separation $< 2''$.

Table 5.4: Contrast Limits for Systems without Detected Companions

Primary	Technique	ΔK^a								
		10-20	20-40	40-80	80-160	160-240	240-320	320-500	500-1000	>1000
2MASS J15514032-2146103	Imaging	1.72	3.39	4.64	7.48	6.97	8.12	8.41
2MASS J15514032-2146103	Coronagraph
2MASS J15514032-2146103	Masking	0.00	2.34	3.56	3.22	2.55	1.13
2MASS J15521088-2125372	Imaging	0.75	2.24	4.27	4.39	5.98	6.45
2MASS J15521088-2125372	Coronagraph
2MASS J15521088-2125372	Masking	0.00	0.00	0.00	0.00	0.00	0.00
2MASS J15530132-2114135	Imaging	0.81	3.27	4.45	7.33	6.88	7.78	8.26
2MASS J15530132-2114135	Coronagraph
2MASS J15530132-2114135	Masking	0.00	1.42	2.84	2.45	1.75	0.31
2MASS J15551704-2322165	Imaging	1.50	2.96	3.92	5.01	5.93	7.77	8.15
2MASS J15551704-2322165	Coronagraph	7.25	8.86	11.34
2MASS J15551704-2322165	Masking	0.00	0.00	0.33	0.10	0.00	0.00
2MASS J15554883-2512240	Imaging	2.66	3.63	4.42	5.86	6.29	7.03	7.21
2MASS J15554883-2512240	Coronagraph	4.62	5.95	9.02
2MASS J15554883-2512240	Masking	0.00	2.83	3.91	3.60	3.04	1.79
2MASS J15562477-2225552	Imaging	1.57	3.23	4.47	7.77	7.10	8.09	8.39
2MASS J15562477-2225552	Coronagraph
2MASS J15562477-2225552	Masking	0.00	1.76	3.10	2.73	2.03	0.54
2MASS J15570641-2206060	Imaging	1.35	2.99	4.34	3.20	7.28	8.43	8.70
2MASS J15570641-2206060	Coronagraph
2MASS J15570641-2206060	Masking	0.55	3.61	4.66	4.42	3.79	2.72
2MASS J15581270-2328364	Imaging	2.50	3.48	4.34	6.38	6.34	7.59	8.02
2MASS J15581270-2328364	Coronagraph	0.65	5.59	9.39
2MASS J15581270-2328364	Masking	3.12	4.93	5.77	5.67	5.42	5.02
2MASS J15582981-2310077	Imaging	1.64	3.21	4.33	5.48	6.89	8.04	8.41
2MASS J15582981-2310077	Coronagraph	6.75	7.52	7.89
2MASS J15582981-2310077	Masking	0.00	1.51	2.91	2.53	1.84	0.40
2MASS J15583692-2257153	Imaging	4.00	5.00	10.00

Table 5.4: Contrast Limits for Systems without Detected Companions

Primary	Technique	ΔK^a								
		10-20	20-40	40-80	80-160	160-240	240-320	320-500	500-1000	>1000
2MASS J15583692-2257153	Coronagraph
2MASS J15583692-2257153	Masking	...	3.49	5.06	5.43	5.35
2MASS J15584772-1757595	Imaging	2.27	3.26	4.15	5.59	6.58	7.07	7.31
2MASS J15584772-1757595	Coronagraph	1.20	5.69	9.38
2MASS J15584772-1757595	Masking	...	3.12	4.71	5.03	4.97
2MASS J16001330-2418106	Imaging	4.00	5.00	7.00
2MASS J16001330-2418106	Coronagraph
2MASS J16001330-2418106	Masking	2.72	4.55	5.27	5.18	4.80	4.26
2MASS J16014157-2111380	Imaging	0.14	1.31	2.92	4.32	6.03	6.71
2MASS J16014157-2111380	Coronagraph
2MASS J16014157-2111380	Masking	0.00	2.61	3.65	3.45	2.73	1.29
2MASS J16020039-2221237	Imaging	4.00	5.00	8.00
2MASS J16020039-2221237	Coronagraph
2MASS J16020039-2221237	Masking	0.45	3.46	4.46	4.32	4.21	4.10
2MASS J16020287-2236139	Imaging	0.00	0.82	2.50	3.58
2MASS J16020287-2236139	Coronagraph
2MASS J16020287-2236139	Masking
2MASS J16020757-2257467	Imaging	1.87	3.67	4.92	7.62	7.46	7.76	7.97
2MASS J16020757-2257467	Coronagraph	7.81	8.52	10.47
2MASS J16020757-2257467	Masking	0.79	3.83	4.77	4.49	3.93	2.79
2MASS J16024152-2138245	Imaging	0.36	1.82	2.91	5.30	6.96	7.53
2MASS J16024152-2138245	Coronagraph
2MASS J16024152-2138245	Masking	0.00	2.19	3.43	3.22	2.48	0.79
2MASS J16025123-2401574	Imaging	1.57	3.08	4.25	6.13	6.39	7.79	8.33
2MASS J16025123-2401574	Coronagraph	7.70	8.97	11.72
2MASS J16025123-2401574	Masking	...	2.52	4.08	4.58	4.50
2MASS J16030161-2207523	Imaging	0.70	2.38	3.56	5.75	5.58	7.51	8.03
2MASS J16030161-2207523	Coronagraph
2MASS J16030161-2207523	Masking	0.00	0.58	2.10	1.61	0.63	0.00
2MASS J16031329-2112569	Imaging	1.34	2.84	4.02	5.99	5.98	7.57	8.29
2MASS J16031329-2112569	Coronagraph
2MASS J16031329-2112569	Masking	0.00	0.58	2.09	1.60	0.63	0.00
2MASS J16032225-2413111	Imaging	1.72	3.32	4.30	4.59	6.88	8.08	8.12
2MASS J16032225-2413111	Coronagraph	7.17	8.52	10.47
2MASS J16032225-2413111	Masking	0.40	3.42	4.40	4.17	3.59	2.41
2MASS J16035767-2031055	Imaging	4.00	5.00	9.00
2MASS J16035767-2031055	Coronagraph
2MASS J16035767-2031055	Masking	...	2.86	4.45	4.94	4.86
2MASS J16035793-1942108	Imaging	1.69	3.16	4.03	4.00	6.28	6.55	6.65
2MASS J16035793-1942108	Coronagraph	6.91	8.48	10.19
2MASS J16035793-1942108	Masking	0.05	2.99	4.07	3.76	3.18	1.92
2MASS J16041740-1942287	Imaging	0.90	2.41	4.37	5.65	7.63	7.77
2MASS J16041740-1942287	Coronagraph
2MASS J16041740-1942287	Masking
2MASS J16042165-2130284	Imaging	4.00	5.00	8.00
2MASS J16042165-2130284	Coronagraph
2MASS J16042165-2130284	Masking	3.57	5.43	6.23	6.15	5.79	5.50
2MASS J16050231-1941554	Imaging	0.01	0.45	2.67	3.66	5.05
2MASS J16050231-1941554	Coronagraph
2MASS J16050231-1941554	Masking
2MASS J16052459-1954419	Imaging	0.00	1.67	3.41	5.18

Table 5.4: Contrast Limits for Systems without Detected Companions

Primary	Technique	ΔK^a								
		10-20	20-40	40-80	80-160	160-240	240-320	320-500	500-1000	>1000
2MASS J16052459-1954419	Coronagraph
2MASS J16052459-1954419	Masking
2MASS J16053215-1933159	Imaging	1.52	2.95	3.87	5.26	6.93	8.11	8.59
2MASS J16053215-1933159	Coronagraph
2MASS J16053215-1933159	Masking	0.04	2.99	4.07	3.76	3.17	1.95
2MASS J16054540-2023088	Imaging	0.54	2.11	3.35	5.04	5.90	7.33	7.88
2MASS J16054540-2023088	Coronagraph
2MASS J16054540-2023088	Masking
2MASS J16055863-1949029	Imaging	0.98	2.52	4.47	5.33	6.91	7.41
2MASS J16055863-1949029	Coronagraph	5.52	7.29	8.84
2MASS J16055863-1949029	Masking	0.00	1.12	2.66	2.32	1.55	0.13
2MASS J16061144-1935405	Imaging	0.62	2.27	3.55	6.04	6.58	7.72	7.91
2MASS J16061144-1935405	Coronagraph
2MASS J16061144-1935405	Masking	0.00	2.92	4.06	3.73	3.15	1.83
2MASS J16061330-2212537	Imaging	0.83	2.70	4.23	6.37	6.08	7.87	8.22
2MASS J16061330-2212537	Coronagraph	7.51	9.41	10.81
2MASS J16061330-2212537	Masking
2MASS J16062277-2011243	Imaging	1.62	3.20	4.47	6.52	7.41	8.42	8.39
2MASS J16062277-2011243	Coronagraph
2MASS J16062277-2011243	Masking	1.15	4.01	5.12	4.87	4.29	3.24
2MASS J16063539-2516510	Imaging	0.61	2.19	3.4	6.13	7.02	7.53	7.87
2MASS J16063539-2516510	Coronagraph
2MASS J16063539-2516510	Masking	0.00	2.27	3.46	3.13	2.49	1.02
2MASS J16064102-2455489	Imaging	0.05	0.81	2.90	4.00	5.13
2MASS J16064102-2455489	Coronagraph
2MASS J16064102-2455489	Masking	0.00	0.39	1.75	1.35	0.47	0.00
2MASS J16064115-2517044	Imaging	2.03	3.63	4.86	6.87	7.10	8.25	8.57
2MASS J16064115-2517044	Coronagraph
2MASS J16064115-2517044	Masking	0.00	2.56	3.65	3.42	2.76	1.26
2MASS J16064385-1908056	Imaging	4.00	5.00	8.00
2MASS J16064385-1908056	Coronagraph
2MASS J16064385-1908056	Masking
2MASS J16070014-2033092	Imaging	2.03	3.83	5.46	9.66	7.66	7.72	7.87
2MASS J16070014-2033092	Coronagraph	7.53	8.75	10.81
2MASS J16070014-2033092	Masking	2.28	4.75	5.70	5.50	4.90	3.78
2MASS J16071971-2020555	Imaging	0.00	0.69	2.37	1.40	4.96	6.46	6.80
2MASS J16071971-2020555	Coronagraph
2MASS J16071971-2020555	Masking	0.00	1.71	3.18	2.89	2.24	0.58
2MASS J16072625-2432079	Imaging	1.70	3.14	4.1	6.51	6.89	7.44	7.53
2MASS J16072625-2432079	Coronagraph	6.93	8.36	10.47
2MASS J16072625-2432079	Masking	0.18	3.17	4.18	3.91	3.29	2.07
2MASS J16073939-1917472	Imaging	0.18	1.64	3.14	1.79	5.72	7.49	8.50
2MASS J16073939-1917472	Coronagraph
2MASS J16073939-1917472	Masking	0.93	3.87	4.90	4.66	4.58	4.37
2MASS J16081566-2222199	Imaging	2.47	4.33	5.36	6.58	7.80	8.28	8.52
2MASS J16081566-2222199	Coronagraph	7.77	8.58	10.70
2MASS J16081566-2222199	Masking	0.48	3.53	4.46	4.22	3.59	2.46
2MASS J16082324-1930009	Imaging	4.00	5.00	8.00
2MASS J16082324-1930009	Coronagraph
2MASS J16082324-1930009	Masking	3.79	5.64	6.46	6.35	6.20	5.77
2MASS J16082733-2217292	Imaging	0.03	0.40	0.65	1.06	0.85	6.30	7.15

Table 5.4: Contrast Limits for Systems without Detected Companions

Primary	Technique	ΔK^a								
		10-20	20-40	40-80	80-160	160-240	240-320	320-500	500-1000	>1000
2MASS J16082733-2217292	Coronagraph	7.20	8.83	10.10
2MASS J16082733-2217292	Masking	1.90	3.57	4.99	3.32	7.49	7.97	7.98
2MASS J16082870-2137198	Imaging	1.13	3.14	5.23	7.08	7.44	8.43	8.82
2MASS J16082870-2137198	Coronagraph
2MASS J16082870-2137198	Masking	0.00	2.99	4.34	4.08	3.42	2.24
2MASS J16083455-2211559	Imaging	0.02	0.85	2.99	5.38	6.47
2MASS J16083455-2211559	Coronagraph
2MASS J16083455-2211559	Masking	0.00	2.19	3.65	3.38	2.71	1.21
2MASS J16084894-2400045	Imaging	2.12	3.69	4.77	6.77	7.16	8.31	8.52
2MASS J16084894-2400045	Coronagraph
2MASS J16084894-2400045	Masking	0.64	3.71	4.80	4.53	3.97	2.85
2MASS J16090002-1908368	Imaging	1.91	3.57	4.85	6.72	7.13	8.49	8.67
2MASS J16090002-1908368	Coronagraph
2MASS J16090002-1908368	Masking	0.14	3.12	4.15	3.83	3.25	2.08
2MASS J16090075-1908526	Imaging	4.00	5.00	8.00
2MASS J16090075-1908526	Coronagraph
2MASS J16090075-1908526	Masking	3.81	5.63	6.38	6.33	6.14	5.72
2MASS J16093558-1828232	Imaging	0.99	2.82	4.57	3.48	7.14	8.29	8.83
2MASS J16093558-1828232	Coronagraph
2MASS J16093558-1828232	Masking	0.17	3.16	4.13	3.78	3.19	2.00
2MASS J16094098-2217594	Imaging	4.00	5.00	9.00
2MASS J16094098-2217594	Coronagraph
2MASS J16094098-2217594	Masking	...	2.34	3.93	4.43	4.30
2MASS J16095361-1754474	Imaging	1.69	3.28	4.65	6.86	7.07	8.06	8.18
2MASS J16095361-1754474	Coronagraph
2MASS J16095361-1754474	Masking	0.00	2.73	4.00	3.68	3.11	1.78
2MASS J16095441-1906551	Imaging	4.00	5.00	7.00
2MASS J16095441-1906551	Coronagraph
2MASS J16095441-1906551	Masking	3.59	5.42	6.26	6.09	5.68	4.96
2MASS J16095933-1800090	Imaging	1.17	2.59	3.75	5.76	6.26	7.34	7.67
2MASS J16095933-1800090	Coronagraph	6.86	8.00	9.91
2MASS J16095933-1800090	Masking	0.24	3.24	4.27	3.96	3.38	2.23
2MASS J16101473-1919095	Imaging	0.14	1.59	3.16	1.93	5.98	7.58	8.39
2MASS J16101473-1919095	Coronagraph
2MASS J16101473-1919095	Masking	1.10	4.00	5.02	4.85	4.74	4.59
2MASS J16101888-2502325	Imaging	0.55	2.16	3.38	4.20	6.51	7.55
2MASS J16101888-2502325	Coronagraph
2MASS J16101888-2502325	Masking
2MASS J16102174-1904067	Imaging	4.00	5.00	7.00
2MASS J16102174-1904067	Coronagraph
2MASS J16102174-1904067	Masking	3.22	5.07	5.85	5.72	5.48	4.99
2MASS J16103956-1916524	Imaging	0.00	0.90	2.91	6.06
2MASS J16103956-1916524	Coronagraph	2.77	4.78	7.06
2MASS J16103956-1916524	Masking	0.00	0.00	0.78	0.58	0.00	0.00
2MASS J16104202-2101319	Imaging	4.00	5.00	8.00
2MASS J16104202-2101319	Coronagraph
2MASS J16104202-2101319	Masking	3.23	5.06	5.89	5.80	5.54	5.20
2MASS J16104636-1840598	Imaging	0.02	0.84	2.32	4.00	5.42	6.06
2MASS J16104636-1840598	Coronagraph
2MASS J16104636-1840598	Masking	0.00	1.06	2.62	2.24	1.41	0.13
2MASS J16111330-2019029	Imaging	2.38	5.01	5.75	7.02	7.57	7.89	8.06

Table 5.4: Contrast Limits for Systems without Detected Companions

Primary	Technique	ΔK^a								
		10-20	20-40	40-80	80-160	160-240	240-320	320-500	500-1000	>1000
2MASS J16111330-2019029	Coronagraph	7.53	8.78	10.95
2MASS J16111330-2019029	Masking	1.91	4.48	5.37	5.15	4.55	3.51
2MASS J16111534-1757214	Imaging	4.00	5.00	8.00
2MASS J16111534-1757214	Coronagraph
2MASS J16111534-1757214	Masking	3.80	5.63	6.45	6.31	6.15	5.72
2MASS J16111705-2213085	Imaging	2.26	3.89	4.94	7.03	7.57	8.65	8.98
2MASS J16111705-2213085	Coronagraph
2MASS J16111705-2213085	Masking	0.01	2.94	3.93	3.72	3.04	1.73
2MASS J16112057-1820549	Imaging	4.00	5.00	8.00
2MASS J16112057-1820549	Coronagraph
2MASS J16112057-1820549	Masking	...	3.28	4.86	5.28	5.23
2MASS J16115091-2012098	Imaging	2.21	3.94	5.14	6.72	7.95	7.94	8.00
2MASS J16115091-2012098	Coronagraph	8.08	8.54	10.17
2MASS J16115091-2012098	Masking	0.43	3.43	4.34	4.15	3.50	2.31
2MASS J16122737-2009596	Imaging	0.33	1.76	3.68	4.33	6.00	6.32
2MASS J16122737-2009596	Coronagraph
2MASS J16122737-2009596	Masking	0.00	1.12	2.66	2.32	1.55	0.13
2MASS J16123916-1859284	Imaging	1.58	3.21	5.10	3.57	7.67	7.87	8.25
2MASS J16123916-1859284	Coronagraph	7.55	8.72	11.65
2MASS J16123916-1859284	Masking	2.38	4.83	5.66	5.46	4.86	3.83
2MASS J16124893-1800525	Imaging	0.00	0.88	2.81	5.42
2MASS J16124893-1800525	Coronagraph
2MASS J16124893-1800525	Masking
2MASS J16125533-2319456	Imaging	0.26	1.47	3.16	3.97	4.99	6.08
2MASS J16125533-2319456	Coronagraph	1.66	2.53	6.97
2MASS J16125533-2319456	Masking	0.00	0.00	0.35	0.13	0.00	0.00
2MASS J16130996-1904269	Imaging	0.00	0.23	1.29	3.57	5.88	7.45
2MASS J16130996-1904269	Coronagraph
2MASS J16130996-1904269	Masking	0.00	2.24	3.65	3.37	2.67	1.26
2MASS J16142029-1906481	Imaging	3.09	4.00	4.60	5.80	7.20	10.20
2MASS J16142029-1906481	Coronagraph
2MASS J16142029-1906481	Masking
2MASS J16143367-1900133	Imaging	2.04	3.76	5.08	4.57	8.31	8.19	8.51
2MASS J16143367-1900133	Coronagraph	8.39	8.71	11.83
2MASS J16143367-1900133	Masking	2.69	5.09	5.95	5.75	5.15	4.16
2MASS J16145918-2750230	Imaging	2.74	4.34	5.14	5.84	6.24	7.90	8.49
2MASS J16145918-2750230	Coronagraph	8.04	9.26	11.80
2MASS J16145918-2750230	Masking	0.74	3.82	4.83	4.59	4.11	2.97
2MASS J16145928-2459308	Imaging	1.83	3.39	4.60	3.89	6.27	8.44	8.60
2MASS J16145928-2459308	Coronagraph
2MASS J16145928-2459308	Masking	0.56	3.60	4.60	4.35	3.88	2.90
2MASS J16151239-2420091	Imaging	0.34	1.76	3.05	4.05	6.39	7.21	7.68
2MASS J16151239-2420091	Coronagraph
2MASS J16151239-2420091	Masking	0.00	2.71	3.92	3.60	2.96	1.66
2MASS J16154416-1921171	Imaging	1.00	2.91	4.12	5.91	6.72	8.28	8.73
2MASS J16154416-1921171	Coronagraph	6.75	8.37	11.42
2MASS J16154416-1921171	Masking	2.39	4.83	5.78	5.58	4.92	3.89
2MASS J16163345-2521505	Imaging	2.23	3.99	5.20	7.47	8.18	8.33	8.45
2MASS J16163345-2521505	Coronagraph	8.20	8.74	10.63
2MASS J16163345-2521505	Masking	1.79	4.39	5.27	5.06	4.41	3.43
2MASS J16181904-2028479	Imaging	1.61	3.14	4.37	6.79	7.16	8.01	8.30

Table 5.4: Contrast Limits for Systems without Detected Companions

Primary	Technique	ΔK^a								
		10-20	20-40	40-80	80-160	160-240	240-320	320-500	500-1000	>1000
2MASS J16181904-2028479	Coronagraph
2MASS J16181904-2028479	Masking	0.16	3.14	4.25	3.90	3.35	2.22
2MASS J16215466-2043091	Imaging	4.00	5.00	8.00
2MASS J16215466-2043091	Coronagraph
2MASS J16215466-2043091	Masking	...	1.90	3.52	3.98	3.91
2MASS J16230783-2300596	Imaging	4.00	5.00	9.00
2MASS J16230783-2300596	Coronagraph
2MASS J16230783-2300596	Masking	...	3.31	4.87	5.18	5.08
2MASS J16235385-2946401	Imaging	0.09	0.99	2.05	3.50	4.70	5.40
2MASS J16235385-2946401	Coronagraph	0.91	2.06	6.30
2MASS J16235385-2946401	Masking	0.00	0.00	0.45	0.23	0.00	0.00
2MASS J16270942-2148457	Imaging	0.11	1.53	3.01	3.01	5.41	7.02	7.51
2MASS J16270942-2148457	Coronagraph
2MASS J16270942-2148457	Masking	0.00	0.39	1.75	1.36	0.49	0.00
2MASS J16294879-2137086	Imaging	0.03	0.84	3.59	5.18	6.23
2MASS J16294879-2137086	Coronagraph
2MASS J16294879-2137086	Masking
2MASS J16303390-2428062	Imaging	0.53	2.09	3.37	5.17	6.47	7.13	7.37
2MASS J16303390-2428062	Coronagraph	6.51	7.70	9.39
2MASS J16303390-2428062	Masking	0.00	2.92	3.98	3.66	3.11	1.88
2MASS J16310240-2408431	Imaging	2.37	3.87	4.74	6.41	7.30	8.24	8.51
2MASS J16310240-2408431	Coronagraph
2MASS J16310240-2408431	Masking	0.06	3.01	4.13	3.79	3.24	2.09

^a Separation bins are reported in units of mas and ΔK in units of magnitude.

Selection of Candidate Companions

The sources we detected are not necessarily bound companions to the host star. With only a single epoch of observations, we cannot use common proper motion to rule out the chance alignment of a field star. Instead, we use the brightness and separation of sources to distinguish between field stars and candidate companions. Figure 5.1 shows the K magnitudes and separations of the 67 sources found by imaging and masking and the 12 literature companions listed in Table 5.2. We used the TRILEGAL galactic population models (Girardi et al. 2005) to simulate the population of field stars as a function of K magnitude in the direction of Upper Sco. We find a density of 2.2×10^{-4} field objects per square arcsecond brighter than $K = 15$. For our full sample of 112 targets, we would expect a total of less than one such field star to be within $2''$ of a target star by chance. We therefore consider any sources brighter than $K = 15$ and within $2''$ of a target star likely to be a candidate bound companion. These limits are the same as those used in Kraus et al. (2008) to identify candidate companions in Upper Sco and are shown in Figure 5.1 as dashed lines. Sources that meet these criteria are indicated in the ‘‘Candidate

Companion” column of Table 5.3. For consistency, we apply these criteria to the previously known companions in Table 5.2, even if objects beyond these limits have been confirmed to be associated by other methods.

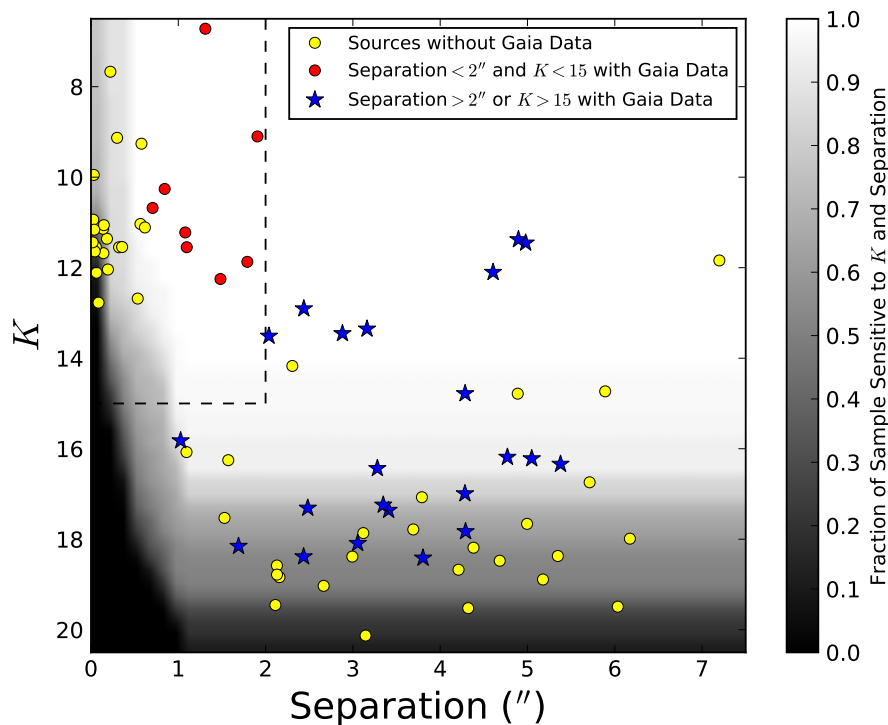


Figure 5.1: Projected separations and K magnitudes of the 79 detected sources around Upper Sco stars with disks. We consider sources within $2''$ and brighter than $K = 15$ to be candidate companions. This region is shown with dashed lines. A number of sources outside these limits may also be physically bound, but we expect significant background contamination among these sources. Red circles show sources that met our bound criteria and for which Gaia data was available, while blue stars show sources with Gaia data that did not meet our criteria. Sources with Gaia data are also shown in Figure 5.2. The yellow circles show sources for which no Gaia data was available. The grayscale background indicates the fraction of primary stars in the sample where the observations are sensitive to each K magnitude and separation.

Figure 5.2 presents the color-magnitude diagram for sources in the Gaia DR2 Catalog (Gaia Collaboration et al. 2016, 2018). The candidate companions that meet our criteria for physical association lie along the same sequence as the primary stars, as would be expected for co-evolutionary companions at the same distance from Earth. The sources that do not meet these criteria include a small number of objects

that match the colors and magnitudes of the candidate companions and primaries. However, the majority of objects outside of our selection criteria are fainter and bluer than the primary star sequence, as would be expected for background field stars. While we cannot rule out that a fraction of sources fainter than $K = 15$ and separated by more than $2''$ are physically associated companions, there is a significant fraction of field objects beyond these limits.

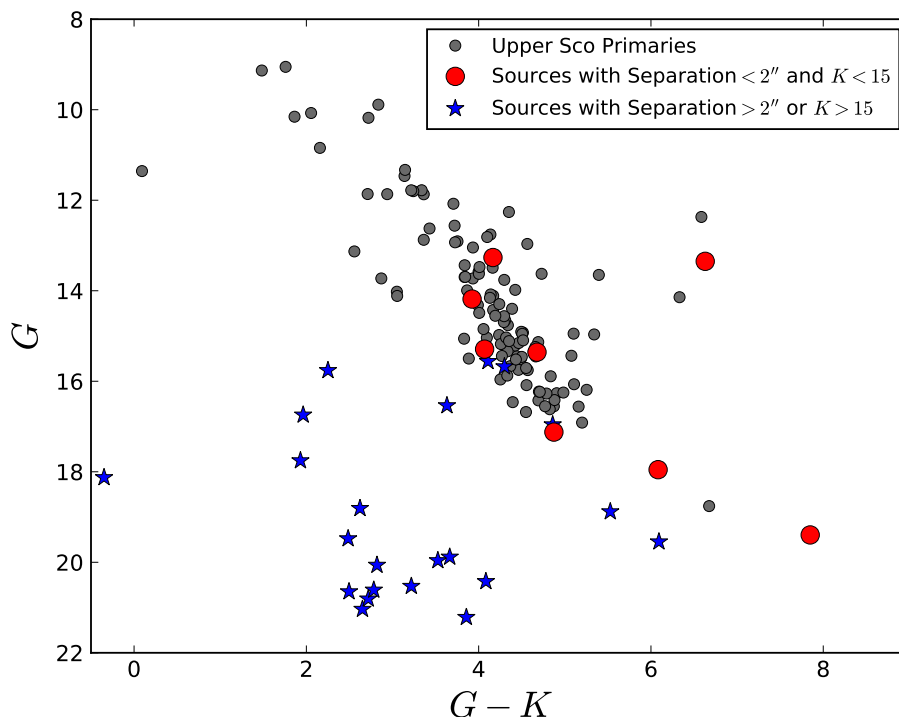


Figure 5.2: Color-magnitude diagram of Upper Sco primaries in our sample (gray points) and additional sources that meet (red circles) and fail to meet (blue stars) our criteria of separation $< 2''$ and $K < 15$ to be considered candidate companions. Sources that meet our criteria lie along the same color-magnitude sequence as the Upper Sco primaries, as expected. Sources outside of these criteria are typically bluer and fainter than this sequence, consistent with background stars.

We note that the sources beyond $2''$ that are fainter than $K \sim 12.5 - 13$ would be candidate brown dwarfs ($M \lesssim 0.08 M_{\odot}$) if they were associated, assuming a distance and age of 145 pc and 5-10 Myr (Chabrier et al. 2000; Baraffe et al. 2002). Similarly, sources fainter than $K \sim 15.5 - 16$ would be potential giant planets ($M \lesssim 13 M_{\text{Jup}}$) if they were bound. While these objects are most likely field stars, they may be worth observing in the future to look for common proper motion.

Candidate Wide Companions with Gaia

To search for potential companions at wider projected separations, we used the Gaia DR2 Catalog to identify any sources within $1'$ of a target star in our Upper Sco disk sample. Figure 5.3 shows the Gaia parallaxes and proper motions of these sources. The majority of sources have parallaxes and proper motions concentrated close to zero, as expected for background objects. For each primary star in the sample, we searched for any additional sources with similar parallax and proper motions that stood out from the background sources. Figure 5.3 shows these candidate wide companions and primaries, which are clearly separated from the main cluster of background objects. These sources, listed in Table 5.5, have parallaxes within three milliarcseconds of their potential primaries and proper motions in right ascension and declination within five milliarcseconds per year.

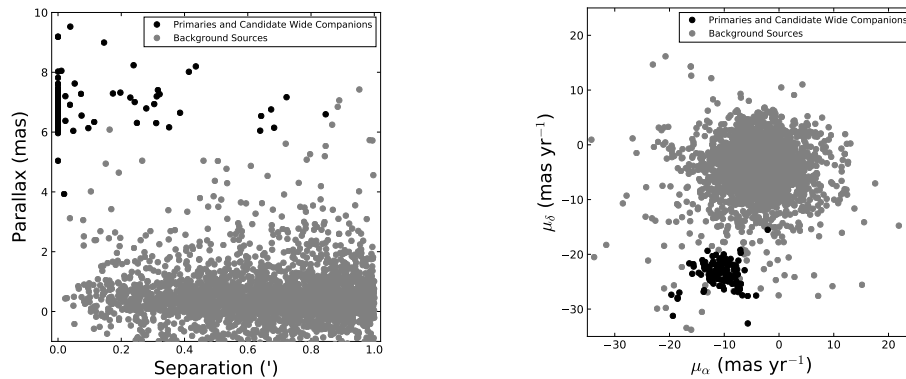


Figure 5.3: Parallaxes (left) and proper motions (right) of all sources in the Gaia DR2 Catalog within $1'$ of the targets in our Upper Sco disk sample. Most sources have parallaxes and proper motions close to zero, as expected for background objects. The black points show the primaries and candidate wide companions. The candidate wide companions have parallaxes and proper motions similar to their primaries and clearly distinct from the background sources.

5.4 Disks and Multiplicity in Upper Sco

In this section, we describe the Upper Sco candidate companions discovered in our survey. We determine the locations of the millimeter disks in these systems relative to the primary and companion(s). We then compare the companion fractions of stars with and without disks in Upper Sco.

Table 5.5: Candidate Wide Companions from Gaia

System	Primary				Companion					
	G (mag)	μ_α (mas yr $^{-1}$)	μ_δ (mas yr $^{-1}$)	Parallax (mas)	Separation ($''$)	Gaia Source Designation	G (mag)	μ_α (mas yr $^{-1}$)	μ_δ (mas yr $^{-1}$)	Parallax (mas)
2MASS J15551704-2322165	8.306 ± 0.001	-18.53 ± 0.12	-28.11 ± 0.07	8.24 ± 0.10	14.8989 ± 0.0807	6237252529183461248	13.491 ± 0.001	-19.66 ± 0.20	-27.38 ± 0.13	8.02 ± 0.11
2MASS J15551704-2322165	8.306 ± 0.001	-18.53 ± 0.12	-28.11 ± 0.07	8.24 ± 0.10	16.3749 ± 0.1173	6237252529183460992	14.150 ± 0.002	-18.20 ± 0.18	-26.98 ± 0.12	8.02 ± 0.09
2MASS J15551704-2322165	8.306 ± 0.001	-18.53 ± 0.12	-28.11 ± 0.07	8.24 ± 0.10	17.9029 ± 0.1522	6237252529178690432	15.393 ± 0.006	-18.51 ± 0.29	-27.91 ± 0.18	8.20 ± 0.14
2MASS J15554883-2512240	10.155 ± 0.002	-15.85 ± 0.10	-23.56 ± 0.06	6.95 ± 0.05	8.8551 ± 0.1552	6235742349962814592	13.918 ± 0.001	-15.59 ± 0.44	-22.23 ± 0.26	8.99 ± 0.22
2MASS J15554883-2512240	10.155 ± 0.002	-15.85 ± 0.10	-23.56 ± 0.06	6.95 ± 0.05	14.5251 ± 0.1366	6235742349962814848	16.898 ± 0.005	-15.64 ± 0.31	-21.79 ± 0.18	7.01 ± 0.16
2MASS J16014086-2258103	14.948 ± 0.019	-8.80 ± 0.26	-24.20 ± 0.12	8.05 ± 0.10	0.6950 ± 0.0936	6243135809748290688	15.357 ± 0.001	-13.77 ± 0.52	-26.85 ± 0.20	9.19 ± 0.43
2MASS J16025123-2401574	11.866 ± 0.003	-11.85 ± 0.12	-24.03 ± 0.05	6.95 ± 0.07	7.2151 ± 0.0837	6236273895118890112	16.364 ± 0.001	-12.70 ± 0.32	-23.87 ± 0.19	6.34 ± 0.20
2MASS J16035767-2031055	12.078 ± 0.003	-11.60 ± 0.08	-22.90 ± 0.04	7.01 ± 0.04	50.2880 ± 0.1497	6244083039015457152	12.298 ± 0.002	-10.51 ± 0.34	-21.64 ± 0.22	6.60 ± 0.22
2MASS J16041740-1942287	14.761 ± 0.002	-9.70 ± 0.19	-21.63 ± 0.09	6.20 ± 0.09	5.4847 ± 0.0888	6247221285718007680	15.561 ± 0.001	-9.13 ± 0.23	-21.16 ± 0.11	6.13 ± 0.11
2MASS J16041740-1942287	14.761 ± 0.002	-9.70 ± 0.19	-21.63 ± 0.09	6.20 ± 0.09	38.7849 ± 0.0886	62472212857180073088	17.272 ± 0.002	-8.26 ± 0.33	-22.83 ± 0.16	6.05 ± 0.17
2MASS J16042165-2130284	11.868 ± 0.016	-12.33 ± 0.10	-23.83 ± 0.05	6.66 ± 0.06	16.2112 ± 0.0666	6243393817024156288	13.607 ± 0.002	-12.64 ± 0.18	-24.73 ± 0.09	6.79 ± 0.10
2MASS J16061144-1935405	15.748 ± 0.001	-11.94 ± 0.33	-21.73 ± 0.19	7.29 ± 0.14	10.7768 ± 0.1387	6247238293789181440	16.552 ± 0.004	-11.52 ± 0.35	-21.94 ± 0.20	7.17 ± 0.14
2MASS J16070014-2033092	13.781 ± 0.001	-13.86 ± 0.18	-21.61 ± 0.13	7.32 ± 0.10	11.8052 ± 0.1059	62441061631113915904	14.082 ± 0.002	-13.28 ± 0.16	-22.22 ± 0.11	7.18 ± 0.09
2MASS J16070211-2019387	16.560 ± 0.003	-9.99 ± 0.36	-21.41 ± 0.24	6.70 ± 0.22	1.4975 ± 0.3257	6244125331552799488	17.123 ± 0.011	-9.96 ± 0.71	-20.95 ± 0.53	3.93 ± 0.42
2MASS J16070873-1927341	13.732 ± 0.001	-10.55 ± 0.27	-20.66 ± 0.19	6.64 ± 0.14	23.4170 ± 0.1070	6247244203663970944	15.442 ± 0.001	-9.92 ± 0.19	-21.43 ± 0.13	6.84 ± 0.09
2MASS J16075796-2040087	14.115 ± 0.048	-7.15 ± 0.26	-26.31 ± 0.18	5.04 ± 0.20	41.0394 ± 0.1838	6243914435774449280	15.974 ± 0.001	-9.50 ± 0.33	-22.61 ± 0.17	6.15 ± 0.20
2MASS J16075796-2040087	14.115 ± 0.048	-7.15 ± 0.26	-26.31 ± 0.18	5.04 ± 0.20	14.5344 ± 0.2013	6243914607573142784	16.440 ± 0.002	-10.29 ± 0.35	-25.90 ± 0.24	6.31 ± 0.25
2MASS J16075796-2040087	14.115 ± 0.048	-7.15 ± 0.26	-26.31 ± 0.18	5.04 ± 0.20	21.5220 ± 0.1492	6243914641932881664	17.557 ± 0.002	-9.68 ± 0.42	-22.91 ± 0.27	6.16 ± 0.28
2MASS J16082324-1930009	12.823 ± 0.002	-12.27 ± 0.11	-21.78 ± 0.08	7.15 ± 0.05	13.4420 ± 0.0659	6245759521996902272	13.131 ± 0.007	-12.70 ± 0.12	-22.26 ± 0.09	7.25 ± 0.06
2MASS J16090002-1908368 ^a	12.908 ± 0.007	-9.29 ± 0.14	-24.92 ± 0.09	7.27 ± 0.08	18.9511 ± 0.0874	6245777283349431552	15.462 ± 0.001	-10.04 ± 0.23	-24.81 ± 0.16	7.19 ± 0.14
2MASS J16090075-1908526 ^a	12.908 ± 0.007	-9.29 ± 0.14	-24.92 ± 0.09	7.27 ± 0.08	18.9511 ± 0.0874	6245777283349431552	15.462 ± 0.001	-10.04 ± 0.23	-24.81 ± 0.16	7.19 ± 0.14
2MASS J16101888-2502325	11.356 ± 0.002	-10.76 ± 0.16	-23.49 ± 0.11	6.55 ± 0.08	4.9015 ± 0.1327	6049748786908497408	15.677 ± 0.001	-10.06 ± 0.30	-24.64 ± 0.23	6.42 ± 0.16
2MASS J16102174-1904067	13.627 ± 0.002	-9.41 ± 0.14	-24.07 ± 0.10	7.46 ± 0.06	4.6059 ± 0.0780	6245781131640479360	16.959 ± 0.002	-9.25 ± 0.36	-24.76 ± 0.23	7.28 ± 0.15
2MASS J16104202-2101319	11.799 ± 0.004	-9.82 ± 0.11	-23.34 ± 0.07	7.14 ± 0.05	3.2033 ± 0.2418	6243833724749589760	15.517 ± 0.002	-10.89 ± 0.61	-25.78 ± 0.38	7.62 ± 0.27
2MASS J16111330-2019029	13.981 ± 0.016	-7.84 ± 0.10	-22.13 ± 0.07	6.44 ± 0.06	18.3302 ± 0.0765	6243940617895463296	14.818 ± 0.003	-7.65 ± 0.20	-22.77 ± 0.13	6.30 ± 0.13
2MASS J16111534-1757214	12.930 ± 0.002	-9.12 ± 0.12	-24.75 ± 0.09	7.33 ± 0.06	40.4631 ± 0.2150	62490018417154440512	13.692 ± 0.003	-7.53 ± 0.49	-23.66 ± 0.36	6.76 ± 0.27
2MASS J161113134-1838259	12.370 ± 0.042	-7.45 ± 0.20	-26.89 ± 0.14	7.82 ± 0.10	1.3123 ± 0.1477	6245891976152406016	13.350 ± 0.035	-9.48 ± 0.47	-23.17 ± 0.43	6.38 ± 0.19
2MASS J16123916-1859284	10.396 ± 0.002	-8.26 ± 0.11	-21.92 ± 0.08	7.40 ± 0.05	19.1170 ± 0.0838	6245821092014031616	13.045 ± 0.005	-8.54 ± 0.16	-25.39 ± 0.11	7.19 ± 0.08
2MASS J16124893-1800525	14.553 ± 0.001	-7.42 ± 0.16	-21.15 ± 0.11	6.32 ± 0.07	3.1844 ± 0.1887	6249313690697472512	18.881 ± 0.003	-7.00 ± 0.70	-19.74 ± 0.51	6.04 ± 0.32

Table 5.5: Candidate Wide Companions from Gaia

System	Primary				Companion					
	G (mag)	μ_α (mas yr ⁻¹)	μ_δ (mas yr ⁻¹)	Parallax (mas)	Separation ($''$)	Gaia Source Designation	G (mag)	μ_α (mas yr ⁻¹)	μ_δ (mas yr ⁻¹)	Parallax (mas)
2MASS J16125533-2319456	9.053 ± 0.001	-9.56 ± 0.11	-23.63 ± 0.07	6.57 ± 0.04	38.3021 ± 0.0526	6242176829446854656	11.763 ± 0.002	-8.32 ± 0.10	-23.92 ± 0.07	6.54 ± 0.04
2MASS J16142029-1906481	13.235 ± 0.011	-8.17 ± 0.13	-26.79 ± 0.09	7.17 ± 0.07	43.7319 ± 0.0681	6245801816200921088	14.143 ± 0.034	-7.16 ± 0.22	-26.40 ± 0.16	6.99 ± 0.12
2MASS J16151239-2420091	16.680 ± 0.001	-12.13 ± 0.24	-20.31 ± 0.16	6.51 ± 0.13	17.8773 ± 0.1938	6049726040762143488	18.124 ± 0.002	-11.51 ± 0.45	-20.08 ± 0.31	6.94 ± 0.22
2MASS J16153456-2242421	12.260 ± 0.004	-7.55 ± 0.11	-25.94 ± 0.07	7.16 ± 0.04	1.9157 ± 0.0375	6242598526515738112	13.266 ± 0.001	-10.05 ± 0.16	-26.41 ± 0.07	7.20 ± 0.05
2MASS J16220961-1953005	13.626 ± 0.001	-5.72 ± 0.21	-27.61 ± 0.13	7.22 ± 0.10	1.7979 ± 0.4106	6245095242538868992	17.954 ± 0.005	-7.52 ± 1.02	-25.38 ± 0.70	9.53 ± 0.56
2MASS J16220961-1953005	13.626 ± 0.001	-5.72 ± 0.21	-27.61 ± 0.13	7.22 ± 0.10	2.8881 ± 0.2891	6245095345618083968	19.546 ± 0.007	-4.18 ± 1.81	-27.54 ± 1.03	6.91 ± 0.71

^a 2MASS J16090002-1908368 and 2MASS J16090075-1908526 are an 18 $''$ 9511 pair with matching parallaxes and proper motions.

Properties of Upper Sco Systems with Disks and Companions

We found 30 candidate companions in 27 systems brighter than $K = 15$ and with separations of less than $2''$. This includes the previously known companions listed in Table 5.2 that meet these criteria. Newly discovered candidates are indicated in Table 5.3 by the “Candidate Companion” column. Of the 81 primordial disk systems in the sample, 22 contain a candidate companion, along with five of the 31 debris/evolved transitional disks. The companions range in separation from $0''.02$ to $1''.91$, corresponding to projected separations of 2.8 to 265 au assuming distances listed in Table 5.1. K -band magnitudes of these objects range from 6.72 to 12.77. NIRC2 K' images of the 12 systems with new companions discovered by imaging are shown in Figure 5.4. Ten of these systems include a single candidate companion, while two targets, 2MASS J15534211-2049282 and 2MASS J16052556-2035397, appear to be triple systems.

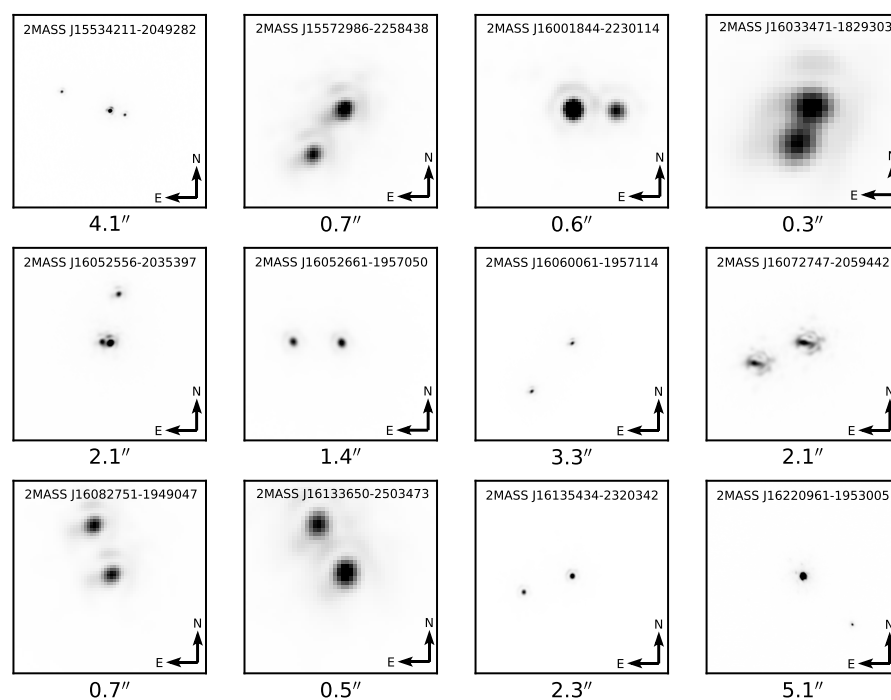
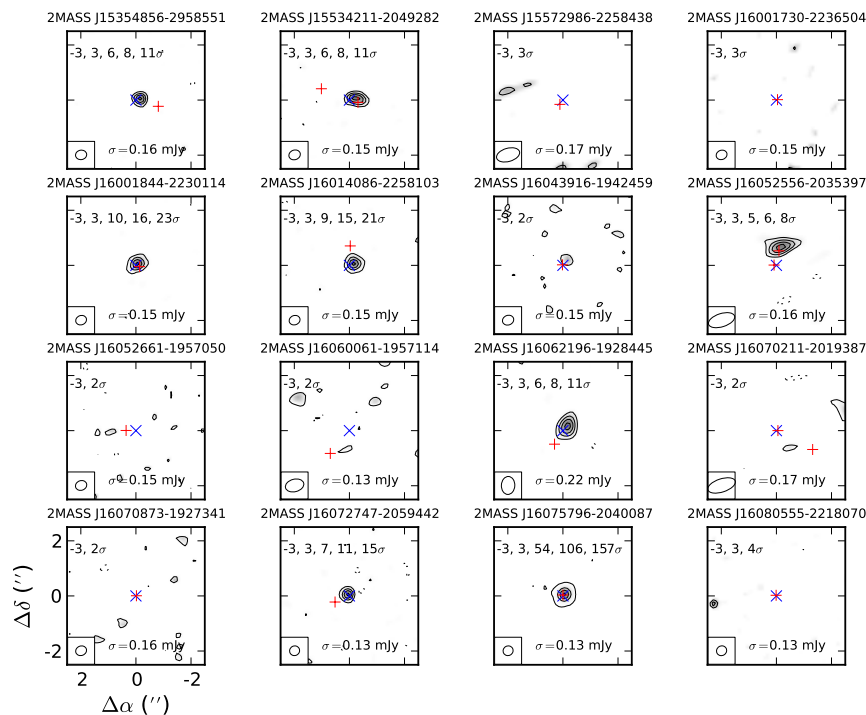


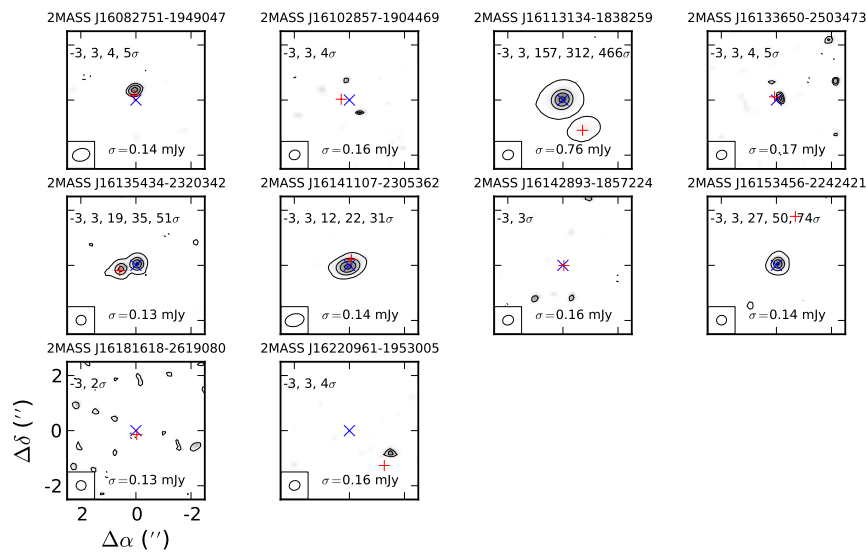
Figure 5.4: NIRC2 K' images of the Upper Sco disk systems with new companions discovered by imaging in this survey. The angular extent of each image is indicated for each panel.



(a)

Figure 5.5: ALMA 880 μm continuum images of the Upper Sco systems with disks and companions in this sample. This excludes 2MASS J16033471-1829303, which was not observed with ALMA. The relative positions of the primary (blue "X") and companion(s) (red "+") are overlaid. SEDs of the seven sources where the millimeter-wavelength emission cannot be conclusively assigned to the primary or secondary are shown in Figure 5.6.

Figure 5.5 shows ALMA 880 μm continuum images of the 26 systems with companions for which we have ALMA data (Barenfeld et al. 2016). This excludes 2MASS J16033471-1829303, an M5 star with a disk identified by infrared excess (Luhman and Mamajek 2012) that was not observed with ALMA. The relative positions of the primary and companion(s) are overlaid in each image. The locations of the primary stars at the time of the ALMA observations were calculated using positions and proper motions from the Gaia DR2 Catalog. When Gaia proper motions or positions were unavailable, we used data from the PPMXL catalog (Roeser, Demleitner, and Schilbach 2010). For 16 systems, the millimeter emission is only at the location of the primary star or is not detected toward either component. Individual disks are detected around each component of 2MASS J16113134-1838259 and 2MASS J16135434-2320342. The disk in 2MASS J16052556-2035397 appears to be lo-



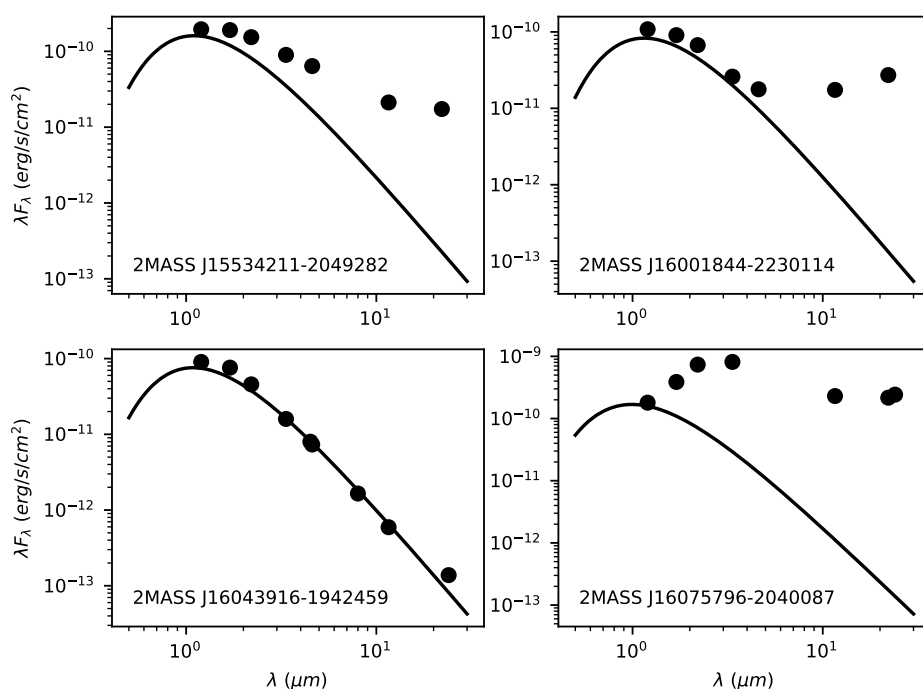
(b)

Figure 5.5: Continued.

cated around the wider companion of this triple system. This may also be the case for 2MASS J16082751-1949047. However, the uncertainties of the right ascension and declination of the primary star are $0''.11$ due to only data from PPMXL being available for this system. We therefore cannot definitively determine the relative positions of the disk and stars. Six other systems, 2MASS J15534211-2049282, 2MASS J16001844-2230114, 2MASS J16043916-1942459, 2MASS J16075796-2040087, 2MASS J16133650-2503473, 2MASS J16141107-2305362 show disk millimeter emission that encompasses both stellar components at the resolution of the ALMA observations. The disks in 2MASS J16082751-1949047 and these six other systems may exist around one or both stars individually or may be circumbinary.

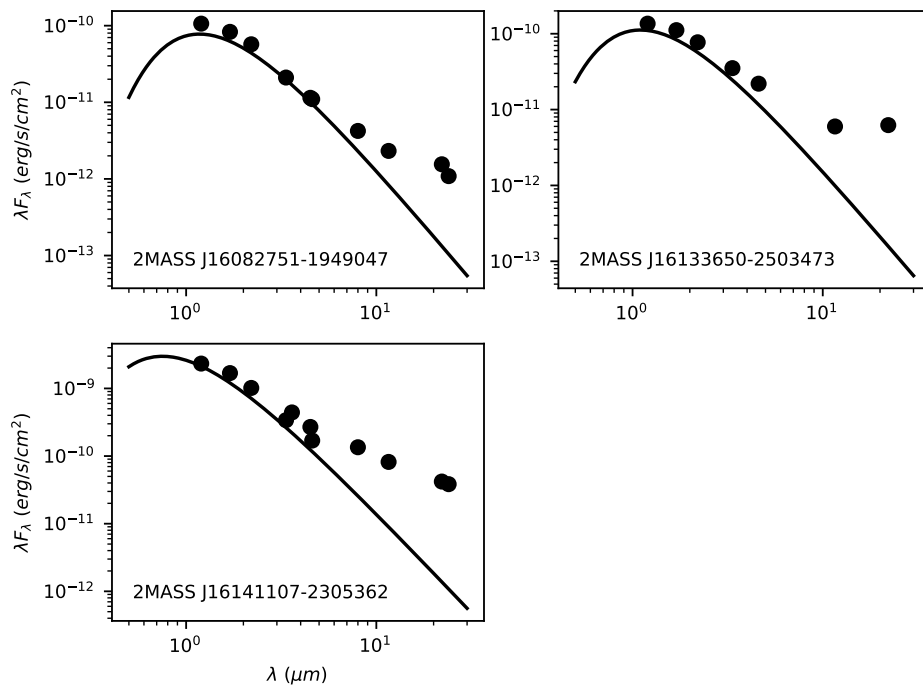
Figure 5.6 shows the infrared spectral energy distributions of the seven systems where the millimeter-wavelength emission cannot be conclusively assigned to the primary or secondary given the angular resolution of the ALMA observations. Infrared photometry is from 2MASS (Cutri et al. 2003), Spitzer, and WISE (Luhman and Mamajek 2012). Stellar photospheres were estimated assuming blackbody

emission with the same stellar parameters as in Barenfeld et al. (2016). Six systems show infrared excess at wavelengths shorter than $10 \mu\text{m}$, indicating the presence of warm dust. This does not necessarily rule out circumbinary disks, but we can say that there must be dust around one or both individual stars. Since 2MASS J16043916-1942459 exhibits an infrared excess only at $24 \mu\text{m}$ and has a companion with a projected separation of only 3.8 au, this system is likely to be a circumbinary disk. However, given the weakness of the $24 \mu\text{m}$ excess and low signal-to-noise ratio of the ALMA image, its nature is difficult to determine with certainty.



(a)

Figure 5.6: Infrared SEDs of the systems in Figure 5.5 for which the millimeter-wavelength emission cannot be conclusively assigned to the primary or secondary. Stellar photospheric emission is estimated assuming blackbody emission with the stellar parameters calculated in Barenfeld et al. (2016). With the exception of 2MASS J16043916-1942459, all systems show excess at wavelengths $\leq 8 \mu\text{m}$, indicating that warm dust is present around the primary and/or companion(s) in these systems.



(b)

Figure 5.6: Continued.

A Comparison of Upper Sco Systems With and Without Disks

We now compare the stellar companion fraction for Upper Sco stars with and without circumstellar disks. As described in Section 5.3, we have detected 30 candidate companions brighter than $K = 15$ and with separations of less than $2''$ in 27 of 112 systems with disks identified from infrared colors (see Section 5.2). Our comparison sample is composed of the 77 Upper Sco stars without such disks surveyed for stellar companions by Kraus et al. (2008) using similar observations to those presented here. This sample, listed in Table 5.6, ranges in spectral type from G0 to M4 (inclusive) and is described in detail by Kraus et al. (2008). Companions identified in this sample meet the same brightness and separation criteria used in this work.

To ensure a meaningful comparison of systems with and without disks, we examined the spectral type distributions of these samples. The distributions of primary star spectral types for the two samples are shown in Figure 5.7. Only two of the 77 systems without disks have spectral types later than M3, compared to 62 of the 112 systems in the disk sample. The latter sample was extended to later spectral

types in order to include a larger number of Upper Sco systems with disks in the studies by Barenfeld et al. (2016) and Barenfeld et al. (2017). Given the lack of M4 and M5 stars in the Kraus et al. (2008) sample, we restrict our comparison of companion fractions to systems with primary spectral types of M3 or earlier. With this restriction, the spectral types of the two samples are consistent with being drawn from the same distribution, with a p -value of 0.17, according to the χ^2 test implemented with the *R Project for Statistical Computing* (R Core Team 2014). This result is independent of how the spectral types are categorically binned.

Table 5.6: Upper Sco Systems without Disks

Primary	Spectral Type	$K_{\text{prim}}^{\text{a}}$ (mag)	Separation ^b (mas)	ΔK^{c} (mag)	$K_{\text{comp}}^{\text{c}}$ (mag)	Position Angle ^c (deg)
2MASS J15355780-2324046	K3	9.43 ± 0.02	54.68 ± 0.16	2.97 ± 0.01	12.40 ± 0.05	173.76 ± 0.19
2MASS J15500499-2311537	M2	8.93 ± 0.02	26.93 ± 0.04	0.76 ± 0.04	9.69 ± 0.07	222.07 ± 0.11
2MASS J15505641-2534189	G0	7.91 ± 0.02	128 ± 1	0.03 ± 0.01	7.94 ± 0.05	72.70 ± 0.06
2MASS J15510660-2402190	M2	9.73 ± 0.02
2MASS J15545986-2347181	G3	7.03 ± 0.02	766 ± 3	1.99 ± 0.01	9.02 ± 0.05	232.0 ± 0.1
2MASS J15562941-2348197	M1.5	8.75 ± 0.02	92 ± 6	0.62 ± 0.05	9.37 ± 0.07	169.8 ± 5.0
2MASS J15565545-2258403	M0	9.43 ± 0.02
2MASS J15570234-1950419	K7	8.37 ± 0.02	558 ± 1	0.54 ± 0.01	8.91 ± 0.05	292.1 ± 0.3
2MASS J15571998-2338499	M0	8.88 ± 0.02	124 ± 1	0.58 ± 0.02	9.46 ± 0.06	166.5 ± 0.4
2MASS J15572575-2354220	M0.5	9.09 ± 0.03	1324 ± 3	0.63 ± 0.12	9.72 ± 0.13	226.0 ± 0.4
2MASS J15573430-2321123	M1	8.99 ± 0.02	53.86 ± 0.19	0.78 ± 0.01	9.77 ± 0.05	68.93 ± 0.20
2MASS J15575002-2305094	M0	9.27 ± 0.02
2MASS J15590208-1844142	K6.5	8.11 ± 0.02	846 ± 1	0.85 ± 0.01	8.96 ± 0.05	58.0 ± 0.1
2MASS J15595995-2220367	M1	8.63 ± 0.02	25.40 ± 0.12	0.03 ± 0.01	8.66 ± 0.05	113.55 ± 0.62
2MASS J16003134-2027050	M1	8.83 ± 0.02	189 ± 4	0.43 ± 0.04	9.26 ± 0.07	171.7 ± 0.5
2MASS J16004056-2200322	G9	8.44 ± 0.02
2MASS J16004277-2127380	K8	8.92 ± 0.02
2MASS J16010519-2227311	M3	8.75 ± 0.02	193 ± 5	0.60 ± 0.11	9.35 ± 0.12	313.7 ± 1.2
2MASS J16010801-2113184	K8	8.80 ± 0.02
2MASS J16012563-2240403	K3	8.52 ± 0.02
2MASS J16014743-2049457	M0	8.61 ± 0.02	205 ± 3	0.58 ± 0.03	9.19 ± 0.06	324.7 ± 0.9
2MASS J16015149-2445249	K7	8.49 ± 0.03	76 ± 5	1.00 ± 0.07	9.49 ± 0.09	289.6 ± 10.0
2MASS J16015822-2008121	G7	7.67 ± 0.02	39.31 ± 1.57	2.14 ± 0.13	9.81 ± 0.14	217.67 ± 0.59
2MASS J16020845-2254588	M1	9.55 ± 0.02
2MASS J16021045-2241280	K6	8.06 ± 0.03	300 ± 3	0.65 ± 0.02	8.71 ± 0.06	346.0 ± 0.3
2MASS J16025243-2402226	K0	7.65 ± 0.02
2MASS J16025396-2022480	K6	8.19 ± 0.03	310 ± 8	0.18 ± 0.07	8.37 ± 0.09	5.3 ± 0.3
2MASS J16030269-1806050	K6	8.73 ± 0.02
2MASS J16032367-1751422	M2	8.61 ± 0.03
2MASS J16033550-2245560	K0	8.36 ± 0.02
2MASS J16034187-2005577	M2	9.49 ± 0.02
2MASS J16034334-2015314	M2	9.72 ± 0.02
2MASS J16035496-2031383	M0	8.62 ± 0.02	121 ± 3	0.53 ± 0.04	9.15 ± 0.07	140.9 ± 0.6
2MASS J16042839-1904413	M3	9.28 ± 0.02	881 ± 1	0.04 ± 0.01	9.32 ± 0.05	128.13 ± 0.10
2MASS J16044776-1930230	K2.5	8.04 ± 0.02	43.18 ± 0.12	0.70 ± 0.03	8.74 ± 0.06	68.63 ± 0.29
2MASS J16051791-2024195	M3	9.14 ± 0.02	16.15 ± 0.59	0.40 ± 0.07	9.54 ± 0.09	251.12 ± 1.11
2MASS J16052726-1938466	M1	9.55 ± 0.02
2MASS J16053936-2152338	M3.5	9.47 ± 0.02

Table 5.6: Upper Sco Systems without Disks

Primary	Spectral Type	$K_{\text{prim}}^{\text{a}}$ (mag)	Separation ^b (mas)	ΔK^{c} (mag)	$K_{\text{comp}}^{\text{c}}$ (mag)	Position Angle ^c (deg)
2MASS J16054266-2004150	M2	9.16 ± 0.03	643 ± 3	0.56 ± 0.03	9.72 ± 0.07	352.6 ± 0.4
2MASS J16061254-2036472	K5	8.90 ± 0.02
2MASS J16063169-2036232	K6	8.73 ± 0.02
2MASS J16063741-2108404	M1	9.11 ± 0.03	1279 ± 3	0.09 ± 0.01	9.20 ± 0.06	33.9 ± 0.3
2MASS J16065436-2416107	M3	8.86 ± 0.03	1500 ± 500	1.3 ± 0.5	10.2 ± 0.5	270 ± 9
2MASS J16070356-2036264	M0	8.10 ± 0.02	184 ± 1	0.15 ± 0.03	8.25 ± 0.06	344.2 ± 0.3
2MASS J16070373-2043074	M2	9.53 ± 0.02
2MASS J16070393-1911338	M1	9.22 ± 0.03	599 ± 3	1.47 ± 0.01	10.69 ± 0.06	87.6 ± 0.3
2MASS J16070767-1927161	M2	9.80 ± 0.02	105.25 ± 0.21	2.33 ± 0.01	12.13 ± 0.05	0.90 ± 0.09
2MASS J16080141-2027416	K8	9.29 ± 0.02
2MASS J16081474-1908327	K2	8.43 ± 0.02	24.6 ± 5.2	2.44 ± 1.16	10.87 ± 1.16	42.5 ± 3.6
2MASS J16082234-1930052	M1	9.06 ± 0.02
2MASS J16082387-1935518	M1	9.25 ± 0.02	652 ± 1	0.98 ± 0.01	10.23 ± 0.05	65.61 ± 0.11
2MASS J16082511-2012245	M1	9.87 ± 0.02
2MASS J16083138-1802414	M0	8.91 ± 0.02
2MASS J16085673-2033460	K5	8.62 ± 0.02
2MASS J16090844-2009277	M4	9.52 ± 0.03
2MASS J16091684-1835226	M2	9.67 ± 0.02
2MASS J16093030-2104589	M0	8.92 ± 0.02
2MASS J16094644-1937361	M1	9.63 ± 0.02
2MASS J16103196-1913062	K7	8.99 ± 0.02	145.55 ± 0.43	2.96 ± 0.02	11.95 ± 0.06	81.63 ± 0.14
2MASS J16110890-1904468	K2	7.69 ± 0.02
2MASS J16115633-2304051	M1	8.82 ± 0.03	1981 ± 4	0.37 ± 0.01	9.19 ± 0.06	155.29 ± 0.06
2MASS J16115927-1906532	K0	8.09 ± 0.03
2MASS J16124051-1859282	K6	7.49 ± 0.02	144 ± 5	1.10 ± 0.10	8.59 ± 0.11	162.15 ± 1.76
2MASS J16130271-2257446	K4.5	8.46 ± 0.03
2MASS J16131858-2212489	K0	7.43 ± 0.02
2MASS J16132929-2311075	K1	8.49 ± 0.02	1430 ± 2	2.70 ± 0.05	11.19 ± 0.07	91.41 ± 0.05
2MASS J16134750-1835004	M2	9.91 ± 0.02
2MASS J16135815-1848290	M2	9.88 ± 0.02
2MASS J16140211-2301021	G4	8.61 ± 0.02
2MASS J16161795-2339476	G8	8.10 ± 0.02
2MASS J16173138-2303360	G1	7.97 ± 0.03
2MASS J16193396-2228294	K0.5	8.51 ± 0.02
2MASS J16204596-2348208	K3	8.93 ± 0.02
2MASS J16245136-2239325	G7	7.08 ± 0.02	44.30 ± 0.07	0.45 ± 0.01	7.53 ± 0.05	230.74 ± 0.08
2MASS J16273956-2245230	K2	8.08 ± 0.03
2MASS J16294869-2152118	K2	7.76 ± 0.02
2MASS J16354836-2148396	M0	8.48 ± 0.02

^a Primary K magnitude.

^b Ellipses indicate single stars.

^c ΔK , K_{comp} , and Position Angle are defined as in Table 5.2.

We note that while similar techniques were used to observe the disk and comparison samples, different observing conditions may have led to discrepancies in the sensitivity to companions between the two samples. In addition, literature data that did not include aperture masking was used for several systems in the disk sample, reducing our sensitivity to close-in companions relative to the comparison sample.

We estimate below the number of companions this may have caused us to miss in the disk sample.

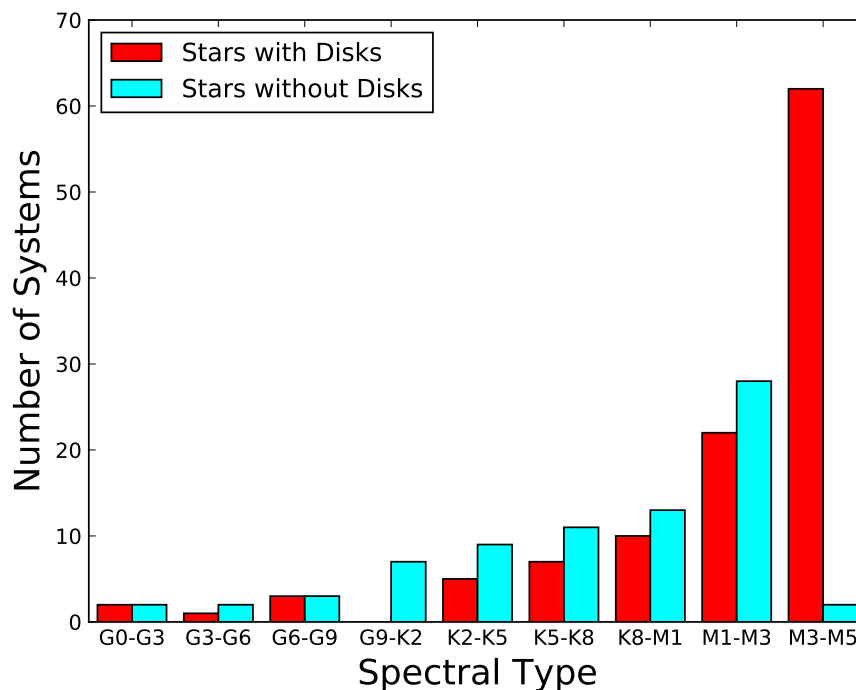


Figure 5.7: Spectral type distributions of Upper Sco primary stars with (red) and without (cyan) disks. This disk sample includes 62 systems with spectral types later than M3, compared to only two such systems without disks. Restricting to spectral types M3 and earlier, the samples are consistent with being drawn from the same parent distribution.

Our aim in this study was to determine if the fraction of disk systems with a stellar companion is lower than that of systems without disks. Thus, to compare survey completeness, we estimated the number of companions detected in diskless systems that would have been missed if they existed with the same brightness and separation around stars in the disk sample. Figure 5.8 shows the limiting magnitude as a function of separation of the disk systems for which no companion was found. Also plotted are the magnitudes and separations of the companions found in the diskless sample for systems with primary spectral type M3 or earlier. The majority of these companions would have been detected had they existed around the stars in our disk sample. The companions that may have been missed were found using aperture masking by Kraus et al. (2008). Our sensitivities to these close-in sources are lower for a number of stars in our sample due to masking data

not being available, calibration issues due to data being taken in position angle mode, and tip-tilt correction problems (see Section 5.2). For example, 2MASS J16142029-1906481 was observed without masking by Lafrenière et al. (2014). If the 75 systems in the diskless sample had been observed with the same sensitivity achieved for this source, companions detected by Kraus et al. (2008) would have been missed in 14 systems, equal to 19% of the diskless sample. If 2MASS J16142029-1906481 followed the same underlying companion probability distribution as the diskless sample, we would thus have expected to miss 0.19 companions on average. Similarly, our observations of 2MASS J16103956-1916524, which suffered from poor tip-tilt correction, would not have detected five companions from the diskless sample for an expected value of 0.07 companions missed. The fraction of Kraus et al. (2008) companions in systems without disks that would have been missed in our disk sample can be calculated in this manner for each star in the sample. With this calculation, we found that even if systems with and without disks shared the same distribution of companion brightnesses and separations, we would have only expected to not detect approximately two to three companions in the disk sample due to lower sensitivities. Restricting to the primordial disks in our sample, we would have expected to miss less than one companion relative to the diskless sample.

With this caveat in mind, we now compare the companion fractions of Upper Sco systems with and without disks. For spectral types M3 and earlier, 35 out of 75 stars without disks have at least one companion. By contrast, only seven out of 50 systems with disks include companions. From the Fisher Exact Test, the probability that the lower companion fraction in star-disk systems is due to chance is 2×10^{-4} . Even if our previous estimate of three missed companions were added to the total number of companions observed around stars with disks, the Fisher Exact Test would still give a probability of 2×10^{-3} that the companion fractions are the same for stars with and without disks. Since this includes the debris/evolved transitional disks and we are primarily concerned with the evolution of primordial disks, we eliminated the potential debris disks and repeated the comparison. We found that six of the 26 primordial disk systems with spectral types M3 and earlier host companions, giving a p -value of 0.04 when compared to the stars without disks. Thus, the fraction of multiple systems among stars with primordial disks is lower than that of stars without disks with marginal significance.

Kuruwita et al. (2018) have also studied the effect of binarity on the presence of disks in Upper Sco in a radial velocity search for stellar companions to 55 Upper

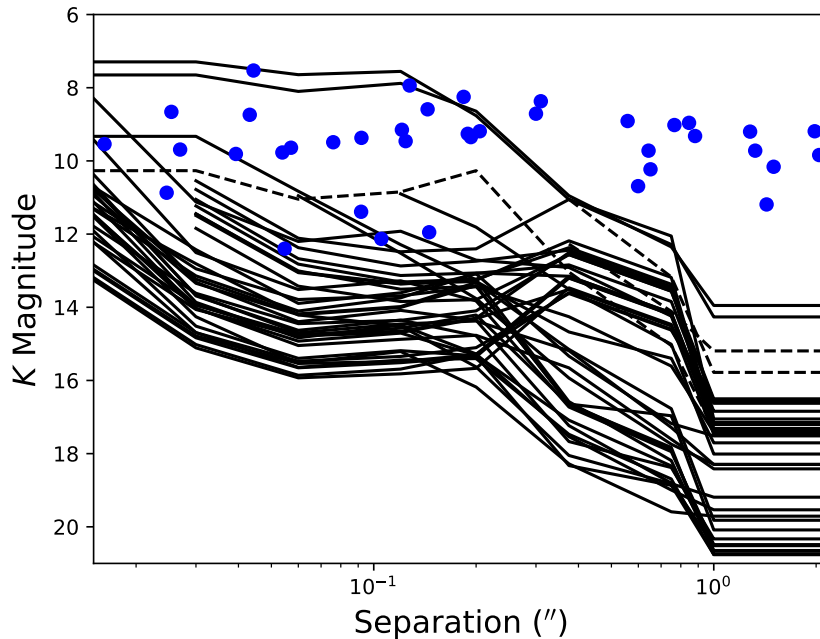


Figure 5.8: Apparent magnitude detection limits as a function of separation for Upper Sco disk-hosts with no candidate companions and spectral types of M3 or earlier. The dashed curves show the contrast limits for the three sources with poor tip-tilt in this spectral type range. The blue points show the companions found by Kraus et al. (2008) among a sample of Upper Sco stars without disks. The majority of observations in the current disk sample were sensitive enough to have detected all of these companions if they were present around the disk-hosting stars. Under the assumption that the stars with disks have the same population of companions as those without disks, we would have only expected to miss approximately two to three of these companions due to lower sensitivities.

Sco G, K, and M stars with an infrared excess. The authors find a stellar companion fraction for these systems of $0.06^{+0.07}_{-0.02}$ for periods less than 20 years. This is lower than the fraction expected for field stars with the same primary mass distribution, $0.12^{+0.02}_{-0.01}$, although the fractions agree within uncertainties. This survey probes separations within $\sim 0''.05$ at the ~ 145 pc distance of Upper Sco, separations similar to and within the inner working angle of our current aperture masking observations. Thus, it would be possible with a larger radial-velocity sample to test if the lower companion fraction in systems with disks relative to those without disks found in the present study holds for closer-separation companions. Such a sample was recently provided by Esplin et al. (2018), who compiled an updated census of 484 Upper Sco disks identified by infrared excess.

2MASS J16075796-2040087: An Accreting Circumbinary Disk

While the majority of the disks in the Upper Sco multiple systems in our sample appear to be located around a single star within each system, the disk in 2MASS J16075796-2040087 is likely to be circumbinary. This system has a stellar companion at a projected separation of 6.3 au and a disk with 880 μm flux density of 23.49 mJy, one of the brighter millimeter sources in the present sample. Corrected for the updated Gaia distance to this system in Table 5.1, Barenfeld et al. (2017) found that the dust disk in this system extends to 15 ± 1 au while the gas component reaches to 46_{-2}^{+6} au, well beyond the projected companion separation. While it is possible that the physical separation of the components of this system is wider than their projected separation, the physical separation would have to be over a factor of seven larger to be outside of the gas disk. Harris et al. (2012) constructed the probability distribution for the ratio of physical to projected separation of a binary using a Monte Carlo simulation of the underlying orbital parameters. Depending on the assumed priors for orbital parameters, the distribution peaks between a ratio of 0.5 and 1.5, with only a low probability tail extending beyond a ratio of 3. 2MASS J16075796-2040087 is therefore most likely to be a circumbinary disk.

However, in Figure 5.6, there is a strong infrared excess at wavelengths as short as 1.7 μm , indicating the presence of hot dust close to one or both of the stars. We note that the stellar photospheric emission calculated for this system assumes a spectral type of M1 (Luhman and Mamajek 2012), while the primary star may have an earlier spectral type (see Kraus and Hillenbrand 2009; Cody et al. 2017). Despite the uncertainty in the stellar photosphere, it is clear that there is significant circumstellar material around at least one of the stars in this system. Kraus and Hillenbrand (2009) found that there is likely to be an accretion-powered outflow based on strong optical emission lines, while Cody et al. (2017) observed bursting behavior on a ~ 15 day timescale in the optical light curve, consistent with episodic accretion.

One possible explanation for these observations is that material from the inner edge of the circumbinary disk is streaming across the dynamically cleared inner gap and accreting onto one or both of the stars (e.g., Artymowicz and Lubow 1996; Günther and Kley 2002). The details of this process depend strongly on the mass ratio and orbital parameters of the binary, but it is generally expected that this accretion will be modulated with a period of order that of the binary orbit (Muñoz and Lai 2016). Modulated accretion has been observed in spectroscopic binaries with circumbinary

disks such as DQ Tau (Mathieu et al. 1997), UZ Tau E (Jensen et al. 2007), and TWA 3A (Tofflemire et al. 2017a, 2017b). However, 2MASS J16075796-2040087 exhibits optical variability on a ~ 15 day timescale, much shorter than the orbital period of a binary with a projected separation of 4.6 au. Direct accretion onto the stars in the binary is only expected for spectroscopic binaries with separations of a fraction of an au. In wider systems, inner circumprimary and circumsecondary disks are expected to be fed and maintained by the streams (Günther and Kley 2002; Dutrey et al. 2016). Observations of GG Tau (Dutrey, Guilloteau, and Simon 1994; Dutrey et al. 2014), with a projected separation of ~ 35 au, UY Aur (Close et al. 1998; Duvert et al. 1998; Tang et al. 2014), ~ 125 au, and L1551 (Takakuwa et al. 2014), ~ 70 au, fit such a scenario. A similar process may be taking place in 2MASS J16075796-2040087. Though the 4.6 au binary separation makes this system an intermediate case between spectroscopic binaries and wider pairs such as GG Tau, a circumprimary and/or circumsecondary disk replenished by streams from the outer circumbinary disk may be present. Accretion from the inner disk(s) may then be causing the observed optical emission lines, infrared excess, and variability on timescales unrelated to the binary orbital period.

5.5 Discussion

In this section we investigate how the relationship between disks and stellar companions varies with age. We compare the fractions of disk systems with close companions and examine the relationship between companion separation and disk millimeter luminosity in the 1-2 Myr old Taurus and 5-11 Myr old Upper Sco regions. We then discuss the implications of these results for disk evolution.

Companion Frequency of Disk Systems in Taurus and Upper Sco

Studies of how disks are affected by stellar companions in Taurus and other young star forming regions have shown that multiplicity has a significant impact during the first 1-2 Myr of disk evolution. The infrared-detected disk fraction of 1-2 Myr old stars with close companions (≤ 40 au separation) is lower by approximately a factor of two to three than that of single stars of the same age (Cieza et al. 2009; Kraus et al. 2012; Cheetham et al. 2015). In Upper Sco (age 5-11 Myr), infrared-detected disks are also less frequent for systems with a close companion than for single stars, but by approximately the same factor of two to three seen for 1-2 Myr old systems (Kraus et al. 2012). This suggests that after the first 1-2 Myr of a disk's evolution, the presence of a companion has no further effect on disk frequency as traced by

dust infrared emission.

We tested the effect of stellar companions on disks between the ages of Taurus and Upper Sco using the expanded sample of Upper Sco binaries presented in this work. Our sample was specifically chosen to include Upper Sco systems with infrared-detected disks. Due to this selection criterion, we could not compare the disk frequencies of close binaries to that of single stars. Instead, we compared the fraction of close companions among systems with disks in Taurus and Upper Sco. Of the 83 Taurus G, K, and M stars with infrared-detected disks listed in Kraus et al. (2012) that have been surveyed for companions, 13 host a stellar companion within a projected separation of 40 au. In the present Upper Sco survey, we find 11 stars with such companions among the 82 primordial infrared-detected disks in our sample. These close companion fractions are consistent according to the Fisher exact test, with a p -value of 0.83. This supports the Kraus et al. (2012) result that stellar companions have little to no effect on disk evolution as traced by infrared-emitting dust after the first 1-2 Myr. Instead, the lower companion fraction for systems with infrared-detected disks in Upper Sco relative to those without disks (Section 5.4) is simply due to the reduction in the disk fraction of multiple systems that occurs before an age of 1-2 Myr.

Millimeter Emission and Multiplicity

Harris et al. (2012) found a clear relationship between companion separation and disk millimeter luminosity in Taurus multiple systems. Taurus disks in systems with projected companion separations between 30 and 300 au are fainter by a factor of five than those in single-star and wider-companion systems, while disks in systems with companions projected within 30 au are an additional factor of five fainter. We now use the current sample to test this relationship in Upper Sco and compare the results to Taurus.

Our goal was to isolate the effect of binarity on disk evolution. For Upper Sco, we used the Upper Sco primordial disk systems in the current sample with ALMA 0.88 mm continuum flux density measurements from Barenfeld et al. (2016). For Taurus, we used the compilation of 1.3 millimeter flux densities of infrared-identified Class II Taurus systems from Akeson et al. (2019) and selected systems classified as primordial disks by Luhman et al. (2010). Flux densities, originally measured by Andrews et al. (2013), Akeson and Jensen (2014), Ward-Duong et al. (2018), and Akeson et al. (2019), have been scaled to 0.88 mm using the scaling factor of 2.55

assumed for Taurus disks by Andrews et al. (2013). We restricted the Taurus sample to systems with single or primary stellar mass between $0.14 M_{\odot}$ and $1.7 M_{\odot}$ to match the stellar mass range of the Upper Sco sample (Barenfeld et al. 2016). Within this range, 78% of Taurus systems in our final comparison sample have a single star or primary stellar mass below $0.6 M_{\odot}$, compared to 87% of Upper Sco systems. We note, however, that the Upper Sco sample is skewed towards slightly lower stellar masses than that of Taurus, with 69% of systems $< 0.3 M_{\odot}$ compared to 24% in Taurus. For both samples, we excluded triple and higher-order systems in order to isolate the effect of a single companion separation. We also excluded circumbinary disks to focus on the effects of disk truncation by an external companion.

Figure 5.9 shows the 0.88 mm continuum flux densities of the binary and single systems in the Taurus and Upper Sco samples defined above. Flux densities have been scaled to a common distance of 145 pc. Binaries are divided into systems with separation < 300 au and > 300 au, with flux densities representing the total emission of both components, following Harris et al. (2012). We note that the Taurus and Upper Sco samples contain only eight and eleven systems, respectively, with separation > 300 au. The flux density distinction between single stars and binaries separated by < 300 au observed in Taurus is not present in Upper Sco. The difference is clearly apparent in Figure 5.10, which shows the cumulative flux distributions of single stars, systems with a companion beyond 300 au, and systems with a companion within 300 au. These distributions were calculated using the Kaplan-Meier product-limit estimator to account for the sources without a millimeter detection.

In the case of Taurus, the flux distributions of systems with companions beyond 300 au and single-star systems are statistically indistinguishable, with p -values of 0.50 and 0.79 given by the log-rank and Peto & Peto Generalized Wilcoxon two-sample tests, implemented in *R*. The brightnesses of the systems with companions within 300 au are clearly lower, however. The log-rank and Peto & Peto Generalized Wilcoxon two-sample tests give p -values of 7.36×10^{-5} and 4.22×10^{-5} that these systems are drawn from the same brightness distribution as single stars. These results are consistent with those originally found by Harris et al. (2012, see also Akeson et al. 2019). We note that when comparing disk millimeter brightnesses, the observed correlation between disk brightness and stellar mass (Andrews et al. 2013; Carpenter, Ricci, and Isella 2014; Barenfeld et al. 2016; Ansdell et al. 2016; Pascucci et al. 2016; Ansdell et al. 2017), must be taken into account. We find

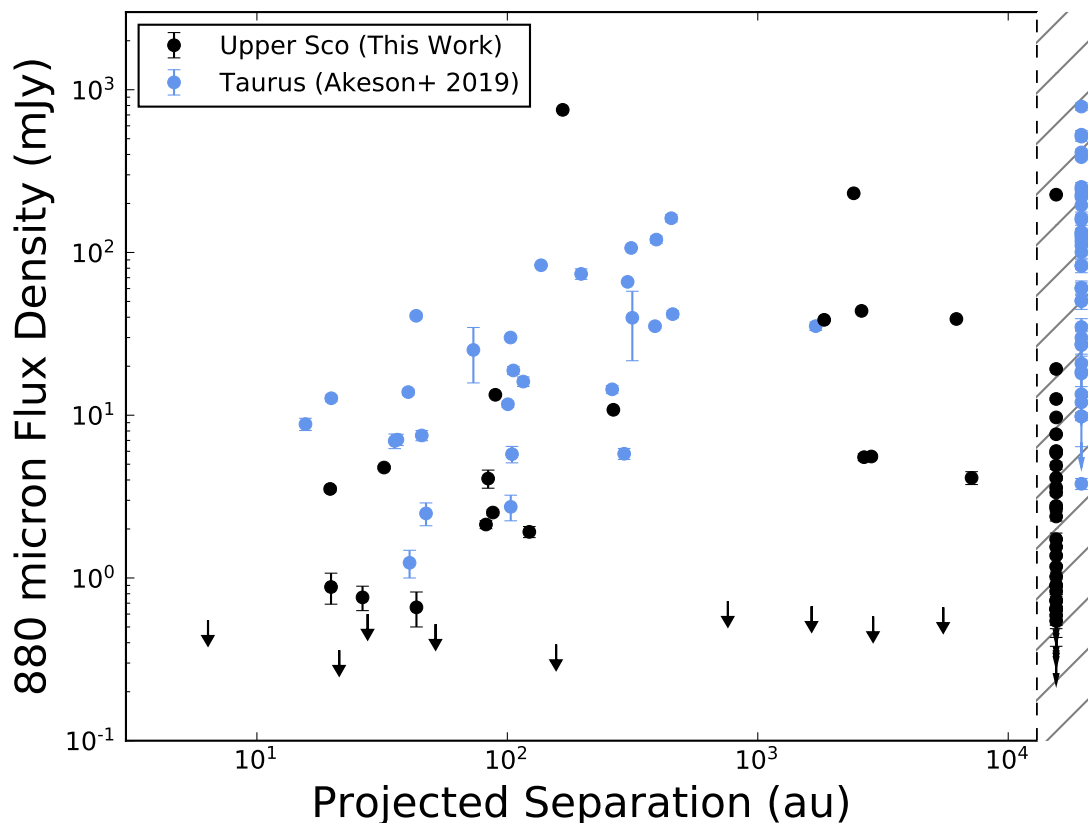


Figure 5.9: Total $880 \mu\text{m}$ continuum flux density and project companion separations of Upper Sco systems with primordial disks. Flux densities have been scaled to a common distance of 145 pc. Single stars are shown in the hatched region to the right of the figure. Taurus systems from Akeson et al. (2019) are shown in blue. Unlike in Taurus, where disks are significantly fainter in systems with companions, the brightness distributions of disks in systems with and without companions are indistinguishable in Upper Sco.

that the distributions of Taurus single star masses and primary masses for binaries with a separation of < 300 au are statistically consistent with p -values of 0.69 and 0.62 given by the two versions of the Anderson-Darling test, implemented in *R*. Therefore, the comparison of the disk luminosity distributions in these two samples are not affected by stellar mass bias.

For Upper Sco, the measured flux densities for single stars, wide companions, and close companions are all shifted to lower fluxes relative to Taurus. As with Taurus, the single-star and > 300 au-separation companion flux distributions are indistinguishable, with p -values of 0.43 and 0.10 given by the two-sample tests,

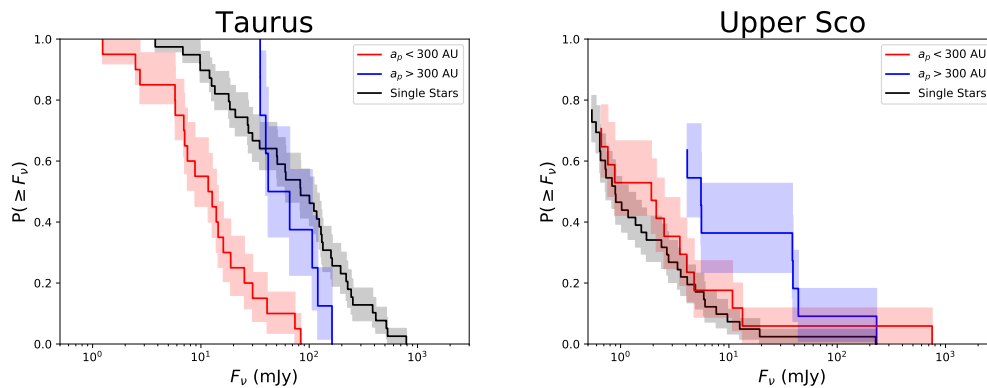


Figure 5.10: Cumulative distributions of $880 \mu\text{m}$ continuum flux density for the Taurus (left) and Upper Sco (right) systems shown in Figure 5.9, calculated using the Kaplan-Meier product-limit estimator. Flux densities have been scaled to a common distance of 145 pc. In the case of Upper Sco, the distribution is only shown to the flux density of the faintest detection. Below this, the assumptions of the Kaplan-Meier product-limit estimator are violated, as all sources are upper limits. In Taurus, single stars are significantly brighter than systems with companions within a projected separation of 300 au. In Upper Sco, however, the brightnesses are similar.

although the sample size of wide companions is small. In contrast to Taurus, however, the flux distribution of < 300 au-companion systems is consistent with that of single stars in Upper Sco, with p -values of 0.85 and 0.62. As is the case for Taurus, stellar mass does not influence this result; the stellar mass distributions of Upper Sco stars with and without companions within 300 au are consistent, with p -values of 0.75 and 0.73. Thus, it appears that while young disks in Taurus are strongly influenced by the presence of stellar companions, by the 5-11 Myr age of Upper Sco disk evolution has proceeded in such a way as to erase these initial effects.

In Figure 5.11, we compare the $^{12}\text{CO } J = 3 - 2$ integrated line flux and projected separation for the Upper Sco primordial disks in binary systems. Figure 5.12 shows the cumulative flux distributions, calculated using the Kaplan-Meier estimator as above. Both figures show similar CO flux distributions for single stars and systems with companions at CO fluxes greater than 0.5 Jy km s^{-1} , independent of companion separation. However, none of the 14 systems with a companion within 300 au and CO flux below 0.5 Jy km s^{-1} are detected in CO, while 11 of the 37 such single stars are detected. The Kaplan-Meier estimator is not reliable below 0.5 Jy km s^{-1} due to the lack of detections in the former 14 systems. Therefore, the effects of binarity on gas and dust in disks may be different in Upper Sco. It is difficult to precisely

quantify any such difference, however, as a 20% reduction in the CO flux of these single systems would result in only three being detected, while a 30% reduction would lead to none being detected. Thus, the lack of CO detections below 0.5 Jy km s^{-1} in multiple systems may be due to only a small difference in flux. Higher-sensitivity observations are necessary to definitively determine if a difference exists in the CO integrated fluxes of disks with and without companions.

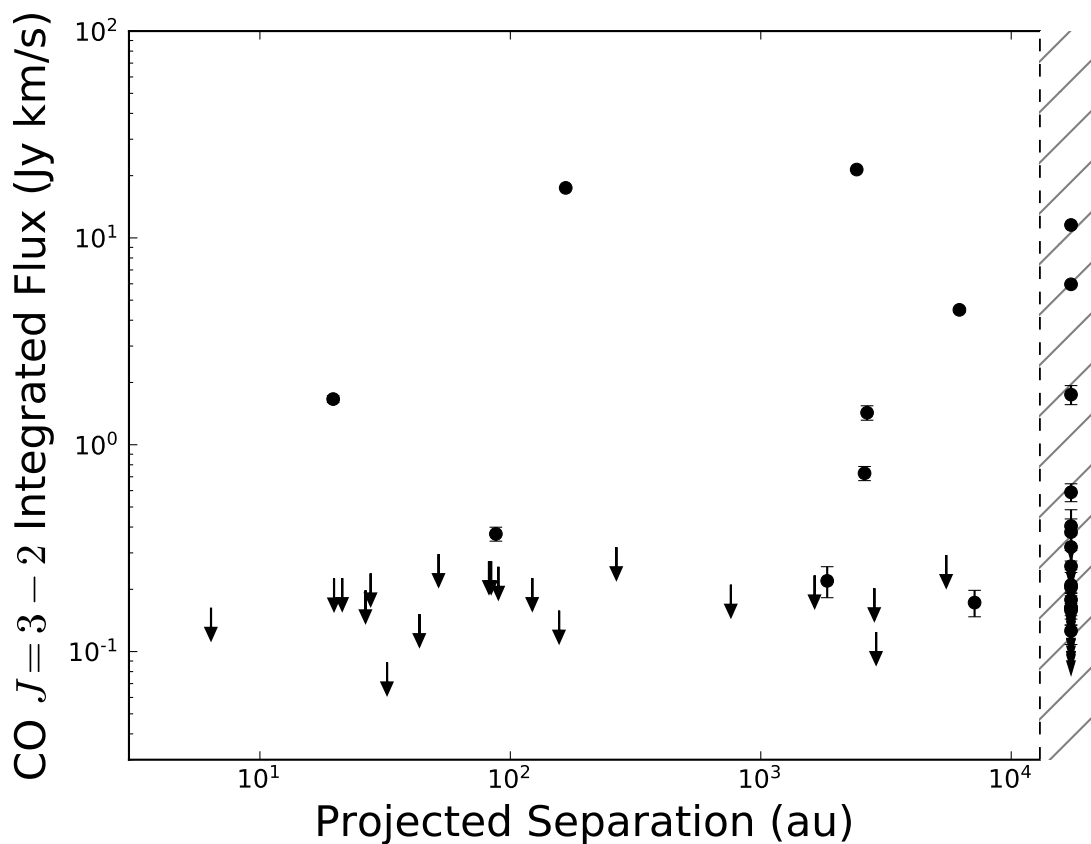


Figure 5.11: CO $J = 3 - 2$ integrated line fluxes versus projected companion separations of Upper Sco systems with disks. Fluxes have been scaled to a common distance of 145 pc. Single stars are shown in the hatched region to the right of the figure. Although the distributions of fluxes for the single stars and systems with companions within 300 au are statistically indistinguishable, 11 out of 37 single-star systems with fluxes below 0.5 Jy km s^{-1} are detected, compared to none of the 14 such systems with companions separated by less than 300 au.

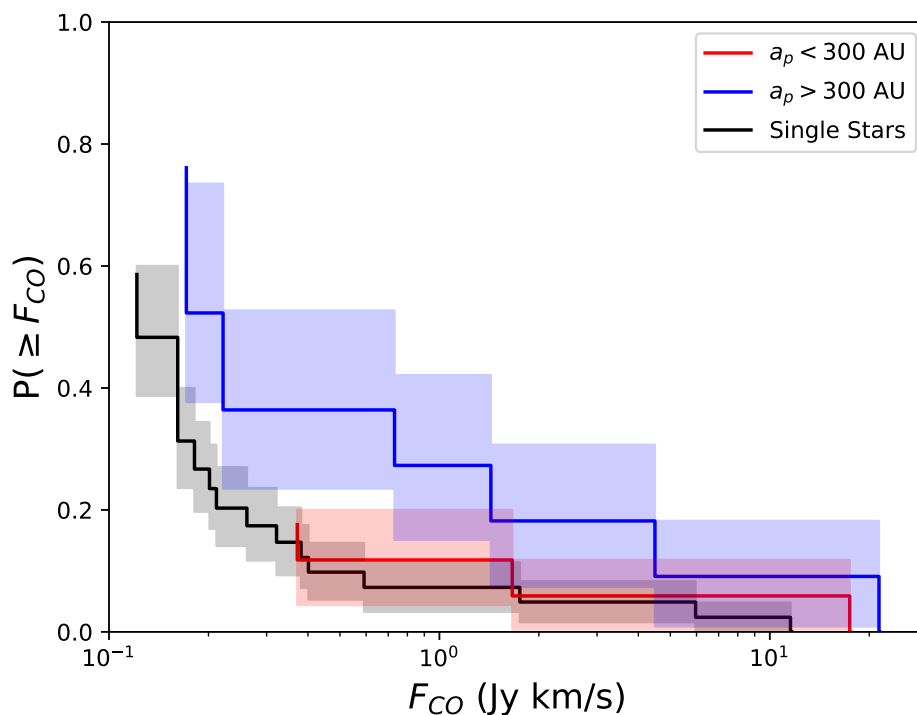


Figure 5.12: Cumulative distributions of the CO $J = 3 - 2$ integrated line fluxes of Upper Sco systems with disks, calculated using the Kaplan-Meier product-limit estimator. Fluxes have been scaled to a common distance of 145 pc. The distribution is only shown to the flux of the faintest detection. Below this, the assumptions of the Kaplan-Meier product-limit estimator are violated, as all sources are upper limits. The log-rank and Peto & Peto Generalized Wilcoxon two-sample tests cannot distinguish between the flux distributions of single stars and systems with a companion within a projected separation of 300 au.

Stellar Companions and Disk Evolution

The observed correlation between the radial extent of millimeter-emitting grains and disk millimeter luminosity (Tripathi et al. 2017; Barenfeld et al. 2017) suggests that the results of Section 5.5 can be explained by the evolution of dust disk sizes in single and multiple systems. Disks in binary systems that are initially truncated by a stellar companion and survive to an age of 1-2 Myr will be smaller in size than their counterparts in single-star systems. These truncated disks will thus be fainter, as is seen in Taurus (Harris et al. 2012; Akeson et al. 2019). A surface brightness comparison of disks in Taurus binary systems with those around single stars could measure the extent to which lower flux densities of binary system disks are due to this loss of the outer disk.

Barenfeld et al. (2017) measured the sizes of dust disks in Upper Sco, finding that these disks are smaller than younger systems by a factor of ~ 3 on average. This suggests that the population of millimeter-sized grains in the outer disk is lost as disks evolve, providing a natural explanation for the similar luminosity distributions of disks in single and multiple systems in Upper Sco. Dust disks in multiple systems are truncated by their stellar companions, but their subsequent evolution is not as strongly affected by the presence of the companion after an age of 1-2 Myr, as shown in Section 5.5. Conversely, the outside-in evolution of single-star disks effectively allows them to “catch-up” to the smaller sizes of disks in multiple systems by an age of 5-11 Myr. The end result of dust disks tens of au in size with similar millimeter brightnesses is the same regardless of the presence or absence of a stellar companion.

Gorti, Hollenbach, and Dullemond (2015) have modeled disk evolution under the effects of viscous accretion, photoevaporation, dust radial migration, and dust growth and fragmentation, finding that the radial extent of millimeter-sized dust grains is expected to decline over time due to migration. The resulting millimeter dust disk sizes are similar to those measured for Upper Sco by Barenfeld et al. (2017). In this scenario, millimeter-sized grains from the outer disk replenish some of the dust lost from the inner disk due to viscous accretion, so that at the age of Upper Sco the inner disk is all that remains. However, disks in binary systems would lack this outer reservoir of millimeter-emitting grains due to tidal truncation, preventing the inner disk from being replenished. This scenario would result in disks in binaries being fainter than disks in single systems, in contrast to what is observed in Section 5.5. Thus, the shrinking of dust disks around single stars cannot simply be due to millimeter grains migrating inwards and remaining observable in the inner disk.

In addition to depletion through migration, the models of Gorti, Hollenbach, and Dullemond (2015) predict that millimeter-sized grains will also be depleted in the outer disk through fragmentation. As photoevaporation lowers the density of gas in the outer disk, collisional velocities of millimeter dust grains will increase, leading to fragmentation into smaller grains that are not detectable at millimeter wavelengths. If this process occurs on a more rapid timescale than radial migration, it could provide a mechanism to remove outer disk millimeter grains without transporting them to the inner disk. Dust disks would therefore shrink in size without replenishment of the inner disk, resulting in disks having the same millimeter brightnesses in multiple and single systems.

On the other hand, local gas pressure maxima in disks are expected to trap concen-

trations of dust that would appear optically thick at millimeter wavelengths (e.g., Whipple 1972; Pinilla et al. 2012). Optically thick dust substructure formed in this way has been suggested as an explanation of the observed correlation between dust disk size and millimeter luminosity seen in Taurus (Tripathi et al. 2017) and Upper Sco (Barenfeld et al. 2017). If millimeter grains in the inner disk are confined by dust traps to optically thick, unresolved substructures, dust could migrate into the inner disk without increasing its observed luminosity. Disks around single stars in Upper Sco would thus have higher dust masses than disks in multiple systems, but this extra material would be hidden by optical depth effects, causing single and multiple system disks to have the same millimeter brightnesses.

5.6 Summary

We have conducted a census of stellar companions around 112 stars with disks in the Upper Scorpius OB Association. Combining new observations with results from the literature, we find 30 sources brighter than $K = 15$ and with separations of less than $2''$ from the target stars in 27 systems. These objects are likely to be companions based on the expected density of field stars. We compared the companion fraction of this sample to that of Upper Sco systems without disks (Kraus et al. 2008) and investigated how the millimeter properties of these disks depend on companion separation. The key conclusions of this paper are as follows:

1. ALMA images of the systems with disks and companions show that for most such systems, the dust continuum emission is located around the primary or companion individually or is not detected toward either. For the systems with unresolved continuum emission encompassing both primary and companion, infrared SEDs show evidence for warm dust around one or both individual stars in the system.
2. Of the 50 primordial and debris/evolved transitional disk-hosting stars with spectral types G0-M3 in our sample, only seven have stellar companions brighter than $K = 15$ with separations less than $2''$. Thirty-five systems in a comparison sample of 75 Upper Sco stars without disks in this spectral type range have stellar companions meeting the same brightness and separation criteria. The companion fraction for stars with disks is significantly lower, with a p -value of 2×10^{-4} . Restricting this comparison to primordial disks, we find that six of 26 stars with disks have a companion, a marginally lower fraction than that for stars without disks, with a p -value of 0.04.

3. The fraction of Upper Sco disk systems with a companion within 40 au is consistent with that of Taurus disks. While external stellar companions disrupt the early phases in disk evolution, as manifested in the lower disk fraction for close multiple systems than for single stars in Taurus, subsequent evolution appears to be dominated by internal disk processes.
4. The observed distribution of millimeter continuum luminosity in Upper Sco is the same for disks in single-star systems and systems with a companion within a projected separation of 300 au. In contrast, disks in younger Taurus systems with such companions are fainter than those in single systems (Harris et al. 2012; Akeson et al. 2019), likely due to the smaller sizes of disks truncated by a stellar companion. This suggests that dust disks evolve from the outside-in between the ages of Taurus and Upper Sco, such that disks around single stars match the sizes and millimeter brightnesses of disks in binary systems by the 5-11 Myr age of Upper Sco.

ACKNOWLEDGMENTS

We thank the referee for their useful comments, which improved this manuscript. We are grateful to Garreth Ruane, Ji Wang, and Henry Ngo for help reducing the NIRC2 imaging data. We thank Mike Ireland for use of his nonredundant aperture masking analysis code <https://github.com/mikeireland/idlnrm> and Lynne Hillenbrand for valuable discussion regarding 2MASS J16075796-2040087. This material is based upon work supported by the National Science Foundation Graduate Research Fellowship under Grant No. DGE-1144469. S.A.B. acknowledges support from the NSF Grant No. AST-1140063. J.M.C. acknowledges support from the National Aeronautics and Space Administration under Grant No. 15XRP15_20140 issued through the Exoplanets Research Program. Some of the data presented herein were obtained at the W. M. Keck Observatory, which is operated as a scientific partnership among the California Institute of Technology, the University of California, and the National Aeronautics and Space Administration. The Observatory was made possible by the generous financial support of the W. M. Keck Foundation. The authors wish to recognize and acknowledge the very significant cultural role and reverence that the summit of Maunakea has always had within the indigenous Hawaiian community. We are most fortunate to have the opportunity to conduct observations from this mountain. This research has made use of the Keck Observatory Archive (KOA), which is operated by the W. M. Keck Observatory and the NASA Exoplanet Science Institute (NExScI), under contract with the National Aeronautics and Space Administration. We thank Luca Rizzi for his aid with preparations for the NIRC2 observations and with telescope operation. We are grateful to the ALMA staff for their assistance in the data reduction. The National Radio Astronomy Observatory is a facility of the National Science Foundation operated under cooperative agreement by Associated Universities, Inc. ALMA is a partnership of ESO (representing its member states), NSF (USA) and NINS (Japan), together with NRC (Canada) and NSC and ASIAA (Taiwan), in cooperation with the Republic of Chile. The Joint ALMA Observatory is operated by ESO, AUI/NRAO, and NAOJ. This work has made use of data from the European Space Agency (ESA) mission *Gaia* (<https://www.cosmos.esa.int/gaia>), processed by the *Gaia* Data Processing and Analysis Consortium (DPAC, <https://www.cosmos.esa.int/web/gaia/dpac/consortium>). Funding for the DPAC has been provided by national institutions, in particular the institutions participating in the *Gaia* Multilateral Agreement.

This publication makes use of data products from the Two Micron All Sky Survey, which is a joint project of the University of Massachusetts and the Infrared Processing and Analysis Center/California Institute of Technology, funded by the National Aeronautics and Space Administration and the National Science Foundation. This publication makes use of data products from the *Wide-field Infrared Survey Explorer*, which is a joint project of the University of California, Los Angeles, and the Jet Propulsion Laboratory/California Institute of Technology, funded by the National Aeronautics and Space Administration. This work is based in part on observations made with the Spitzer Space Telescope, which is operated by the Jet Propulsion Laboratory, California Institute of Technology under a contract with NASA.

Chapter 6

CONCLUSIONS AND FUTURE DIRECTIONS

The key to understanding the evolution of circumstellar disks is to study the different phases of this process using samples of disks at a range ages. In particular, systems at an age of 5-10 Myr provide a snapshot of the final phase of primordial disk evolution and can be compared to younger systems to measure the effects of this evolution. This thesis represents a crucial step forward in this endeavor. In this thesis, I have studied a sample of over 100 circumstellar disks in the 5-11 Myr old Upper Scorpius OB association with unprecedented sensitivity and resolution using the capabilities of ALMA. By measuring the dust masses of these disks, I have quantified the decline in disk dust masses between an age of 1-2 Myr and 5-10 Myr, while my measurements of disk radii in Upper Sco show the decrease in disk size with age. To complete the picture of these disks, I used the NIRC2 AO imager on Keck II to search for stellar companions within these systems, gaining new insights into the effects of binarity on disk evolution. The key results of this thesis are as follows.

- Dust masses of the 5-11 Myr old disks in Upper Sco are lower by a factor of ~ 4.5 than those of disks in the 1-2 Myr old Taurus region with high statistical significance. Dust mass is correlated with stellar mass in Upper Sco, following the relation $M_{\text{dust}} \propto M_*^{1.67 \pm 0.37}$. This agrees within uncertainties with the shallower dust mass-stellar mass relationship in Taurus calculated over the same stellar mass range.
- Among the disks with well-constrained dust outer radii, the median dust radius is only 21 au, a factor of approximately three times smaller than that of 1-3 Myr old disks in Taurus, Lupus, and Ophiuchus. Despite this difference, Upper Sco disks fall on the same relation between dust disk size and millimeter luminosity as their younger counterparts.
- Only approximately half of the disks detected in the continuum were also detected in CO, despite the fact that any resolved, optically thick CO emission should have easily been detected. This lack of detections is consistent with both the small disk sizes described above and with substantial CO depletion.

- The fraction of disk systems with stellar companions in Upper Sco is lower than that of systems without disks. However, among disk-hosts, the fraction of systems with a companion within 40 au is the same in Upper Sco and Taurus. In addition, disk systems with and without companions in Upper Sco have similar distributions of millimeter luminosities, in contrast to Taurus, where systems with stellar companions within 300 au are significantly fainter.

The observation of a decrease in disk dust masses between Taurus and Upper Sco was the first definitive measurement of this effect. Since this result was published in (Barenfeld et al. 2016, see Chapter 3), it has been confirmed in additional ALMA surveys of other star-forming regions (Ansdell et al. 2016; Pascucci et al. 2016; Ansdell et al. 2017; Law et al. 2017; Ruíz-Rodríguez et al. 2018; Eisner et al. 2018). It is now clear that while disks in 1-3 Myr old regions show similar dust mass distributions, the dust masses of the 5-11 Myr old disks in Upper Sco are significantly lower (see Figure 6.1).

The median dust mass of the primordial disks in Upper Sco is only $0.52 M_{\oplus}$. These low masses suggest that the formation of planetesimals and planets has ceased in these disks. Although, the ALMA observations presented in this thesis are only sensitive to millimeter-sized grains and therefore a large fraction of the solid mass existing in larger bodies cannot be ruled out. Indeed, it is unclear whether the lower dust masses in Upper Sco relative to younger disks truly reflect a reduction in the total mass of all solids or are simply due to grain growth beyond millimeter sizes. Additional observations at longer wavelengths can be used to constrain the distribution of grain sizes in these disks and break this degeneracy.

Pascucci et al. (2016) compared the relationship between disk dust mass and stellar mass for Upper Sco disks with 1-3 Myr old systems in Taurus, Lupus, and Chamaeleon I, confirming that while the relations of the younger systems are statistically consistent, the relation in Upper Sco is marginally steeper. The authors suggest that this can be explained by a more rapid loss of millimeter-sized dust grains around lower mass stars due to shorter radial drift timescales. The importance of radial drift in the evolution of dust disks is also apparent from the smaller dust disk sizes measured in Upper Sco relative to younger disks (Barenfeld et al. 2017, see Chapter 4). In addition, the results of Chapter 5 (Barenfeld et al., submitted) give further evidence that unperturbed dust disks around single stars evolve from the outside-in to match the millimeter brightnesses of initially truncated disks in binaries. The shrinking of dust disks with time suggests that some of the reduction

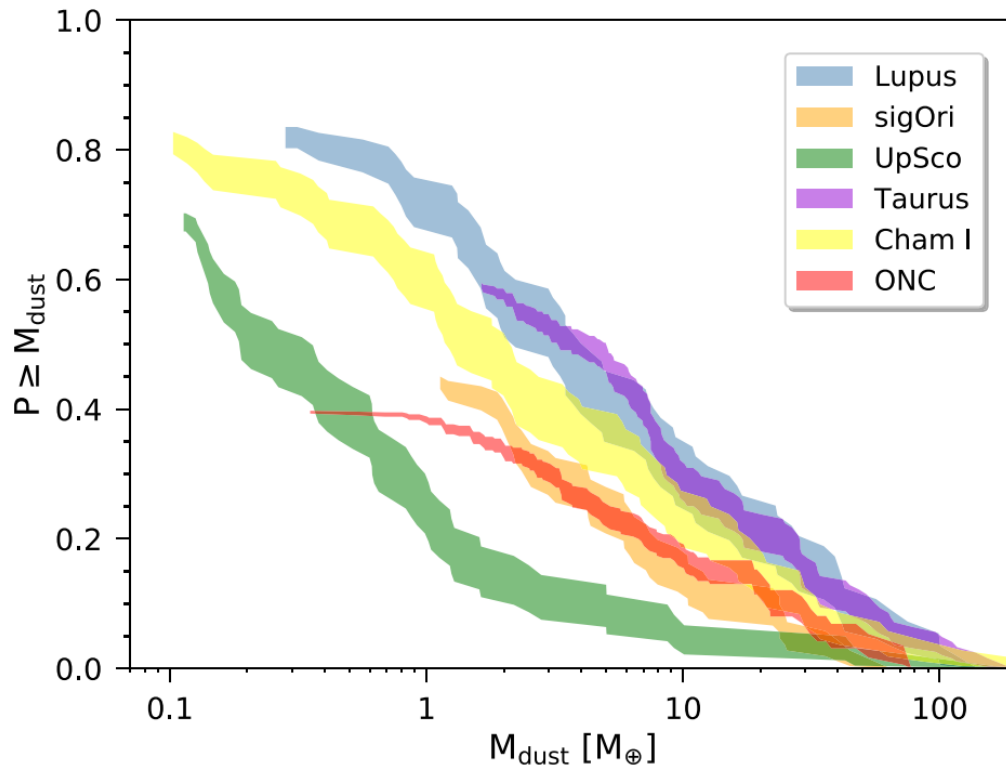


Figure 6.1: Cumulative dust mass distributions of different stellar regions and associations. There is a clear evolutionary trend, with the 1-3 Myr Taurus (Andrews et al. 2013), Lupus (Ansdell et al. 2016), and Chamaeleon I (Pascucci et al. 2016) regions exhibiting similar dust masses to one another, while the 3-5 Myr old σ Orionis (Pascucci et al. 2016) and 5-11 Myr old Upper Sco (Barenfeld et al. 2016, this thesis) regions show successively lower dust masses. Dust masses in the ~ 1 Myr old Orion Nebula Cluster appear lower than those of similarly-aged disks in Taurus, Lupus, and Chamaeleon I, although these masses may be underestimated (Eisner et al. 2018). Figure from Eisner et al. (2018).

in dust mass between the ages of 1-3 Myr and 5-11 Myr is due to the loss of dust in the outer disk. This material may either be removed from the system, or may be migrating inwards and becoming hidden in an optically thick inner disk. The Upper Sco disks modeled in Chapter 4 are optically thin in the continuum beyond ~ 1 au, with dust surface densities similar to or less than those of younger disks. Thus, assuming a smooth dust surface density distribution, there is no evidence of dust from the outer disk being redistributed to the inner disk.

However, long-baseline observations with ALMA show dust substructure is common among the bright disks observed at high resolution (ALMA Partnership et al. 2015; Andrews et al. 2016; Isella et al. 2016; Canovas et al. 2016; Hendlar et al. 2017a;

Loomis et al. 2017; van der Plas et al. 2017; Fedele et al. 2017, 2018; Dipierro et al. 2018; Sheehan and Eisner 2018). If such optically thick substructure exists in fainter Upper Sco disks, this would provide a way for outer-disk dust to migrate inwards and become hidden from view, even if the disk appears optically thin at the resolution of current observations. Optically thick dust traps are in fact expected to form at gas pressure maxima and are a favored solution to the problem of rapid radial drift timescales of millimeter and centimeter sized dust grains (Whipple 1972; Haghighipour and Boss 2003, see Section 2.1). This idea also provides a natural explanation for the observed correlation between dust disk size and millimeter luminosity seen in both Upper Sco and younger disks (Tripathi et al. 2017, Chapter 4). Future observations of these disks at higher resolution may be able to detect this substructure and would represent an important next step in studying these objects.

It should be noted that the decrease in dust disk size found in Chapter 4 was measured by comparing disk radii obtained in different ways. While it is clear that Upper Sco dust disks are smaller than their younger counterparts, precisely quantifying this change requires a more homogeneous analysis. Now that disks in several star-forming regions have been surveyed with ALMA, this data can be used to more rigorously compare disk sizes at different ages. One possible technique, used by Andrews et al. (2018) to confirm the disk size-millimeter luminosity relation using ALMA observations of disks in Lupus, involves fitting the continuum surface brightness profile, rather than the dust surface density profile. In this way, the radii enclosing a chosen percentage of the total continuum flux can be easily calculated and compared for different regions without relying on assumptions regarding the dust properties and underlying emission physics.

While this thesis represents substantial progress in understanding disk evolution, the majority of the work presented relates to the evolution of dust disks. Yet, it is the gas that dominates disks and gas dissipation that sets the timescale available for giant planet formation (see Section 1.1). Thus, a key next step in understanding disk evolution is measuring changes in the gaseous component of disks. Follow-up observations with higher sensitivity and resolution of the Upper Sco disks lacking CO detections in Chapter 3 can be used to distinguish between these non-detections being caused by small disk sizes or a depletion of CO. In addition, observations of these disks targeting the optically thin emission lines of ^{13}CO and C^{18}O can be used to measure total CO masses in 5-11 Myr old disks to further quantify CO depletion relative to younger disks. Finally, a comparison of gas disk sizes in

Upper Sco with those of younger disks observed in other regions can be used to determine if the shrinking of dust disks found in this thesis is primarily due to dust migration or if the entire disk, including the gas, is evolving from the outside-in, perhaps due to photoevaporation or accretion driven by MHD winds. Gas radii of 22 1-3 Myr old disks in Lupus have been recently measured by Ansdell et al. (2018). These disks, ranging in size from 68 au to 462 au, with a median of 194 au, are clearly more extended in CO emission than the Upper Sco disks modeled in Chapter 4, which ranged from 12 to 169 au, with a median of 54 au, among sources with well-constrained outer radii. However, these Upper Sco disks exclude four of the five brightest and potentially largest CO disks in the sample, while the Lupus sample is selected to include only disks that were bright and clearly resolved in CO. Therefore, as described above for the dust, a more rigorous comparison of gas radii of disks at different ages requires more homogeneous sample selections and analysis techniques.

ALMA has brought us into an era of studying the demographics of large samples of disks without the restrictions of observing only the brightest objects. While comparing populations of disks at different ages in this way has led to a tremendous step forward in our understanding of disk evolution in only a few short years, we are still only scratching the surface. With the already unmatched capabilities of ALMA continuously improving, further observations of the dust and gas in these disks promise to enhance our understanding of how these systems evolve. Additional analyses of the data already in-hand offer intriguing avenues of study as well. Indeed, while evolutionary effects cause circumstellar disks to fade over time, the future of studies of disk evolution remains bright.

BIBLIOGRAPHY

- Acke, B., et al. 2012. “Herschel images of Fomalhaut. An extrasolar Kuiper belt at the height of its dynamical activity”. *A&A* 540, A125 (): A125. doi:10.1051/0004-6361/201118581. arXiv: 1204.5037 [astro-ph.SR].
- Adams, F. C., C. J. Lada, and F. H. Shu. 1987. “Spectral evolution of young stellar objects”. *ApJ* 312 (): 788–806. doi:10.1086/164924.
- . 1988. “The disks of T Tauri stars with flat infrared spectra”. *ApJ* 326 (): 865–883. doi:10.1086/166144.
- Adams, F. C., and F. H. Shu. 1986. “Infrared spectra of rotating protostars”. *ApJ* 308 (): 836–853. doi:10.1086/164555.
- Adams, F. C., et al. 2004. “Photoevaporation of Circumstellar Disks Due to External Far-Ultraviolet Radiation in Stellar Aggregates”. *ApJ* 611 (): 360–379. doi:10.1086/421989. eprint: astro-ph/0404383.
- Aikawa, Y., and H. Nomura. 2006. “Physical and Chemical Structure of Protoplanetary Disks with Grain Growth”. *ApJ* 642 (): 1152–1162. doi:10.1086/501114. eprint: astro-ph/0601230.
- Aikawa, Y., et al. 1999. “Evolution of Molecular Abundances in Protoplanetary Disks with Accretion Flow”. *ApJ* 519 (): 705–725. doi:10.1086/307400.
- Akeson, R. L., and E. L. N. Jensen. 2014. “Circumstellar Disks around Binary Stars in Taurus”. *ApJ* 784, 62 (): 62. doi:10.1088/0004-637X/784/1/62. arXiv: 1402.5363 [astro-ph.SR].
- Akeson, R. L., et al. 2019. “Resolved Young Binary Systems and Their Disks”. *ApJ* 872, 158 (): 158. doi:10.3847/1538-4357/aaff6a. arXiv: 1901.05029 [astro-ph.SR].
- Alexander, R. D. 2008. “[NeII] emission-line profiles from photoevaporative disc winds”. *MNRAS* 391 (): L64–L68. doi:10.1111/j.1745-3933.2008.00556.x. arXiv: 0809.0316.
- Alexander, R. D., C. J. Clarke, and J. E. Pringle. 2006a. “Photoevaporation of protoplanetary discs - I. Hydrodynamic models”. *MNRAS* 369 (): 216–228. doi:10.1111/j.1365-2966.2006.10293.x. eprint: astro-ph/0603253.
- . 2006b. “Photoevaporation of protoplanetary discs - II. Evolutionary models and observable properties”. *MNRAS* 369 (): 229–239. doi:10.1111/j.1365-2966.2006.10294.x. eprint: astro-ph/0603254.
- Alexander, R., et al. 2014. “The Dispersal of Protoplanetary Disks”. *Protostars and Planets VI*: 475–496. doi:10.2458/azu_uapress_9780816531240-ch021. arXiv: 1311.1819 [astro-ph.EP].

- ALMA Partnership et al. 2015. “The 2014 ALMA Long Baseline Campaign: First Results from High Angular Resolution Observations toward the HL Tau Region”. *ApJ* 808, L3 (): L3. doi:10.1088/2041-8205/808/1/L3. arXiv: 1503.02649 [astro-ph.SR].
- Amara, A., and S. P. Quanz. 2012. “PYNPOINT: an image processing package for finding exoplanets”. *MNRAS* 427 (): 948–955. doi:10.1111/j.1365-2966.2012.21918.x. arXiv: 1207.6637 [astro-ph.IM].
- Andre, P., and T. Montmerle. 1994. “From T Tauri stars to protostars: Circumstellar material and young stellar objects in the rho Ophiuchi cloud”. *ApJ* 420 (): 837–862. doi:10.1086/173608.
- Andre, P., D. Ward-Thompson, and M. Barsony. 1993. “Submillimeter continuum observations of Rho Ophiuchi A - The candidate protostar VLA 1623 and prestellar clumps”. *ApJ* 406 (): 122–141. doi:10.1086/172425.
- André, P., et al. 2014. “From Filamentary Networks to Dense Cores in Molecular Clouds: Toward a New Paradigm for Star Formation”. *Protostars and Planets VI*: 27–51. doi:10.2458/azu_uapress_9780816531240-ch002. arXiv: 1312.6232.
- Andrews, S. M. 2015. “Observations of Solids in Protoplanetary Disks”. *PASP* 127 (): 961. doi:10.1086/683178. arXiv: 1507.04758 [astro-ph.SR].
- Andrews, S. M., and J. P. Williams. 2005. “Circumstellar Dust Disks in Taurus-Auriga: The Submillimeter Perspective”. *ApJ* 631 (): 1134–1160. doi:10.1086/432712. eprint: astro-ph/0506187.
- . 2007. “High-Resolution Submillimeter Constraints on Circumstellar Disk Structure”. *ApJ* 659 (): 705–728. doi:10.1086/511741. eprint: astro-ph/0610813.
- Andrews, S. M., et al. 2009. “Protoplanetary Disk Structures in Ophiuchus”. *ApJ* 700 (): 1502–1523. doi:10.1088/0004-637X/700/2/1502. arXiv: 0906.0730 [astro-ph.EP].
- . 2010a. “Protoplanetary Disk Structures in Ophiuchus. II. Extension to Fainter Sources”. *ApJ* 723 (): 1241–1254. doi:10.1088/0004-637X/723/2/1241. arXiv: 1007.5070 [astro-ph.SR].
- . 2010b. “Protoplanetary Disk Structures in Ophiuchus. II. Extension to Fainter Sources”. *ApJ* 723 (): 1241–1254. doi:10.1088/0004-637X/723/2/1241. arXiv: 1007.5070 [astro-ph.SR].
- Andrews, S. M., et al. 2011. “Resolved Images of Large Cavities in Protoplanetary Transition Disks”. *ApJ* 732, 42 (): 42. doi:10.1088/0004-637X/732/1/42. arXiv: 1103.0284.
- Andrews, S. M., et al. 2016. “Ringed Substructure and a Gap at 1 au in the Nearest Protoplanetary Disk”. *ApJ* 820, L40 (): L40. doi:10.3847/2041-8205/820/2/L40. arXiv: 1603.09352 [astro-ph.EP].

- Andrews, S. M., et al. 2018. “Scaling Relations Associated with Millimeter Continuum Sizes in Protoplanetary Disks”. *ArXiv e-prints* (). arXiv: 1808.10510 [astro-ph.EP].
- Andrews, S. M., et al. 2013. “The Mass Dependence between Protoplanetary Disks and their Stellar Hosts”. *ApJ* 771, 129 (): 129. doi:10.1088/0004-637X/771/2/129. arXiv: 1305.5262 [astro-ph.SR].
- Andrews, S. M., et al. 2012. “The TW Hya Disk at 870 μm : Comparison of CO and Dust Radial Structures”. *ApJ* 744, 162 (): 162. doi:10.1088/0004-637X/744/2/162. arXiv: 1111.5037 [astro-ph.EP].
- Andrews, S. M., et al. 2010c. “Truncated Disks in TW Hya Association Multiple Star Systems”. *ApJ* 710 (): 462–469. doi:10.1088/0004-637X/710/1/462. arXiv: 0912.3537 [astro-ph.SR].
- Ansdell, M., J. P. Williams, and L. A. Cieza. 2015. “A SCUBA-2 850-micron Survey of Circumstellar Disks in the λ Orionis Cluster”. *ApJ* 806, 221 (): 221. doi:10.1088/0004-637X/806/2/221. arXiv: 1505.00262 [astro-ph.EP].
- Ansdell, M., et al. 2016. “ALMA Survey of Lupus Protoplanetary Disks. I. Dust and Gas Masses”. *ApJ* 828, 46 (): 46. doi:10.3847/0004-637X/828/1/46. arXiv: 1604.05719 [astro-ph.EP].
- Ansdell, M., et al. 2018. “ALMA Survey of Lupus Protoplanetary Disks. II. Gas Disk Radii”. *ApJ* 859, 21 (): 21. doi:10.3847/1538-4357/aab890. arXiv: 1803.05923 [astro-ph.EP].
- Ansdell, M., et al. 2017. “An ALMA Survey of Protoplanetary Disks in the σ Orionis Cluster”. *AJ* 153, 240 (): 240. doi:10.3847/1538-3881/aa69c0. arXiv: 1703.08546 [astro-ph.EP].
- Artymowicz, P., and S. H. Lubow. 1994. “Dynamics of binary-disk interaction. 1: Resonances and disk gap sizes”. *ApJ* 421 (): 651–667. doi:10.1086/173679.
- . 1996. “Mass Flow through Gaps in Circumbinary Disks”. *ApJ* 467 (): L77. doi:10.1086/310200.
- Bae, J., Z. Zhu, and L. Hartmann. 2017. “On the Formation of Multiple Concentric Rings and Gaps in Protoplanetary Disks”. *ApJ* 850, 201 (): 201. doi:10.3847/1538-4357/aa9705. arXiv: 1706.03066 [astro-ph.EP].
- Bae, J., et al. 2013. “The Long-term Evolution of Photoevaporating Protoplanetary Disks”. *ApJ* 774, 57 (): 57. doi:10.1088/0004-637X/774/1/57. arXiv: 1307.2585 [astro-ph.SR].
- Bai, X.-N. 2014. “Hall-effect-Controlled Gas Dynamics in Protoplanetary Disks. I. Wind Solutions at the Inner Disk”. *ApJ* 791, 137 (): 137. doi:10.1088/0004-637X/791/2/137. arXiv: 1402.7102 [astro-ph.EP].

- Bai, X.-N., and J. M. Stone. 2013. “Wind-driven Accretion in Protoplanetary Disks. I. Suppression of the Magnetorotational Instability and Launching of the Magnetocentrifugal Wind”. *ApJ* 769, 76 (>): 76. doi:10.1088/0004-637X/769/1/76. arXiv: 1301.0318 [astro-ph.EP].
- Bai, X.-N., et al. 2016. “Magneto-thermal Disk Winds from Protoplanetary Disks”. *ApJ* 818, 152 (>): 152. doi:10.3847/0004-637X/818/2/152. arXiv: 1511.06769 [astro-ph.EP].
- Bailer-Jones, C. A. L., et al. 2018. “Estimating Distance from Parallaxes. IV. Distances to 1.33 Billion Stars in Gaia Data Release 2”. *AJ* 156, 58 (>): 58. doi:10.3847/1538-3881/aacb21. arXiv: 1804.10121 [astro-ph.SR].
- Balbus, S. A., and J. F. Hawley. 1991. “A powerful local shear instability in weakly magnetized disks. I - Linear analysis. II - Nonlinear evolution”. *ApJ* 376 (>): 214–233. doi:10.1086/170270.
- Baldovin-Saavedra, C., et al. 2012. “On the origin of [Ne II] emission in young stars: mid-infrared and optical observations with the Very Large Telescope”. *A&A* 543, A30 (>): A30. doi:10.1051/0004-6361/201118329. arXiv: 1205.2182 [astro-ph.SR].
- Baldovin-Saavedra, C., et al. 2011. “Searching for gas emission lines in Spitzer Infrared Spectrograph (IRS) spectra of young stars in Taurus”. *A&A* 528, A22 (>): A22. doi:10.1051/0004-6361/201015622. arXiv: 1101.3707 [astro-ph.SR].
- Bally, J., and N. Z. Scoville. 1982. “Structure and evolution of molecular clouds near H II regions. II - The disk constrained H II region, S106”. *ApJ* 255 (>): 497–509. doi:10.1086/159850.
- Balog, Z., et al. 2007. “Spitzer/IRAC-MIPS Survey of NGC 2244: Protostellar Disk Survival in the Vicinity of Hot Stars”. *ApJ* 660 (>): 1532–1540. doi:10.1086/513311. eprint: astro-ph/0701741.
- Banzatti, A., et al. 2011. “New constraints on dust grain size and distribution in CQ Tauri”. *A&A* 525, A12 (>): A12. doi:10.1051/0004-6361/201015206. arXiv: 1009.2697.
- Baraffe, I., et al. 2002. “Evolutionary models for low-mass stars and brown dwarfs: Uncertainties and limits at very young ages”. *A&A* 382 (>): 563–572. doi:10.1051/0004-6361:20011638. eprint: astro-ph/0111385.
- Baraffe, I., et al. 2015. “New evolutionary models for pre-main sequence and main sequence low-mass stars down to the hydrogen-burning limit”. *A&A* 577, A42 (>): A42. doi:10.1051/0004-6361/201425481. arXiv: 1503.04107 [astro-ph.SR].
- Barenfeld, S. A., et al. 2016. “ALMA Observations of Circumstellar Disks in the Upper Scorpius OB Association”. *ApJ* 827, 142 (>): 142, doi:10.3847/0004-637X/827/2/142. arXiv: 1605.05772 [astro-ph.EP].

- Barenfeld, S. A., et al. 2017. “Measurement of Circumstellar Disk Sizes in the Upper Scorpius OB Association with ALMA”. *ApJ* 851, 85 (): 85, doi:10.3847/1538-4357/aa989d. arXiv: 1711.04045 [astro-ph.SR].
- Barge, P., and J. Sommeria. 1995. “Did planet formation begin inside persistent gaseous vortices?” *A&A* 295 (): L1–L4. eprint: astro-ph/9501050.
- Barrado y Navascués, D., et al. 2007. “Spitzer: Accretion in Low-Mass Stars and Brown Dwarfs in the λ Orionis Cluster”. *ApJ* 664 (): 481–500. doi:10.1086/518816. arXiv: 0704.1963.
- Batalha, N. M., and Kepler Team. 2012. “Transiting Planet Candidates Observed by Kepler”. In *American Astronomical Society Meeting Abstracts #220*, 220:306.01. American Astronomical Society Meeting Abstracts.
- Bayo, A., et al. 2012. “Spectroscopy of very low-mass stars and brown dwarfs in the Lambda Orionis star-forming region. II. Rotation, activity and other properties of spectroscopically confirmed members of Collinder 69”. *A&A* 547, A80 (): A80. doi:10.1051/0004-6361/201219374. arXiv: 1208.6149 [astro-ph.SR].
- Beckwith, S. V. W., and A. I. Sargent. 1993. “Molecular line emission from circumstellar disks”. *ApJ* 402 (): 280–291. doi:10.1086/172131.
- . 1991. “Particle emissivity in circumstellar disks”. *ApJ* 381 (): 250–258. doi:10.1086/170646.
- Beckwith, S. V. W., et al. 1990. “A survey for circumstellar disks around young stellar objects”. *AJ* 99 (): 924–945. doi:10.1086/115385.
- Bergfors, C., et al. 2010. “Lucky Imaging survey for southern M dwarf binaries”. *A&A* 520, A54 (): A54. doi:10.1051/0004-6361/201014114. arXiv: 1006.2377 [astro-ph.SR].
- Bergin, E. A., et al. 2013. “An old disk still capable of forming a planetary system”. *Nature* 493 (): 644–646. doi:10.1038/nature11805. arXiv: 1303.1107 [astro-ph.SR].
- Bergin, E. A., et al. 2014. “Exploring the Origins of Carbon in Terrestrial Worlds”. *Faraday Discussions* 168 (). doi:10.1039/C4FD00003J. arXiv: 1405.7394 [astro-ph.EP].
- Bertout, C., L. Siess, and S. Cabrit. 2007. “The evolution of stars in the Taurus-Auriga T association”. *A&A* 473 (): L21–L24. doi:10.1051/0004-6361:20078276. arXiv: 0708.3040.
- Birnstiel, T., and S. M. Andrews. 2014. “On the Outer Edges of Protoplanetary Dust Disks”. *ApJ* 780, 153 (): 153. doi:10.1088/0004-637X/780/2/153. arXiv: 1311.5222 [astro-ph.EP].
- Birnstiel, T., C. P. Dullemond, and F. Brauer. 2010. “Gas- and dust evolution in protoplanetary disks”. *A&A* 513, A79 (): A79. doi:10.1051/0004-6361/200913731. arXiv: 1002.0335 [astro-ph.EP].

- Bisschop, S. E., et al. 2006. “Desorption rates and sticking coefficients for CO and N₂ interstellar ices”. *A&A* 449 (): 1297–1309. doi:10.1051/0004-6361:20054051. eprint: astro-ph/0601082.
- Blandford, R. D., and D. G. Payne. 1982. “Hydromagnetic flows from accretion discs and the production of radio jets”. *MNRAS* 199 (): 883–903. doi:10.1093/mnras/199.4.883.
- Bohlin, R. C., B. D. Savage, and J. F. Drake. 1978. “A survey of interstellar H I from L-alpha absorption measurements. II”. *ApJ* 224 (): 132–142. doi:10.1086/156357.
- Borucki, W. J., et al. 2010. “Kepler Planet-Detection Mission: Introduction and First Results”. *Science* 327 (): 977. doi:10.1126/science.1185402.
- Bouwman, J., et al. 2006. “Binarity as a Key Factor in Protoplanetary Disk Evolution: Spitzer Disk Census of the η Chamaeleontis Cluster”. *ApJ* 653 (): L57–L60. doi:10.1086/510365. eprint: astro-ph/0610853.
- Bouy, H., et al. 2006. “Multiplicity of very low-mass objects in the Upper Scorpius OB association: a possible wide binary population”. *A&A* 451 (): 177–186. doi:10.1051/0004-6361:20054252. eprint: astro-ph/0512258.
- Bradley, L., et al. 2016. *Photutils: Photometry tools*. Astrophysics Source Code Library. ascl: 1609.011.
- Brauer, F., C. P. Dullemond, and T. Henning. 2008. “Coagulation, fragmentation and radial motion of solid particles in protoplanetary disks”. *A&A* 480 (): 859–877. doi:10.1051/0004-6361:20077759. arXiv: 0711.2192.
- Brauer, F., et al. 2007. “Survival of the mm-cm size grain population observed in protoplanetary disks”. *A&A* 469 (): 1169–1182. doi:10.1051/0004-6361:20066865. arXiv: 0704.2332.
- Brown, J. M., et al. 2009. “Evidence for Dust Clearing Through Resolved Submillimeter Imaging”. *ApJ* 704 (): 496–502. doi:10.1088/0004-637X/704/1/496.
- Brown, J. M., et al. 2008. “LkH α 330: Evidence for Dust Clearing through Resolved Submillimeter Imaging”. *ApJ* 675 (): L109. doi:10.1086/533464. arXiv: 0802.0998.
- Burke, C. J., et al. 2014. “Planetary Candidates Observed by Kepler IV: Planet Sample from Q1-Q8 (22 Months)”. *ApJS* 210, 19 (): 19. doi:10.1088/0067-0049/210/2/19. arXiv: 1312.5358 [astro-ph.EP].
- Calvet, N., and E. Gullbring. 1998. “The Structure and Emission of the Accretion Shock in T Tauri Stars”. *ApJ* 509 (): 802–818. doi:10.1086/306527.
- Calvet, N., et al. 2005. “Disks in Transition in the Taurus Population: Spitzer IRS Spectra of GM Aurigae and DM Tauri”. *ApJ* 630 (): L185–L188. doi:10.1086/491652.

- Calvet, N., et al. 1991. “Irradiation of accretion disks around young objects. I - Near-infrared CO bands”. *ApJ* 380 (): 617–630. doi:10.1086/170618.
- Calvet, N., et al. 1992. “Irradiation of Accretion Disks around Young Objects. II. Continuum Energy Distribution”. *Rev. Mex. AA* 24 ().
- Cameron, A. G. W. 1962. “The formation of the sun and planets”. *Icarus* 1:13–69. doi:10.1016/0019-1035(62)90005-2.
- Canovas, H., et al. 2016. “A ring-like concentration of mm-sized particles in Sz 91”. *MNRAS* 458 (): L29–L33. doi:10.1093/mnrasl/slw006. arXiv: 1601.06801 [astro-ph.SR].
- Cardelli, J. A., G. C. Clayton, and J. S. Mathis. 1989. “The relationship between infrared, optical, and ultraviolet extinction”. *ApJ* 345 (): 245–256. doi:10.1086/167900.
- Carmona, A., et al. 2008. “A search for mid-infrared molecular hydrogen emission from protoplanetary disks”. *A&A* 477 (): 839–852. doi:10.1051/0004-6361:20077846. arXiv: 0710.2813.
- Carpenter, J. M. 2002. “Constraints on the Circumstellar Disk Masses in the IC 348 Cluster”. *AJ* 124 (): 1593–1600. doi:10.1086/342052. eprint: astro-ph/0205554.
- Carpenter, J. M., L. A. Hillenbrand, and M. F. Skrutskie. 2001. “Near-Infrared Photometric Variability of Stars toward the Orion A Molecular Cloud”. *AJ* 121 (): 3160–3190. doi:10.1086/321086. eprint: astro-ph/0102446.
- Carpenter, J. M., L. Ricci, and A. Isella. 2014. “An ALMA Continuum Survey of Circumstellar Disks in the Upper Scorpius OB Association”. *ApJ* 787, 42 (): 42. doi:10.1088/0004-637X/787/1/42. arXiv: 1404.0387 [astro-ph.SR].
- Carpenter, J. M., et al. 2006. “Evidence for Mass-dependent Circumstellar Disk Evolution in the 5 Myr Old Upper Scorpius OB Association”. *ApJ* 651 (): L49–L52. doi:10.1086/509121. eprint: astro-ph/0609372.
- Chabrier, G., et al. 2000. “Evolutionary Models for Very Low-Mass Stars and Brown Dwarfs with Dusty Atmospheres”. *ApJ* 542 (): 464–472. doi:10.1086/309513. eprint: astro-ph/0005557.
- Chabrier, G., et al. 2014. “Giant Planet and Brown Dwarf Formation”. *Protostars and Planets VI*: 619–642. doi:10.2458/azu_uapress_9780816531240-ch027. arXiv: 1401.7559 [astro-ph.SR].
- Chapillon, E., et al. 2010. “C I observations in the CQ Tauri proto-planetary disk: evidence of a very low gas-to-dust ratio ?” *A&A* 520, A61 (): A61. doi:10.1051/0004-6361/201014841. arXiv: 1006.5244.
- Chapillon, E., et al. 2008. “Disks around CQ Tauri and MWC 758: dense PDR or gas dispersal?” *A&A* 488 (): 565–578. doi:10.1051/0004-6361:200809523. arXiv: 0805.3473.

- Cheetham, A. C., et al. 2015. “Mapping the Shores of the Brown Dwarf Desert. IV. Ophiuchus”. *ApJ* 813, 83 (): 83. doi:10.1088/0004-637X/813/2/83. arXiv: 1509.05217 [astro-ph.SR].
- Chen, C. H., et al. 2011. “A Magellan MIKE and Spitzer MIPS Study of 1.5-1.0 M_{sun} Stars in Scorpius-Centaurus”. *ApJ* 738, 122 (): 122. doi:10.1088/0004-637X/738/2/122.
- Chen, X., et al. 2013. “SMA Observations of Class 0 Protostars: A High Angular Resolution Survey of Protostellar Binary Systems”. *ApJ* 768, 110 (): 110. doi:10.1088/0004-637X/768/2/110. arXiv: 1304.0436 [astro-ph.SR].
- Chen, Y.-J., et al. 2014. “Vacuum Ultraviolet Emission Spectrum Measurement of a Microwave-discharge Hydrogen-flow Lamp in Several Configurations: Application to Photodesorption of CO Ice”. *ApJ* 781, 15 (): 15. doi:10.1088/0004-637X/781/1/15.
- Chiang, E. I., and P. Goldreich. 1997. “Spectral Energy Distributions of T Tauri Stars with Passive Circumstellar Disks”. *ApJ* 490 (): 368–376. doi:10.1086/304869. eprint: astro-ph/9706042.
- Cieza, L. A., et al. 2016. “Imaging the water snow-line during a protostellar outburst”. *Nature* 535 (): 258–261. doi:10.1038/nature18612. arXiv: 1607.03757 [astro-ph.SR].
- Cieza, L. A., et al. 2009. “Primordial Circumstellar Disks in Binary Systems: Evidence for Reduced Lifetimes”. *ApJ* 696 (): L84–L88. doi:10.1088/0004-637X/696/1/L84. arXiv: 0903.3057 [astro-ph.SR].
- Cieza, L. A., et al. 2013. “The Herschel DIGIT Survey of Weak-line T Tauri Stars: Implications for Disk Evolution and Dissipation”. *ApJ* 762, 100 (): 100. doi:10.1088/0004-637X/762/2/100. arXiv: 1211.4510.
- Cieza, L., et al. 2007. “The Spitzer c2d Survey of Weak-Line T Tauri Stars. II. New Constraints on the Timescale for Planet Building”. *ApJ* 667 (): 308–328. doi:10.1086/520698. arXiv: 0706.0563.
- Clarke, C. 2011. “The Dispersal of Disks around Young Stars”. In *Physical Processes in Circumstellar Disks around Young Stars*, ed. by P. J. V. Garcia, 355–418.
- Clarke, C. J., A. Gendrin, and M. Sotomayor. 2001. “The dispersal of circumstellar discs: the role of the ultraviolet switch”. *MNRAS* 328 (): 485–491. doi:10.1046/j.1365-8711.2001.04891.x.
- Close, L. M., et al. 1998. “Adaptive Optics Imaging of the Circumbinary Disk around the T Tauri Binary UY Aurigae: Estimates of the Binary Mass and Circumbinary Dust Grain Size Distribution”. *ApJ* 499 (): 883–888. doi:10.1086/305672.
- Cody, A. M., et al. 2017. “A Continuum of Accretion Burst Behavior in Young Stars Observed by K2”. *ApJ* 836, 41 (): 41. doi:10.3847/1538-4357/836/1/41. arXiv: 1612.05599 [astro-ph.SR].

- Collings, M. P., et al. 2003. “Carbon Monoxide Entrapment in Interstellar Ice Analogs”. *ApJ* 583 (): 1058–1062. doi:10.1086/345389.
- Currie, T., et al. 2008. “The Rise and Fall of Debris Disks: MIPS Observations of θ and χ Persei and the Evolution of Mid-IR Emission from Planet Formation”. *ApJ* 672 (): 558–574. doi:10.1086/523698. arXiv: 0709.2510.
- Cutri, R. M., et al. 2003. “VizieR Online Data Catalog: 2MASS All-Sky Catalog of Point Sources (Cutri+ 2003)”. *VizieR Online Data Catalog* 2246 ().
- Daemgen, S., et al. 2016. “The frequency of accretion disks around single stars: Chamaeleon I”. *A&A* 586, A12 (): A12. doi:10.1051/0004-6361/201525897. arXiv: 1511.05965 [astro-ph.SR].
- Dahm, S. E. 2010. “Evidence for Evolution Among Primordial Disks in the 5 Myr Old Upper Scorpius OB Association”. *AJ* 140 (): 1444–1455. doi:10.1088/0004-6256/140/5/1444. arXiv: 1009.2531 [astro-ph.SR].
- Dahm, S. E., and J. M. Carpenter. 2009. “Spitzer Spectroscopy of Circumstellar Disks in the 5 Myr Old Upper Scorpius OB Association”. *AJ* 137 (): 4024–4045. doi:10.1088/0004-6256/137/4/4024. arXiv: 0901.4120 [astro-ph.SR].
- Dahm, S. E., and L. A. Hillenbrand. 2007. “Spitzer Observations of NGC 2362: Primordial Disks at 5 Myr”. *AJ* 133 (): 2072–2086. doi:10.1086/512156.
- Dahm, S. E., C. L. Slesnick, and R. J. White. 2012. “A Correlation between Circumstellar Disks and Rotation in the Upper Scorpius OB Association”. *ApJ* 745, 56 (): 56. doi:10.1088/0004-637X/745/1/56. arXiv: 1110.0536 [astro-ph.SR].
- D’Alessio, P., N. Calvet, and L. Hartmann. 2001. “Accretion Disks around Young Objects. III. Grain Growth”. *ApJ* 553 (): 321–334. doi:10.1086/320655. eprint: astro-ph/0101443.
- D’Angelo, G., R. H. Durisen, and J. J. Lissauer. 2010. “Giant Planet Formation”. In *Exoplanets*, ed. by S. Seager, 319–346.
- Dauphas, N., and M. Chaussidon. 2011. “A Perspective from Extinct Radionuclides on a Young Stellar Object: The Sun and Its Accretion Disk”. *Annual Review of Earth and Planetary Sciences* 39 (): 351–386. doi:10.1146/annurev-earth-040610-133428. arXiv: 1105.5172 [astro-ph.EP].
- David, T. J., and L. A. Hillenbrand. 2015. “The Ages of Early-type Stars: Strömgren Photometric Methods Calibrated, Validated, Tested, and Applied to Hosts and Prospective Hosts of Directly Imaged Exoplanets”. *ApJ* 804, 146 (): 146. doi:10.1088/0004-637X/804/2/146. arXiv: 1501.03154 [astro-ph.SR].
- de Boer, J., et al. 2016. “Multiple rings in the transition disk and companion candidates around RX J1615.3-3255. High contrast imaging with VLT/SPHERE”. *A&A* 595, A114 (): A114. doi:10.1051/0004-6361/201629267. arXiv: 1610.04038 [astro-ph.EP].

- de Geus, E. J., P. T. de Zeeuw, and J. Lub. 1989. “Physical parameters of stars in the Scorpio-Centaurus OB association”. *A&A* 216 (): 44–61.
- de Zeeuw, P. T., et al. 1999. “A HIPPARCOS Census of the Nearby OB Associations”. *AJ* 117 (): 354–399. doi:10.1086/300682. eprint: astro-ph/9809227.
- DENIS Consortium. 2005. “VizieR Online Data Catalog: The DENIS database (DENIS Consortium, 2005)”. *VizieR Online Data Catalog* 2263 ().
- Dent, W. R. F., et al. 2013. “GASPS—A Herschel Survey of Gas and Dust in Protoplanetary Disks: Summary and Initial Statistics”. *PASP* 125 (): 477–505. doi:10.1086/670826. arXiv: 1306.0275.
- Dent, W. R. F., et al. 2014. “Molecular Gas Clumps from the Destruction of Icy Bodies in the β Pictoris Debris Disk”. *Science* 343 (): 1490–1492. doi:10.1126/science.1248726. arXiv: 1404.1380 [astro-ph.SR].
- Dipierro, G., et al. 2018. “Rings and gaps in the disc around Elias 24 revealed by ALMA”. *MNRAS* 475 (): 5296–5312. doi:10.1093/mnras/sty181. arXiv: 1801.05812 [astro-ph.EP].
- Dobbs, C. L., et al. 2014. “Formation of Molecular Clouds and Global Conditions for Star Formation”. *Protostars and Planets VI*: 3–26. doi:10.2458/azu_uapress_9780816531240-ch001. arXiv: 1312.3223.
- Dong, R., et al. 2017. “The Sizes and Depletions of the Dust and Gas Cavities in the Transitional Disk J160421.7-213028”. *ApJ* 836, 201 (): 201. doi:10.3847/1538-4357/aa5abf. arXiv: 1701.05189 [astro-ph.SR].
- Draine, B. T. 2006. “On the Submillimeter Opacity of Protoplanetary Disks”. *ApJ* 636 (): 1114–1120. doi:10.1086/498130. eprint: astro-ph/0507292.
- Dullemond, C. P., and C. Dominik. 2005. “Dust coagulation in protoplanetary disks: A rapid depletion of small grains”. *A&A* 434 (): 971–986. doi:10.1051/0004-6361:20042080. eprint: astro-ph/0412117.
- Dullemond, C. P., et al. 2012. *RADMC-3D: A multi-purpose radiative transfer tool*. Astrophysics Source Code Library. ascl: 1202.015.
- Dupuy, T. J., et al. 2016. “Orbital Architectures of Planet-hosting Binaries. I. Forming Five Small Planets in the Truncated Disk of Kepler-444A”. *ApJ* 817, 80 (): 80. doi:10.3847/0004-637X/817/1/80. arXiv: 1512.03428 [astro-ph.EP].
- Dutrey, A., S. Guilloteau, and M. Simon. 1994. “Images of the GG Tauri rotating ring”. *A&A* 286 (): 149–159.
- . 2003. “The BP Tau disk: A missing link between Class II and III objects?” *A&A* 402 (): 1003–1011. doi:10.1051/0004-6361:20030317.
- Dutrey, A., et al. 1996. “Dust and gas distribution around T Tauri stars in Taurus-Auriga. I. Interferometric 2.7mm continuum and ^{13}CO J=1-0 observations”. *A&A* 309 (): 493–504.

- Dutrey, A., et al. 2016. “GG Tau: the ringworld and beyond. Mass accretion and planetary formation in young multiple stellar systems”. *A&A Rev.* 24, 5 (): 5. doi:10.1007/s00159-015-0091-5.
- Dutrey, A., et al. 2014. “Physical and Chemical Structure of Planet-Forming Disks Probed by Millimeter Observations and Modeling”. *Protostars and Planets VI*: 317–338. doi:10.2458/azu_uapress_9780816531240-ch014. arXiv: 1402.3503.
- Duvert, G., et al. 1998. “Disks in the UY Aurigae binary”. *A&A* 332 (): 867–874.
- Eisner, J. A., et al. 2005. “Observations of T Tauri Disks at Sub-AU Radii: Implications for Magnetospheric Accretion and Planet Formation”. *ApJ* 623 (): 952–966. doi:10.1086/428828. eprint: astro-ph/0501308.
- Eisner, J. A., et al. 2018. “Protoplanetary Disk Properties in the Orion Nebula Cluster: Initial Results from Deep, High-resolution ALMA Observations”. *ApJ* 860, 77 (): 77. doi:10.3847/1538-4357/aac3e2. arXiv: 1805.03669 [astro-ph.SR].
- Eisner, J. A., et al. 2016. “Protoplanetary Disks in the Orion OMC1 Region Imaged with ALMA”. *ApJ* 826, 16 (): 16. doi:10.3847/0004-637X/826/1/16. arXiv: 1604.03134 [astro-ph.SR].
- Ercolano, B., C. J. Clarke, and J. J. Drake. 2009. “X-Ray Irradiated Protoplanetary Disk Atmospheres. II. Predictions from Models in Hydrostatic Equilibrium”. *ApJ* 699 (): 1639–1649. doi:10.1088/0004-637X/699/2/1639. arXiv: 0905.1001 [astro-ph.GA].
- Ercolano, B., and J. E. Owen. 2010. “Theoretical spectra of photoevaporating protoplanetary discs: an atlas of atomic and low-ionization emission lines”. *MNRAS* 406 (): 1553–1569. doi:10.1111/j.1365-2966.2010.16798.x. arXiv: 1004.1203.
- Ercolano, B., and I. Pascucci. 2017. “The dispersal of planet-forming discs: theory confronts observations”. *Royal Society Open Science* 4, 170114 (): 170114. doi:10.1098/rsos.170114. arXiv: 1704.00214 [astro-ph.EP].
- Ercolano, B., et al. 2008. “X-Ray-Irradiated Protoplanetary Disk Atmospheres. I. Predicted Emission-Line Spectrum and Photoevaporation”. *ApJ* 688 (): 398–407. doi:10.1086/590490. arXiv: 0805.4625.
- Espaillet, C. C., et al. 2017. “An Incipient Debris Disk in the Chamaeleon I Cloud”. *ApJ* 844, 60 (): 60. doi:10.3847/1538-4357/aa7a10. arXiv: 1706.05032 [astro-ph.SR].
- Espaillet, C., et al. 2014. “An Observational Perspective of Transitional Disks”. *Protostars and Planets VI*: 497–520. doi:10.2458/azu_uapress_9780816531240-ch022. arXiv: 1402.7103 [astro-ph.SR].

- Esplin, T. L., et al. 2018. “A WISE Survey of Circumstellar Disks in the Upper Scorpius Association”. *AJ* 156, 75 (): 75. doi:10.3847/1538-3881/aacce0. arXiv: 1807.07895 [astro-ph.SR].
- Evans, N. J., II, et al. 2009. “The Spitzer c2d Legacy Results: Star-Formation Rates and Efficiencies; Evolution and Lifetimes”. *ApJS* 181 (): 321–350. doi:10.1088/0067-0049/181/2/321. arXiv: 0811.1059.
- Facchini, S., et al. 2017. “Different dust and gas radial extents in protoplanetary disks: consistent models of grain growth and CO emission”. *A&A* 605, A16 (): A16. doi:10.1051/0004-6361/201630329. arXiv: 1705.06235 [astro-ph.SR].
- Fang, M., et al. 2009. “Star and protoplanetary disk properties in Orion’s suburbs”. *A&A* 504 (): 461–489. doi:10.1051/0004-6361/200912468. arXiv: 0907.2380 [astro-ph.SR].
- Fang, M., et al. 2012. “Star formation and disk properties in Pismis 24”. *A&A* 539, A119 (): A119. doi:10.1051/0004-6361/201015914. arXiv: 1201.0833 [astro-ph.SR].
- Fayolle, E. C., et al. 2011. “CO Ice Photodesorption: A Wavelength-dependent Study”. *ApJ* 739, L36 (): L36. doi:10.1088/2041-8205/739/2/L36. arXiv: 1109.0281 [astro-ph.GA].
- Fedele, D., et al. 2018. “ALMA continuum observations of the protoplanetary disk AS 209. Evidence of multiple gaps opened by a single planet”. *A&A* 610, A24 (): A24. doi:10.1051/0004-6361/201731978. arXiv: 1711.05185 [astro-ph.EP].
- Fedele, D., et al. 2017. “ALMA unveils rings and gaps in the protoplanetary system <ASTROBJ>HD 169142</ASTROBJ>: signatures of two giant protoplanets”. *A&A* 600, A72 (): A72. doi:10.1051/0004-6361/201629860. arXiv: 1702.02844 [astro-ph.SR].
- Fedele, D., et al. 2010. “Timescale of mass accretion in pre-main-sequence stars”. *A&A* 510, A72 (): A72. doi:10.1051/0004-6361/200912810. arXiv: 0911.3320 [astro-ph.SR].
- Feiden, G. A., J. Jones, and B. Chaboyer. 2015. “Updating the Dartmouth Stellar Evolution Model Grid: Pre-main-sequence Models & Magnetic Fields”. In *18th Cambridge Workshop on Cool Stars, Stellar Systems, and the Sun*, ed. by G. T. van Belle and H. C. Harris, 18:171–176. Cambridge Workshop on Cool Stars, Stellar Systems, and the Sun. arXiv: 1408.1791 [astro-ph.SR].
- Feigelson, E., et al. 2007. “X-Ray Properties of Young Stars and Stellar Clusters”. *Protostars and Planets V*: 313–328. eprint: astro-ph/0602603.
- Finkbeiner, D. P., M. Davis, and D. J. Schlegel. 1999. “Extrapolation of Galactic Dust Emission at 100 Microns to Cosmic Microwave Background Radiation Frequencies Using FIRAS”. *ApJ* 524 (): 867–886. doi:10.1086/307852. eprint: astro-ph/9905128.

- Fischer, D. A., and G. W. Marcy. 1992. “Multiplicity among M dwarfs”. *ApJ* 396 (): 178–194. doi:10.1086/171708.
- Flaherty, K. M., and J. Muzerolle. 2008. “Evidence for Early Circumstellar Disk Evolution in NGC 2068/71”. *AJ* 135 (): 966–983. doi:10.1088/0004-6256/135/3/966. arXiv: 0712.1601.
- Flaherty, K. M., et al. 2015. “Weak Turbulence in the HD 163296 Protoplanetary Disk Revealed by ALMA CO Observations”. *ApJ* 813, 99 (): 99. doi:10.1088/0004-637X/813/2/99. arXiv: 1510.01375 [astro-ph.SR].
- Font, A. S., et al. 2004. “Photoevaporation of Circumstellar Disks around Young Stars”. *ApJ* 607 (): 890–903. doi:10.1086/383518. eprint: astro-ph/0402241.
- Foreman-Mackey, D., et al. 2013. “emcee: The MCMC Hammer”. *PASP* 125 (): 306. doi:10.1086/670067. arXiv: 1202.3665 [astro-ph.IM].
- Gaia Collaboration et al. 2018. “Gaia Data Release 2. Summary of the contents and survey properties”. *A&A* 616, A1 (): A1. doi:10.1051/0004-6361/201833051. arXiv: 1804.09365.
- Gaia Collaboration et al. 2016. “The Gaia mission”. *A&A* 595, A1 (): A1. doi:10.1051/0004-6361/201629272. arXiv: 1609.04153 [astro-ph.IM].
- Gammie, C. F. 1996. “Layered Accretion in T Tauri Disks”. *ApJ* 457 (): 355. doi:10.1086/176735.
- Garaud, P., et al. 2013. “From Dust to Planetesimals: An Improved Model for Collisional Growth in Protoplanetary Disks”. *ApJ* 764, 146 (): 146. doi:10.1088/0004-637X/764/2/146. arXiv: 1209.0013 [astro-ph.EP].
- Garcia Lopez, R., et al. 2006. “Accretion rates in Herbig Ae stars”. *A&A* 459 (): 837–842. doi:10.1051/0004-6361:20065575. eprint: astro-ph/0609032.
- Gatti, T., et al. 2008. “Accretion properties of T Tauri stars in σ Orionis”. *A&A* 481 (): 423–432. doi:10.1051/0004-6361:20078971. arXiv: 0801.2886.
- Ghez, A. M., G. Neugebauer, and K. Matthews. 1993. “The multiplicity of T Tauri stars in the star forming regions Taurus-Auriga and Ophiuchus-Scorpius: A 2.2 micron speckle imaging survey”. *AJ* 106 (): 2005–2023. doi:10.1086/116782.
- Ginski, C., et al. 2016. “Direct detection of scattered light gaps in the transitional disk around HD 97048 with VLT/SPHERE”. *A&A* 595, A112 (): A112. doi:10.1051/0004-6361/201629265. arXiv: 1609.04027 [astro-ph.EP].
- Girardi, L., et al. 2005. “Star counts in the Galaxy. Simulating from very deep to very shallow photometric surveys with the TRILEGAL code”. *A&A* 436 (): 895–915. doi:10.1051/0004-6361:20042352. eprint: astro-ph/0504047.
- Glassgold, A. E., J. R. Najita, and J. Igea. 2007. “Neon Fine-Structure Line Emission by X-Ray Irradiated Protoplanetary Disks”. *ApJ* 656 (): 515–523. doi:10.1086/510013. eprint: astro-ph/0611094.

- Goldsmith, P. F., E. A. Bergin, and D. C. Lis. 1997. “Carbon Monoxide and Dust Column Densities: The Dust-to-Gas Ratio and Structure of Three Giant Molecular Cloud Cores”. *ApJ* 491 (): 615–637. doi:10.1086/304986.
- Gomez Gonzalez, C. A., et al. 2017. “VIP: Vortex Image Processing Package for High-contrast Direct Imaging”. *AJ* 154, 7 (): 7. doi:10.3847/1538-3881/aa73d7. arXiv: 1705.06184 [astro-ph.IM].
- Gorti, U., C. P. Dullemond, and D. Hollenbach. 2009. “Time Evolution of Viscous Circumstellar Disks due to Photoevaporation by Far-Ultraviolet, Extreme-Ultraviolet, and X-ray Radiation from the Central Star”. *ApJ* 705 (): 1237–1251. doi:10.1088/0004-637X/705/2/1237. arXiv: 0909.1836 [astro-ph.SR].
- Gorti, U., and D. Hollenbach. 2008. “Line Emission from Gas in Optically Thick Dust Disks around Young Stars”. *ApJ* 683 (): 287–303. doi:10.1086/589616. arXiv: 0804.3381.
- . 2004. “Models of Chemistry, Thermal Balance, and Infrared Spectra from Intermediate-Aged Disks around G and K Stars”. *ApJ* 613 (): 424–447. doi:10.1086/422406. eprint: astro-ph/0405244.
- Gorti, U., D. Hollenbach, and C. P. Dullemond. 2015. “The Impact of Dust Evolution and Photoevaporation on Disk Dispersal”. *ApJ* 804, 29 (): 29. doi:10.1088/0004-637X/804/1/29. arXiv: 1502.07369 [astro-ph.EP].
- Gorti, U., et al. 2016. “Disk Dispersal: Theoretical Understanding and Observational Constraints”. *Space Sci. Rev.* 205 (): 125–152. doi:10.1007/s11214-015-0228-x. arXiv: 1512.04622 [astro-ph.EP].
- Gressel, O., et al. 2015. “Global Simulations of Protoplanetary Disks With Ohmic Resistivity and Ambipolar Diffusion”. *ApJ* 801, 84 (): 84. doi:10.1088/0004-637X/801/2/84. arXiv: 1501.05431 [astro-ph.EP].
- Güdel, M., et al. 2010. “On the origin of [NeII] 12.81 μm emission from pre-main sequence stars: Disks, jets, and accretion”. *A&A* 519, A113 (): A113. doi:10.1051/0004-6361/200913971. arXiv: 1006.2848 [astro-ph.SR].
- Guidi, G., et al. 2016. “Dust properties across the CO snowline in the HD 163296 disk from ALMA and VLA observations”. *A&A* 588, A112 (): A112. doi:10.1051/0004-6361/201527516. arXiv: 1601.07542 [astro-ph.SR].
- Guilloteau, S., et al. 2011. “A dual-frequency sub-arcsecond study of proto-planetary disks at mm wavelengths: first evidence for radial variations of the dust properties”. *A&A* 529, A105 (): A105. doi:10.1051/0004-6361/201015209. arXiv: 1103.1296.
- Gullbring, E., et al. 1998. “Disk Accretion Rates for T Tauri Stars”. *ApJ* 492 (): 323–341. doi:10.1086/305032.
- Günther, R., and W. Kley. 2002. “Circumbinary disk evolution”. *A&A* 387 (): 550–559. doi:10.1051/0004-6361:20020407. eprint: astro-ph/0204175.

- Gutermuth, R. A., et al. 2008. “Spitzer Observations of NGC 1333: A Study of Structure and Evolution in a Nearby Embedded Cluster”. *ApJ* 674 (): 336–356. doi:10.1086/524722. arXiv: 0710.1860.
- Gutermuth, R. A., et al. 2004. “The NGC 7129 Young Stellar Cluster: A Combined Spitzer, MMT, and Two Micron All Sky Survey Census of Disks, Protostars, and Outflows”. *ApJS* 154 (): 374–378. doi:10.1086/422358. eprint: astro-ph/0406091.
- Haghighipour, N., and A. P. Boss. 2003. “On Gas Drag-Induced Rapid Migration of Solids in a Nonuniform Solar Nebula”. *ApJ* 598 (): 1301–1311. doi:10.1086/378950. eprint: astro-ph/0305594.
- Hardy, A., et al. 2015. “Probing the final stages of protoplanetary disk evolution with ALMA”. *A&A* 583, A66 (): A66. doi:10.1051/0004-6361/201526504. arXiv: 1504.05562 [astro-ph.EP].
- Harris, R. J., et al. 2012. “A Resolved Census of Millimeter Emission from Taurus Multiple Star Systems”. *ApJ* 751, 115 (): 115. doi:10.1088/0004-637X/751/2/115. arXiv: 1203.6353 [astro-ph.SR].
- Hartigan, P., S. Edwards, and L. Ghandour. 1995. “Disk Accretion and Mass Loss from Young Stars”. *ApJ* 452 (): 736. doi:10.1086/176344.
- Hartigan, P., et al. 1991. “Optical excess emission in T Tauri stars”. *ApJ* 382 (): 617–635. doi:10.1086/170749.
- Hartmann, L. 2001. “On Age Spreads in Star-forming Regions”. *AJ* 121 (): 1030–1039. doi:10.1086/318770.
- Hartmann, L., et al. 1998. “Accretion and the Evolution of T Tauri Disks”. *ApJ* 495 (): 385–400. doi:10.1086/305277.
- Hartmann, L., et al. 2005. “IRAC Observations of Taurus Pre-Main-Sequence Stars”. *ApJ* 629 (): 881–896. doi:10.1086/431472. eprint: astro-ph/0505323.
- Hasegawa, T. I., and E. Herbst. 1993. “Three-Phase Chemical Models of Dense Interstellar Clouds - Gas Dust Particle Mantles and Dust Particle Surfaces”. *MNRAS* 263 (): 589. doi:10.1093/mnras/263.3.589.
- Hayashi, C. 1981. “Structure of the Solar Nebula, Growth and Decay of Magnetic Fields and Effects of Magnetic and Turbulent Viscosities on the Nebula”. *Progress of Theoretical Physics Supplement* 70:35–53. doi:10.1143/PTPS.70.35.
- Helled, R., et al. 2014. “Giant Planet Formation, Evolution, and Internal Structure”. *Protostars and Planets VI*: 643–665. doi:10.2458/azu_uapress_9780816531240-ch028. arXiv: 1311.1142 [astro-ph.EP].
- Hendler, N. P., et al. 2017a. “A likely planet-induced gap in the disk around T Cha”. *ArXiv e-prints* (). arXiv: 1711.09933 [astro-ph.EP].

- Hendler, N. P., et al. 2017b. “Hints for Small Disks around Very Low Mass Stars and Brown Dwarfs”. *ApJ* 841, 116 (1): 116. doi:10.3847/1538-4357/aa71b8. arXiv: 1705.01952 [astro-ph.EP].
- Herczeg, G. J. 2007. “Observational constraints on disk photoevaporation by the central star”. In *Star-Disk Interaction in Young Stars*, ed. by J. Bouvier and I. Appenzeller, 243:147–154. IAU Symposium. doi:10.1017/S1743921307009507.
- Herczeg, G. J., and L. A. Hillenbrand. 2015. “Empirical Isochrones for Low Mass Stars in Nearby Young Associations”. *ApJ* 808, 23 (1): 23. doi:10.1088/0004-637X/808/1/23. arXiv: 1505.06518 [astro-ph.SR].
- . 2008. “UV Excess Measures of Accretion onto Young Very Low Mass Stars and Brown Dwarfs”. *ApJ* 681 (1): 594–625. doi:10.1086/586728. arXiv: 0801.3525.
- Herczeg, G. J., et al. 2002. “The Far-Ultraviolet Spectrum of TW Hydrae. I. Observations of H₂ Fluorescence”. *ApJ* 572 (1): 310–325. doi:10.1086/339731. eprint: astro-ph/0201319.
- Hernández, J., et al. 2007a. “A Spitzer Space Telescope Study of Disks in the Young σ Orionis Cluster”. *ApJ* 662 (1): 1067–1081. doi:10.1086/513735. eprint: astro-ph/0701476.
- Hernández, J., et al. 2008. “A Spitzer View of Protoplanetary Disks in the γ Velorum Cluster”. *ApJ* 686 (1): 1195–1208. doi:10.1086/591224. arXiv: 0806.2639.
- Hernández, J., et al. 2007b. “Spitzer Observations of the Orion OB1 Association: Disk Census in the Low-Mass Stars”. *ApJ* 671 (1): 1784–1799. doi:10.1086/522882. arXiv: 0709.0912.
- Hildebrand, R. H. 1983. “The Determination of Cloud Masses and Dust Characteristics from Submillimetre Thermal Emission”. *QJRAS* 24 (1): 267.
- Hillenbrand, L. A. 2008. “Disk-dispersal and planet-formation timescales”. *Physica Scripta Volume T* 130, no. 1, 014024 (1): 014024. doi:10.1088/0031-8949/2008/T130/014024. arXiv: 0805.0386.
- Hirsch, L. A., et al. 2017. “Assessing the Effect of Stellar Companions from High-resolution Imaging of Kepler Objects of Interest”. *AJ* 153, 117 (1): 117. doi:10.3847/1538-3881/153/3/117. arXiv: 1701.06577 [astro-ph.EP].
- Hogerheijde, M. R., et al. 2016. “Steepening of the 820 μ m continuum surface brightness profile signals dust evolution in TW Hydrae’s disk”. *A&A* 586, A99 (1): A99. doi:10.1051/0004-6361/201527754. arXiv: 1512.05553 [astro-ph.SR].
- Hollenbach, D., and U. Gorti. 2009. “Diagnostic Line Emission from Extreme Ultraviolet and X-ray-illuminated Disks and Shocks Around Low-mass Stars”. *ApJ* 703 (1): 1203–1223. doi:10.1088/0004-637X/703/2/1203. arXiv: 0908.1975 [astro-ph.SR].

- Hollenbach, D., et al. 1994. “Photoevaporation of disks around massive stars and application to ultracompact H II regions”. *ApJ* 428 (): 654–669. doi:10.1086/174276.
- Holman, M. J., and P. A. Wiegert. 1999. “Long-Term Stability of Planets in Binary Systems”. *AJ* 117 (): 621–628. doi:10.1086/300695. eprint: astro-ph/9809315.
- Howell, S. B., et al. 2014. “The K2 Mission: Characterization and Early Results”. *PASP* 126 (): 398. doi:10.1086/676406. arXiv: 1402.5163 [astro-ph.IM].
- Hoyle, F. 1960. “The Origin of the Solar Nebula”. *QJRAS* 1 (): 28.
- Huber, K. P., and G. Herzberg. 1979. *Molecular Spectra and Molecular Structure—IV. Constants of Diatomic Molecules*. New York: Van Nostrand Reinhold.
- Hughes, A. M., G. Duchene, and B. Matthews. 2018. “Debris Disks: Structure, Composition, and Variability”. *ArXiv e-prints* (). arXiv: 1802.04313 [astro-ph.EP].
- Hughes, A. M., et al. 2007. “An Inner Hole in the Disk around TW Hydrae Resolved in 7 mm Dust Emission”. *ApJ* 664 (): 536–542. doi:10.1086/518885. arXiv: 0704.2422.
- Hughes, A. M., et al. 2008. “Gas and Dust Emission at the Outer Edge of Protoplanetary Disks”. *ApJ* 678 (): 1119–1126. doi:10.1086/586730. arXiv: 0801.4763.
- Hughes, A. M., et al. 2017. “Radial Surface Density Profiles of Gas and Dust in the Debris Disk around 49 Ceti”. *ApJ* 839, 86 (): 86. doi:10.3847/1538-4357/aa6b04. arXiv: 1704.01972 [astro-ph.EP].
- Hughes, A. M., et al. 2009. “Stringent Limits on the Polarized Submillimeter Emission from Protoplanetary Disks”. *ApJ* 704 (): 1204–1217. doi:10.1088/0004-637X/704/2/1204. arXiv: 0909.1345 [astro-ph.SR].
- Hughes, A. M., et al. 2010. “Structure and Composition of Two Transitional Circumstellar Disks in Corona Australis”. *AJ* 140 (): 887–896. doi:10.1088/0004-6256/140/3/887. arXiv: 1007.3267 [astro-ph.SR].
- Isella, A., J. M. Carpenter, and A. I. Sargent. 2010. “Investigating Planet Formation in Circumstellar Disks: CARMA Observations of Ry Tau and Dg Tau”. *ApJ* 714 (): 1746–1761. doi:10.1088/0004-637X/714/2/1746. arXiv: 1003.4318 [astro-ph.SR].
- . 2009. “Structure and Evolution of Pre-main-sequence Circumstellar Disks”. *ApJ* 701 (): 260–282. doi:10.1088/0004-637X/701/1/260. arXiv: 0906.2227 [astro-ph.SR].
- Isella, A., et al. 2007. “Millimeter imaging of HD 163296: probing the disk structure and kinematics”. *A&A* 469 (): 213–222. doi:10.1051/0004-6361:20077385. arXiv: 0704.0616.

- Isella, A., et al. 2010. “Millimeter Imaging of MWC 758: Probing the Disk Structure and Kinematics”. *ApJ* 725 (): 1735–1741. doi:10.1088/0004-637X/725/2/1735. arXiv: 1010.3016 [astro-ph.SR].
- Isella, A., et al. 2016. “Ringed Structures of the HD 163296 Protoplanetary Disk Revealed by ALMA”. *Physical Review Letters* 117, no. 25, 251101 (): 251101. doi:10.1103/PhysRevLett.117.251101.
- Jang-Condell, H. 2015. “On the Likelihood of Planet Formation in Close Binaries”. *ApJ* 799, 147 (): 147. doi:10.1088/0004-637X/799/2/147. arXiv: 1501.00617 [astro-ph.EP].
- Jensen, E. L. N., R. D. Mathieu, and G. A. Fuller. 1994. “A connection between submillimeter continuum flux and separation in young binaries”. *ApJ* 429 (): L29–L32. doi:10.1086/187405. eprint: astro-ph/9404034.
- . 1996. “The Connection between Submillimeter Continuum Flux and Binary Separation in Young Binaries: Evidence of Interaction between Stars and Disks”. *ApJ* 458 (): 312. doi:10.1086/176814. eprint: astro-ph/9508099.
- Jensen, E. L. N., et al. 2007. “Periodic Accretion from a Circumbinary Disk in the Young Binary UZ Tau E”. *AJ* 134 (): 241–251. doi:10.1086/518408. arXiv: 0704.0307.
- Jewitt, D. 2008. “Kuiper Belt and Comets: An Observational Perspective”. In *Saas-Fee Advanced Course 35: Trans-Neptunian Objects and Comets*, ed. by D. Jewitt, A. Morbidelli, and H. Rauer, 132.
- Johansen, A., H. Klahr, and T. Henning. 2011. “High-resolution simulations of planetesimal formation in turbulent protoplanetary discs”. *A&A* 529, A62 (): A62. doi:10.1051/0004-6361/201015979. arXiv: 1010.4757 [astro-ph.EP].
- Johansen, A., A. Youdin, and H. Klahr. 2009. “Zonal Flows and Long-lived Axisymmetric Pressure Bumps in Magnetorotational Turbulence”. *ApJ* 697 (): 1269–1289. doi:10.1088/0004-637X/697/2/1269. arXiv: 0811.3937.
- Johansen, A., et al. 2007. “Rapid planetesimal formation in turbulent circumstellar disks”. *Nature* 448 (): 1022–1025. doi:10.1038/nature06086. arXiv: 0708.3890.
- Johansen, A., et al. 2014. “The Multifaceted Planetesimal Formation Process”. *Protostars and Planets VI*: 547–570. doi:10.2458/azu_uapress_9780816531240-ch024. arXiv: 1402.1344 [astro-ph.EP].
- Kalas, P., et al. 2013. “STIS Coronagraphic Imaging of Fomalhaut: Main Belt Structure and the Orbit of Fomalhaut b”. *ApJ* 775, 56 (): 56. doi:10.1088/0004-637X/775/1/56. arXiv: 1305.2222 [astro-ph.EP].
- Kama, M., et al. 2016. “Observations and modelling of CO and [C I] in protoplanetary disks. First detections of [C I] and constraints on the carbon abundance”. *A&A* 588, A108 (): A108. doi:10.1051/0004-6361/201526791. arXiv: 1601.01449 [astro-ph.SR].

- Kant, I. 1755. In *Allgemeine Naturgeschichte und Theorie des Himmels*.
- Kato, M. T., M. Fujimoto, and S. Ida. 2012. “Planetesimal Formation at the Boundary between Steady Super/Sub-Keplerian Flow Created by Inhomogeneous Growth of Magnetorotational Instability”. *ApJ* 747, 11 (): 11. doi:10.1088/0004-637X/747/1/11. arXiv: 1112.5264 [astro-ph.EP].
- Kelly, B. C. 2007. “Some Aspects of Measurement Error in Linear Regression of Astronomical Data”. *ApJ* 665 (): 1489–1506. doi:10.1086/519947. arXiv: 0705.2774.
- Kennedy, G. M., and S. J. Kenyon. 2009. “Stellar Mass Dependent Disk Dispersal”. *ApJ* 695 (): 1210–1226. doi:10.1088/0004-637X/695/2/1210. arXiv: 0901.2603 [astro-ph.SR].
- Kennedy, G. M., and M. C. Wyatt. 2014. “Do two-temperature debris discs have multiple belts?” *MNRAS* 444 (): 3164–3182. doi:10.1093/mnras/stu1665. arXiv: 1408.4116 [astro-ph.EP].
- Kenyon, S. J., and L. Hartmann. 1995. “Pre-Main-Sequence Evolution in the Taurus-Auriga Molecular Cloud”. *ApJS* 101 (): 117. doi:10.1086/192235.
- . 1987. “Spectral energy distributions of T Tauri stars - Disk flaring and limits on accretion”. *ApJ* 323 (): 714–733. doi:10.1086/165866.
- Kitamura, Y., et al. 2002. “Investigation of the Physical Properties of Protoplanetary Disks around T Tauri Stars by a 1 Arcsecond Imaging Survey: Evolution and Diversity of the Disks in Their Accretion Stage”. *ApJ* 581 (): 357–380. doi:10.1086/344223.
- Köhler, R., and C. Leinert. 1998. “Multiplicity of T Tauri stars in Taurus after ROSAT”. *A&A* 331 (): 977–988.
- Köhler, R., et al. 2000. “Multiplicity of X-ray selected T Tauri stars in the Scorpius-Centaurus OB association”. *A&A* 356 (): 541–558.
- Kokubo, E., and S. Ida. 2002. “Formation of Protoplanet Systems and Diversity of Planetary Systems”. *ApJ* 581 (): 666–680. doi:10.1086/344105.
- Kóspál, Á., et al. 2013. “ALMA Observations of the Molecular Gas in the Debris Disk of the 30 Myr Old Star HD 21997”. *ApJ* 776, 77 (): 77. doi:10.1088/0004-637X/776/2/77. arXiv: 1310.5068 [astro-ph.SR].
- Kral, Q., et al. 2016. “A self-consistent model for the evolution of the gas produced in the debris disc of β Pictoris”. *MNRAS* 461 (): 845–858. doi:10.1093/mnras/stw1361. arXiv: 1606.01247 [astro-ph.EP].
- Kral, Q., et al. 2017. “Predictions for the secondary CO, C and O gas content of debris discs from the destruction of volatile-rich planetesimals”. *MNRAS* 469 (): 521–550. doi:10.1093/mnras/stx730. arXiv: 1703.10693 [astro-ph.EP].

- Kraus, A. L., and L. A. Hillenbrand. 2012. “Multiple Star Formation to the Bottom of the Initial Mass Function”. *ApJ* 757, 141 (): 141. doi:10.1088/0004-637X/757/2/141. arXiv: 1206.4995 [astro-ph.SR].
- . 2009. “The Coevality of Young Binary Systems”. *ApJ* 704 (): 531–547. doi:10.1088/0004-637X/704/1/531. arXiv: 0909.0509 [astro-ph.SR].
- Kraus, A. L., et al. 2008. “Mapping the Shores of the Brown Dwarf Desert. I. Upper Scorpius”. *ApJ* 679 (): 762–782. doi:10.1086/587435. arXiv: 0801.2387.
- Kraus, A. L., et al. 2011. “Mapping the Shores of the Brown Dwarf Desert. II. Multiple Star Formation in Taurus-Auriga”. *ApJ* 731, 8 (): 8. doi:10.1088/0004-637X/731/1/8. arXiv: 1101.4016 [astro-ph.SR].
- Kraus, A. L., et al. 2016. “The Impact of Stellar Multiplicity on Planetary Systems. I. The Ruinous Influence of Close Binary Companions”. *AJ* 152, 8 (): 8. doi:10.3847/0004-6256/152/1/8. arXiv: 1604.05744 [astro-ph.EP].
- Kraus, A. L., et al. 2015. “The Mass-Radius Relation of Young Stars. I. USco 5, an M4.5 Eclipsing Binary in Upper Scorpius Observed by K2”. *ApJ* 807, 3 (): 3. doi:10.1088/0004-637X/807/1/3. arXiv: 1505.02446 [astro-ph.SR].
- Kraus, A. L., et al. 2012. “The Role of Multiplicity in Disk Evolution and Planet Formation”. *ApJ* 745, 19 (): 19. doi:10.1088/0004-637X/745/1/19. arXiv: 1109.4141 [astro-ph.EP].
- Kretke, K. A., and D. N. C. Lin. 2007. “Grain Retention and Formation of Planetesimals near the Snow Line in MRI-driven Turbulent Protoplanetary Disks”. *ApJ* 664 (): L55–L58. doi:10.1086/520718. arXiv: 0706.1272.
- Kuruwita, R. L., et al. 2018. “Multiplicity of disc-bearing stars in Upper Scorpius and Upper Centaurus-Lupus”. *MNRAS* 480 (): 5099–5112. doi:10.1093/mnras/sty2108. arXiv: 1808.00620 [astro-ph.EP].
- Lada, C. J., and B. A. Wilking. 1984. “The nature of the embedded population in the Rho Ophiuchi dark cloud - Mid-infrared observations”. *ApJ* 287 (): 610–621. doi:10.1086/162719.
- Lada, C. J., et al. 2006. “Spitzer Observations of IC 348: The Disk Population at 2-3 Million Years”. *AJ* 131 (): 1574–1607. doi:10.1086/499808. eprint: astro-ph/0511638.
- Lafrenière, D., et al. 2008. “A Multiplicity Census of Young Stars in Chamaeleon I”. *ApJ* 683 (): 844–861. doi:10.1086/590239. arXiv: 0803.0561.
- Lafrenière, D., et al. 2014. “An Adaptive Optics Multiplicity Census of Young Stars in Upper Scorpius”. *ApJ* 785, 47 (): 47. doi:10.1088/0004-637X/785/1/47.
- Lahuis, F., et al. 2007. “c2d Spitzer IRS Spectra of Disks around T Tauri Stars. III. [Ne II], [Fe I], and H₂ Gas-Phase Lines”. *ApJ* 665 (): 492–511. doi:10.1086/518931. arXiv: 0704.2305.

- Laplace, P.S. 1796. In *Exposition du Système du Monde*.
- Lauer, T. R., et al. 1995. “The Centers of Early-Type Galaxies with HST.I.An Observational Survey”. *AJ* 110 (): 2622. doi:10.1086/117719.
- Law, C. J., et al. 2017. “An SMA Continuum Survey of Circumstellar Disks in the Serpens Star-forming Region”. *AJ* 154, 255 (): 255. doi:10.3847/1538-3881/aa9752. arXiv: 1711.01266.
- Lawrence, A., et al. 2007. “The UKIRT Infrared Deep Sky Survey (UKIDSS)”. *MNRAS* 379 (): 1599–1617. doi:10.1111/j.1365-2966.2007.12040.x. eprint: astro-ph/0604426.
- Lee, N., J. P. Williams, and L. A. Cieza. 2011. “Protoplanetary Disk Masses in IC348: A Rapid Decline in the Population of Small Dust Grains After 1 Myr”. *ApJ* 736, 135 (): 135. doi:10.1088/0004-637X/736/2/135. arXiv: 1105.2046 [astro-ph.SR].
- Leinert, C., et al. 1993. “A systematic approach for young binaries in Taurus”. *A&A* 278 (): 129–149.
- Li, A., and B. T. Draine. 2001. “Infrared Emission from Interstellar Dust. II. The Diffuse Interstellar Medium”. *ApJ* 554 (): 778–802. doi:10.1086/323147. eprint: astro-ph/0011319.
- Li, Z.-Y., et al. 2014. “The Earliest Stages of Star and Planet Formation: Core Collapse, and the Formation of Disks and Outflows”. *Protostars and Planets VI*: 173–194. doi:10.2458/azu_uapress_9780816531240-ch008. arXiv: 1401.2219 [astro-ph.SR].
- Lodders, K. 2003. “Solar System Abundances and Condensation Temperatures of the Elements”. *ApJ* 591 (): 1220–1247. doi:10.1086/375492.
- Lodieu, N., et al. 2015. “An eclipsing double-line spectroscopic binary at the stellar/substellar boundary in the Upper Scorpius OB association”. *A&A* 584, A128 (): A128. doi:10.1051/0004-6361/201527464. arXiv: 1511.03083 [astro-ph.SR].
- Lohmann, A. W., G. Weigelt, and B. Wirtitzer. 1983. “Speckle masking in astronomy - Triple correlation theory and applications”. *Appl. Opt.* 22 (): 4028–4037. doi:10.1364/AO.22.004028.
- Lommen, D., et al. 2007. “Investigating grain growth in disks around southern T Tauri stars at millimetre wavelengths”. *A&A* 462 (): 211–220. doi:10.1051/0004-6361:20066255. eprint: astro-ph/0610667.
- Lommen, D., et al. 2009. “Large grains in discs around young stars: ATCA observations of WW Chamaeleontis, RU Lupi, and CS Chamaeleontis”. *A&A* 495 (): 869–879. doi:10.1051/0004-6361:200810999. arXiv: 0812.3849.

- Long, F., et al. 2017. “An ALMA Survey of CO Isotopologue Emission from Protoplanetary Disks in Chamaeleon I”. *ApJ* 844, 99 (): 99. doi:10.3847/1538-4357/aa78fc. arXiv: 1706.03320 [astro-ph.SR].
- Long, F., et al. 2018. “An ALMA Survey of Faint Disks in the Chamaeleon I Star-forming Region: Why Are Some Class II Disks so Faint?” *ApJ* 863, 61 (): 61. doi:10.3847/1538-4357/aacce9. arXiv: 1806.04826 [astro-ph.SR].
- Loomis, R. A., et al. 2017. “A Multi-ringed, Modestly Inclined Protoplanetary Disk around AA Tau”. *ApJ* 840, 23 (): 23. doi:10.3847/1538-4357/aa6c63. arXiv: 1704.02006 [astro-ph.EP].
- Lubow, S. H., and G. D’Angelo. 2006. “Gas Flow across Gaps in Protoplanetary Disks”. *ApJ* 641 (): 526–533. doi:10.1086/500356. eprint: astro-ph/0512292.
- Luhman, K. L. 1999. “Young Low-Mass Stars and Brown Dwarfs in IC 348”. *ApJ* 525 (): 466–481. doi:10.1086/307902. eprint: astro-ph/9905287.
- Luhman, K. L., and E. E. Mamajek. 2012. “The Disk Population of the Upper Scorpius Association”. *ApJ* 758, 31 (): 31. doi:10.1088/0004-637X/758/1/31. arXiv: 1209.5433.
- Luhman, K. L., et al. 2018. “New Young Stars and Brown Dwarfs in the Upper Scorpius Association”. *AJ* 156, 76 (): 76. doi:10.3847/1538-3881/aacc6d. arXiv: 1807.07955 [astro-ph.SR].
- Luhman, K. L., et al. 2010. “The Disk Population of the Taurus Star-Forming Region”. *ApJS* 186 (): 111–174. doi:10.1088/0067-0049/186/1/111. arXiv: 0911.5457.
- Lynden-Bell, D., and J. E. Pringle. 1974. “The evolution of viscous discs and the origin of the nebular variables.” *MNRAS* 168 (): 603–637. doi:10.1093/mnras/168.3.603.
- Lyra, W., et al. 2009. “Standing on the shoulders of giants. Trojan Earths and vortex trapping in low mass self-gravitating protoplanetary disks of gas and solids”. *A&A* 493 (): 1125–1139. doi:10.1051/0004-6361:200810797. arXiv: 0810.3192.
- MacGregor, M. A., et al. 2017. “A Complete ALMA Map of the Fomalhaut Debris Disk”. *ApJ* 842, 8 (): 8. doi:10.3847/1538-4357/aa71ae. arXiv: 1705.05867 [astro-ph.EP].
- Malbet, F., and C. Bertout. 1991. “The vertical structure of T Tauri accretion disks. I - Heating by the central star”. *ApJ* 383 (): 814–819. doi:10.1086/170839.
- Mangum, J. G., and Y. L. Shirley. 2015. “How to Calculate Molecular Column Density”. *PASP* 127 (): 266. doi:10.1086/680323. arXiv: 1501.01703 [astro-ph.IM].
- Mannings, V., and J. P. Emerson. 1994. “Dust in discs around T Tauri stars: Grain growth?” *MNRAS* 267 (): 361–378. doi:10.1093/mnras/267.2.361.

- Martí-Vidal, I., et al. 2014. “UVMULTIFIT: A versatile tool for fitting astronomical radio interferometric data”. *A&A* 563, A136 (): A136. doi:10.1051/0004-6361/201322633. arXiv: 1401.4984 [astro-ph.IM].
- Mathews, G. S., et al. 2013. “A Herschel PACS survey of the dust and gas in Upper Scorpius disks”. *A&A* 558, A66 (): A66. doi:10.1051/0004-6361/201321228. arXiv: 1308.6020 [astro-ph.SR].
- Mathews, G. S., et al. 2012. “The Late Stages of Protoplanetary Disk Evolution: A Millimeter Survey of Upper Scorpius”. *ApJ* 745, 23 (): 23. doi:10.1088/0004-637X/745/1/23. arXiv: 1111.0101 [astro-ph.SR].
- Mathieu, R. D., et al. 1997. “The Classical T Tauri Spectroscopic Binary DQ Tau.I.Orbital Elements and Light Curves”. *AJ* 113 (): 1841. doi:10.1086/118395.
- Matrà, L., et al. 2017. “Detection of Exocometary CO within the 440 Myr Old Fomalhaut Belt: A Similar CO+CO₂ Ice Abundance in Exocomets and Solar System Comets”. *ApJ* 842, 9 (): 9. doi:10.3847/1538-4357/aa71b4. arXiv: 1705.05868 [astro-ph.EP].
- Matthews, B. C., et al. 2014. “Observations, Modeling, and Theory of Debris Disks”. *Protostars and Planets VI*: 521–544. doi:10.2458/azu_uapress_9780816531240-ch023. arXiv: 1401.0743 [astro-ph.SR].
- Mawet, D., et al. 2014. “Fundamental Limitations of High Contrast Imaging Set by Small Sample Statistics”. *ApJ* 792, 97 (): 97. doi:10.1088/0004-637X/792/2/97. arXiv: 1407.2247 [astro-ph.IM].
- Mayama, S., et al. 2012. “Subaru Imaging of Asymmetric Features in a Transitional Disk in Upper Scorpius”. *ApJ* 760, L26 (): L26. doi:10.1088/2041-8205/760/2/L26. arXiv: 1211.3284 [astro-ph.SR].
- McCaughrean, M. J., and C. R. O’dell. 1996. “Direct Imaging of Circumstellar Disks in the Orion Nebula”. *AJ* 111 (): 1977. doi:10.1086/117934.
- McClure, M. K., et al. 2016. “Mass Measurements in Protoplanetary Disks from Hydrogen Deuteride”. *ApJ* 831, 167 (): 167. doi:10.3847/0004-637X/831/2/167. arXiv: 1608.07817 [astro-ph.SR].
- McMullin, J. P., et al. 2007. “CASA Architecture and Applications”. In *Astronomical Data Analysis Software and Systems XVI*, ed. by R. A. Shaw, F. Hill, and D. J. Bell, 376:127. Astronomical Society of the Pacific Conference Series.
- Megeath, S. T., et al. 2005. “Spitzer/IRAC Photometry of the η Chameleontis Association”. *ApJ* 634 (): L113–L116. doi:10.1086/498503. eprint: astro-ph/0511314.
- Menu, J., et al. 2014. “On the structure of the transition disk around TW Hydrae”. *A&A* 564, A93 (): A93. doi:10.1051/0004-6361/201322961. arXiv: 1402.6597 [astro-ph.SR].

- Metchev, S. A., and L. A. Hillenbrand. 2009. “The Palomar/Keck Adaptive Optics Survey of Young Solar Analogs: Evidence for a Universal Companion Mass Function”. *ApJS* 181 (0): 62–109. doi:10.1088/0067-0049/181/1/62. arXiv: 0808.2982.
- Miguel, Y., O. M. Guilera, and A. Brunini. 2011. “The role of the initial surface density profiles of the disc on giant planet formation: comparing with observations”. *MNRAS* 412 (0): 2113–2124. doi:10.1111/j.1365-2966.2010.17887.x. arXiv: 1010.5061 [astro-ph.EP].
- Miotello, A. 2018. “Lupus disks with faint CO isotopologues: low gas/dust or high carbon depletion?” In *IAU Symposium*, ed. by M. Cunningham, T. Millar, and Y. Aikawa, 332:124–128. IAU Symposium. doi:10.1017/S1743921317006603.
- Miotello, A., S. Bruderer, and E. F. van Dishoeck. 2014. “Protoplanetary disk masses from CO isotopologue line emission”. *A&A* 572, A96 (0): A96. doi:10.1051/0004-6361/201424712. arXiv: 1410.2093 [astro-ph.SR].
- Miotello, A., et al. 2017. “Lupus disks with faint CO isotopologues: low gas/dust or high carbon depletion?” *A&A* 599, A113 (0): A113. doi:10.1051/0004-6361/201629556. arXiv: 1612.01538 [astro-ph.SR].
- Mohanty, S., R. Jayawardhana, and G. Basri. 2005. “The T Tauri Phase Down to Nearly Planetary Masses: Echelle Spectra of 82 Very Low Mass Stars and Brown Dwarfs”. *ApJ* 626 (0): 498–522. doi:10.1086/429794. eprint: astro-ph/0502155.
- Montesinos, B., et al. 2016. “Incidence of debris discs around FGK stars in the solar neighbourhood”. *A&A* 593, A51 (0): A51. doi:10.1051/0004-6361/201628329. arXiv: 1605.05837 [astro-ph.SR].
- Mordasini, C., et al. 2010. “Theory of planet formation”. *ArXiv e-prints* (0). arXiv: 1012.5281 [astro-ph.EP].
- Morishima, R. 2012. “Gap opening beyond dead zones by photoevaporation”. *MNRAS* 420 (0): 2851–2858. doi:10.1111/j.1365-2966.2011.19940.x. arXiv: 1110.2250 [astro-ph.EP].
- Motte, F., P. Andre, and R. Neri. 1998. “The initial conditions of star formation in the rho Ophiuchi main cloud: wide-field millimeter continuum mapping”. *A&A* 336 (0): 150–172.
- Müller, H. S. P., et al. 2001. “The Cologne Database for Molecular Spectroscopy, CDMS”. *A&A* 370 (0): L49–L52. doi:10.1051/0004-6361:20010367.
- Müller, H. S. P., et al. 2005. “The Cologne Database for Molecular Spectroscopy, CDMS: a useful tool for astronomers and spectroscopists”. *Journal of Molecular Structure* 742 (0): 215–227. doi:10.1016/j.molstruc.2005.01.027.
- Muñoz, D. J., and D. Lai. 2016. “Pulsed Accretion onto Eccentric and Circular Binaries”. *ApJ* 827, 43 (0): 43. doi:10.3847/0004-637X/827/1/43. arXiv: 1604.00004 [astro-ph.EP].

- Muzerolle, J., et al. 2003. “Accretion in Young Stellar/Substellar Objects”. *ApJ* 592 (): 266–281. doi:10.1086/375704. eprint: astro-ph/0304078.
- Najita, J. R., et al. 2009. “High-Resolution Spectroscopy of [Ne II] Emission from AA Tau and GM Aur”. *ApJ* 697 (): 957–963. doi:10.1088/0004-637X/697/1/957. arXiv: 0904.1597 [astro-ph.GA].
- Natta, A., et al. 2004. “Accretion in brown dwarfs: An infrared view”. *A&A* 424 (): 603–612. doi:10.1051/0004-6361:20040356. eprint: astro-ph/0406106.
- Nesvorný, D., et al. 2011. “Dynamical Model for the Zodiacal Cloud and Sporadic Meteors”. *ApJ* 743, 129 (): 129. doi:10.1088/0004-637X/743/2/129. arXiv: 1109.2983 [astro-ph.EP].
- Nuernberger, D., R. Chini, and H. Zinnecker. 1997. “A 1.3mm dust continuum survey of H α selected T Tauri stars in Lupus.” *A&A* 324 (): 1036–1045.
- Öberg, K. I. 2016. “Laboratory constraints on ice formation, restructuring and desorption”. *IAU Focus Meeting 29*, no. 27 (): 309–312. doi:10.1017/S1743921316003136.
- Öberg, K. I., S. Bottinelli, and E. F. van Dishoeck. 2009. “Cold gas as an ice diagnostic toward low mass protostars”. *A&A* 494 (): L13–L16. doi:10.1051/0004-6361:200811228. arXiv: 0901.1019 [astro-ph.SR].
- Öberg, K. I., E. F. van Dishoeck, and H. Linnartz. 2009. “Photodesorption of ices I: CO, N₂, and CO₂”. *A&A* 496 (): 281–293. doi:10.1051/0004-6361/200810207. arXiv: 0809.1333.
- Öberg, K. I., et al. 2015. “Double DCO⁺ Rings Reveal CO Ice Desorption in the Outer Disk Around IM Lup”. *ApJ* 810, 112 (): 112. doi:10.1088/0004-637X/810/2/112. arXiv: 1508.07296.
- O’deh, C. R., and Z. Wen. 1994. “Postrefurbishment mission Hubble Space Telescope images of the core of the Orion Nebula: Proplyds, Herbig-Haro objects, and measurements of a circumstellar disk”. *ApJ* 436 (): 194–202. doi:10.1086/174892.
- O’deh, C. R., Z. Wen, and X. Hu. 1993. “Discovery of new objects in the Orion nebula on HST images - Shocks, compact sources, and protoplanetary disks”. *ApJ* 410 (): 696–700. doi:10.1086/172786.
- Osterbrock, D. E., and G. J. Ferland. 2006. *Astrophysics of gaseous nebulae and active galactic nuclei*.
- Owen, J. E., C. J. Clarke, and B. Ercolano. 2012. “On the theory of disc photoevaporation”. *MNRAS* 422 (): 1880–1901. doi:10.1111/j.1365-2966.2011.20337.x. arXiv: 1112.1087 [astro-ph.SR].
- Owen, J. E., B. Ercolano, and C. J. Clarke. 2011. “Protoplanetary disc evolution and dispersal: the implications of X-ray photoevaporation”. *MNRAS* 412 (): 13–25. doi:10.1111/j.1365-2966.2010.17818.x. arXiv: 1010.0826 [astro-ph.SR].

- Owen, J. E., et al. 2010. “Radiation-hydrodynamic models of X-ray and EUV photoevaporating protoplanetary discs”. *MNRAS* 401 (): 1415–1428. doi:10.1111/j.1365-2966.2009.15771.x. arXiv: 0909.4309 [astro-ph.SR].
- Panić, O., et al. 2009. “A break in the gas and dust surface density of the disc around the T Tauri star IM Lupi”. *A&A* 501 (): 269–278. doi:10.1051/0004-6361/200911883. arXiv: 0904.1127 [astro-ph.EP].
- Papaloizou, J., and J. E. Pringle. 1977. “Tidal torques on accretion discs in close binary systems”. *MNRAS* 181 (): 441–454. doi:10.1093/mnras/181.3.441.
- Pascucci, I., and M. Sterzik. 2009. “Evidence for Disk Photoevaporation Driven by the Central Star”. *ApJ* 702 (): 724–732. doi:10.1088/0004-637X/702/1/724. arXiv: 0908.2367 [astro-ph.EP].
- Pascucci, I., and S. Tachibana. 2010. “The Clearing of Protoplanetary Disks and of the Protosolar Nebula”. In *Protoplanetary Dust: Astrophysical and Cosmochemical Perspectives*, ed. by D. A. Apai and D. S. Lauretta, 263–298.
- Pascucci, I., et al. 2016. “A Steeper than Linear Disk Mass-Stellar Mass Scaling Relation”. *ApJ* 831, 125 (): 125. doi:10.3847/0004-637X/831/2/125. arXiv: 1608.03621 [astro-ph.EP].
- Pascucci, I., et al. 2007. “Detection of [Ne II] Emission from Young Circumstellar Disks”. *ApJ* 663 (): 383–393. doi:10.1086/518535. eprint: astro-ph/0703616.
- Pascucci, I., et al. 2006. “Formation and Evolution of Planetary Systems: Upper Limits to the Gas Mass in Disks around Sun-like Stars”. *ApJ* 651 (): 1177–1193. doi:10.1086/507761. eprint: astro-ph/0606669.
- Pecaut, M. J., and E. E. Mamajek. 2013. “Intrinsic Colors, Temperatures, and Bolometric Corrections of Pre-main-sequence Stars”. *ApJS* 208, 9 (): 9. doi:10.1088/0067-0049/208/1/9. arXiv: 1307.2657 [astro-ph.SR].
- Pecaut, M. J., E. E. Mamajek, and E. J. Bubar. 2012. “A Revised Age for Upper Scorpius and the Star Formation History among the F-type Members of the Scorpius-Centaurus OB Association”. *ApJ* 746, 154 (): 154. doi:10.1088/0004-637X/746/2/154. arXiv: 1112.1695 [astro-ph.SR].
- Pérez, L. M., et al. 2012. “Constraints on the Radial Variation of Grain Growth in the AS 209 Circumstellar Disk”. *ApJ* 760, L17 (): L17. doi:10.1088/2041-8205/760/1/L17. arXiv: 1210.5252 [astro-ph.SR].
- Pérez, L. M., et al. 2015. “Grain Growth in the Circumstellar Disks of the Young Stars CY Tau and DoAr 25”. *ApJ* 813, 41 (): 41. doi:10.1088/0004-637X/813/1/41. arXiv: 1509.07520 [astro-ph.SR].
- Pérez, L. M., et al. 2016. “Spiral density waves in a young protoplanetary disk”. *Science* 353 (): 1519–1521. doi:10.1126/science.aaf8296. arXiv: 1610.05139.

- Pichardo, B., L. S. Sparke, and L. A. Aguilar. 2005. "Circumstellar and circumbinary discs in eccentric stellar binaries". *MNRAS* 359 (): 521–530. doi:10.1111/j.1365-2966.2005.08905.x. eprint: astro-ph/0501244.
- Piétu, V., S. Guilloteau, and A. Dutrey. 2005. "Sub-arcsec imaging of the AB Aur molecular disk and envelope at millimeter wavelengths: a non Keplerian disk". *A&A* 443 (): 945–954. doi:10.1051/0004-6361:20042050. eprint: astro-ph/0504023.
- Piétu, V., et al. 2014. "Faint disks around classical T Tauri stars: Small but dense enough to form planets". *A&A* 564, A95 (): A95. doi:10.1051/0004-6361/201322388. arXiv: 1402.5312 [astro-ph.EP].
- Pinilla, P., et al. 2018. "Homogeneous Analysis of the Dust Morphology of Transition Disks Observed with ALMA: Investigating Dust Trapping and the Origin of the Cavities". *ApJ* 859, 32 (): 32. doi:10.3847/1538-4357/aabf94. arXiv: 1804.07301 [astro-ph.EP].
- Pinilla, P., et al. 2012. "Trapping dust particles in the outer regions of protoplanetary disks". *A&A* 538, A114 (): A114. doi:10.1051/0004-6361/201118204. arXiv: 1112.2349 [astro-ph.EP].
- Pinilla, P., et al. 2015. "Variability and dust filtration in the transition disk J160421.7-213028 observed in optical scattered light". *A&A* 584, L4 (): L4. doi:10.1051/0004-6361/201526981. arXiv: 1510.00412 [astro-ph.EP].
- Pohl, A., et al. 2017. "The Circumstellar Disk HD 169142: Gas, Dust, and Planets Acting in Concert?" *ApJ* 850, 52 (): 52. doi:10.3847/1538-4357/aa94c2. arXiv: 1710.06485 [astro-ph.EP].
- Pollack, J. B., et al. 1994. "Composition and radiative properties of grains in molecular clouds and accretion disks". *ApJ* 421 (): 615–639. doi:10.1086/173677.
- Pontoppidan, K. M., et al. 2014. "Volatiles in Protoplanetary Disks". *Protostars and Planets VI*: 363–385. doi:10.2458/azu_uapress_9780816531240-ch016. arXiv: 1401.2423 [astro-ph.EP].
- Prato, L., T. P. Greene, and M. Simon. 2003. "Astrophysics of Young Star Binaries". *ApJ* 584 (): 853–874. doi:10.1086/345828. eprint: astro-ph/0211376.
- Preibisch, T., and E. Mamajek. 2008. "The Nearest OB Association: Scorpius-Centaurus (Sco OB2)". In *Handbook of Star Forming Regions, Volume II*, ed. by B. Reipurth, 235.
- Preibisch, T., et al. 2002. "Exploring the Full Stellar Population of the Upper Scorpius OB Association". *AJ* 124 (): 404–416. doi:10.1086/341174.
- Pringle, J. E. 1981. "Accretion discs in astrophysics". *ARA&A* 19:137–162. doi:10.1146/annurev.aa.19.090181.001033.

- Qi, C., et al. 2011. “Resolving the CO Snow Line in the Disk around HD 163296”. *ApJ* 740, 84 (): 84. doi:10.1088/0004-637X/740/2/84. arXiv: 1107.5061 [astro-ph.SR].
- R Core Team. 2014. *R: A Language and Environment for Statistical Computing*. Vienna, Austria: R Foundation for Statistical Computing. <http://www.R-project.org/>.
- Rafikov, R. R. 2017. “Protoplanetary Disks as (Possibly) Viscous Disks”. *ApJ* 837, 163 (): 163. doi:10.3847/1538-4357/aa6249. arXiv: 1701.02352 [astro-ph.EP].
- Raghavan, D., et al. 2010. “A Survey of Stellar Families: Multiplicity of Solar-type Stars”. *ApJS* 190 (): 1–42. doi:10.1088/0067-0049/190/1/1. arXiv: 1007.0414 [astro-ph.SR].
- Ratzka, T., R. Köhler, and C. Leinert. 2005. “A multiplicity survey of the ρ Ophiuchi molecular clouds”. *A&A* 437 (): 611–626. doi:10.1051/0004-6361/20042107. eprint: astro-ph/0504593.
- Raymond, S. N., T. Quinn, and J. I. Lunine. 2005. “Terrestrial Planet Formation in Disks with Varying Surface Density Profiles”. *ApJ* 632 (): 670–676. doi:10.1086/433179. eprint: astro-ph/0507004.
- Readhead, A. C. S., et al. 1988. “Diffraction-limited imaging with ground-based optical telescopes”. *AJ* 95 (): 1278–1296. doi:10.1086/114724.
- Reboussin, L., et al. 2015. “Sensitive survey for ^{13}CO , CN, H_2CO , and SO in the disks of T Tauri and Herbig Ae stars. II. Stars in ρ Ophiuchi and upper Scorpius”. *A&A* 578, A31 (): A31. doi:10.1051/0004-6361/201525705. arXiv: 1504.04542 [astro-ph.SR].
- Rebull, L. M., et al. 2010. “The Taurus Spitzer Survey: New Candidate Taurus Members Selected Using Sensitive Mid-Infrared Photometry”. *ApJS* 186 (): 259–307. doi:10.1088/0067-0049/186/2/259. arXiv: 0911.3176 [astro-ph.SR].
- Ribas, Á., H. Bouy, and B. Merín. 2015. “Protoplanetary disk lifetimes vs. stellar mass and possible implications for giant planet populations”. *A&A* 576, A52 (): A52. doi:10.1051/0004-6361/201424846. arXiv: 1502.00631 [astro-ph.SR].
- Ribas, Á., et al. 2014. “Disk evolution in the solar neighborhood. I. Disk frequencies from 1 to 100 Myr”. *A&A* 561, A54 (): A54. doi:10.1051/0004-6361/201322597. arXiv: 1312.0609 [astro-ph.SR].
- Ricci, L., et al. 2010a. “Dust grain growth in ρ -Ophiuchi protoplanetary disks”. *A&A* 521, A66 (): A66. doi:10.1051/0004-6361/201015039. arXiv: 1008.1144 [astro-ph.SR].
- Ricci, L., et al. 2010b. “Dust properties of protoplanetary disks in the Taurus-Auriga star forming region from millimeter wavelengths”. *A&A* 512, A15 (): A15. doi:10.1051/0004-6361/200913403. arXiv: 0912.3356 [astro-ph.EP].

- . 2010c. “Dust properties of protoplanetary disks in the Taurus-Auriga star forming region from millimeter wavelengths”. *A&A* 512, A15 (): A15. doi:10.1051/0004-6361/200913403. arXiv: 0912.3356 [astro-ph.EP].
- Roccatagliata, V., et al. 2011. “Disk Evolution in OB Associations: Deep Spitzer/IRAC Observations of IC 1795”. *ApJ* 733, 113 (): 113. doi:10.1088/0004-637X/733/2/113. arXiv: 1103.5770 [astro-ph.SR].
- Roeser, S., M. Demleitner, and E. Schilbach. 2010. “The PPMXL Catalog of Positions and Proper Motions on the ICRS. Combining USNO-B1.0 and the Two Micron All Sky Survey (2MASS)”. *AJ* 139 (): 2440–2447. doi:10.1088/0004-6256/139/6/2440. arXiv: 1003.5852.
- Ruíz-Rodríguez, D., et al. 2018. “ALMA survey of circumstellar discs in the young stellar cluster IC 348”. *MNRAS* 478 (): 3674–3692. doi:10.1093/mnras/sty1351. arXiv: 1805.07590 [astro-ph.SR].
- Sacco, G. G., et al. 2012. “High-resolution Spectroscopy of Ne II Emission from Young Stellar Objects”. *ApJ* 747, 142 (): 142. doi:10.1088/0004-637X/747/2/142. arXiv: 1201.0184 [astro-ph.SR].
- Salyk, C., et al. 2014. “ALMA Observations of the T Tauri Binary System AS 205: Evidence for Molecular Winds and/or Binary Interactions”. *ApJ* 792, 68 (): 68. doi:10.1088/0004-637X/792/1/68. arXiv: 1407.2652 [astro-ph.SR].
- Schmidt-Kaler, T. 1982. “Automated spectral classification. A survey”. *Bulletin d'Information du Centre de Données Stellaires* 23 (): 2.
- Schwarz, K. R., et al. 2016. “The Radial Distribution of H₂ and CO in TW Hya as Revealed by Resolved ALMA Observations of CO Isotopologues”. *ApJ* 823, 91 (): 91. doi:10.3847/0004-637X/823/2/91. arXiv: 1603.08520 [astro-ph.SR].
- Service, M., et al. 2016. “A New Distortion Solution for NIRC2 on the Keck II Telescope”. *PASP* 128, no. 9 (): 095004. doi:10.1088/1538-3873/128/967/095004.
- Shakura, N. I., and R. A. Sunyaev. 1973. “Black holes in binary systems. Observational appearance.” *A&A* 24:337–355.
- Sheehan, P. D., and J. A. Eisner. 2018. “Multiple Gaps in the Disk of the Class I Protostar GY 91”. *ApJ* 857, 18 (): 18. doi:10.3847/1538-4357/aaae65. arXiv: 1803.02847 [astro-ph.SR].
- Shu, F. H., F. C. Adams, and S. Lizano. 1987. “Star formation in molecular clouds - Observation and theory”. *ARA&A* 25:23–81. doi:10.1146/annurev.aa.25.090187.000323.
- Shu, F. H., D. Johnstone, and D. Hollenbach. 1993. “Photoevaporation of the solar nebula and the formation of the giant planets”. *Icarus* 106 (): 92. doi:10.1006/icar.1993.1160.

- Sibthorpe, B., et al. 2018. “Analysis of the Herschel DEBRIS Sun-like star sample”. *MNRAS* 475 (): 3046–3064. doi:10.1093/mnras/stx3188. arXiv: 1803.00072 [astro-ph.EP].
- Sicilia-Aguilar, A., T. Henning, and L. W. Hartmann. 2010. “Accretion in Evolved and Transitional Disks in CEP OB2: Looking for the Origin of the Inner Holes”. *ApJ* 710 (): 597–612. doi:10.1088/0004-637X/710/1/597. arXiv: 1001.3026 [astro-ph.SR].
- Sicilia-Aguilar, A., et al. 2006. “Disk Evolution in Cep OB2: Results from the Spitzer Space Telescope”. *ApJ* 638 (): 897–919. doi:10.1086/498085.
- Siess, L., E. Dufour, and M. Forestini. 2000. “An internet server for pre-main sequence tracks of low- and intermediate-mass stars”. *A&A* 358 (): 593–599. eprint: astro-ph/0003477.
- Simon, J. B., K. Beckwith, and P. J. Armitage. 2012. “Emergent mesoscale phenomena in magnetized accretion disc turbulence”. *MNRAS* 422 (): 2685–2700. doi:10.1111/j.1365-2966.2012.20835.x. arXiv: 1203.0314 [astro-ph.SR].
- Simon, J. B., et al. 2015. “Magnetically driven accretion in protoplanetary discs”. *MNRAS* 454 (): 1117–1131. doi:10.1093/mnras/stv2070. arXiv: 1508.00904 [astro-ph.SR].
- Skrutskie, M. F., et al. 2006. “The Two Micron All Sky Survey (2MASS)”. *AJ* 131 (): 1163–1183. doi:10.1086/498708.
- Slesnick, C. L., J. M. Carpenter, and L. A. Hillenbrand. 2006. “A Large-Area Search for Low-Mass Objects in Upper Scorpius. I. The Photometric Campaign and New Brown Dwarfs”. *AJ* 131 (): 3016–3027. doi:10.1086/503560. eprint: astro-ph/0602298.
- Slesnick, C. L., L. A. Hillenbrand, and J. M. Carpenter. 2008. “A Large-Area Search for Low-Mass Objects in Upper Scorpius. II. Age and Mass Distributions”. *ApJ* 688 (): 377–397. doi:10.1086/592265. arXiv: 0809.1436.
- Soummer, R., L. Pueyo, and J. Larkin. 2012. “Detection and Characterization of Exoplanets and Disks Using Projections on Karhunen-Loève Eigenimages”. *ApJ* 755, L28 (): L28. doi:10.1088/2041-8205/755/2/L28. arXiv: 1207.4197 [astro-ph.IM].
- Straizys, V. 1992. *Multicolor stellar photometry*.
- Strom, K. M., et al. 1989. “Circumstellar material associated with solar-type pre-main-sequence stars - A possible constraint on the timescale for planet building”. *AJ* 97 (): 1451–1470. doi:10.1086/115085.
- Suzuki, T. K., and S.-i. Inutsuka. 2009. “Disk Winds Driven by Magnetorotational Instability and Dispersal of Protoplanetary Disks”. *ApJ* 691 (): L49–L54. doi:10.1088/0004-637X/691/1/L49. arXiv: 0812.0844.

- Takakuwa, S., et al. 2014. “Angular Momentum Exchange by Gravitational Torques and Infall in the Circumbinary Disk of the Protostellar System L1551 NE”. *ApJ* 796, 1 (): 1. doi:10.1088/0004-637X/796/1/1. arXiv: 1409.4903 [astro-ph.SR].
- Tang, Y.-W., et al. 2014. “Circumbinary Ring, Circumstellar Disks, and Accretion in the Binary System UY Aurigae”. *ApJ* 793, 10 (): 10. doi:10.1088/0004-637X/793/1/10. arXiv: 1407.4561.
- Tazzari, M., et al. 2016. “Multiwavelength analysis for interferometric (sub-)mm observations of protoplanetary disks. Radial constraints on the dust properties and the disk structure”. *A&A* 588, A53 (): A53. doi:10.1051/0004-6361/201527423. arXiv: 1512.05679.
- Tazzari, M., et al. 2017. “Physical properties of dusty protoplanetary disks in Lupus: evidence for viscous evolution?” *A&A* 606, A88 (): A88. doi:10.1051/0004-6361/201730890. arXiv: 1707.01499 [astro-ph.EP].
- Testi, L., et al. 2016. “Brown dwarf disks with ALMA: Evidence for truncated dust disks in Ophiuchus”. *A&A* 593, A111 (): A111. doi:10.1051/0004-6361/201628623. arXiv: 1606.06448 [astro-ph.SR].
- Testi, L., et al. 2014. “Dust Evolution in Protoplanetary Disks”. *Protostars and Planets VI*: 339–361. doi:10.2458/azu_uapress_9780816531240-ch015. arXiv: 1402.1354 [astro-ph.SR].
- Tofflemire, B. M., et al. 2017a. “Accretion and Magnetic Reconnection in the Classical T Tauri Binary DQ Tau”. *ApJ* 835, 8 (): 8. doi:10.3847/1538-4357/835/1/8. arXiv: 1612.02431 [astro-ph.SR].
- Tofflemire, B. M., et al. 2017b. “Pulsed Accretion in the T Tauri Binary TWA 3A”. *ApJ* 842, L12 (): L12. doi:10.3847/2041-8213/aa75cb. arXiv: 1706.07073 [astro-ph.SR].
- Tognelli, E., P. G. Prada Moroni, and S. Degl’Innocenti. 2011. “The Pisa pre-main sequence tracks and isochrones. A database covering a wide range of Z, Y, mass, and age values”. *A&A* 533, A109 (): A109. doi:10.1051/0004-6361/200913913. arXiv: 1107.2318 [astro-ph.SR].
- Tripathi, A., et al. 2017. “A millimeter Continuum Size-Luminosity Relationship for Protoplanetary Disks”. *ApJ* 845, 44 (): 44. doi:10.3847/1538-4357/aa7c62. arXiv: 1706.08977 [astro-ph.EP].
- Tripathi, A., et al. 2018. “The Millimeter Continuum Size-Frequency Relationship in the UZ Tau E Disk”. *ApJ* 861, 64 (): 64. doi:10.3847/1538-4357/aac5d6. arXiv: 1805.06457 [astro-ph.EP].
- Trotta, F., et al. 2013. “Constraints on the radial distribution of the dust properties in the CQ Tauri protoplanetary disk”. *A&A* 558, A64 (): A64. doi:10.1051/0004-6361/201321896. arXiv: 1308.5070 [astro-ph.SR].

- Turner, N. J., M. H. Lee, and T. Sano. 2014. “Magnetic Coupling in the Disks around Young Gas Giant Planets”. *ApJ* 783, 14 (): 14. doi:10.1088/0004-637X/783/1/14. arXiv: 1306.2276 [astro-ph.EP].
- Ubach, C., et al. 2012. “Grain growth signatures in the protoplanetary discs of Chamaeleon and Lupus”. *MNRAS* 425 (): 3137–3161. doi:10.1111/j.1365-2966.2012.21603.x. arXiv: 1207.0260 [astro-ph.SR].
- Valenti, J. A., G. Basri, and C. M. Johns. 1993. “T Tauri stars in blue”. *AJ* 106 (): 2024–2050. doi:10.1086/116783.
- van Boekel, R., et al. 2009. “An outflow origin of the [Ne II] emission in the T Tauri triplet”. *A&A* 497 (): 137–144. doi:10.1051/0004-6361/200811440. arXiv: 0902.1101 [astro-ph.SR].
- van Boekel, R., et al. 2017. “Three Radial Gaps in the Disk of TW Hydrae Imaged with SPHERE”. *ApJ* 837, 132 (): 132. doi:10.3847/1538-4357/aa5d68. arXiv: 1610.08939 [astro-ph.EP].
- van der Marel, N. 2017. “The ALMA Revolution: Gas and Dust in Transitional Disks”. In *Astrophysics and Space Science Library*, ed. by M. Pessah and O. Gressel, 445:39. Astrophysics and Space Science Library. doi:10.1007/978-3-319-60609-5_2.
- van der Marel, N., et al. 2013. “A Major Asymmetric Dust Trap in a Transition Disk”. *Science* 340 (): 1199–1202. doi:10.1126/science.1236770. arXiv: 1306.1768 [astro-ph.EP].
- van der Marel, N., et al. 2015. “Gas density drops inside dust cavities of transitional disks around young stars observed with ALMA”. *A&A* 579, A106 (): A106. doi:10.1051/0004-6361/201525658. arXiv: 1504.03927 [astro-ph.EP].
- van der Plas, G., et al. 2017. “Cavity and other radial substructures in the disk around HD 97048”. *A&A* 597, A32 (): A32. doi:10.1051/0004-6361/201629523. arXiv: 1609.02488 [astro-ph.SR].
- van der Plas, G., et al. 2016. “Dust Masses of Disks around 8 Brown Dwarfs and Very Low-mass Stars in Upper Sco OB1 and Ophiuchus”. *ApJ* 819, 102 (): 102. doi:10.3847/0004-637X/819/2/102. arXiv: 1602.01724 [astro-ph.SR].
- van Lieshout, R., et al. 2014. “Near-infrared emission from sublimating dust in collisionally active debris disks”. *A&A* 571, A51 (): A51. doi:10.1051/0004-6361/201322090. arXiv: 1404.3271 [astro-ph.EP].
- van Zadelhoff, G.-J., et al. 2003. “Axi-symmetric models of ultraviolet radiative transfer with applications to circumstellar disk chemistry”. *A&A* 397 (): 789–802. doi:10.1051/0004-6361:20021592. eprint: astro-ph/0211014.
- Visser, R., E. F. van Dishoeck, and J. H. Black. 2009. “The photodissociation and chemistry of CO isotopologues: applications to interstellar clouds and circumstellar disks”. *A&A* 503 (): 323–343. doi:10.1051/0004-6361/200912129. arXiv: 0906.3699.

- Wahhaj, Z., et al. 2010. “The Spitzer c2d Survey of Weak-line T Tauri Stars. III. The Transition from Primordial Disks to Debris Disks”. *ApJ* 724 (): 835–854. doi:10.1088/0004-637X/724/2/835. arXiv: 1009.4460 [astro-ph.SR].
- Walsh, C., et al. 2016. “ALMA Reveals the Anatomy of the mm-sized Dust and Molecular Gas in the HD 97048 Disk”. *ApJ* 831, 200 (): 200. doi:10.3847/0004-637X/831/2/200. arXiv: 1609.02011 [astro-ph.EP].
- Wang, J., et al. 2014a. “Influence of Stellar Multiplicity on Planet Formation. I. Evidence of Suppressed Planet Formation due to Stellar Companions within 20 AU and Validation of Four Planets from the Kepler Multiple Planet Candidates”. *ApJ* 783, 4 (): 4. doi:10.1088/0004-637X/783/1/4. arXiv: 1309.7097 [astro-ph.EP].
- Wang, J., et al. 2014b. “Influence of Stellar Multiplicity on Planet Formation. II. Planets are Less Common in Multiple-star Systems with Separations Smaller than 1500 AU”. *ApJ* 791, 111 (): 111. doi:10.1088/0004-637X/791/2/111. arXiv: 1407.3344 [astro-ph.EP].
- Wang, J., et al. 2015a. “Influence of Stellar Multiplicity On Planet Formation. III. Adaptive Optics Imaging of Kepler Stars With Gas Giant Planets”. *ApJ* 806, 248 (): 248. doi:10.1088/0004-637X/806/2/248. arXiv: 1505.05363 [astro-ph.EP].
- Wang, J., et al. 2015b. “Influence of Stellar Multiplicity on Planet Formation. IV. Adaptive Optics Imaging of Kepler Stars with Multiple Transiting Planet Candidates”. *ApJ* 813, 130 (): 130. doi:10.1088/0004-637X/813/2/130. arXiv: 1510.01964 [astro-ph.EP].
- Ward-Duong, K., et al. 2018. “The Taurus Boundary of Stellar/Substellar (TBOSS) Survey. II. Disk Masses from ALMA Continuum Observations”. *AJ* 155, 54 (): 54. doi:10.3847/1538-3881/aaa128. arXiv: 1712.07669 [astro-ph.EP].
- Wardle, M., and A. Koenigl. 1993. “The structure of protostellar accretion disks and the origin of bipolar flows”. *ApJ* 410 (): 218–238. doi:10.1086/172739.
- Watson, D. 2009. “Mineralization, Grain Growth, and Disk Structure: Observations of the Evolution of Dust in Protoplanetary Disks”. In *Cosmic Dust - Near and Far*, ed. by T. Henning, E. Grün, and J. Steinacker, 414:77. Astronomical Society of the Pacific Conference Series. arXiv: 0902.2744 [astro-ph.SR].
- Weidenschilling, S. J. 1977. “Aerodynamics of solid bodies in the solar nebula”. *MNRAS* 180 (): 57–70. doi:10.1093/mnras/180.1.57.
- Werner, M. W., et al. 2004. “The Spitzer Space Telescope Mission”. *ApJS* 154 (): 1–9. doi:10.1086/422992. eprint: astro-ph/0406223.
- Whipple, F. L. 1972. “On certain aerodynamic processes for asteroids and comets”. In *From Plasma to Planet*, ed. by A. Elvius, 211.

- White, R. J., and G. Basri. 2003. “Very Low Mass Stars and Brown Dwarfs in Taurus-Auriga”. *ApJ* 582 (): 1109–1122. doi:10.1086/344673. eprint: astro-ph/0209164.
- Williams, J. P., and W. M. J. Best. 2014. “A Parametric Modeling Approach to Measuring the Gas Masses of Circumstellar Disks”. *ApJ* 788, 59 (): 59. doi:10.1088/0004-637X/788/1/59. arXiv: 1312.0151 [astro-ph.EP].
- Williams, J. P., and L. A. Cieza. 2011. “Protoplanetary Disks and Their Evolution”. *ARA&A* 49 (): 67–117. doi:10.1146/annurev-astro-081710-102548. arXiv: 1103.0556 [astro-ph.GA].
- Williams, J. P., et al. 2013. “A SCUBA-2 850- μ m survey of protoplanetary discs in the σ Orionis cluster”. *MNRAS* 435 (): 1671–1679. doi:10.1093/mnras/stt1407. arXiv: 1307.7174.
- Wilner, D. J., et al. 2005. “Toward Planetesimals in the Disk around TW Hydrae: 3.5 Centimeter Dust Emission”. *ApJ* 626 (): L109–L112. doi:10.1086/431757. eprint: astro-ph/0506644.
- Windmark, F., et al. 2012. “Planetesimal formation by sweep-up: how the bouncing barrier can be beneficial to growth”. *A&A* 540, A73 (): A73. doi:10.1051/0004-6361/201118475. arXiv: 1201.4282 [astro-ph.EP].
- Winn, J. N., and D. C. Fabrycky. 2015. “The Occurrence and Architecture of Exoplanetary Systems”. *ARA&A* 53 (): 409–447. doi:10.1146/annurev-astro-082214-122246. arXiv: 1410.4199 [astro-ph.EP].
- Wizinowich, P. L., et al. 2006. “The W. M. Keck Observatory Laser Guide Star Adaptive Optics System: Overview”. *PASP* 118 (): 297–309. doi:10.1086/499290.
- Woitke, P. 2015. “Heating and cooling processes in disks”. In *European Physical Journal Web of Conferences*, 102:00011. European Physical Journal Web of Conferences. doi:10.1051/epjconf/201510200011.
- Woitke, P., et al. 2011. “The unusual protoplanetary disk around the T Tauri star ET Chamaeleontis”. *A&A* 534, A44 (): A44. doi:10.1051/0004-6361/201116684. arXiv: 1103.5309 [astro-ph.EP].
- Wright, E. L., et al. 2010. “The Wide-field Infrared Survey Explorer (WISE): Mission Description and Initial On-orbit Performance”. *AJ* 140 (): 1868–1881. doi:10.1088/0004-6256/140/6/1868. arXiv: 1008.0031 [astro-ph.IM].
- Wright, J. T., et al. 2011. “The Exoplanet Orbit Database”. *PASP* 123 (): 412. doi:10.1086/659427. arXiv: 1012.5676 [astro-ph.SR].
- Wyatt, M. C., et al. 2015. “Five steps in the evolution from protoplanetary to debris disk”. *Ap&SS* 357, 103 (): 103. doi:10.1007/s10509-015-2315-6. arXiv: 1412.5598 [astro-ph.EP].

- Yang, H., et al. 2012. “A Far-ultraviolet Atlas of Low-resolution Hubble Space Telescope Spectra of T Tauri Stars”. *ApJ* 744, 121 (): 121. doi:10.1088/0004-637X/744/2/121. arXiv: 1205.4789 [astro-ph.SR].
- Yasui, C., et al. 2014. “Rapid evolution of the innermost dust disc of protoplanetary discs surrounding intermediate-mass stars”. *MNRAS* 442 (): 2543–2559. doi:10.1093/mnras/stu1013. arXiv: 1405.5284 [astro-ph.SR].
- Yelda, S., et al. 2010. “Improving Galactic Center Astrometry by Reducing the Effects of Geometric Distortion”. *ApJ* 725 (): 331–352. doi:10.1088/0004-637X/725/1/331. arXiv: 1010.0064.
- Youdin, A. N., and J. Goodman. 2005. “Streaming Instabilities in Protoplanetary Disks”. *ApJ* 620 (): 459–469. doi:10.1086/426895. eprint: astro-ph/0409263.
- Yu, M., et al. 2017. “Disk Masses around Solar-mass Stars are Underestimated by CO Observations”. *ApJ* 841, 39 (): 39. doi:10.3847/1538-4357/aa6e4c. arXiv: 1704.05508 [astro-ph.EP].
- Zhang, K., et al. 2014. “Comparison of the Dust and Gas Radial Structure in the Transition Disk [PZ99] J160421.7-213028”. *ApJ* 791, 42 (): 42. doi:10.1088/0004-637X/791/1/42. arXiv: 1406.6974 [astro-ph.EP].
- Zhang, K., et al. 2016. “On the Commonality of 10-30 AU Sized Axisymmetric Dust Structures in Protoplanetary Disks”. *ApJ* 818, L16 (): L16. doi:10.3847/2041-8205/818/1/L16. arXiv: 1601.05182 [astro-ph.EP].
- Zhu, Z., and C. Baruteau. 2016. “Gas and dust hydrodynamical simulations of massive lopsided transition discs - I. Gas distribution”. *MNRAS* 458 (): 3918–3926. doi:10.1093/mnras/stw202. arXiv: 1511.03497 [astro-ph.EP].
- Zuckerman, B., T. Forveille, and J. H. Kastner. 1995. “Inhibition of giant-planet formation by rapid gas depletion around young stars”. *Nature* 373 (): 494–496. doi:10.1038/373494a0.
- Zuckerman, B., and I. Song. 2012. “A 40 Myr Old Gaseous Circumstellar Disk at 49 Ceti: Massive CO-rich Comet Clouds at Young A-type Stars”. *ApJ* 758, 77 (): 77. doi:10.1088/0004-637X/758/2/77. arXiv: 1207.1747 [astro-ph.SR].